Probing the Deformation of Ductile Polycrystals by Synchrotron X-ray Micro-diffraction

Felix Hofmann

Trinity College

under the supervision of

Prof. Alexander M Korsunsky

This thesis has been submitted to the University of Oxford

for the degree of Doctor of Philosophy

in the Department of Engineering Science

January 2011

Abstract

Microscopic beams of penetrating synchrotron radiation provide a unique tool for the analysis of material structure and deformation. This thesis describes my contributions to the development of new synchrotron X-ray micro-beam diffraction experimental techniques and data interpretation, and the use of experimental results for the validation of material deformation models.

To study deeply buried material volumes in thick samples, the micro-beam Laue technique was extended to higher photon energies. Through-thickness resolution was achieved either by a wire scanning approach similar to Differential Aperture X-ray Microscopy (DAXM), or by applying tomographic reconstruction principles to grain-specific Laue pattern intensity. Both techniques gave promising first results.

For reliable micro-beam Laue diffraction measurements of elastic strains in individual grains of a polycrystal, understanding of the error sources is vital. A novel simulation-based error analysis framework allowed the assessment of individual contributions to the total measurement error. This provides a rational basis for the further improvement of experimental setups.

For direct comparison of experimental measurements and dislocation dynamics simulations, diffraction post-processing of dislocation models in two and three dimensions was developed. Simulated diffraction patterns of two-dimensional dislocation cell/wall type structures captured correctly some of the features observed experimentally in reciprocal space maps of a large-grained, lightly deformed aluminium alloy sample. Crystal lattice rotations computed from three-dimensional dislocation dynamics simulations of a Frank-Read source showed anisotropic orientation spread similar to that observed in micro-beam Laue experiments.

For the experimental study of crystal lattice distortion, a novel technique was proposed that combines micro-beam Laue diffraction with scanning white-beam topography. Diffraction topography allows the study of lattice rotation at scales smaller than the scanning beam size. The new technique makes it possible to apply classical topography methods to deformed samples.

Contents

Acknowledgements

I would like to thank my supervisor, Prof. Alexander M Korsunsky, for his help, guidance, advice and support throughout this project, and am very grateful for the many opportunities he has given me. Working with him over the past four years has been a great pleasure; I cannot imagine a better supervisor.

My wholehearted thanks go to my wonderful girlfriend Sinéad Keegan. She helped with many of the finer mathematical points and tirelessly proofread every draft. Her encouragement throughout this thesis was invaluable.

I am very grateful to my parents for their proactive approach at every stage of my education. Without them, I would not be where I am today.

A number of people in Oxford and elsewhere have helped and contributed to this project. In particular my thanks go to: Brian Abbey, Nikolaos Baimpas, Jonathan Belnoue, Thomas Buslaps, Stuart Carter, Benjamin Cartlidge, Steve Collins, Leigh Connor, Andrei Constantinescu, Igor Dolbnya, Kalin Dragnevski, Michael Drakopoulos, Richard Duffin, Sophie Eve, Dick Froud, Guillaume Gaucherin, Eveline Hofmann, Tea-sung Jun, Maurice Keeble-Smith, Taehoon Kim, Steve R Lett, Wencai Liu, Ian R Lloyd, Andrew Malandain, Jean-Sébastien Micha, Wolfgang Mix, Cristian Mocuta, John Mooney, Matthew Peel, Alexander Rack, Christina Reinhard, Kawal Sawhney, Xu Song, Tan Sui, Dominique Thiaudiere, Wim Vorster, Neil Warland, Mengyin Xie, Xuejuan Xu, and Shu-Yan Zhang.

My thanks also go to the staff and students of Trinity College. It has been a delightful place to live, study and work.

I would like to acknowledge the funding I received from the EPSRC and the beamtime allocations from the DLS, Soleil and the ESRF.

Finally I would very much like to thank my examiners, Dr. John Huber and Prof. Olivier Castelnau, for taking the time to read my thesis so thoroughly and for sparking some interesting discussions in the viva.

Common abbreviations

ALS	Advanced Light Source, Berkeley, CA, USA
AMPW	Asymmetric Multipole Wiggler
APD	Avalanche Photo Diode
APS	Advanced Photon Source, Argonne, IL, USA
BCC	Body Centered Cubic (Crystal Structure)
CCD	Charge-coupled Device
CLS	Canadian Light Source, Saskatoon, Canada
CP	Commercially Pure
CRSS	Critical Resolved Shear Stress
DAXM	Differential Aperture X-ray Microscopy
DCM	Double Crystal Monochromator
DCT	Diffraction Contrast Tomography
DDD	Discrete Dislocation Dynamics
DIC	Digital Image Correlation
DLS	Diamond Light Source, Didcot, UK
EBSD	Electron Backscatter Diffraction
ESRF	European Synchrotron Radiation Facility, Grenoble, France
FCC	Face Centered Cubic (Crystal Structure)
FWHM	Full Width at Half Maximum
GNB	Geometrically Necessary Boundary
GND	Geometrically Necessary Dislocation
HEDAXM	High Energy Differential Aperture X-ray Microscopy
HETL	High Energy Transmission Laue (Diffraction)
KB	Kirkpatrick-Baez (Focussing Mirrors)

LOT	Laue Orientation Tomography
RSM	Reciprocal Space Mapping
SEM	Scanning Electron Microscopy
SLS	Swiss Light Source, Villigen, Switzerland
SSD	Statistically Stored Dislocations
STXM	Scanning Transmission X-ray Microscopy
TEM	Transmission Electron Microscopy

Chapter 1

Introduction

Reliable, cheap and safe air travel is a commodity most of us take for granted. Over the past four decades demand has steadily increased, with passenger numbers growing by more than half in the past ten years. At the same time the pressure to lower emissions from air travel is increasing and fuel prices are rising. Manufacturers are meeting these difficult needs of the market with the introduction of aeroplanes of increasing size and with improved efficiency. A prime example for this is the Airbus A380, powered by four Rolls-Royce Trent 900 engines. The sheer increase in the size of this engine compared to some of its predecessors is evident from figure 1.1 which shows a Trent 900 engine mounted on an Airbus A340-300 testbed for flight testing. Each Trent 900 engine produces more than twice as much thrust as the CFM56-5C4 engines which are normally fitted to the A340-300. Such an increase in engine size brings new complexities with it. It is not simply a case of up-scaling an existing engine, but in many areas a complete re-design, with new manufacturing methods and new materials, is necessary. To maximise engine efficiency, the performance of the materials used has to be pushed to the limit. However, this must be done reliably and most importantly safely. For this a thorough understanding of material behaviour from the macroscopic to the microscopic scale, its response to complex loading conditions, the evolution of its properties over time and its failure modes is essential.

In the modern engineering alloys used in aeroengines, deformation behaviour at the grain scale becomes important when the length scale of macroscopic, struc-

Figure 1.1: Rolls-Royce Trent 900 engine mounted on an Airbus A340-300 testbed for flight testing [1].

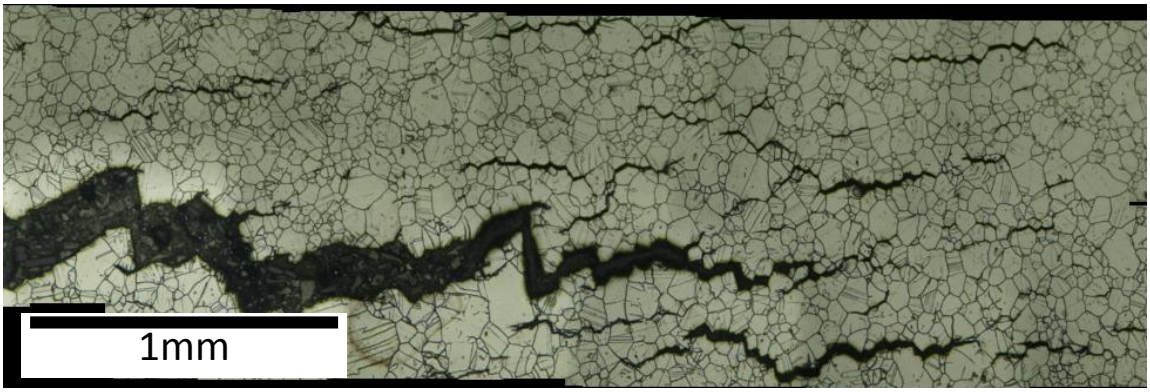

Figure 1.2: Intragranular crack growth from a notch in a C263 nickel-base superalloy subjected to cyclic loading and creep at 750°C [2].

tural features approaches the microstructural length scale. This is illustrated by the growth of a fatigue crack from a notch in a C263 nickel superalloy subjected to cyclic loading and creep [2] (figure 1.2). Nickel superalloys show excellent mechanical strength and good creep resistance at high temperatures. This makes them very suitable for applications such as turbine blades and vanes, or structural components in the "hot" parts of aeroengines. Component failure in these applications is not acceptable. At best, it would lead to significant financial losses and, at worst, to a loss of life.

The overall lifetime of a component under a given service loading is determined by the number of cycles required for initiation and propagation of a flaw or crack. To prevent in-service failure a stringent inspection regime is required. This must be based on an understanding of crack initiation and growth. In modern, intricately designed components, notches are present with radii approaching the local microstructural length scale (e.g. screw thread, fine cooling holes, machining marks, etc.). The greatest loading due to the stress concentration at the tip of the notch is only experienced by a small number of grains in this location. In fact, it is their behaviour that determines the length of time required for a crack to initiate, and thereby the largest part of the component life. Once a crack has initiated, the exact path it follows depends on the applied loading at the component level and the way it is distributed at the micro-scale. This is turn depends on the local microstructure, lattice orientations of grains, manufacturing defects, phase distribution, micro-scale residual stresses, etc. Clearly a quantitative understanding of these effects is vital for improved accuracy of component service life predictions.

A common problem in consumer electronics is the growth of tin whiskers illustrated in figure 1.3. Tin is used to coat the copper frames on which electronic components are mounted. At the interface between the substrate and coating, Cu_6Sn_5 is formed. This introduces compressive stress in the tin coating which can be relieved by whisker growth. Lengths of tin whiskers can reach up to several millimetres. In microelectronic circuits, whiskers can cause short circuits and critical damage to components, sometimes with dramatic consequences. To develop

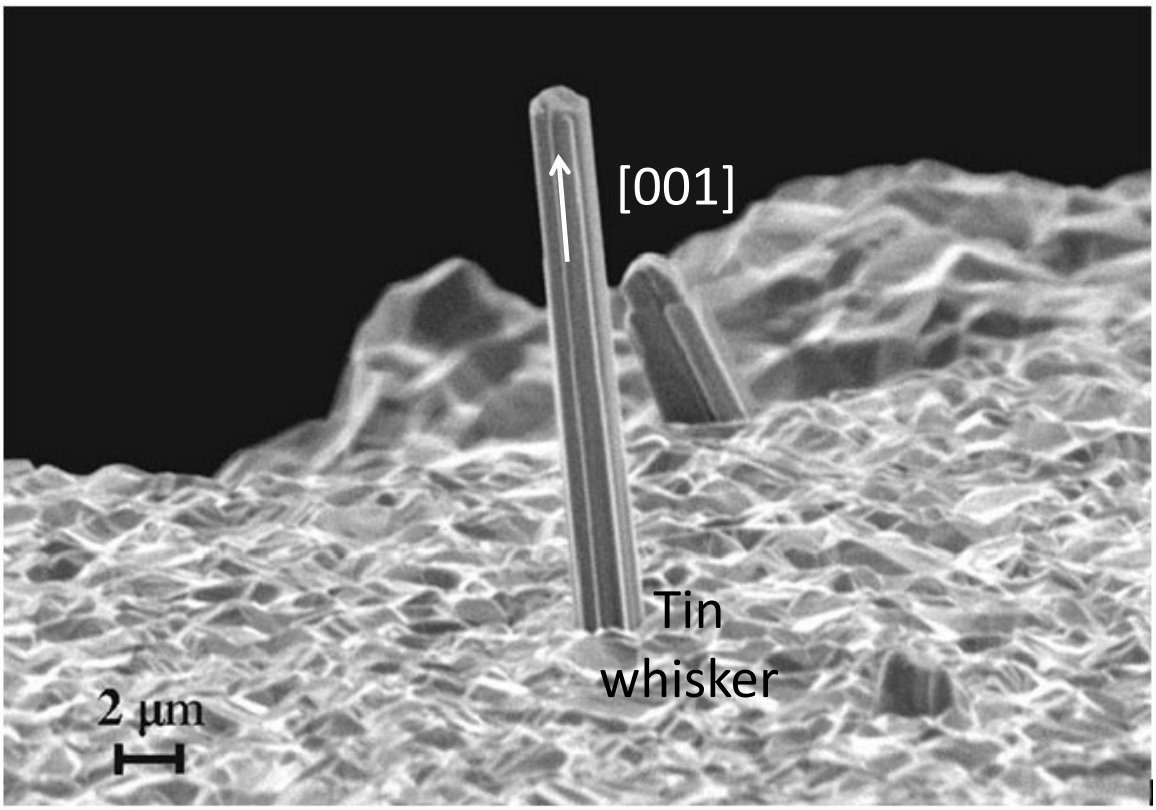

Figure 1.3: Tin whisker growth from a tin coated copper leadframe [3]

techniques to eliminate this problem, in-depth understanding is required of the local, microstructural features and stress states that give rise to whisker growth.

The above examples demonstrate the importance of detailed knowledge of local microstructure and deformation response in components for modern mechanical and electrical engineering applications. For efficient and reliable designs, the effects of the deformation behaviour at the microstructural scale must be incorporated in the macroscopic design.

Historically, mechanical design was concerned with the building of large scale structures and macroscopic components. In the 19th century, the development of the steam engine by James Watt, based on the design of Thomas Newcomen and Thomas Savery, was a major driving force behind the industrial revolution. It allowed the building of mechanically powered machines, fundamentally changing manufacturing methods and transport. The design of individual components was function-oriented. The selection of suitable materials was based on experience and their metallurgical properties at the macro-scale. Often a trial-and-error approach was required to determine if a given component was fit for purpose. Many

of the finer points of material behaviour, such as the response to cyclic loading or failure by fracture, were not well understood. The disaster of the Titanic is a prime example of this.

In early material deformation theories for engineering design, the macroscopic response of polycrystalline alloys was captured by a set of empirical equations based on macroscopic experimental measurements. These averaged over a large number of constituent grains and captured bulk properties, such as stiffness or yield stress. However, whilst these phenomenological approaches reproduced macroscopic material behaviour within the experimentally explored envelope, they did not provide any physical insight or predictive capability.

From the 1960s, the descriptions of material behaviour evolved to include the effects of microstructural features at the grain scale. This development was driven by the needs of the mechanical engineering industry, but also by the developing electronics industry with the need for miniaturisation. With the advent of computer simulation tools in the 1970s and 1980s, and the development of finite element codes, the modelling of complex mechanical components based on constitutive material equations became feasible. Greater physical understanding could be achieved with the introduction of crystal plasticity models. These captured deformation by continuum description of crystallographic slip at the microscopic scale of individual crystallites.

The predominant trend since has been to study material deformation behaviour at decreasing length scales, right down to the atomistic level. At the same time refinements were introduced to models at the coarser scales to capture better the underlying physics.

Bridging the gap between the scale of continuum crystal plasticity and atomistic simulations of deformation are discrete dislocation dynamics (DDD) models. Dislocations are line defects, each carrying a small amount of inelastic deformation. By their motion in a crystal, inelastic strain is accommodated. Whilst classical analytical solutions for dislocation statics have long been available, only the advent of high performance computing made it feasible to simulate the motion of large numbers of dislocations. These simulations have proven very powerful in explaining

macroscopically observed material behaviour. They can provide a physical basis for formulating the empirical laws used in crystal plasticity simulations. DDD simulations in turn are informed by models of deformation at the yet finer, atomistic scale.

For the quantitative validation of DDD and crystal plasticity models, they must be compared with experimental measurements made at the same scale. Ideally, these measurements should provide information about dislocation positions, or at least about dislocation densities, and spatially resolved measures of the associated lattice rotation and strain fields. Scanning electron microscopy (SEM) combined with electron backscatter diffraction (EBSD) allows high resolution measurements of lattice rotation and strain on the sample surface. Transmission Electron Microscopy (TEM) provides a means of imaging dislocation structure within a thin sliver of material ($\sim 100\mathrm{nm}$ thick). The restrictions of electron microscopy techniques to the sample surface or thin sections make them limited, if very useful aids, but not sufficiently versatile means for three-dimensional microstructure characterisation.

Highly penetrating synchrotron X-rays provide a powerful tool for the study of material behaviour in the bulk. Over the past two decades, high brilliance X-ray beams have become available to the scientific community at third generation synchrotron sources. A number of different experimental techniques have been developed to allow the probing of material structure and deformation behaviour at the micro- and nano-scale. The structure of materials at these levels can be determined by micro-tomography methods. Features that are still too small to be resolved by this technique can be studied by small angle scattering or by coherent diffractive imaging techniques.

Diffraction measurements allow the probing of elastic strain in crystalline samples. A particulary useful tool for the study of grain deformation response is microbeam Laue diffraction. A polychromatic X-ray beam probe is used, focused or collimated to a spot size smaller than the local grain size. By rastering this probe across the sample surface, intragranular sampling volumes can be studied. Diffraction patterns consisting of a number of Laue peaks are captured on an area detector. Based on their indexation and the refinement of Laue peak positions, the

local lattice orientation and elastic strain tensor can be computed. A wide range of applications of this technique have been reported in the literature, from the study of tin whisker growth and electromigration in microelectronics, to the investigation of deformation behaviour of thin films. To achieve three-dimensional resolutions a number of triangulation techniques were proposed, with the aim of determining the exact position of the scattering volume giving rise to each diffraction peak. The most successful approach was the differential aperture X-ray microscopy (DAXM) technique, which was used in particular for the study of samples with steep orientation gradients after large plastic deformation.

To maximise the benefit that can be derived from these advanced characterisation techniques, the direct comparison of experimental measurements with mechanical models at the same scale must be made.

The aims of this thesis are to contribute to the establishment of this vital connection, to develop further the existing micro-beam Laue diffraction technique, and to extend its range of capabilities. The thesis is arranged into the following chapters:

Chapter 2 gives an overview of the relevant literature. It starts with the techniques of material deformation modelling, moving from the macroscopic scale down to the finer scale of grain-level deformation. A detailed description of different approaches to discrete dislocation dynamics modelling is given, focusing on the differences between two-dimensional and three-dimensional models. Next, the relevant diffraction techniques are reviewed, concentrating on reciprocal space mapping and micro-beam Laue diffraction.

Chapter 3 describes the development of a novel experimental setup on beamline B16 (DLS) to allow the study of misorientation within the scattering volume. It combines micro-beam Laue diffraction and scanning white beam topography. For the reliable measurement of lattice strains in micro-beam Laue diffraction experiments, an understanding of the errors involved is essential. A simulation-based error analysis framework is developed which allows the assessment of individual contributions to the total measurement error. It is validated by comparison with measurement results from beamline BM32

(ESRF) and provides a rational basis for the further refinement of experimental configurations.

Chapter 4 considers the post-processing of discrete dislocation models to provide a comparison with experimentally collected diffraction patterns. Diffraction post-processing of a simple, two-dimensional cell/wall-type dislocation model is compared to experimental reciprocal space maps from a large-grained, mildly deformed aluminium alloy sample. Next, a procedure is developed for computing lattice rotations from three-dimensional dislocation structures discretised into segments. This is used to map the lattice rotations due to a Frank-Read source at different stages of the emission of a dislocation loop, based on dislocation positions computed using the ParaDiS DDD simulation code.

Chapter 5 describes the extension of the micro-beam Laue diffraction technique to higher photon energies for the measurement of grains buried in thick samples. Initially measurements were made on a pseudo two-dimensional nickel sample at beamline ID15 (ESRF). Through-thickness resolution was achieved either by applying tomographic reconstruction principles to the grain-specific scattered intensity, or by using a scanning wire approach similar to the DAXM technique. Both methods were tested on beamline I12 (DLS). An overview of the first results is given.

At the end of every chapter some suggestions for further work are made. Conclusions are drawn in **Chapter 6**.

Chapter 2

Scientific background and methods

This chapter provides an overview of the literature on the types of X-ray diffraction and material deformation modelling relevant to this thesis. First (§ 2.1), material modelling and experiment will be discussed, moving from the macro- to the micro-scale. Then, a more detailed description of dislocation dynamics models will be given, focusing in particular on the two-dimensional Needleman and van der Giessen framework [4] and the three dimensional Bulatov, Cai and Arsenlis [5–7] approach. Next (§ 2.2), some basics of X-ray diffraction will be recalled, along with an overview of experimental techniques. Then the methods of particular interest to this thesis, namely reciprocal space mapping and micro-beam Laue diffraction, will be presented in more detail.

2.1 Material deformation and its modelling at different scales

2.1.1 Deformation at the macro-scale (continuum)

At the macroscopic scale of classical continuum solid mechanics, material properties of metallic polycrystals are observed as an average over a large number of constituent grains. The material can be treated as a homogenous continuum and deformation behaviour captured by a set of empirical constitutive equations. These constitutive equations implicitly take into account a homogenised form of the de-

tails of behaviour at the finer, underlying scales. A summary of such macroscopic continuum models and their possible implementations is given by Lemaitre and Chaboche [8], Crisfield [9], Hill [10] and Dunne and Petrinic [11].

2.1.2 Deformation at the grain/micro scale

Moving to the next, finer, scale, deformation can be considered at the level of individual grains in the polycrystal. Grain-size strengthening effect was first reported by Hall [12] and Petch [13]. Experimental evidence of sample size effects was determined by Fleck et al. [14] and Stölken and Evans [15] using micro-bending and torsion. Micro-indentation results [16] and the deformation behaviour of metal matrix composites [17] showed the strong influence of deformation gradients on material response. In polycrystalline metal aggregates, strain gradients arise primarily due to incompatibilities associated with the inhomogeneous plastic deformation of neighbouring grains. The lattice rotations arising from steep deformation gradients have to be accommodated. Ashby [18] pointed out the fundamental difference between homogeneous plastic deformation, that can be accommodated by arbitrary distribution of dislocations, referred to as statistically stored dislocations (SSD), and the particular nature of dislocation distributions required to accommodate plastic strain gradients, referred to as geometrically necessary dislocations (GND).

2.1.3 Strain gradient plasticity

This distinction was affirmed by the development of strain gradient theories of deformation that are clearly linked to the presence of GNDs [14, 19–21]. The introduction of GNDs, in addition to the inherently random SSDs, results in additional strengthening of the material.

Gradient-dependent behaviour becomes important when the length scale on which the deformation gradient is present approaches the scale of the dominant microstructural feature. Thus, polycrystals with smaller grain size tend to exhibit stronger mechanical response due to the presence of GNDs associated with strain

gradients. Strain gradient plasticity concepts are often used to describe scale effects in metallic polycrystals. A number of phenomenological theories incorporating higher-order strain gradients, couple stresses and higher-order boundary conditions were proposed [14, 22, 23]. Alternative, physically-based approaches describe strain gradient effects without higher order stresses or additional boundary conditions [24–30]. Here, strain gradient effects are introduced directly into the evolution laws of the internal slip system state variables. These types of theories have been shown capable of providing physical insight into the effects of microstructure on macroscopically observed phenomena, such as rate-independent plastic deformation and visco-plasticity in both single crystal and polycrystalline materials [31, 32].

2.1.4 Discrete dislocation dynamics modelling

Dislocations are line defects in crystals and fall into the category of self equilibrating deformation states known as nuclei of strain in continuum elastic theory (figure 2.1). The quantities associated with a dislocation are Burgers vector, dislocation line direction, slip plane and slip direction as defined for example by Hull and Bacon [33]. Discrete dislocation dynamics modelling (DDD) fills the gap in the progressively refined sequence of scales from macroscopic continuum strain gradient crystal plasticity models down to simulations at the atomistic level. Modelling of deformation at the atomistic scale constitutes within itself a vast body of research, that is here omitted for brevity. However many of the results from atomistic calculations are of direct importance for DDD models and will be referred to occasionally. A summary of techniques is provided by Bulatov and Cai [5].

DDD simulations model the motion of individual dislocations to accommodate externally imposed displacements or to support applied stress. In order to achieve an accurate description of the mechanical behaviour of ductile materials, it is necessary to identify suitable dislocation mobilities [5, 35, 36], represent the mechanisms of dislocation interaction [37, 38] and account for different boundary conditions of the simulation volume [4, 5, 39]. Some important examples of the number of different approaches that can be considered, are discussed below.

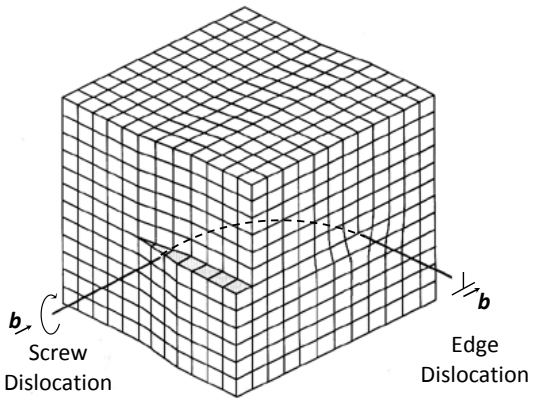

Figure 2.1: A dislocation line in a crystal displaying screw (left) and edge character (right) (Warnes [34]).

2D dislocation dynamics modelling

Van der Giessen and Needleman [4] consider a two-dimensional framework where edge dislocations lie perpendicular to the simulation plane and glide along discrete, predefined slip systems. Dislocations are nucleated from a number of randomly distributed sources, and their motion and interaction is governed by a set of constitutive rules. The boundary value problem is solved by a finite element model that provides a continuous stress field which is superimposed on the dislocation stress field to produce the total stress field at each time step.

The elastic displacement field induced by an edge dislocation, $\perp_{z,x}$, with line direction along the z-axis and Burgers vector, b_x, along the x-axis, in an isotropically elastic material with shear modulus μ and Poisson's ratio ν, is:

$$u_{x,\perp_{zx}}(x,y) = \frac{b_x}{2\pi}\left[\arctan\left(\frac{y}{x}\right) + \frac{yx}{2(1-\nu)(x^2+y^2)}\right], \tag{2.1}$$

$$u_{y,\perp_{zx}}(x,y) = -\frac{b_x}{2\pi}\left[\frac{(1-2\nu)}{4(1-\nu)}\ln(y^2+x^2) + \frac{x^2-y^2}{4(1-\nu)(x^2+y^2)}\right], \tag{2.2}$$

$$u_{z,\perp_{zx}}(x,y) = 0. \tag{2.3}$$

Based on these displacements and making the plane strain assumption, the stresses in the x - y plane due to the dislocation can be found as:

$$\sigma_{xx} = \frac{\mu b_x}{2\pi(1-\nu)} \frac{y(3x^2+y^2)}{(x^2+y^2)^2}, \tag{2.4}$$

$$\sigma_{yy} = \frac{\mu b_x}{2\pi(1-\nu)} \frac{y(x^2-y^2)}{(x^2+y^2)^2}, \tag{2.5}$$

$$\sigma_{xy} = \frac{\mu b_x}{2\pi(1-\nu)} \frac{x(x^2-y^2)}{(x^2+y^2)^2}. \tag{2.6}$$

Motion of the ith edge dislocation in the simulation plane is controlled by the component, F_i, of the Peach-Koehler force in the slip plane and normal to the dislocation line:

$$F_i = \tau_i b_i, \tag{2.7}$$

where b_i is the Burgers vector component in the slip plane of the ith dislocation and τ_i the scalar resolved shear stress acting in the slip plane, perpendicular to the dislocation line. τ_i is given by:

$$\tau_i = \hat{\mathbf{n}}_i \cdot \left((\tilde{\sigma} + \sum_{j \neq i} \sigma_j) \cdot \hat{\mathbf{s}}_i \right), \tag{2.8}$$

where $\hat{\mathbf{n}}_i$ is the normal to the slip plane on which the ith dislocation propagates, and $\hat{\mathbf{s}}_i$ is the slip direction. $\tilde{\sigma}$ is the externally applied stress. This also contains the contribution from the elastic finite element model used to solve the boundary value problem. The $\sum_{j \neq i} \sigma_j$ term is the stress tensor due to all other dislocations enumerated by j. The velocity of the ith dislocation, v_i, in the slip plane, perpendicular to the dislocation line direction is related to the Peach-Koehler force by a simple linear drag relation with a drag coefficient B:

$$v_i = \frac{F_i}{B}. \tag{2.9}$$

Dislocation motion is obstructed by randomly placed obstacles (other lattice defects, precipitates of other phases etc.). When a dislocation reaches an obstacle it is pinned. Pinned dislocations often give rise to dislocations pile-ups. When a critical shear stress, τ_{obs} is reached at the pinned dislocation, the pinned disloca-

tion is released. Grain boundaries may be modelled as impenetrable or partially penetrable to dislocations.

Dislocations are introduced from a number of randomly distributed point sources that mimic Frank-Read sources in 3D. A dislocation dipole is emitted from a source when the shear stress at the source exceeds a critical value τ_{nuc}. The initial distance L_{nuc} between the two dislocations in the dipole is:

$$L_{\mathrm{nuc}} = \frac{\mu}{2\pi(1-\nu)} \frac{b}{\tau_{\mathrm{nuc}}}. \tag{2.10}$$

This ensures that, when the new dislocation dipole is created, the total resolved shear stress, τ_{nuc}, balances the attractive shear stress the two dislocations exert on each other.

Dislocation motion is computed using an incremental, explicit time integration scheme.

This basic framework is common to the whole family of two-dimensional DDD simulations that were built on the initial Van der Giessen and Needleman model [4]. Extensions to finite deformations and rotations were proposed by Deshpande et al. [40]. To overcome some of the limitations of the model due to its confinement to two dimensions, the set of constitutive rules was extended to include Frank-Read source formation and annihilation, and dislocation line tension [41].

The two-dimensional DDD framework has been applied to a wide range of problems. Bittencourt [42] presented a comparison with the continuum crystal viscoplasticity model proposed by Gurtin [43] and discussed the importance of the inherent length scale formed by the blocked dislocation boundary layer that forms at the interface between a thin film and its substrate. Similar size effects were observed in the case of single- and polycrystalline thin films [44, 45] and in free standing single- and polycrystals as a function of the specimen boundary conditions [46–49].

Widjaja et al. [50–52] and Balint et al. [53] used the dislocation framework to model micro-indentation, and Deshpande et al. [54, 55] considered fatigue crack growth. A recent implementation of the framework was presented by Gaucherin et al. [56], successfully capturing the orientation dependance of yield, Hall-Petch

behaviour and cyclic hardening. Similarly successful capturing of grain size dependance of flow stress in polycrystals was reported by Balint et al. [57].

The attraction of the two-dimensional DDD framework are its comparative simplicity and ease of implementation. It has been shown capable of capturing numerous experimentally observed effects and allowed their explanation in terms of dislocation interactions, and the confining effects of grain boundaries and specimen geometry. However, the framework does remain constrained to two dimensions. It considers edge dislocations only and hence does not allow the modelling of three-dimensional dislocation interactions. This limits the physical validity of the simulation results.

3D dislocation dynamics modelling - Devincre and Kubin

Devincre and Kubin [39, 58, 59] developed a three-dimensional approach to DDD simulations using a discrete lattice-based framework. Dislocations are considered to move on a prescribed mesh of material points. This mesh does not necessarily correspond to the real crystal lattice, but constitutes a convenient way of discretising the spatial description of dislocation positions. Within each cell of the lattice a dislocation can lie along a number of different directions corresponding to the crystal slip systems. Dislocation motion is computed based on a mobility function approach, and interaction is specified via a set of constitutive laws. The use of a computational lattice reduces the complexity of tabulating and following dislocation motion and monitoring dislocation line connectivity, since there is only a discrete number of possible dislocation positions. Initially, dislocation types were limited to either pure edge or pure screw character. Computational efficiency could be increased by including dislocations of mixed character [39]. Similarly, non-FCC materials could be modelled by modifying the computational lattice, as illustrated by Monnet et al. [35] in the case of zirconium via axes transformation to an orthorhombic system.

Lattice-based models have been extensively used to investigate the relative strengthening effects that can be attributed to dislocation reactions during the de-

formation of single crystals [60–63]. On this basis a physically-based model of single crystal strain hardening in FCC materials was developed [64–66].

The DDD modelling approach chosen by Devincre and Kubin is an interesting compromise between accurate physical representation of dislocation structure evolution in three dimensions and efficient computations due to the finite possible number of dislocation segment locations.

3D dislocation dynamics modelling - Arsenlis, Bulatov and Cai

A more general framework was proposed by Arsenlis, Cai, Bulatov et al. [5–7]. Here dislocations are no longer limited to certain spatial positions, but rather propagate as line defects within an elastic continuum. Each dislocation line is discretised into straight segments carrying a Burgers vector and linking two nodes. Each node must be connected to at least two dislocation segments and the sum of Burgers vectors at a node must be zero to ensure conservation of Burgers vector along dislocation lines. The force $\mathbf{F}_i$ acting on the ith node is defined as the negative derivative of the stored energy ε in the system with respect to the nodal position:

$$\mathbf{F}_i \equiv -\frac{\delta\varepsilon\left(\mathbf{X}_j, \mathbf{b}_{jk}, \mathbf{T}^s\right)}{\delta\mathbf{X}_i}. \tag{2.11}$$

The stored energy ε is a function of the positions of all nodes $\mathbf{X}_j$, the connections between them via dislocation segments with Burgers vectors $\mathbf{b}_{jk}$, and the externally applied surface traction $\mathbf{T}^s$. It is convenient to split the stored energy into two parts, ε^c the dislocation core energy contribution and ε^{el} which is the energy associated with the long range elastic distortion.

In the classical elastic dislocation description, the behaviour of the strain and stress fields at the dislocation core is singular. Cai et al. [67] overcame this problem by radial spreading of the dislocation core with an isotropic distribution function. To achieve efficient computation of nodal forces in large scale simulations, Arsenlis et al. [6] use a fast multipole method (Greengard and Rokhlin [68]) with a hierarchical grid structure to account for the force contribution from remote dislocation segments.

The motion response of individual nodes to the forces acting upon them is specified by mobility functions. These capture the effects of lattice orientation, the presence of solute elements, hydrostatic stress, etc. on dislocation motion. Assuming dislocation motion is overdamped, mobility functions take the form:

$$v\left(x\right) = M\left(f\left(x\right)\right), \tag{2.12}$$

where $v\left(x\right)$ is the velocity at point x on the dislocation line, M is a general mobility function and $f(x)$ is the force per unit length acting on the dislocation line at point x. For discrete dislocation line description, this is more conveniently expressed as:

$$f^{drag}\left(x\right) = -M^{-1}\left(v\left(x\right)\right) = -B\, v\left(x\right), \tag{2.13}$$

where B is the drag coefficient, the same as in expression 2.9. As dislocation segments are constrained to remain straight, velocity can only vary linearly along a dislocation segment. Hence, the local equilibrium of the driving force f being equal to the drag force f^{drag} cannot be enforced at every point along the line segment, but it is enforced in the weaker sense at nodes so that:

$$F_i = -F_i^{drag}. \tag{2.14}$$

Bulatov and Cai [5, 69] present simple models for FCC and BCC mobility functions. The FCC mobility function takes account of the strong confinement of dislocations with edge character to the slip plane. Screw dislocations experience some confinement to the glide plane due to dissociation into partials, however, scope for occasional screw cross slip events is also incorporated. This model is called FCC0 [69].

In BCC materials, screw dislocations do not dissociate into partials. Hence, as a first approximation, isotropic mobility can be assumed. Dislocations with combined edge and screw character will assume screw character for most of the length with kinks to accommodate the non screw dislocation parts. Since the screw parts have isotropic mobility, they can move out of the kink plane. In that case the kinks

become jogs which have to climb and hence exert an extra drag force on the dislocation segment. This behaviour is captured in a three parameter model referred to as BCC0 [69].

The parameters required for both mobility models can be derived from molecular dynamics (MD) simulations, as reported for example by Marian et al. [70] for dislocation motion in BCC iron at a range of temperatures and stresses, or by Deo et al. [71, 72] using a Kinetic Monte Carlo (KMC) kink model to determine the dislocation propagation velocity in molybdenum and tantalum alloys.

The simplest numerical time integration scheme would be a forward Euler or Euler predictor-corrector type scheme. However, this would require the use of very small time steps, reducing computational efficiency. Instead, Arsenlis et al [6] propose an implicit scheme in which time step size is dynamically adjusted at each increment.

All topological operations are based on two routines, *Mergenode* and *Splitnode*. *Mergenode* merges two nodes, whilst *Splitnode* splits a node into two nodes, connecting them by a dislocation segment, if required for Burgers vector conservation. All topological procedures required for mesh refinement and dislocation core reactions can be constructed using these two elementary operations.

Mesh refinement/coarsening is carried out, such that the lengths of dislocation segments are maintained within a given envelope of maximum and minimum length. Nodes are periodically redistributed along each dislocation line to ensure a smooth distribution of segment lengths, with shorter segment lengths in areas of higher curvature.

Dislocation core reactions are a key feature in DDD simulations, however, there does not seem to be a consensus as to their treatment in the literature. Kubin et al. [58], Schwarz [73] and Ghoniem et al [74] have topological operations for annihilation but not junction formation, whilst Rhee et al [75] treat dislocation interactions that might lead to junction formation or annihilation using the same procedure. In the Bulatov, Cai and Arsenlis dislocation model two separate scenarios are considered for dislocation core reactions: collision procedures and dissociation procedures.

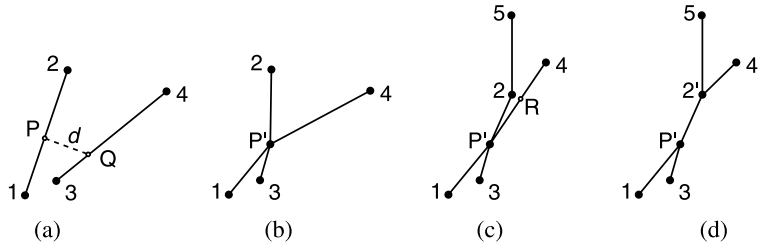

Figure 2.2: (a) The minimum distance $d_{\min}$ between two unconnected segments 1-2 and 3-4 is reached at points P and Q. Two segments are considered to be in contact if $d_{\min} < r_{\text{ann}}$. New nodes are introduced at P and Q. (b) Nodes P and Q are merged into a single node P‘. (c) Segment 2-5 comes into contact with segment P‘-4, on which a new node R is added. (d) Merging nodes 2 and R into a new node 2‘ leads to the formation of junction segment P‘-2‘, if the Burgers vectors of segments P‘-2 and P‘-R do not cancel each other. If the Burgers vectors do cancel, segment P‘-2‘ is deleted leading to a dislocation annihilation reaction. Figure taken from Arsenlis et al. [6]

A collision procedure is carried out when the distance between two dislocations, $d_{\min}$, falls below a given threshold value, r_{ann}. In this case a common node connecting the two dislocations is established. This procedure can deal with both dislocation annihilation and junction formation (figure 2.2 from Arsenlis et al. [6]).

In the dissociation procedure any node connected to four or more segments is split into two nodes connected by a dislocation segment if this reduces the stored energy of the system. A difficulty is the placing of the newly created nodes. Ideally, both should be placed at the same location as the original node and then allowed to move in the next time step. However in this scenario both nodes would fulfil the criterion for a node merging operation. Therefore the newly created nodes are placed a small distance, r_{dis}, apart and their motion is computed in the next time increment.

The method described thus far is applicable to any arbitrary set of dislocations in an infinite solid. Although DDD simulations can cover much larger volumes than atomistic simulations, the simulation volumes currently feasible are still relatively small (several microns). Periodic boundary conditions provide a convenient way of mimicking a much larger crystal volume and eliminating unwanted surface effects. However the simulation volume needs to be large enough to avoid self-interaction [5].

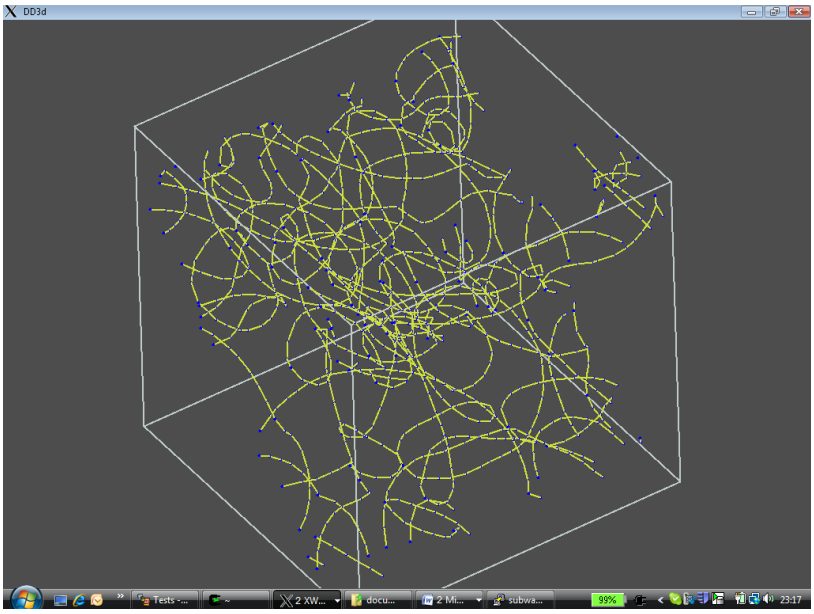

Figure 2.3: Typical dislocation microstructure output from a small ParaDiS simulation.

This three-dimensional dislocation dynamics simulation framework has been implemented numerically in the ParaDiS (Parallel Dislocation Simulator) code. To model realistic deformation effects it is essential to consider a sufficiently large material volume. This will typically involve the motion of several million dislocation segments, with the number of dislocations increasing continuously as the simulation progresses. All of the dislocation segments will need to be tracked for many hundreds of thousands of timesteps (Arsenlis et al [6] and Bulatov and Cai [5]). For illustration, figure 2.3 shows the output generated by a small ParaDiS simulation. Large parallel computing facilities are the only way of making these calculations feasible. It is crucial that the code exhibits good scalability and that the computational load is evenly distributed between processors. In ParaDiS this is achieved by a spatial domain decomposition scheme that, every few timesteps, balances the number of nodes dealt with by each processor. A detailed evaluation of the performance and scalability of the code is given by Arsenlis et al. [6].

Recently, Bulatov et al. [76] applied the ParaDiS code to the investigation of the role of dislocation multi-junctions in controlling strain hardening. Their large scale simulation successfully captured the details of individual junctions and showed good agreement with atomistic models.

The great advantages of the ParaDiS code are its generality and its accurate physical representation of dislocations. Due to the complexity of the simulations, the inclusion of anisotropic elasticity or more realistic boundary conditions is difficult and has not yet been implemented. The high computational cost means that only relatively small and simple examples can be analysed using conventional lab machines. This limits the widespread use of the framework.

2.2 X-ray diffraction

X-ray diffraction is an ideal tool for the investigation of material properties from the macro- to the nano-scale. As opposed to optical, SEM or EBSD methods that are limited to the sample surface, and TEM measurements in which only thin sections can be considered, diffraction measurements can provide information about the behaviour of the material in the bulk.

In this section, a brief overview of some of the fundamentals of X-ray diffraction is given. Then, the specific techniques relevant to this thesis are discussed in greater detail. Namely these are:

- Reciprocal space mapping (RSM) applied to the study of dislocation patterning during deformation of pure FCC metals.
- Micro-beam Laue diffraction and differential aperture X-ray microscopy (DAXM) for the study of intragranular lattice orientation and elastic strain.

2.2.1 Fundamentals of X-ray diffraction

The foundations for the diffraction of X-rays by crystals were laid by Laue, Friedrich and Knipping [77], W.H. and W.L. Bragg [78] and Ewald [79]. Hammond [80] gives an outline of the individual contributions that will be summarised here.

Laue envisaged diffraction in crystals in terms of atoms forming a 3D diffraction grating. The simplest case to consider is a cubic crystal with a motif of one atom acting as a scattering centre at lattice points. Considering diffraction from a row of

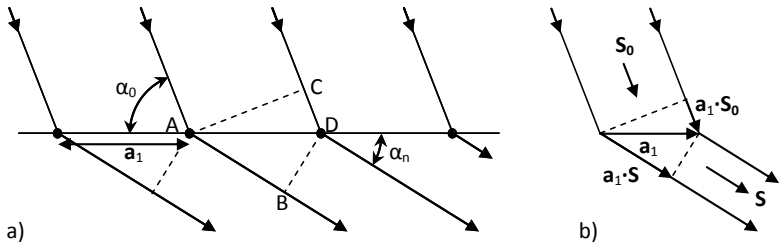

Figure 2.4: Diffraction from a line of atoms

atoms with spacing a_1 along the x-axis (figure 2.4 a)), the condition for constructive interference can be written as:

$$(AB - CD) = a_1(\cos\alpha_n - \cos\alpha_0) = n_x\lambda. \tag{2.15}$$

This can be rewritten (figure 2.4 b) in vector notation as:

$$a_1(\cos\alpha_n - \cos\alpha_0) = \mathbf{a}_1 \cdot (\mathbf{s} - \mathbf{s}_0) = n_x\lambda. \tag{2.16}$$

Solutions to this equation lie on the so-called Laue cones. The same considerations apply to rows of atoms in the y and z directions. Hence, two more equations can be established:

$$a_2(\cos\beta_n - \cos\beta_0) = \mathbf{a}_2 \cdot (\mathbf{s} - \mathbf{s}_0) = n_y\lambda, \tag{2.17}$$

$$a_3(\cos\gamma_n - \cos\gamma_0) = \mathbf{a}_3 \cdot (\mathbf{s} - \mathbf{s}_0) = n_z\lambda. \tag{2.18}$$

Constructive interference from the whole crystal occurs when all three equations are satisfied. Each diffracted beam can be characterised by three integers, n_x, n_y and n_z, which are the h, k and l Laue indices of the reflection. In diffraction experiments, constructive interference is marked by a peak in the scattered intensity.

W.H. and W.L. Bragg envisaged diffraction differently, in terms of an incident beam being reflected by crystal lattice planes (figure 2.5). This approach is derived geometrically, considering constructive interference in terms of path-length and gives the relationship:

$$n\lambda = 2d_{hkl}\sin\theta, \tag{2.19}$$

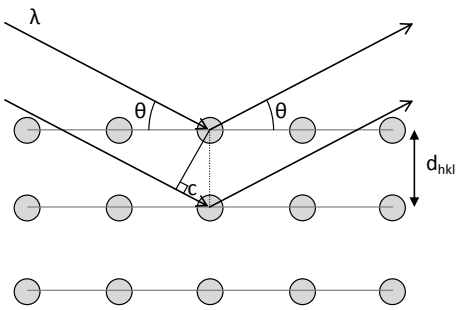

Figure 2.5: Classical diagram of Bragg diffraction based on the simple atom plane model.

where d_{hkl} corresponds to the distance between the reflecting planes.

It is convenient to introduce the concept of a reciprocal lattice that provides a framework for the analysis of X-ray diffraction in crystals. The definition of the reciprocal space lattice vectors $\mathbf{b}_1$, $\mathbf{b}_2$ and $\mathbf{b}_3$ in terms of the real space lattice vectors $\mathbf{a}_1$, $\mathbf{a}_2$ and $\mathbf{a}_3$ is:

$$\mathbf{b}_1 = \frac{\mathbf{a}_2 \times \mathbf{a}_3}{V}, \tag{2.20}$$

$$\mathbf{b}_2 = \frac{\mathbf{a}_3 \times \mathbf{a}_1}{V}, \tag{2.21}$$

$$\mathbf{b}_3 = \frac{\mathbf{a}_1 \times \mathbf{a}_2}{V}, \tag{2.22}$$

where $V = \mathbf{a}_1 \cdot (\mathbf{a}_2 \times \mathbf{a}_3)$ is the unit cell volume. A useful way of characterising Bragg planes is by their reciprocal space vector, $\mathbf{H}_{hkl}$:

$$\mathbf{H}_{hkl} = h\mathbf{b}_1 + k\mathbf{b}_2 + l\mathbf{b}_3. \tag{2.23}$$

The inter-planar spacing in real space, d_{hkl}, is then given by:

$$d_{hkl} = \frac{1}{|\mathbf{H}_{hkl}|}. \tag{2.24}$$

Similarly, the real space plane normal unit direction vector, $\hat{\mathbf{n}}_{hkl}$, is:

$$\hat{\mathbf{n}}_{hkl} = \frac{\mathbf{H}_{hkl}}{|\mathbf{H}_{hkl}|}. \tag{2.25}$$

A useful model for the visualisation of the direction of diffracted beams and the relationship between radiation wavelength, scattering angle and lattice structure is the Ewald sphere construction, involving a sphere of reflection and the reciprocal lattice.

Thus far only the directions of scattered X-rays have been considered. The intensities of the diffracted beams can be described by the kinematic theory of X-ray diffraction that considers only elastic scattering. A more complex approach is given by the dynamic theory of X-ray diffraction. A review of either theory is beyond the scope of this thesis. Good overviews of the kinematic and the dynamic theories of X-ray diffraction are given by Warren [81] and Authier [82] respectively.

2.2.2 Experimental diffraction setups

In this section an overview of the different experimental setups is given.

Powder diffraction

The key assumption in powder diffraction is that each scattering volume contains a large number (> 2500) of crystallites, such that for any orientation of the sample some of the crystallites will satisfy the diffraction condition. There are two possible experimental configurations:

Monochromatic setup: A monochromatic beam is used to illuminate the sample. A point detector is scanned in 2θ scattering angle direction, to collect a pattern of counts versus angle, corresponding to a section through the Debye-Sherrer powder diffraction rings [83]. Alternatively an area detector can be used to collect entire Debye-Sherrer rings, e.g. for texture or strain analysis. High resolution instruments can provide profiles with very little instrumental broadening contribution that are particularly suitable for line profile analysis, although data collection may be slow.

Polychromatic setup: A white beam with a smooth photon energy spectrum is used to illuminate the sample. An energy-dispersive point detector is mounted at a fixed scattering angle, 2θ, to collect a pattern of counts versus energy.

The instrumental broadening contribution is larger. Hence these measurements are less suitable for line profile analysis. However, measurement time is typically much shorter, making rapid strain measurements for engineering applications possible.

Single crystal diffraction

Similar to powder diffraction, either a monochromatic or a polychromatic setup can be used.

Monochromatic setup: If a point detector is used, it must be set at the correct 2θ angle for the reflection to be measured. Then the sample is rotated until the reflection comes into view. This is the setup used for reciprocal space mapping (RSM). Very high resolution maps of the details in reciprocal space of individual reflections can be collected. However, sample rotation can lead to "wandering" of the gauge volume. Measurements tend to be very time intensive.

Polychromatic setup: A white beam is used to illuminate the sample. An area detector, placed with its centre at $2\theta = 0°$, $2\theta = 90°$ or $2\theta = 180°$, is used to capture a pattern of counts versus spatial coordinates. This method is known as the Laue technique. It allows much faster measurements, however, unless resolution in energy is achieved, the radial direction of reciprocal space cannot be resolved.

The remainder of this thesis concentrates on single crystal diffraction methods.

2.2.3 Reciprocal space / lattice rotation mapping

The concept of reciprocal space mapping refers to measurement techniques exploring the scattering intensity distribution in the reciprocal space beyond simple X-ray diffraction 1D line scans. Generally, a monochromatic diffraction setup with a point detector is used, with the aim of characterising lattice orientation, orientation spread and d-spacing variation within individual crystallites. First, the chosen

reflection from the single crystal is centred in the diffractometer. A θ - 2θ scan of sample and detector corresponds to a conventional X-ray line scan in which the length of the scattering vector is varied to probe d-spacing. If the detector 2θ position is fixed and the sample is rocked about an axis perpendicular to the scattering vector, a rocking curve is obtained, characterising the variation of lattice orientation at the measurement point. If sample rocking is carried out about 2 axes, perpendicular to each other and to the scattering vector, a 2D reciprocal space map of lattice orientation variation in the q_x, q_z plane is obtained (see figure 4.6).

Fewster [84] presents an overview of reciprocal space mapping techniques and their application. Low resolution reciprocal space mapping (LR-RSM) can be carried out on a laboratory source with incoming and diffracted beams collimated by slits, and a single bounce analyser crystal as a coarse energy filter.

In high resolution reciprocal space mapping (HR-RSM), the principle is the same. However, the incident beam is monochromated using a 2- or 4-crystal monochromator to produce an incoming beam with low divergence and narrow bandwidth. The diffracted beam passes through a multi-bounce analyser crystal before reaching the detector. With this setup, high angular resolution reciprocal space maps can be collected, but the resolution comes at the cost of a much reduced flux. In practice, the use of a rotating anode type lab source is possible, though flux remains a major limitation. A synchrotron undulator source is much better suited to this purpose. Fewster [84] lists a number of applications for HR-RSM, e.g. defect analysis in substrate materials, relaxation in layered crystals.

It is well established that in pure FCC metals during deformation, the dislocation distribution does not evolve uniformly. Rather dislocations gather into dislocation-rich walls separating cells or sub-grains of much lower dislocation density. Figure 2.6 (Breuer et al. [85]) shows a TEM micrograph of a Cu single crystal deformed in compression. Dislocation walls and sub-grains are clearly visible. Mughrabi proposed a composite model which provided great physical insight into the behaviour of these dislocations structures [86–88]. It considers the composite behaviour of "hard" dislocation walls and "soft" dislocation cells.

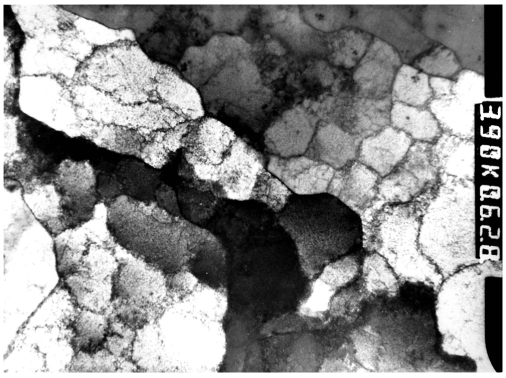

Figure 2.6: TEM micrograph of single crystal Cu deformed in compression at 873K to $\epsilon = 0.21$. The mean sub-grain size is $1\mu m$. The figure is reproduced from Breuer et al. [85]

An application of HR-RSM to the problem of characterising such dislocation distributions was reported by Pantleon et al [89] for a single aluminium grain in the bulk of a large-grained Al polycrystal. The beam size was chosen to illuminate the entire grain. Reciprocal space maps were collected at a number of different deformation increments up to a total strain of 4.5%. Diffraction peak broadening in the direction parallel to the scattering vector (q_y), indicated an increase of d-spacing variation. It also showed some asymmetry that was ascribed to different stress levels in dislocation cells and cell walls. Broadening was also observed in the directions perpendicular to the scattering vector (q_x, q_z). This arises due to an increased lattice orientation spread in the scattering volume. Lattice rotations which cannot be accommodated elastically are provided by the GND part of the dislocations present in the cell walls. Lienert et al [90] presented a similar investigation in a copper polycrystal deformed in tension. They measured the $\{440\}$ reflections of 20 grains oriented with the $\langle 440 \rangle$ direction approximately parallel to the tensile direction at a number of different load increments. Comparison of the spread of measured elastic strain in each grain with the spread of lattice strains in similarly orientated grains in an FEM strain gradient plasticity model showed fair agreement.

Jakobsen et al. [91] used a similar methodology on polycrystalline copper specimens deformed in tension. Maps of intensity projected onto the q_x, q_z plane (see figure 4.6) show a number of sharp peaks superimposed on a cloud of enhanced

intensity. The peaks arise from dislocation depleted regions (dislocation cells), whilst the cloud of enhanced intensity is due to the dislocation-rich walls. As tensile deformation is applied, the sharp peaks display dynamic behaviour. Shifting of the peaks in the q_x, q_z plane corresponds to sub-grain rotation. Peak splitting occurs at intervals due to changes in the dislocation sub-structure. Jakobsen et al. [92, 93] also analysed individual sub-grain peak line profiles in the q_y direction (radial direction of reciprocal space), using the method proposed by Ribarik et al [94] to determine the dislocation density in individual sub-grains. They found that on average, dislocation cells experience a back strain, whilst dislocation walls see a forward strain. This is as expected from the Mughrabi model [87]. The development of a dislocation sub-structure is specific to pure FCC materials. In an Al-Mg alloy investigated for comparison, dislocations arrange in a forest of almost uniform density. This gives rise to a broadened single peak in reciprocal space with no prominent sub-structure [95].

The longer timescale dynamics of dislocation cell/wall structures were studied experimentally by Jakobsen et al. [96] on a polycrystalline copper sample exposed to a sequence of loading and unloading steps. Evolution of the dislocation network occurred intermittently during tensile loading of the specimen. During hold of the load, overall structure of the reciprocal space map did not change. Over a number of hours, a "cleanup" of the dislocation structure occurred, with a narrowing of the sub-grain peaks in all three reciprocal space directions, indicating a diffusion of dislocations from the sub-grains to the cell walls. Upon unloading, the dislocation sub-structure remained unchanged. The dislocation walls were in residual tension whilst the sub-grains/cells remained under slight compression.

In section 4.3 the results of a reciprocal space mapping experiment on a single grain of a large-grained aluminium alloy sample are presented. A "naive" model allows the qualitative assessment of the role played by the GNDs in the cell walls, and captures some of the features observed experimentally.

2.2.4 Micro-beam Laue diffraction

Micro-beam Laue diffraction is as a technique for the probing of deformation and crystal structure at the micron and sub-micron scale, within individual grains of polycrystalline aggregates. The principle is akin to classical Laue diffraction in which a single crystal sample is illuminated with a polychromatic beam. The scattered signal is in the form of Laue diffraction spots that are collected on an area detector. From the diffraction peak positions, lattice orientation and unit cell distortion of the crystal can be deduced. In micro-beam Laue diffraction small beam spots with diameters from a few microns to sub-micron are used. If the crystals under investigation are larger than the beam size, Laue patterns can be collected from intragranular scattering volumes. Hence, the variation of orientation and elastic strain within the crystal can be evaluated.

Interpretation of micro-beam Laue patterns

The fundamental methods of modern automated Laue pattern analysis are described by Chung and Ice [97].

Determination of lattice strain from unit cell parameters: Consider a unit cell with lattice vectors $\mathbf{a}_i$ and corresponding reciprocal space vectors $\mathbf{b}_i$. Attached to the unit cell is a cartesian coordinate system, $\mathbf{u}_1$, $\mathbf{u}_2$ and $\mathbf{u}_3$, defined as $\mathbf{u}_1 = \mathbf{a}_1/|\mathbf{a}_1|$, $\mathbf{u}_3 = (\mathbf{a}_1 \times \mathbf{a}_2)/|\mathbf{a}_1 \times \mathbf{a}_2|$ and $\mathbf{u}_2 = \mathbf{u}_3 \times \mathbf{u}_1$ (figure 2.7). The real space lattice parameters a_i and α_i and the corresponding reciprocal space quantities b_i and β_i, in terms of $\mathbf{a}_i$ and $\mathbf{b}_i$, are:

$$a_1 = |\mathbf{a}_1|, \quad b_1 = |\mathbf{b}_1|, \quad \alpha_1 = \arccos\left(\frac{\mathbf{a}_2 \cdot \mathbf{a}_3}{|\mathbf{a}_2||\mathbf{a}_3|}\right), \quad \beta_1 = \arccos\left(\frac{\mathbf{b}_2 \cdot \mathbf{b}_3}{|\mathbf{b}_2||\mathbf{b}_3|}\right),$$

$$a_2 = |\mathbf{a}_2|, \quad b_2 = |\mathbf{b}_2|, \quad \alpha_2 = \arccos\left(\frac{\mathbf{a}_3 \cdot \mathbf{a}_1}{|\mathbf{a}_3||\mathbf{a}_1|}\right), \quad \beta_2 = \arccos\left(\frac{\mathbf{b}_3 \cdot \mathbf{b}_1}{|\mathbf{b}_3||\mathbf{b}_1|}\right),$$

$$a_3 = |\mathbf{a}_3|, \quad b_3 = |\mathbf{b}_3|, \quad \alpha_3 = \arccos\left(\frac{\mathbf{a}_1 \cdot \mathbf{a}_2}{|\mathbf{a}_1||\mathbf{a}_2|}\right), \quad \beta_3 = \arccos\left(\frac{\mathbf{b}_1 \cdot \mathbf{b}_2}{|\mathbf{b}_1||\mathbf{b}_2|}\right).$$

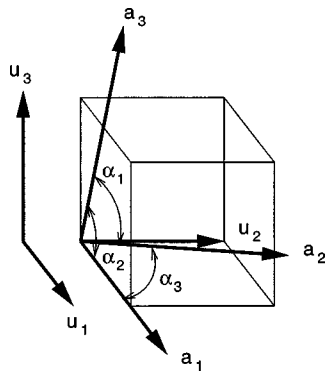

Figure 2.7: Cartesian coordinates attached to real space unit cell. $\mathbf{u}_1 = \mathbf{a}_1/|\mathbf{a}_1|$, $\mathbf{u}_3 = (\mathbf{a}_1 \times \mathbf{a}_2)/|\mathbf{a}_1 \times \mathbf{a}_2|$ and $\mathbf{u}_2 = \mathbf{u}_3 \times \mathbf{u}_1$. Reproduced from Chung and Ice [97].

A position in the lattice can be represented by a vector either in cartesian coordinates, $\mathbf{v}_u$, or in unit cell coordinates, $\mathbf{v}$. The transformation from unit cell coordinates to Cartesian coordinates is given by $\mathbf{v}_u = \mathbf{A}\mathbf{v}$ where $\mathbf{A}$ is:

$$\mathbf{A} = \begin{pmatrix} a_1 & a_2\cos(\alpha_3) & a_3\cos(\alpha_2) \\ 0 & a_2\sin(\alpha_3) & -a_3\sin(\alpha_2)\cos(\beta_1) \\ 0 & 0 & 1/b_3 \end{pmatrix}. \tag{2.26}$$

The average elastic strain of the scattering volume can be determined by comparing the measured unit cell parameters, $\mathbf{A}_{\mathrm{meas}}$, with those of an unstrained reference unit cell, $\mathbf{A}_0$. Now consider a transformation that maps the undeformed crystal $\mathbf{A}_0$ to the deformed crystal $\mathbf{A}_{\mathrm{meas}}$, such that $\mathbf{A}_{\mathrm{meas}} = \mathbf{T}\mathbf{A}_0$. $\mathbf{T}$ in this case contains both rotational and distortional terms. Taking the symmetric part of $\mathbf{T}$, strain in the cartesian crystal coordinate frame can be defined as :

$$\epsilon_{ij} = \frac{(T_{ij} + T_{ji})}{2} - I_{ij}. \tag{2.27}$$

The strain tensor can be converted to the lab reference frame using a rotation matrix $\mathbf{R}$, such that $\epsilon_{\mathrm{sample}} = \mathbf{R}\epsilon\mathbf{R}^{-1}$. ϵ can be split into distortional and dilatational

components:

$$\epsilon = \begin{pmatrix} \epsilon_{11} - \frac{\delta}{3} & \epsilon_{12} & \epsilon_{13} \\ \epsilon_{12} & \epsilon_{22} - \frac{\delta}{3} & \epsilon_{23} \\ \epsilon_{13} & \epsilon_{23} & \epsilon_{33} - \frac{\delta}{3} \end{pmatrix} + \begin{pmatrix} \frac{\delta}{3} & 0 & 0 \\ 0 & \frac{\delta}{3} & 0 \\ 0 & 0 & \frac{\delta}{3} \end{pmatrix}, \tag{2.28}$$

where $\delta = \epsilon_{11} + \epsilon_{22} + \epsilon_{33}$. From the full elastic strain tensor, the stress tensor can be determined as $\sigma_{ij} = \sum_{kl} C_{ijkl}\epsilon_{kl}$, where C_{ijkl} is the stiffness matrix.

Orientation and strain from Laue patterns: Usually in micro-beam Laue diffraction, a significant number of crystal reflections can be collected without rotation of the sample. At least two reflections are required to determine the crystal orientation. Four reflections are needed to find the orientation and the deviatoric elastic strain tensor. To determine the full strain tensor, the energy of at least one reflection must be known. This can be achieved by using an energy scanning monochromatic setup. The experimental implications of this are discussed in section 2.2.4.

Assuming two Laue spots have been indexed correctly, the crystal lattice orientation can be determined using the method described by Busing and Levy [98]. They propose the use of a second cartesian coordinate system xyz attached to the crystal, where x is parallel to reciprocal space axis $\mathbf{b}_1$, the y axis is in the $\mathbf{b}_1$, $\mathbf{b}_2$ plane and perpendicular to the x axis, and the z axis is perpendicular to x and y. A vector $\mathbf{v}_r$ in reciprocal space crystal coordinates can be converted to reciprocal cartesian xyz coordinates, such that $\mathbf{v}_c = \mathbf{B}\mathbf{v}_r$, where:

$$\mathbf{B} = \begin{pmatrix} b_1 & b_2\cos(\beta_3) & b_3\cos(\beta_2) \\ 0 & b_2\sin(\beta_3) & -b_3\sin(\beta_2)\cos(\alpha_1) \\ 0 & 0 & 1/a_3 \end{pmatrix}. \tag{2.29}$$

Matrix $\mathbf{B}$ here is the reciprocal space equivalent of matrix $\mathbf{A}$.

Vector $\mathbf{v}_c$ can then be transformed into the cartesian lab coordinate system $\mathbf{v}_{\text{lab}}$ using an orientation matrix $\mathbf{U}$, such that $\mathbf{v}_{\text{lab}} = \mathbf{U}\mathbf{v}_c$. For a given reflection hkl, the

unit reflection normal, $\hat{\mathbf{n}}_{hkl}$, can be expressed in the lab reference frame as:

$$\hat{\mathbf{n}}_{hkl} = \mathbf{UB} \begin{pmatrix} h \\ k \\ l \end{pmatrix} \div \left| \mathbf{UB} \begin{pmatrix} h \\ k \\ l \end{pmatrix} \right| = \mathbf{U} \left(\frac{\mathbf{H}_{hkl}}{|\mathbf{H}_{hkl}|} \right). \tag{2.30}$$

Now consider the experimental scattered beam unit vector, $\hat{\mathbf{s}}_{hkl}$, pointing from the scattering volume to a given hkl peak on the detector. In diffraction condition the direction of the experimental plane normal, $\hat{\mathbf{n}}^{M}_{hkl}$, corresponds to the direction of the scattering vector. Hence:

$$\hat{\mathbf{n}}^{M}_{hkl} = \frac{\hat{\mathbf{s}}_{hkl} - \hat{\mathbf{s}}_0}{|\hat{\mathbf{s}}_{hkl} - \hat{\mathbf{s}}_0|}, \tag{2.31}$$

where $\hat{\mathbf{s}}_0$ is the incident beam unit vector.

Assuming that $\mathbf{B}$ and the hkl indices for two reflections are known, the orientation matrix $\mathbf{U}$ can be found by equating $\hat{\mathbf{n}}_{hkl}$ and $\hat{\mathbf{n}}^{M}_{hkl}$. In practice, an ideal orientation matrix $\mathbf{U}$ is impossible to find, and $\mathbf{U}$ will generally be determined by minimising the misfit to all indexed reflections.

If the exact unit cell parameters are unknown, e.g. in a strained crystal, then strain and orientation can be determined simultaneously from four independent Laue reflections. Each reflection normal has two direction angles. Hence, there are 8 equations to solve for the 9 unknowns in the $\mathbf{U}$ and $\mathbf{B}$ matrices. Since the dilatory term cannot be determined without energy measurement, one of the unknowns can be eliminated and the distortional (deviatoric) elastic strain and lattice orientation found. If the full strain tensor is required, a monochromatic scan in energy can be used to determine the energy of one reflection. Based on this, the volume of the unit cell can be found, and hence the dilatory component of elastic strain quantified.

Indexation of micro-beam Laue diffraction patterns from crystals of unknown orientation: Reliable indexation of reflections is key to the analysis of micro-beam Laue diffraction patterns. Chung and Ice [97] describe an automated routine designed to index patterns with few $(4-20)$ reflections per grain. Figure 2.8 shows a flowchart of this routine.

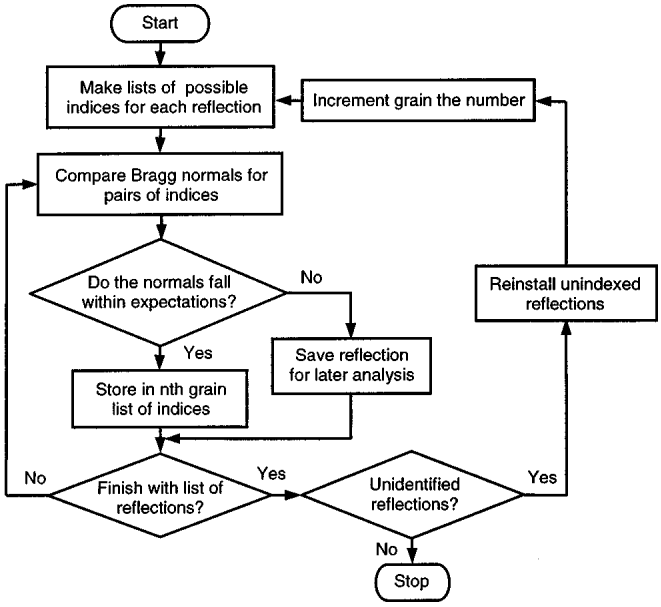

Figure 2.8: Flow diagram for the indexation of diffraction patterns from a crystal with known structure but unknown orientation and lattice strain. Reproduced from Chung and Ice [97].

First, the 2θ position and the Bragg plane normal are computed for each reflection. Then, a list of possible indices is assigned to each reflection based on the photon energy range of the incident beam. Next, a search for reflection pairs from the same grain is performed, based on the expected angle between plane normals. Once a matching pair is found, a search is performed for other reflections predicted for this orientation. If reflections are found which coincide with the predictions, they are assigned to the grain and removed from the experimental pattern. Once all of the reflections from a given grain have been indexed, a search will be performed on any remaining reflections in the pattern to identify peaks belonging to another grain. This loop is repeated until no unidentified reflections remain. Chung and Ice [97] have presented an implementation of this indexation routine in the ORDEX code.

Tamura et al. [99] incorporated a very similar indexation routine in the XMAS (X-Ray Microdiffraction Analysis Software) package, that was extensively used in this thesis. XMAS offers the capability of automated Laue diffraction pattern analysis for large datasets and easy use through a graphical user interface.

Calibration: For indexation and refinement of patterns to function correctly, it is crucial that the parameters characterising the detector position and the detector angles are determined accurately. This calibration of the experimental setup can be carried out two stages. First, the detector position relative to the scattering centre is estimated by triangulating diffraction peak positions, as the sample to detector distance is varied. Then, the detector misorientation angles (pitch, roll, yaw) and the detector position are refined based on measurements of an unstrained reference crystal. Silicon wafer fragments are ideally suited to this purpose. Figure 3.4 shows an example of a silicon calibration pattern recorded on beamline B16 at the Diamond Light Source (DLS).

Experimental layout

There are a number of different micro-beam Laue diffraction beamlines at synchrotron sources around the world. Instruments include BM32 at the European Synchrotron Radiation Facility (ESRF in Grenoble, France); MicroXAS at the Swiss Light Source (SLS in Villingen, Switzerland); 7.3.3 at the Advanced Light Source (ALS in Berkeley, CA, USA); and 7 ID and 34 ID E at the Advanced Photon Source (APS in Argonne, Il, USA). Though this list is by no means exhaustive.

Many of the special features of a micro-beam Laue diffraction beamline can be illustrated on the setup at 7.3.3 (ALS) and 34 ID E (APS) shown schematically in figure 2.9. For the measurement of full Laue patterns, as well as the full strain tensor, the beamline must be able to supply both white beam (broad bandpass from approximately 4 keV to 25 keV) and continuously scannable, high energy resolution monochromatic beam (repeatability of 0.5 eV energy mean, FWHM of energy bandpass of 2 eV, Ice et al. [100]). The position of the illuminated spot on the sample must be well maintained during the change from poly- to monochromatic beam and vice versa. On 7.3.3 (ALS) and 34 ID E (APS), a monochromator setup was chosen such that the white and monochromatic beams coincide downstream of the monochromator. MacDowell et al. [101] describe in detail the four crystal Ge (111) monochromator used on 7.3.3 (ALS). In this configuration the incoming white beam and the post-monochromator white or monochromatic beam all lie on

the same line. A torroidal mirror is used to pre-focus the beam from the bending magnet source to a source image at the monochromator entrance.

On 34 ID E (APS) a different setup was chosen with a two crystal Si (111) monochromator that was initially tested on 7 ID (APS) [100] before installation on 34 ID E (APS) [102]. In white beam mode, off-axis beam from the undulator source is passed directly through the monochromator. The energy spread is sufficient for micro-beam Laue diffraction [103]. In the monochromatic mode, on-axis radiation from the undulator source is used. The difference in height between the on-axis and off-axis beams is $1\mathrm{mm}$, the same as the monochromator offset. Heating of the second crystal makes it possible to steer the monochromatic beam downstream of the monochromator along the same path as the white beam.

The sample is mounted in reflection geometry at an angle of 45° to the incident beam. The area detector is positioned vertically above the sample, with its centre at a 2θ angle of 90°, and collects the Laue diffraction patterns.

Both 7.3.3 (ALS) and 34 ID E (APS) use Kirkpatrick Baez (KB) micro-focusing mirrors [104]. KB mirrors provide achromatic focusing, and sub-micron focal spot sizes can be routinely achieved ($\sim 0.7\mu\mathrm{m}$ on 7.3.3 (ALS) [101], $\sim 0.6\mu\mathrm{m}$ on BM32 (ESRF)). The current record for the smallest focal spot size achieved with KB mirrors stands at $7\mathrm{nm}$ [105].

Applications

One of the first illustrations of the power of micro-beam Laue diffraction was given by Tamura et al. [106, 107]. They investigated the stress distribution in a polycrystalline Al film deposited on a Si substrate exposed to cyclic thermal loading. Stress in individual Al grains varies as a function of temperature due to the thermal expansion mismatch between film and substrate. Also, significant stress variations exist between individual grains. Similar inter- and intra-granular stress variations in Al film deposited on Si substrate were also reported by Spolenak et al. [108].

Phillips et al. [109] present measurements of Al(5% Cu) film deposited on Si, and Cu film deposited on Al_2O_3. Both films show a $\langle 111 \rangle$ texture and significant

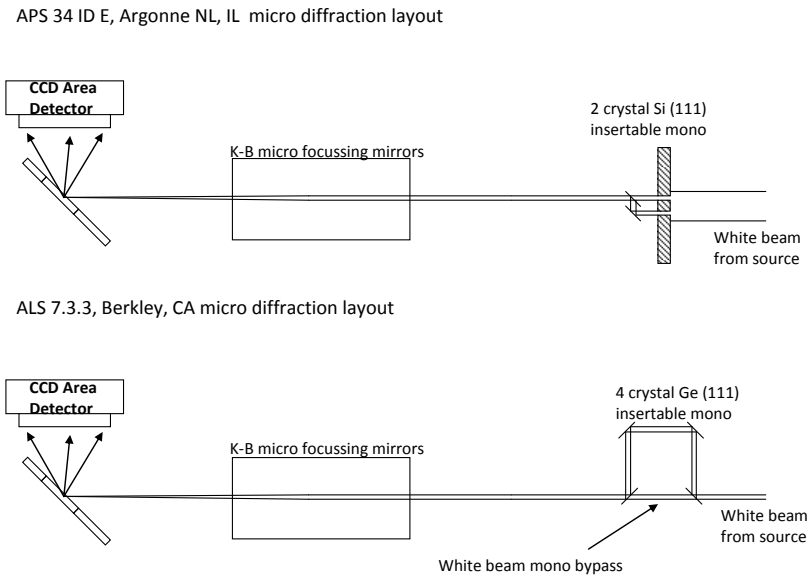

Figure 2.9: Schematic diagrams of the main components at the micro-beam Laue diffraction beamlines 34 ID E (APS) and 7.3.3 (ALS).

inter- and intra-granular stress variations. Intra-granular lattice curvature hints at the presence of GNDs.

Budai et al. [110] present orientation studies of CeO_2 epitaxially grown on a Ni substrate, and establish that a change in growth regime occurs as a function of temperature. Ledge growth dominates at elevated temperatures, whilst island growth occurs at lower temperatures.

Micro-beam Laue diffraction has also been used to characterise GaN layers grown by maskless pendeo-epitaxy on SiC and Si substrates. In pendeo-epitaxy, GaN wings are grown laterally from the sidewalls of a GaN column. The aim is to achieve a lower density of threading dislocations in the wings than is possible in GaN films directly deposited onto a substrate. Threading dislocations significantly reduce the performance of GaN based light emitting devices. Barabash et al. [111, 112] succeeded in characterising wing tilt in a number of different configurations and showed by Laue spot shape analysis that dislocation and defect density in the GaN wings is significantly lower than in the mother column.

A frequent problem in budget consumer electronics is the growth of tin (Sn) whiskers. Tin is used to coat the copper leadframes that are used for mounting of components. In the reaction of tin with copper, Cu_6Sn_5 is formed. This reaction

introduces a net compressive chemical stress in the tin layer. Whisker growth is one means of relaxing this stress. Although whiskers are normally only a few microns in diameter, they can reach lengths of several hundred microns and cause short circuits. Measurements by Choi et al. [113, 114] at beamline 7.3.3 (ALS) confirmed the existence of a stress gradient from the whisker root to the tin mother material. This stress gradient drives whisker growth. Also, it is found that the lattice is oriented with the $\{001\}$ axis along the whisker axis. A possible means of inhibiting whisker growth is to introduce a suitable barrier layer between the copper leadframe and the tin layer to prevent formation of Cu_6Sn_5. Such a barrier coating could be Ni or Cu_3Sn. Suh et al. [115] showed that there exist six preferred orientation relationships between Cu_6Sn_5 grains and the copper substrate. They also established that Cu_6Sn_5 grain morphology varies depending on the lead content of the tin solder, and that Cu_3Sn forms after Cu_6Sn_5, which is consistent with the observations by Choi et al. [113, 114].

Another common problem in microelectronics is electromigration-induced plastic deformation and the generation of residual elastic strains. In Al(Cu) interconnects, Barabash et al. [116] observed material depletion at the cathode, formation of sub-grains under current reversal, and an increase in dislocation density. Cargill et al. [117] reported similar phenomena in both Al and Cu conductor lines.

A frequently observed experimental phenomenon in micro-mechanics is the apparent increasing in material strength as the scale of interest is reduced. The morphology of Focused Ion Beam (FIB) milled Au, Ni, Cu and NiTi micro-pillars was examined by Maaß et al. [118–121] at the MicroXAS beamline (SLS). Although pillars were machined from a low defect parent material, they contained pre-existing strain gradients and defects such as low angle grain boundaries. During compressive deformation, slip did often not occur on the geometrically most favourable slip system, and deformation was found to be non-uniform. The overall trend was for smaller pillars to exhibit higher strengths, but there was significant scatter in the data which might be explained by the initial defects. A clear correlation between defects and the FIB machining procedure could not be established.

A further "smaller is stronger" study was reported by Gruber et al. [122]. They investigated single crystalline Au films ranging from 31 to $858\mathrm{nm}$ on a compliant polyimide substrate. The Au film was deposited on a NaCl substrate by magnetron sputtering. It was then spin coated with polyimide and the NaCl dissolved. The films were deformed in situ during white-beam Laue measurements. Thinner films could support a higher resolved shear stress than thicker films. However, the very thinnest films suffered from defects due to imperfections in the NaCl substrate.

Laue spot modelling

Thus far no explicit reference has been made to the observed shape of the Laue diffraction spots. In the interpretation of Laue patterns presented earlier (§ 2.2.4), it was assumed that each Laue spot could be fitted using a simple function such as a 2D Gaussian peak, to determine the reflection centre. This centre position is the only information about the reflection that is fed forward into the indexation and refinement routine.

In actual fact the Laue diffraction spot shape carries a wealth of information. The peak shape is related to the local lattice rotation/misorientation within the scattering volume. Lattice curvature, in turn, arises due to the underlying dislocation substructure and the presence of GNDs (and SSDs). It is important to realise that the distinction between GNDs and SSDs in this case is scale-dependent. Solving the inverse problem of deducing statistics of the underlying dislocation distribution from Laue spot shape is rather hard. A more straightforward analysis technique is to solve the direct problem of predicting Laue spots for a given dislocation distribution. The output from the direct model can then be compared with the experimentally recorded Laue pattern, and the model input adjusted to achieve a good match. The input to the model then constitutes one possible, approximate solution to the inverse problem.

Barabash et al [123] use such a forward modelling technique to predict Laue diffraction peak shape for a distribution of edge dislocations. By modelling edge dislocations on different slip systems, they predict the "streaking" observed in nano-indentation of a Cu single crystal, and hence deduce the active slip sys-

tems. This framework is extended by Barabash et al. [124] to include the effects of non-uniform edge dislocation distributions. Geometrically necessary boundaries (GNBs) cause Laue spots to fragment, whilst uniformly distributed GNDs result in streaking. Interplay of these parameters is demonstrated by the prediction of active slip systems in a nano-indented Cu single crystal. A more detailed description of the model is given by Barabash et al. [125]. Ice et al. [126] show its application to dislocation microstructure in an Ir weld. Barabash et al. [127] also investigated dislocation structure in the heat affected zone of a Ni single crystal after spot welding, and compared the measurements with TEM observations to good effect. A further extension of the method considers the absorption of X-rays as they penetrate further into the sample, and the variation of dislocation structure with penetration depth (Barabash et al. [128]). This extension in particular needs to be considered in conjunction with the differential aperture X-ray microscopy (DAXM) technique.

Differential aperture X-ray microscopy (DAXM)

A limitation of micro-beam Laue measurements is that the collected images correspond to the integral of all scattering contributions from illuminated volumes along the incident beam path. The depth of origin of a reflection along the line of the incident beam is not known. This is in particular a problem when several grains are illuminated or when a significant amount of lattice distortion is present, such that Laue spots become too distorted for analysis (for example after friction stir processing or other severe plastic deformation techniques).

A possible method of achieving depth resolution along the incident beam would be to vary the detector to sample distance and then triangulate for each individual reflection. This method was used by Stock et al. [129], Larson et al. [130] and Ice and Larson [102]. However, even when conditions were favourable, only grain average positions could be found, and it was not possible to achieve intra-granular resolution. Furthermore, this method does not easily lend itself to automation.

Differential aperture X-ray microscopy (DAXM) is an alternative method of achieving depth resolution along the incident X-ray beam [131, 132]. A tungsten (W) wire is scanned in small steps between the scattering volume and the detector. By

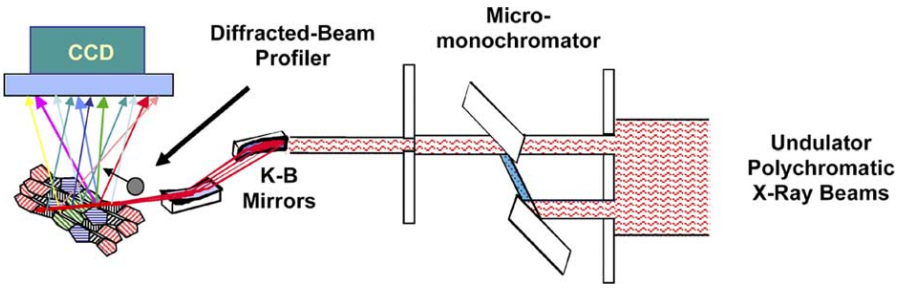

Figure 2.10: Overview of DAXM setup at beamline 34ID E (APS). Reproduced from Yang et al. [132].

subtracting diffraction images from consecutive wire position increments and triangulating using the wire edge and the line of the incident beam, the depth versus intensity profile for each pixel on the detector can be established. From this, depth-resolved Laue patterns are generated that can be analysed using the methods for indexation and refinement described previously (§ 2.2.4). The methodology lends itself readily to automation, which makes the mapping of large material volumes feasible. A schematic overview of the dedicated experimental setup on beamline 34 ID E (APS) [133, 134] is shown in figure 2.10.

Yang et al. [132] used DAXM to study nano-indentation of a Cu single crystal. Larson et al. [131] described misorientation at the grain boundary of an Al tri-crystal deformed in compression. Liu et al. [135] classified grain boundaries in a Ni polycrystal by DAXM measurements and demonstrated good agreement of the orientation angles with a coincident site lattice (CSL) model. A later paper by Ohashi et al. [136] concentrated on the deformation of a Ni bi-crystal. The deformation field near the grain boundary was compared to a strain gradient crystal plasticity model. Dislocation density was extracted by streak analysis and showed reasonable agreement with numerical predictions.

An application of the DAXM methodology to tin whiskers was described by Ice et al. [137, 138]. With DAXM, it is possible to generate microstructural orientation map slices through a sample. These illustrate the orientational relationship in three dimensions of the Sn whiskers and the source grains.

In Friction Stir Processing (FSP) (of which Friction Stir Welding (FSW) is a variant), material is exposed to cold stirring. This involves very high degrees of plastic

deformation of the metal at temperatures close to its melting point. As a result, steep rotation gradients, regions of amorphous material and small, fragmented grains exist within the FSP zone. Using conventional micro-beam Laue diffraction, reflections would be too smeared out and distorted for analysis. Barabash et al. [139, 140] show that using DAXM, depth-resolved Laue patterns can be computed. Laue spots in these patterns are less distorted due to the smaller sampling volume, and analysis by conventional fitting methods outlined previously (§ 2.2.4) becomes possible.

Bei et al. [141] used DAXM for measurements of a Mo fibre, NiAl matrix composite. By selective etching of the matrix, they exposed the ends of the fibres from which the strain free lattice parameters could be determined. In the bulk of the composite, fibre and matrix strain could thus be determined. They agree well with the expected values based on thermal mismatch after matrix solidification. Budai et al. [142] report a similar methodology for the measurement of lattice orientation in ZnO nano rods.

From this brief overview it is clear that the DAXM methodology presents a very promising experimental tool for the study of elastic strain and orientation at the micro-scale, especially if the predicted vast speed-up in measurement time is achieved [137, 138].

2.2.5 3DXRD and diffraction contrast tomography

3DXRD and diffraction contrast tomography (DCT) are two methods alternative to DAXM for the non-destructive mapping of grain structure in three dimensions in thicker specimens.

In 3DXRD, a monochromatic sheet beam, focused in the vertical direction, with a photon energy in the range from 50-100keV, is used to illuminate slices of the specimen under investigation [143–145]. The sample is then rotated about an axis perpendicular to the beam. At each angular position, small angular oscillations are applied and the transmitted beam image is recorded. As individual grains are placed in Bragg condition, diffraction contrast can be observed. This is particularly prominent in highly annealed samples. At the same time, the reflection arising

from the grain in Bragg condition is recorded on a set of area detectors placed at different distances from the sample. Using ray tracing methods the shape of the diffracting grain in the illuminated plane can be reconstructed along with lattice orientation and grain level elastic strain.

This technique has been used to map single [145] and multiple grains within the bulk and has been optimised for automatic analysis [146]. Until recently the use of 3DXRD was largely limited to samples with little misorientation spread within individual grains. This made it particularly suitable for in situ studies of annealing [147, 148], phase transformations [149] and initiation of re-crystallisation [150]. 3DXRD has also been used to follow the evolution of lattice orientation of individual grains during moderate deformation [151, 152]. Recently, the reconstruction algorithm was extended to allow the reconstruction of grain maps from deformed specimens [153]. This was used to study the nucleation of re-crystallisation in 30% deformed, pure aluminium [154].

The 3DXRD method is comparatively time-intensive, since the specimen needs to be reconstructed slice by slice. The accuracy with which lattice orientation can be determined is directly linked to the number of angular steps taken, and the increment of each step. To achieve the high angular resolution available from microbeam Laue diffraction measurements would require a large number of projections. To speed up the technique, it has been suggested to illuminate the sample with a box beam rather than a sheet beam [148]. This would move 3DXRD closer to the DCT technique.

In DCT, a monochromatic box beam is used to illuminate the polycrystalline sample that is rotated in increments about the vertical axis. Just as in 3DXRD, a given grain reaching diffraction condition will give diffraction contrast in the transmitted beam. From this, the grain shape can be reconstructed using an ART (Algebraic Reconstruction Technique) algorithm [155]. An extension to this technique also takes into account the diffracted beam arising from individual grains [156]. This makes it possible to map large numbers of grains (> 100) within the sample volume. The indexation of grain reflections as Friedel pairs opens up the possibility of determining elastic strain at the scale of individual grains [157], which has been

successfully demonstrated for in situ loading of interstitial-free steel [158]. The technique can cope with misorientation in individual grains that is limited to a few tenths of a degree [156].

DCT has been used to study crack propagation and stress corrosion cracking in sensitised austenitic stainless steel [159], and for detailed grain boundary characterisation in three dimensions [160]. The huge benefit of DCT is the high rate of data acquisition that almost makes real time, dynamic studies feasible. However, the limitation to low intragranular misorientations restricts its application to materials only subjected to small deformation. Furthermore, intragranular resolution of orientation and lattice strain is not yet possible with DCT.

Chapter 3

Classical micro-beam Laue development

Micro-beam Laue diffraction is a relatively recently developed technique for the study of deformation at the micro-scale. From the overview of the relevant literature (§ 2.2.4) it is clear that the method is maturing rapidly. Data interpretation is facilitated through the wide availability of analysis codes, such as XMAS [99] which allow straightforward treatment of experimental results. A number of dedicated micro-beam Laue instruments have been developed at synchrotron sources around the world (for example BM32 (ESRF); MicroXAS (SLS); 7.3.3 (ALS); 7 ID and 34 ID E (APS); Vespers (CLS)). As yet, there is no specialised micro-beam Laue diffraction instrument available at the Diamond Light Source (DLS), Didcot, Uk.

This prompted us to develop a micro-beam Laue setup on the test beamline, B16 (DLS). A particular advantage of this beamline over other purpose-built instruments is that if offers great flexibility in terms of the experimental geometry. This makes it possible to develop micro-beam Laue diffraction in combination with other techniques, such as white beam topography, for more complete characterisation of deformation at the micro-scale.

Commercially pure (CP) Nickel was chosen as the case study material. It is easily heat treatable to produce large-grained, low initial defect density polycrystals

(appendix A.1) and its simple FCC structure allows comparatively straightforward modelling of the deformation processes at work.

During the development work on B16 (DLS) it has become particularly clear that a highly stable experimental setup and a very well defined geometry are essential if elastic lattice strains are to be successfully extracted from the measurements. To assess the feasibility of high accuracy strain measurements using micro-beam Laue diffraction, the errors arising on the dedicated micro-beam Laue diffraction setup at beamline BM32 (ESRF) were modelled using a simulation based framework. The predicted experimental errors were validated by the measurement of single crystal silicon and copper beams under four point bending.

In this chapter a detailed description and discussion of the experimental work on B16 (DLS) and BM32 (ESRF) is provided. A number of conclusions for the further development of micro-beam Laue diffraction can be drawn from these results.

3.1 Micro-beam Laue development on B16 (DLS)

3.1.1 Beamline B16 (DLS)

The test beamline B16 (DLS) is designed for the testing and prototyping of new measurement techniques. It caters well for non-standard setups requiring very flexible experimental arrangements. The bending magnet source produces a polychromatic X-ray spectrum with photon energies ranging from 3 to 30 keV (figure 3.1).

Figure 3.2 shows the schematic layout of the beamline. Front end slits (S1) provide initial collimation of the beam. The double crystal monochromator (DCM) at $20\mathrm{m}$ provides monochromatic beam in the energy range from 4 to 25 keV, with an energy resolution of $\delta E/E \approx 5 \times 10^{-4}$ and with a height offset of $25mm$ below the white beam. A toroidal mirror at $22\mathrm{m}$ can be used for focusing with a demagnification of $1:1$ at the sample position, to give a focus of $< 200 \times 200\mu\mathrm{m}^2$. Final collimation before the sample is given by the S4 slits at $41\mathrm{m}$.

Both a Huber diffractometer (figure 3.9) and a KOHZU optics table are available for experimental setups. A number of different detectors are available on B16. In the course of this project, the following were used:

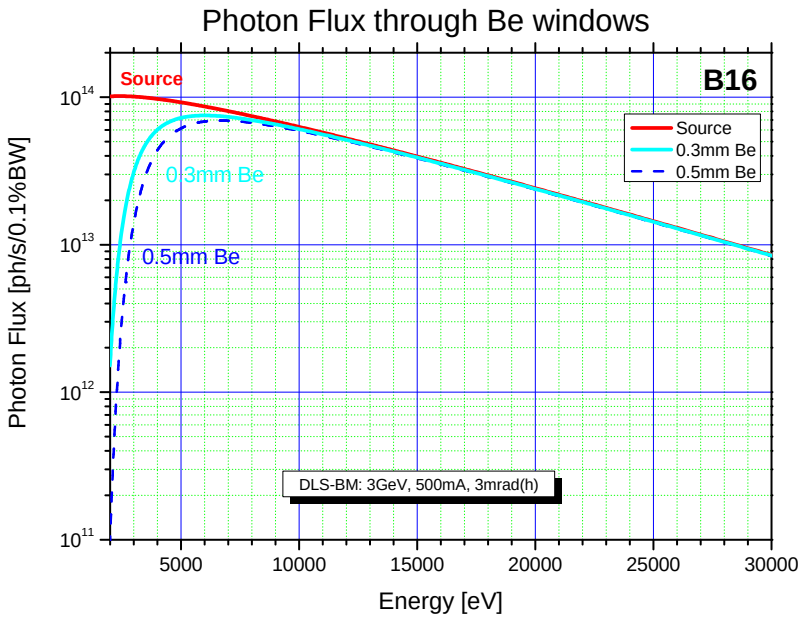

Figure 3.1: Photon flux on beamline B16 (DLS) at the sample position.

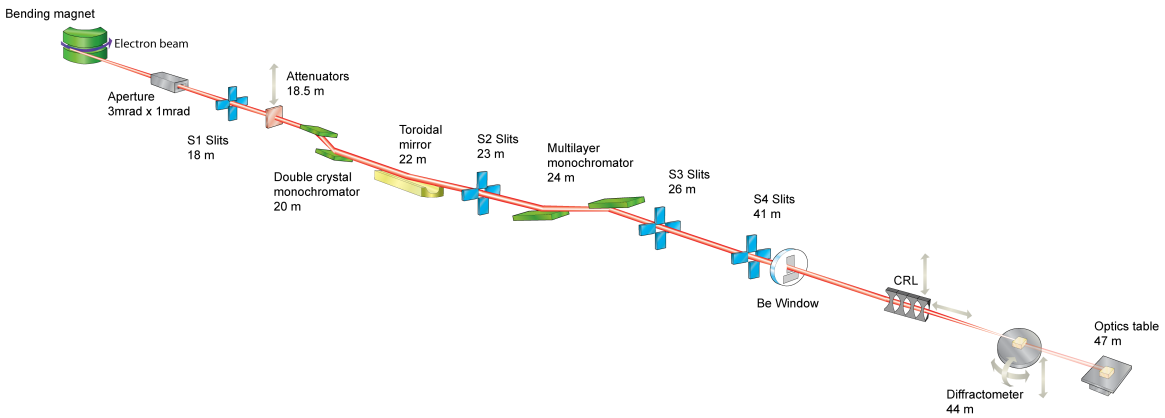

Figure 3.2: Layout of beamline B16 (DLS).

- Photonic Science X-ray Image Star 9000, optical taper coupled large area scintillator CCD detector, 3056×3056 pixels, $95.4\mathrm{mm}$ side length.
- Photonic Science X-ray MiniFDI, 1392×1040 pixels, $6.5\mu\mathrm{m}$ pixel size.
- High Resolution X-ray Microscope with PCO CCD camera, 4008×2672 pixels, 14 bit dynamic range, optical objectives from $1.25\times$ to $40\times$ magnification and a range of different scintillators.
- Passivated ion implanted planar silicon (PIPS) diode with scanning wires for beamsize measurements.

3.1.2 First micro-beam Laue diffraction setup on B16 (DLS)

Experimental setup and calibration

To maximise flexibility of the experimental geometry the micro-beam Laue setup was developed on the KOHZU optics table (figure 3.2). The incident white beam was pre-collimated using the S1 slits to minimise heat loading on the optical elements and collimated again by S4 slits to the size of $100 \times 100\mu\mathrm{m}^2$. Final collimation was provided by a pinhole mounted $200\mathrm{mm}$ upstream of the sample to give a circular spot of $50\mu\mathrm{m}$ diameter at the sample position. Diffraction patterns were collected using the Photonic Science Image Star 9000 area detector, set with the detector centre at a 2θ angle of 90° in the horizontal plane, at a sample-to-detector distance of $\sim 100\mathrm{mm}$. Although optimal positioning of the detector would have been at $2\theta = 90^\circ$ in the vertical plane, this mounting arrangement was not possible for technical reasons. The sample was mounted in 45° reflection geometry in a purpose-build loading rig. The loading direction was oriented perpendicular to the plane defined by the detector normal and the incident beam (figure 3.3).

Calibration of the geometrical parameters of the experimental setup was based on the diffraction patterns collected from a Si single crystal mounted at the sample position. By placing the detector at different distances from the sample, triangulation could be used to estimate the sample-to-detector distance (dd) and the detector centre position ($xcent$ and $ycent$). Refinement of the silicon patterns with

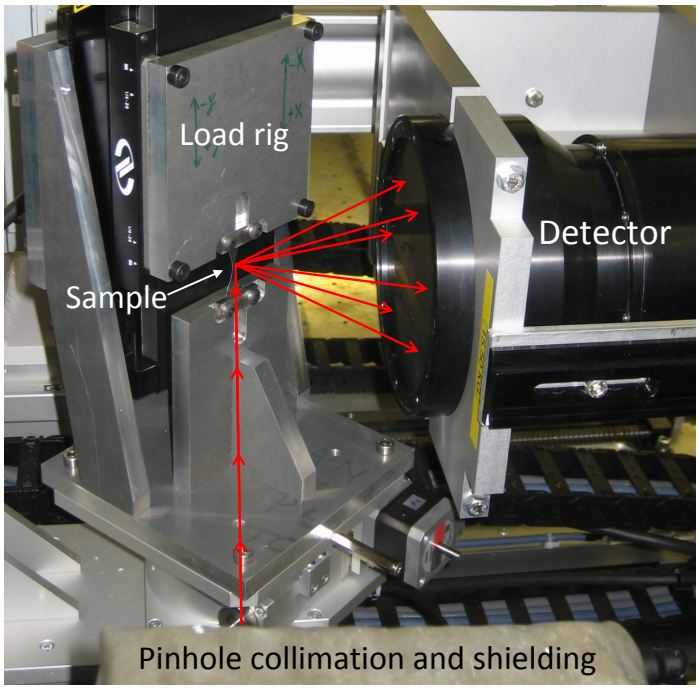

Figure 3.3: Experimental layout for 1st micro-beam Laue experiment on beamline B16 (DLS). The incident beam enters from the bottom of the picture.

the detector in the final measurement position allowed the determination of detector/beam tilts and accurate positions, by assuming the reference Si crystal to be strain-free. Figure 3.4 shows the Si calibration pattern used for the final refinement. Indices of the reflections were omitted for clarity.

Sample

Waisted dogbone-shaped samples (figure 3.5 a)) were machined from $300\mu\mathrm{m}$ thick CP Ni sheet. The samples were heat treated as described in appendix A.1.2. Their microstructure showed similar features to those found in other samples (appendix A.1.3). Figure 3.5 b) shows a micrograph of the sample gauge region with grain size ranging from 200 to $800\mu\mathrm{m}$. To illustrate the different grain orientations present, figure 3.5 c) shows a map of Schmid factor in the gauge region with respect to the vertical loading direction. The Schmid factor f_s is defined as:

$$f_s = \max((\hat{\mathbf{l}} \cdot \hat{\mathbf{n}})(\hat{\mathbf{l}} \cdot \hat{\mathbf{s}})), \tag{3.1}$$

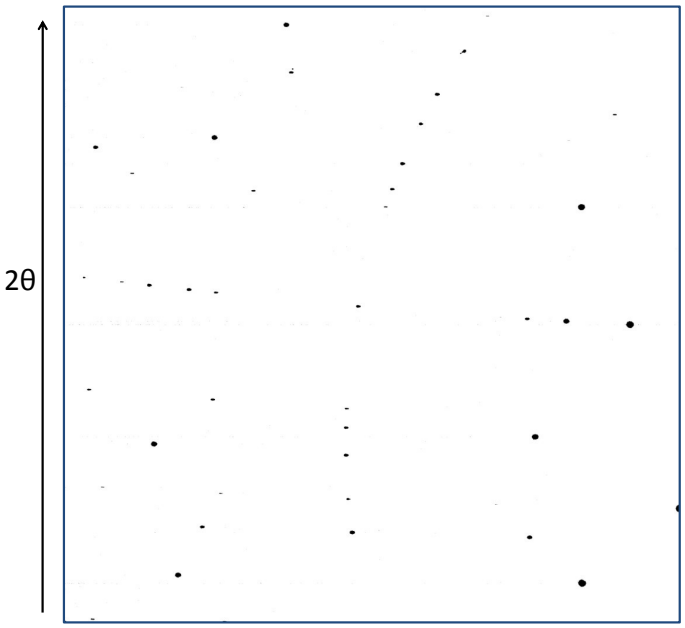

Figure 3.4: Si $\{100\}$ calibration pattern, B16 (DLS), 5-30keV, dd $100\mathrm{mm}$.

evaluated for all the crystal slip systems, where $\hat{\mathbf{l}}$ is the loading direction, $\hat{\mathbf{n}}$ the slip plane normal and $\hat{\mathbf{s}}$ the slip direction. Nickel has FCC crystal structure. Hence there are a total of twelve slip systems; four $\{111\}$ slip planes with three $\langle 110 \rangle$ slip directions each. The Schmid factor links the critical resolved shear stress (CRSS) to the yield stress σ_y of a single crystal as:

$$\mathrm{CRSS} = \sigma_y \cdot f_s. \tag{3.2}$$

Experimental measurements

Six load increments were applied to the Ni specimen, corresponding macroscopically to the elastic limit and 1%, 2%, 6%, 10% and 14% macroscopic plastic strain. In the unloaded sample and thereafter for each load increment a map of Laue diffraction measurements was collected from the central $2 \times 4\mathrm{mm}^2$ gauge region of the specimen (shaded orange in figure 3.5a)). The spacing between measurement points was $50\mu\mathrm{m}$, corresponding to the spot size of the beam incident on the sample. Laue patterns were analysed using the XMAS software [99] (see also § 2.2.4). Based on the geometrical parameters determined using the Si single crystal calibration sample, the diffraction patterns were refined to determine

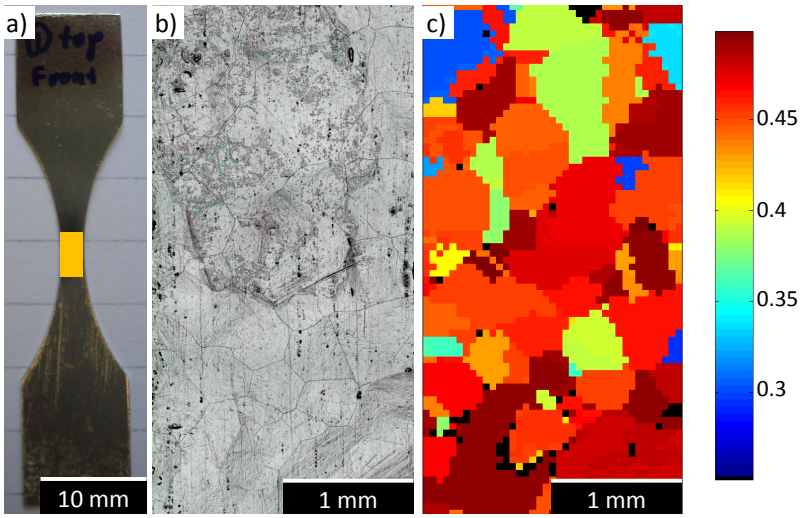

Figure 3.5: $300\mu\mathrm{m}$ thick CP Ni sample. a) Macroscopic view of the sample, with the central $2 \times 4\mathrm{mm}^2$ gauge region highlighted. b) Optical micrograph of the gauge region. c) Map of Schmid factor computed from micro-beam Laue diffraction measurements illustrating the different grain orientations present.

the local lattice orientation and elastic strain. The results were plotted using simple MATLAB scripts which read in the XMAS output and allow the visualisation of different quantities.

Results and discussion

A convenient way of visualising how a given crystallite is likely to behave under tensile loading is to compute its Schmid factor. A high Schmid factor represents a "soft" grain, whilst a low Schmid factor indicates that the grain will look "hard" for the given loading direction. Points at which XMAS could not achieve a satisfactory indexation of the Laue pattern are marked in black.

In the Schmid factor map of the undeformed sample (figure 3.5c)) grains can be clearly identified as regions with approximately uniform Schmid factor. Comparison with the optical micrograph of the gauge region (figure 3.5b)) shows good agreement of the grain boundary positions. Figure 3.6 shows maps of Schmid factor at different loading increments. Grains in the undeformed map can be clearly identified with similar regions at subsequent deformation increments. This confirms the consistency of the XMAS indexation.

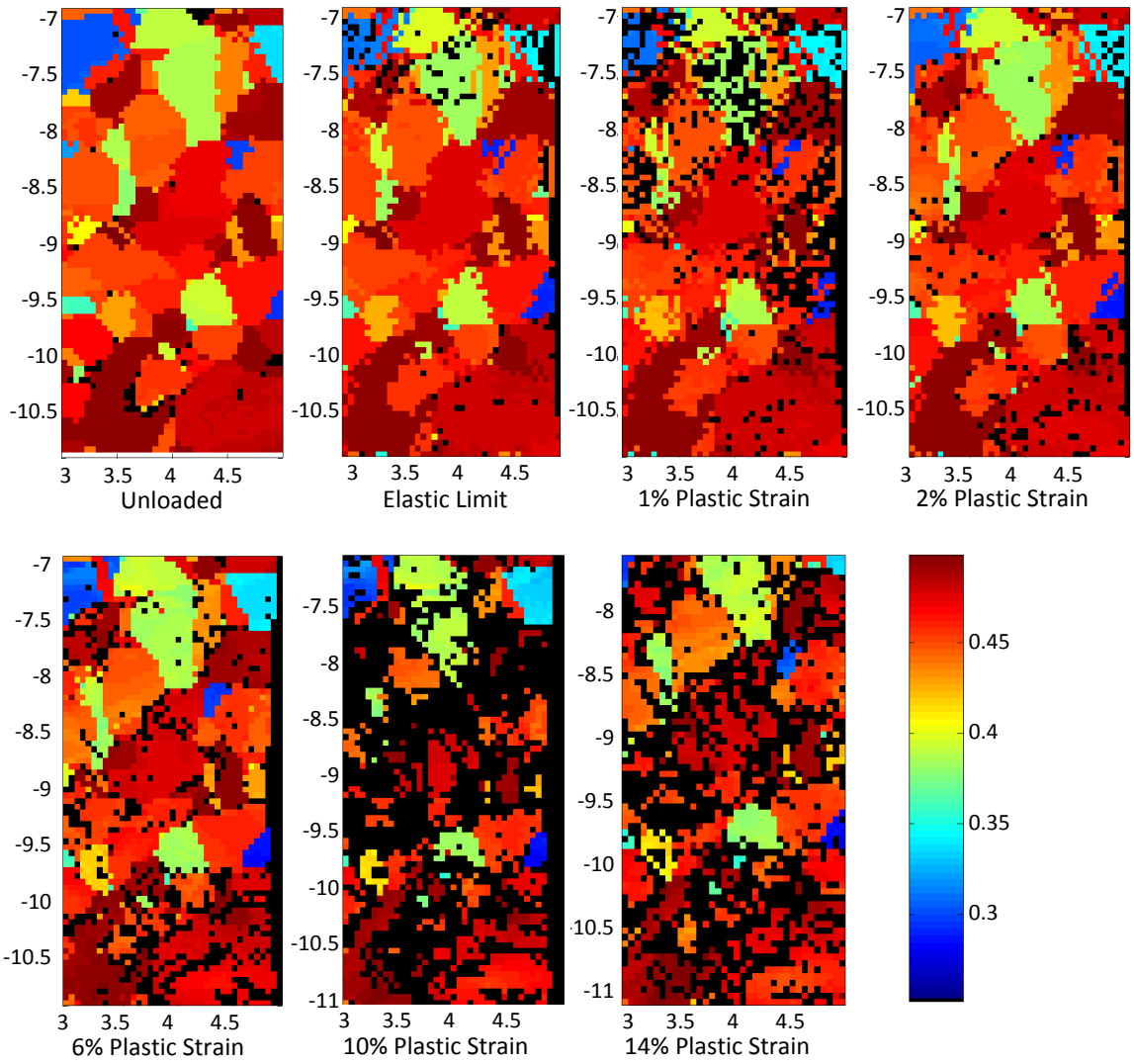

Figure 3.6: Maps of Schmid factor recorded in the mapping region at different loading increments. X and Y axes are plotted in sample translation coordinates in mm.

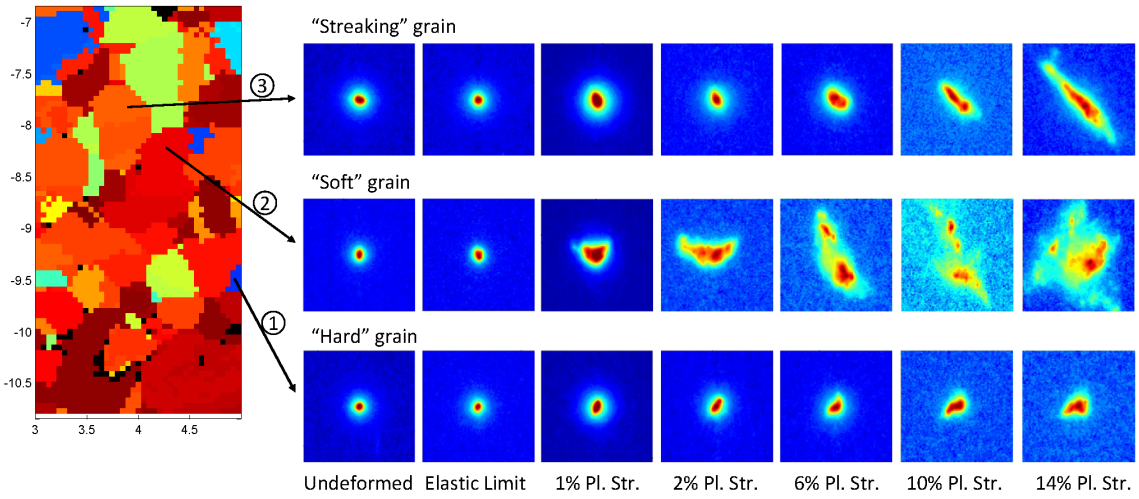

Figure 3.7: Plot of Laue Spot evolution with loading in a "streaking" grain, a "soft" grain and a "hard" grain.

As deformation progresses, the number of un-indexable Laue patterns increases. This is due to increasing lattice misorientation within the gauge volume giving rise to elongated or fragmented Laue spots. These can no longer be fitted with the 2D Gaussian or Lorentzian function used by XMAS to determine diffraction peak centre position. To illustrate this point, a study of diffraction peak shape and its evolution was performed in three grains (figure 3.7).

Grain 1 has a low Schmid factor and is thus expected to behave as a "hard" grain, deforming only little or not at all. In the log plots of intensity showing the evolution of the $(\bar{2}\bar{4}4)$ reflection with deformation, only little broadening and "streaking" (i.e.anisotropic broadening) of the reflection occurs. This suggests that no fragmentation of the crystal occurs within the scattering volume, and confirms that grain 1 indeed acts as a "hard" grain.

Grain 2 has a higher Schmid factor. It is expected to act as a "soft" grain. For this grain the evolution of the $(\bar{1}\bar{3}5)$ reflection is shown. During elastic deformation, the peak shape of the reflection remains unchanged. However, with increasing macroscopic plastic deformation the diffraction peak broadens and fragments. This fragmentation could be explained by the formation of a dislocation cell/wall substructure during plastic deformation of pure FCC metals [91, 161] (§ 2.2.3).

The evolution of Schmid factor with deformation in grain number 3 (figure 3.6) shows a change from an almost uniform distribution in the un-deformed state to a

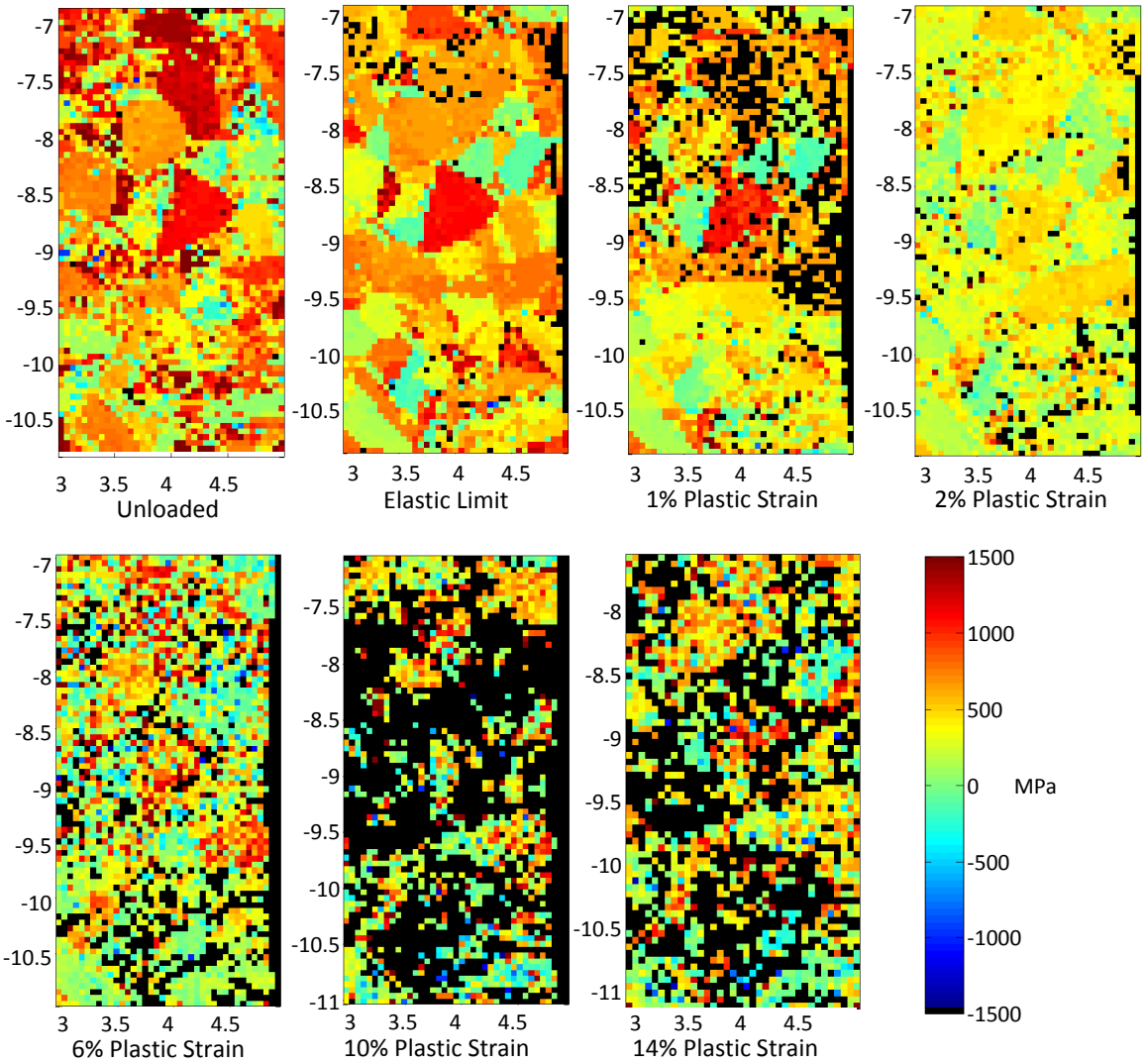

Figure 3.8: Maps of deviatoric stress in the loading direction in MPa at different loading increments. X and Y axis are plotted in sample translation coordinates in mm.

smooth variation across the grain at 14% plastic strain. This suggests the presence of macroscopic lattice curvature in this grain, which is confirmed by the evolution of the $(\bar{3}35)$ reflection (figure 3.7). During elastic deformation almost no change of the diffraction spot occurs. As soon as plastic deformation sets in, the Laue spot becomes steadily elongated. This streaking arises due to the presence of net lattice curvature in the gauge volume due to a more or less uniform distribution of GNDs. Barabash et al. [123–125] presented modelling approaches to interpret the streaking of Laue diffraction spots in terms of GND density and active slip system (§ 2.2.4).

Figure 3.8 shows maps of deviatoric stress (σ_{xx}) in the vertical loading direction determined from XMAS indexation. In the unloaded sample one would expect this stress component to be close to zero. For the other loading increments a value of the order of the macroscopic yield stress of CP Ni of $\sim 60\mathrm{MPa}$ would be expected. Instead the experimental maps show values of σ_{xx} up to $\pm 1500\mathrm{MPa}$. Equilibrium in horizontal slices of the mapped region is not satisfied. Stresses of a particular magnitude are confined to regions which agree well with the spatial extent of grains in the orientation maps (figure 3.7). This suggests that the high stresses are not physical, but rather an artefact of the indexation and refinement, and appear to be a function of lattice orientation, rather than loading. The important question is how these errors arise and how they can be minimised. Understanding the limitations of micro-beam Laue diffraction is particularly important for samples where no a priori "guesses" of reasonable values for elastic stresses and strains are available.

Initial conclusions

Some initial conclusions can be drawn from these early developments on beamline B16 (DLS) and some important questions posed which should lead the further development. The first use of micro-beam Laue diffraction at DLS has been successfully demonstrated. In a large-grained Ni sample, grains could be successfully identified by the indexation of micro-beam Laue patterns, albeit at rather low spatial resolution. Agreement of the determined microstructure with optical micrographs was good. The predicted deformation behaviour of individual grains based on a simple Schmidt factor approach was confirmed by considering the evolution of individual Laue diffraction spots. Whilst lattice orientation could be determined to high angular resolution, lattice strains could not be reliably extracted from the sample. Hence any comparison of the experimental results with simulations - be they crystal plasticity or dislocation dynamics based - should, for the moment, concentrate on the evolution of lattice orientation.

Important questions are:

- Is it possible to reliably extract elastic strains from micro-beam Laue diffraction measurements? What accuracy can be achieved?

- What are the error sources and is it possible to quantify their effect?
- Can one achieve a more quantitative understanding of misorientation within the scattering volume based on Laue diffraction spot shape analysis?
- What is the link between the local misorientation measured by micro-beam Laue diffraction and reciprocal space mapping?
- Can local misorientation be elucidated by comparison with crystal plasticity or dislocation dynamics based models?

3.1.3 Comparison of Laue, RSM and energy scanning maps

Reciprocal space mapping (RSM) is a monochromatic synchrotron X-ray diffraction technique for the study of dislocation arrangements within individual grains buried in the bulk of engineering alloys (§ 2.2.3). A single reflection from a grain is imaged at high angular resolution in all three directions of reciprocal space. The tangential distribution of intensity in reciprocal space gives information about the distribution of lattice orientation in the scattering volume. The radial direction provides information about distribution of the local lattice spacing, i.e. elastic strain along the scattering vector direction.

Micro-beam Laue diffraction, on the other hand, rather than focusing on a single reflection allows simultaneous collection of a large number of reflections from the illuminated scattering volume. This has the obvious advantage of more rapid data acquisition and removes the need for sample tilting to bring a particular set of lattice planes into reflection condition. However, since the energy spread of the incident beam is broad and present day area detectors are not energy sensitive, the photon energy of any given reflection is not known. This has the effect of presenting a reciprocal space map of the sample which has been integrated in the radial direction, i.e. each reflection still contains the information about the tangential misorientation, but not about the lattice plane spacing. Hence only the distortional component of elastic strain can be determined from micro-beam Laue measurements. If resolution in the radial direction of reciprocal space is required,

one has to resort to reciprocal space mapping or scanning of the incident beam energy.

In principle the measurements of misorientation in the scattering volume by micro-beam Laue diffraction, reciprocal space mapping and energy scanning should yield identical results. The aim of this section is to confirm this, based on measurements of a $\langle 311 \rangle$ reflection from a single grain of a plastically deformed, polycrystalline CP Ni foil sample.

Sample

A dogbone-shaped sample was cut from $15\mu m$ thick Ni foil and heat treated at 1200° C in vacuum for 8 hours to achieve complete re-crystallisation of the material (appendix A.1). Grain size was found to vary between 10 and $300\mu\mathrm{m}$, with twin boundaries in most grains. Before the measurement, macroscopic deformation to 9% plastic strain was applied to the sample. The sample thickness was chosen to allow diffraction measurements in transmission geometry. Measured transmission through the sample at 17.5keV was 53%.

Modes of operation and experimental setup

Diffraction measurements were carried out on the diffractometer sample station at beamline B16 (DLS). The incident beam was coarsely pre-focused using the toroidal mirror. The final beam spot size on the sample was defined by a pair of slits mounted on the diffractometer base, just upstream of the sample. This ensured that beam position relative to the sample did not vary when changing from poly- to monochromatic mode and vice versa.

Using automatic alignment routines for the Si (111) DCM, both the rapid changeover between white and mono beam modes and scanning of the incident beam energy in fine increments were possible. Figure 3.9 shows the experimental layout. Superimposed are the sample axes and direction vectors of the incident beam, $\mathbf{s}_0$, the diffracted beam, $\mathbf{s}$, and the scattering vector, $\mathbf{q}$. Loading was applied by a Deben micro-tensile stage mounted on the diffractometer, such that the tensile axis was aligned with the x direction. The sample was oriented, such that the scattering

vector was approximately in the sample plane, transverse to the loading direction (figure 3.9). Prior to the measurements the sample was deformed to 9% macroscopic plastic strain in tension.

Four different experimental configurations were used for the mapping of the $\langle 311 \rangle$ reflection:

1. **Standard white beam Laue setup:** Polychromatic beam with a spectrum from 5 to 30 keV, beam size of $5 \times 5 \mu\mathrm{m}^2$, detector centre position 2θ of $50°$, sample-to-detector distance (dd) of $94.92\mathrm{mm}$ (near field detector position).

2. **High resolution white beam Laue setup:** Polychromatic beam with a spectrum from 5 to 30 keV, beam size of $5 \times 5 \mu\mathrm{m}^2$, detector centre position 2θ of $37°$, sample-to-detector distance (dd) of $494.92\mathrm{mm}$ (far field detector position).

3. **Energy-scanning setup:** Monochromatic beam, diffraction patterns recorded at 15 eV increments between 17 and 19.5 keV, beam size of $10 \times 10 \mu m^2$, detector centre position 2θ of $37°$, dd of $494.92\mathrm{mm}$ (far field detector position).

4. **Reciprocal Space Mapping (RSM) setup:** Monochromatic beam energy of 17.5keV, diffraction patterns recorded at Ω tilts from $19°$ to $31°$ in $0.01°$ increments, beam size of $10 \times 10 \mu\mathrm{m}^2$, detector centre position 2θ of $37°$, dd of $494.92\mathrm{mm}$ (far field detector position).

Setups 3 and 4 both allow the analysis of d-spacing variation, while setups 1 and 2 only provide information about the local orientation spread within the scattering volume.

Results and discussion

After tensile deformation of the sample, a grain was identified with a $\langle 311 \rangle$ reflection close to the $\chi = 0$ position. This reflection was chosen to provide a comparison between the four different misorientation mapping methods. Only the lattice orientation spread was considered.

To allow easy comparison of the results, pixel positions in the maps were converted to angular positions in terms of χ and Ω angles in the laboratory reference

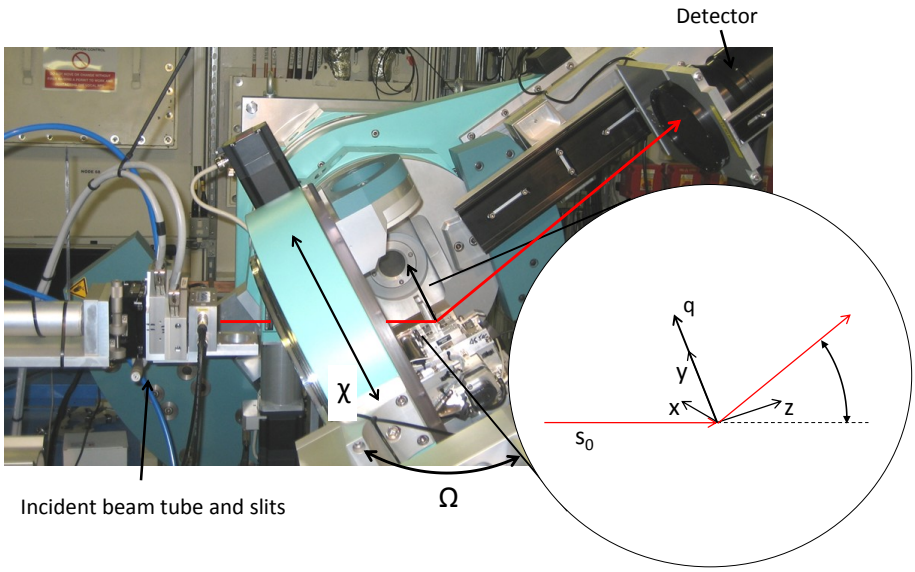

Figure 3.9: Experimental setup on beamline B16 (DLS)

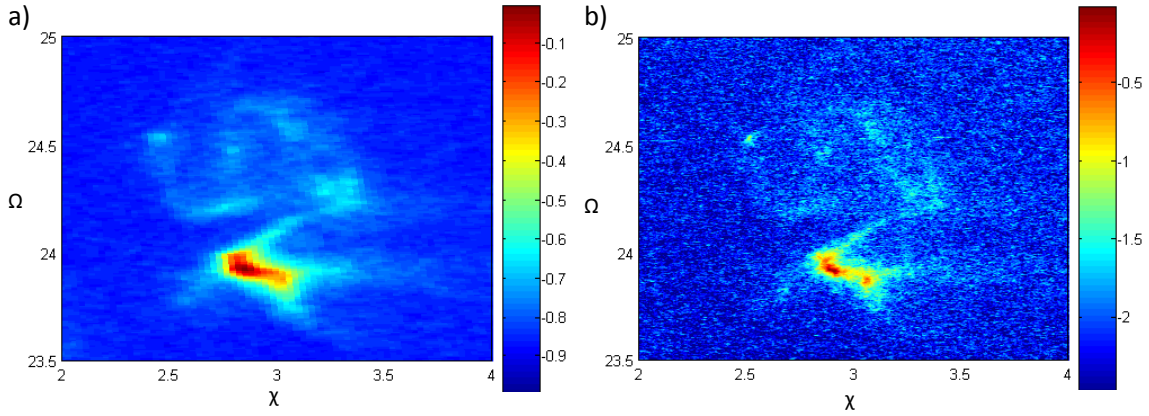

Figure 3.10: a) Micro-beam Laue orientation map of $\langle 311 \rangle$ reflection. b) High-angular resolution micro-beam Laue orientation map of the $\langle 311 \rangle$ reflection

frame. Intensity was plotted on a log scale, normalised against maximum intensity in each map.

Figure 3.10 a) shows the intensity distribution of the $\langle 311 \rangle$ reflection measured using setup (1). Pixellation of the detector can be clearly seen as a result of the small sample-to-detector distance and hence the large solid angle covered by each pixel. The resulting effect is a coarse-grained appearance of the reflection.

Figure 3.10 b) shows the reflection recorded at increased sample-to-detector distance (setup 2). As expected, the pixellation is now less noticeable, and some of the finer angular features of the intensity distribution become visible. The shape

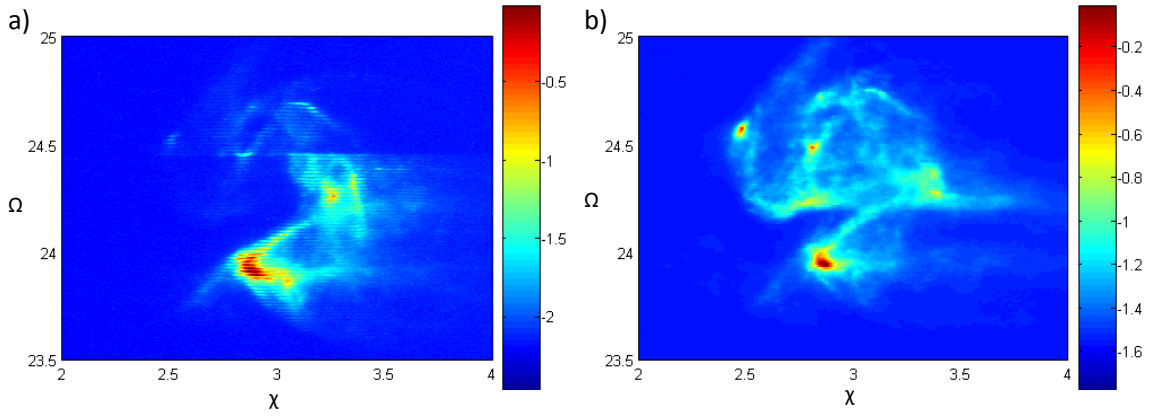

Figure 3.11: a) Composite energy scanning micro-beam orientation map of $\langle 311 \rangle$ reflection. b) Reciprocal Space orientation map for the $\langle 311 \rangle$ reflection

of the reflection is very similar to figure 3.10 a) and the same features can be identified in both maps.

In the energy scanning mode (setup 3), a total of 168 diffraction images were collected; 67 in the energy range from 17 to 18keV and 101 in the range from 18 to 19.5 keV. The overall intensity map shown in figure 3.11 a) was then built up by summing the individual "slices" of the reflection collected at different energies. This slice structure of the reflection can be seen on close inspection of figure 3.11 a), where horizontal lines extended in the χ direction are clearly visible. This slice structure could be avoided by performing energy scans at more closely spaced intervals. At $\Omega = 24.4$ a line appears to run across the map. Intensity contributions at $\Omega > 24.4$ come from the 17-18keV scan range, whilst contributions at $\Omega < 24.4$ come from the 18-19.5 keV scan range. This discontinuity in intensity highlights a limitation of the energy scanning setup: as the monochromator was scanned though the energy spectrum, the flux incident on the sample changed as a function of both the flux available at the selected energy in the bending magnet spectrum and the pitch of the second DCM crystal. Ideally, measurements at each individual energy should be normalised with respect to a measure of the actual flux incident on the sample. Unfortunately no incident beam monitor was available, so this correction could not be carried out.

Figure 3.11 b) shows the reciprocal space map of the $\langle 311 \rangle$ reflection, projected onto the tangential directions of reciprocal space. The energy of the incident beam

was fixed at 17.5keV (setup 4). Diffraction measurements were collected for a range of Ω tilts from 19° to 31°. The resulting patterns were integrated in the 2θ direction and then stacked up to construct a map of intensity variation in Ω, χ space [161].

Comparing figures 3.10 and 3.11 it is clear that the same key features can be identified in all maps. This confirms that the gauge volume probed was maintained consistently in the different setups. Figures 3.10 a) and b) show significantly lower intensities in the higher Ω part of the reflection. This change can be ascribed to the change in beam size from $5 \times 5 \mu m^2$ in setups 1 and 2 to $10 \times 10 \mu m^2$ in setups 3 and 4. Figure 3.11 b) shows significantly sharper diffraction peaks than Figure 3.11 a). Since setup 4 uses a fixed energy monochromatic beam, the intensities of the measured diffraction peaks could be interpreted quantitatively in terms of the volume fraction of the scattering volume taken up by any particular misorientation direction. However this has to be weighed up against the positional inaccuracies caused by sample tilting in setup 4.

Conclusions

Qualitatively, all four diffraction methods of measuring local, dislocation induced, misorientation (micro-beam Laue diffraction, high resolution micro-beam Laue diffraction, energy-scanning and RSM) compared in this section captured the same key reflection features. Angular spread of the intensity distribution was very similar. Direct comparison of the methods highlights the advantages and limitations of each: both micro-beam Laue setups offer no resolution of d-spacing, but rapid data collection and good sampling volume consistency as no tilting is required. Energy scanning setup offers resolution in the radial direction of reciprocal space, without the need for sample tilting, but intensity variations make it difficult to interpret the results quantitatively without an incident beam monitor. RSM suffers from tilting-induced positional sampling volume inconsistencies, but offers constant incident flux and d-spacing resolution.

For studies concentrating solely on the analysis of misorientation in the scattering volume, high resolution micro-beam Laue spot analysis provides equivalent data to RSM in a fraction of the time.

3.1.4 Combined micro-beam Laue and white beam topography

Motivation

The study of individual Laue reflections at high angular resolution using a broad bandpass beam has recently been reported in the different context of scanning white beam topography [162]. Diffraction topography has been employed since the 1940s for the imaging of highly perfect crystals [163–165]. Its contrast mechanisms are very different to those of conventional absorption imaging. The technique is very sensitive to small lattice orientation changes in the sampling volume and is particulary suited to the visualisation of individual line defects, such as dislocations, and small local lattice strains [166]. Classical diffraction topography relies on the shape of the topograph being dominated by the real space dimensions of the illuminated sample. Hence features in the topograph can be related to a physical location in the scattering volume. Local, small, lattice orientation changes and strains provide some contrast in the topographs and can hence be visualised. These local misorientations must be small enough so as not to distort the overall shape of the topograph for ray tracing to be possible. The application of topography to deformable, metallic crystals is much more difficult. Even at small levels of plastic deformation, the lattice misorientations introduced by dislocation motion and substructure formation are sufficient to make ray tracing impossible. This intrinsic problem has thus far prevented X-ray topography from being used to image deformation in (poly) crystals [167], although reports are available for ice [168, 169] and silicon [170–172].

A possible solution has recently been proposed in the form of scanning white micro-beam topography [162]. By using a small scanning beam rastered across the sample, real and reciprocal space can be partially deconvolved. The maximum misorientation in each topograph is limited by the scattering volume size and the

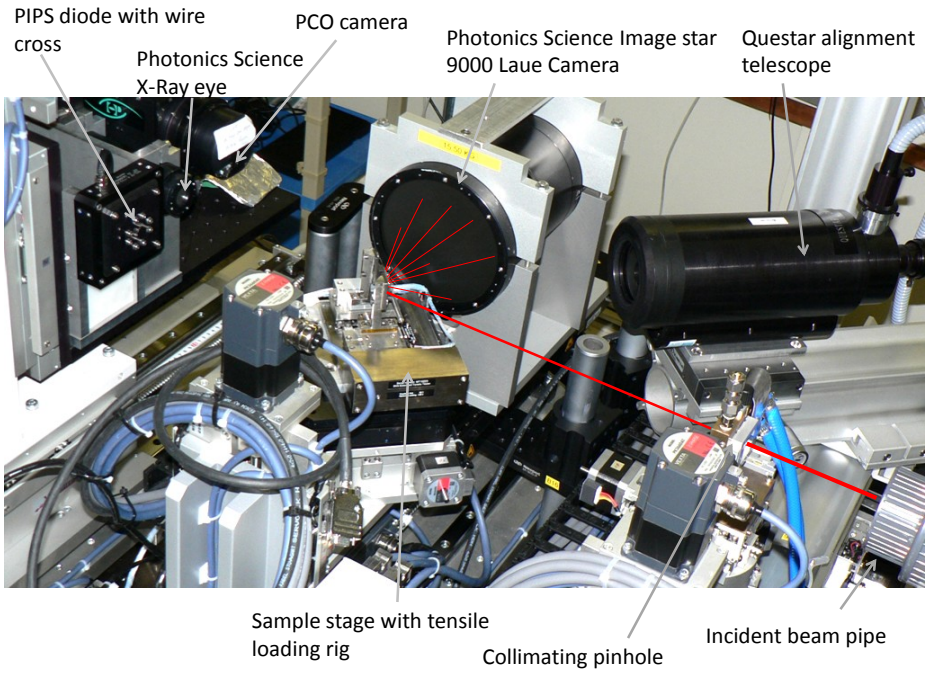

Figure 3.12: Combined micro-beam Laue and white beam topography setup on beamline B16 (DLS).

lattice curvature therein. From the individual scanning topographs it is possible to reconstruct an overall topograph of the scattering volume. In this topograph features can be identified that are smaller than the focal spot size of the incident beam, for example dislocation cell/wall structures in pure FCC metals after deformation.

Whilst scanning beam topography allows very high angular resolution mapping of lattice orientation about axes perpendicular to the scattering vector, topography measurements of at least two lattice reflections would be required to determine the full crystal orientation. The combination of micro-beam Laue diffraction and white beam topography seems to offer a natural extension of the setup on B16 (DLS). Laue diffraction provides high angular resolution lattice orientation, whilst the topographic measurements supply a map of lattice misorientation within the scattering volume.

Experimental setup, alignment and calibration

The combined micro-beam Laue and white beam topography setup was developed on the KOHZU optics table. Figure 3.12 shows an overview of the setup. The incident beam was pre-collimated using $S4$ slits to minimise heat loading and then

collimated to a beamsize of $5 \times 5\mu\mathrm{m}^2$ using a pinhole constructed from 4 Tantalum blades. The pinhole was mounted on a high accuracy, long travel translation. It could be translated into and out of the beam, making rapid changes between small and large beam size possible. Collimation, rather than focusing of the incident beam, meant that divergence was kept to a minimum. The sample was oriented such that Laue diffraction could be carried out in the conventional 45° reflection mode and white beam topographs collected simultaneously in transmission geometry. It was mounted in a purpose-built tensile loading rig, held between two upright post, to allow unrestricted access for incident and diffracted beams. For alignment and positioning a high magnification long range Questar telescope was used. Laue diffraction images were captured with the Photonic Science Image Star 9000 CCD camera mounted at a 2θ angle of 90° in the horizontal plane. To ensure optimum mechanical stability, and to minimise any relative movement between sample and detector, the camera was mounted directly on to the optics table with four stiff posts.

In transmission geometry (downstream of the sample) three further detectors were mounted: PIPS diode, PCO camera and MiniFDI camera (§ 3.1.1). The PIPS diode, with a set of crossed tungsten wires mounted in front of it, was used to monitor the transmitted intensity during pinhole alignment and to determine the collimated beam size, $5 \times 5\mu\mathrm{m}^2$. Transmission radiographs of the sample were recorded with the PCO camera. These constituted a check that the sample area which had been selected using the alignment microscope was illuminated correctly. Due to the sample mounting angle of 45°, radiographs were foreshortened compared to the alignment microscope image taken at 90° to the sample surface. Radiographs were also used to check correct alignment of the pinhole. Initially white beam topographs were to be recorded with the PCO camera. However it was not sufficiently sensitive and excessively long acquisition times were required. Instead the MiniFDI camera was used, giving good sensitivity even at low count rates.

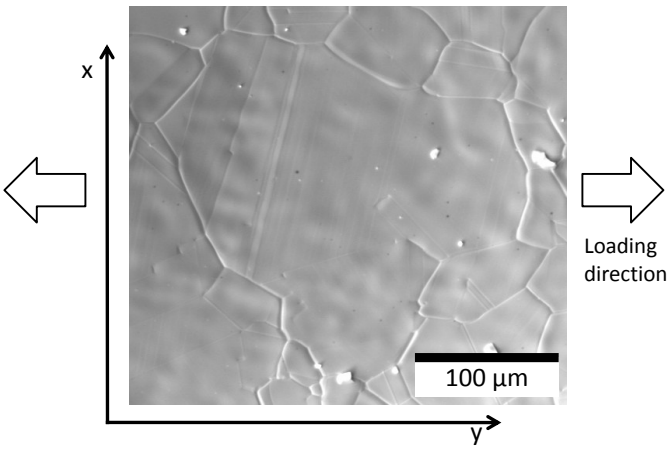

Figure 3.13: SEM micrograph of the undeformed grain of interest, showing clearly the presence of twins. Also shown are the sample coordinate axes and the loading direction.

Sample and loading

A waisted dogbone-shaped sample was cut from $15\mu\mathrm{m}$ thick Ni foil. It was heat treated as described in appendix A.1 and its microstructure showed the same general characteristics as described in appendix A.1.3. In the central gauge region of the sample a large grain measuring approximately $260 \times 170\mu\mathrm{m}^2$ was identified. Figure 3.13 shows an SEM micrograph of the grain and defines the sample reference axes. On the left hand side of the grain twins are clearly visible. The grain was oriented so that the $[0.735, 0.230, -0.637]$ crystallographic direction was aligned with the sample x-axis, the $[0.1803, 0.8399, 0.5120]$ direction with the sample y-axis and the $[0.6533, -0.4914, 0.5761]$ direction with the sample z-axis.

The sample was loaded in tension along the y-axis with nominal displacements of 0, 30, 50, 80, 110 and $145\mu\mathrm{m}$. After each deformation increment a micro-beam Laue map, scanning topograph and whole grain topograph were collected. To estimate the total strain in the grain that these displacements corresponded to, Digital Image Correlation (DIC) was used to track the grain boundaries in the transmission radiographs collected with the PCO camera. Due to intensity variations of the radiographs and phase contrast at the grain boundaries, only a rough estimate of strain could be made. A deformation of $110\mu\mathrm{m}$ corresponded to a total strain ϵ_t of $\sim 4\%$. Based on this the strains corresponding to the deformation increments were estimated to be 0%, $\sim 1\%$, $\sim 1.8\%$, $\sim 2.9\%$, $\sim 4\%$ and $\sim 5.3\%$ respectively.

Data interpretation

Micro-beam Laue diffraction patterns were pre-processed by background subtraction (appendix A.2). They were then indexed and refined using the XMAS software package [99] (§ 2.2.4). Initial calibration of the geometrical parameters of the setup was based on measurements of a silicon single crystal placed at the sample position.

From the refinement of Ni diffraction patterns, lattice orientations were deduced. To gain an overview of the local grain structure, inverse pole figure colour-coded plots were generated from the orientation data, using the MTEX MATLAB toolbox [173]. Smaller intragranular misorientations can be studied by considering a rotation matrix $\mathbf{R}_{dif,c}$ that maps lattice vectors in the crystal reference frame from a reference orientation $\mathbf{R}_{ref}$ to a new orientation $\mathbf{R}_{new}$.

$$\mathbf{R}_{ref} = \mathbf{R}_{new}\mathbf{R}_{dif,c} \Leftrightarrow \mathbf{R}_{dif,c} = \mathbf{R}_{new}^{-1}\mathbf{R}_{ref}, \tag{3.3}$$

where $\mathbf{R}_{new}$ and $\mathbf{R}_{ref}$ are two rotation matrices mapping a vector in the crystal reference frame to the sample reference frame. Both are given as part of the XMAS refinement output. For more convenient visualisation $\mathbf{R}_{dif,c}$ can be expressed in terms of its Rodriguez vector and angle. It is demonstrated in appendix A.4 that for small rotations, such as slight misorientations within a single grain, the Rodriguez vector is additive. Hence the individual components of the Rodriguez vector corresponding to $\mathbf{R}_{dif,c}$ can be plotted separately, corresponding to small rotations about the $[100]$, $[010]$ and $[001]$ crystal axes.

It is sometimes convenient to consider a rotation matrix $\mathbf{R}_{dif,l}$ which, in the laboratory frame of reference, rotates a crystal from a reference orientation, described by rotation matrix $\mathbf{R}_{ref}$, to a new orientation given by rotation matrix $\mathbf{R}_{new}$, such that:

$$\mathbf{R}_{dif,l}\mathbf{R}_{ref} = \mathbf{R}_{new} \Leftrightarrow \mathbf{R}_{dif,l} = \mathbf{R}_{new}\mathbf{R}_{ref}^{-1}. \tag{3.4}$$

Rotation matrix $\mathbf{R}_{dif,l}$ can also be visualised by computing its Rodriguez angle and vector.

Topographs were recorded from a $(0k0)$ sample reflection at a 2θ angle of $28°$. Given the FCC structure, possible reflections would be (020), (040) and (060), occurring at approximate photon energies of 14.6, 29.1 and 43.6 keV respectively. Given the energy spectrum of beamline B16 (DLS) (figure 3.1), the largest contribution to the scattered intensity is likely to arise from the (020) reflection, with a smaller contribution form the (040) and no contribution from the (060) reflection. Of course contributions from all three reflections would scatter to the same position on the detector. Hence, in terms of rotation analysis, it is not necessary to establish how much each order of the $(0k0)$ reflection contributed to the overall detected intensity.

Topographs were recorded in two different regimes:

Whole grain topographs The entire grain was illuminated with a large ($0.4 \times 0.4\mathrm{mm}^2$) beam. Using the radiographs collected by the PCO camera, it was confirmed that the illuminated area was larger than the grain of interest. The resulting whole grain topograph was collected on the mini FDI camera.

Scanning topographs A much smaller beam of $30 \times 30\mu\mathrm{m}^2$ was rastered across the sample in steps of $20\mu\mathrm{m}$. The topographs collected at each step arise from the small illuminated areas. Individual topographs needed to be re-assembled to give an overall compound topograph of the grain.

Whole grain topographs were interpreted by remapping using a linear, projective remapping function (figure 3.14). Four clearly recognisable features were selected in the captured topograph (figure 3.14 a)) that could also be identified in the SEM micrograph (figure 3.14 b)). The SEM micrograph was used as a spatial reference for the topograph. Based on the four selected points, a linear, projective transform was found, that mapped each salient point in the topograph to its corresponding point in the SEM image. This transform was then applied to find the new positions of all other points in the topograph. Since the new positions did not generally coincide with the regular pixel grid of the re-mapped topograph, bi-linear interpolation was used to project the intensity at the new position onto the pixel grid of the re-mapped topograph (figure 3.14 c)). This remapping routine was applied

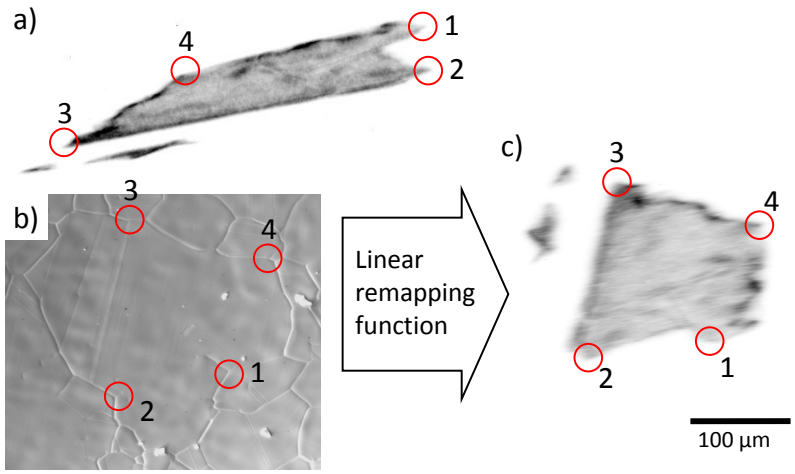

Figure 3.14: Schematic of the re-mapping approach used for whole grain topographs. a) Distorted whole grain topograph as recorded. b) SEM micrograph used as spatial reference for remapping of the whole grain topograph. c) Remapped whole grain topograph.

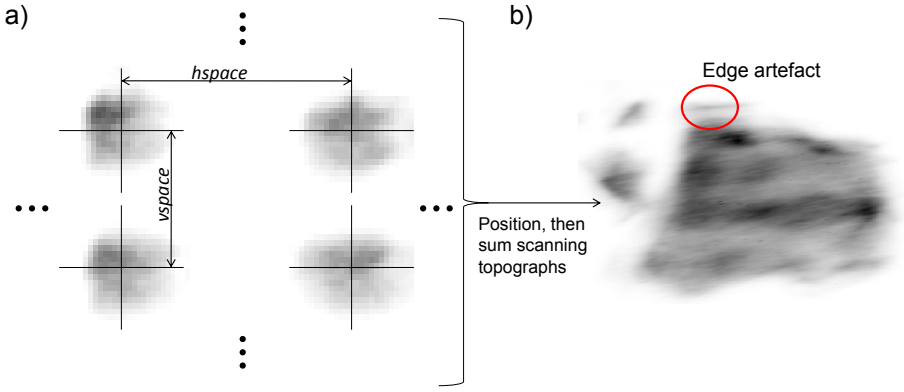

Figure 3.15: Schematic of the assembly procedure used for the scanning topographs. a) Individual re-mapped scanning topographs are positioned according to motor positions and then added to give the compound topograph b).

to the whole grain topographs collected at each deformation increment. The key assumption in this procedure is that the shape of the whole grain topograph is dominated by the shape of the grain in real space and that lattice rotations only give rise to small, local changes in contrast. For undeformed, annealed crystals and crystals that have only undergone small amounts of deformation, these assumptions are reasonable. However, they are likely to break down under more severe deformation and increased local lattice misorientation leading to distortion of the whole grain topograph shape. This is where the partial de-convolution of real and reciprocal space using scanning topographs becomes necessary.

Scanning topographs were collected over a regular grid of sample translation positions with a nominal collimated beamsize of $30 \times 30 \mu\mathrm{m}^2$. Each individual scanning topograph was re-mapped to the sample reference frame using the remapping function established from the undeformed sample whole grain topograph. Then the centre of mass of each topograph was positioned according to the motor positions, with a fixed pixel offset $hspace$ and $vspace$ in the horizontal and vertical direction respectively between adjacent motor positions (figure 3.15 a)). Finally, the contributions from the individual scanning topographs were summed up to produce the compound topograph (figure 3.15 b)).

The key assumption in this procedure is that the area illuminated by the scanning beam is well matched to the measurement step size, so that adjacent topographs only have a small overlapping region and essentially every point of the sample under study has received a constant amount of illumination. In that case the scattered intensity of each scanning topograph can be clearly ascribed to a specific area on the sample. By then shifting the scanning topograph centre of gravity according to the motor positions, the effect of large scale rotations (rigid body) which cause net rotation of gauge volume lattice is removed and only small (local) rotations within the scattering volume remain. This corresponds to a high pass filtering of lattice rotations, i.e. only rotations occurring over length scales shorter than the sampling volume persist. The centre of gravity of individual topographs was chosen for positioning as it was assumed that it corresponds to the mean orientation of the sampling volume. This was not the case on the edge of the grain of interest, where the sampling volume was only partially filled by the reflecting grain. This effect resulted in mis-positioning of scanning topographs at the edge of the compound topograph, leading to multiple images of features at the grain edge (e.g. top of the grain in figure 3.15 b)). An obvious way of minimising edge effects would be to reduce the sampling volume size, so that a smaller portion of the mapped grain suffers from edge effects. Alternatively, an iterative procedure could be used so that for each scanning position the illuminated grain-area is determined based on e.g. an SEM micrograph. More accurate positioning of scanning

topographs might then be achieved. In the present study this refinement was not included.

Undeformed grain

Prior to in situ deformation, the grain was characterised using a number of different techniques. The results are collated in figure 3.16. Figures 3.16 a), b) and c) respectively show an optical polarised light micrograph, a transmission radiograph and an SEM micrograph of the grain. In all images the grain's boundaries can be clearly made out. The transmission radiograph was corrected for foreshortening in the horizontal direction (this happens as the sample is set at an angle of 45° to the incident beam). Grain boundaries are highlighted due to phase contrast. Vertically running boundaries (in the x-z plane) can be seen as two separate lines running at approximately constant distance to each other, one from the front and one from the back face of the sample due to the sample tilt. Horizontal boundaries (in the y-z plane) on the other hand fall approximately on the same line. This confirms the observation in appendix A.1.3 that grain boundaries tend to lie at 90° to the sample surface. In figure 3.16b) the region of interest is highlighted for illustration.

Figures 3.16 g) and h) show inverse pole figure colour-coded orientation maps from micro-beam Laue measurements and EBSD respectively. As expected the agreement of the overall orientations found in both maps is very good. It is interesting to note, however, that some of the fine detail visible in the EBSD map cannot be discerned in in the micro-beam Laue map. Grains 1a and 2a, both thin twinned areas, cannot be distinguished in figure 3.16 g). Similarly grain 6 cannot be made out in figure 3.16 g). This is due to the lower spatial resolution of micro-beam Laue measurements compared to EBSD, but may also be associated with the difference in the bulk versus sample surface sensitivity of the techniques.

The re-mapped whole grain topograph of the undeformed grain (figure 3.16 d)) corresponds in shape well to the outline of grain 1. On the left hand side of the topograph, contributions from grains 5 and 6 can be seen. To confirm that the topograph indeed arises from the intended grain under study, the intensity of the scanning topographs was integrated and plotted according to the motor positions

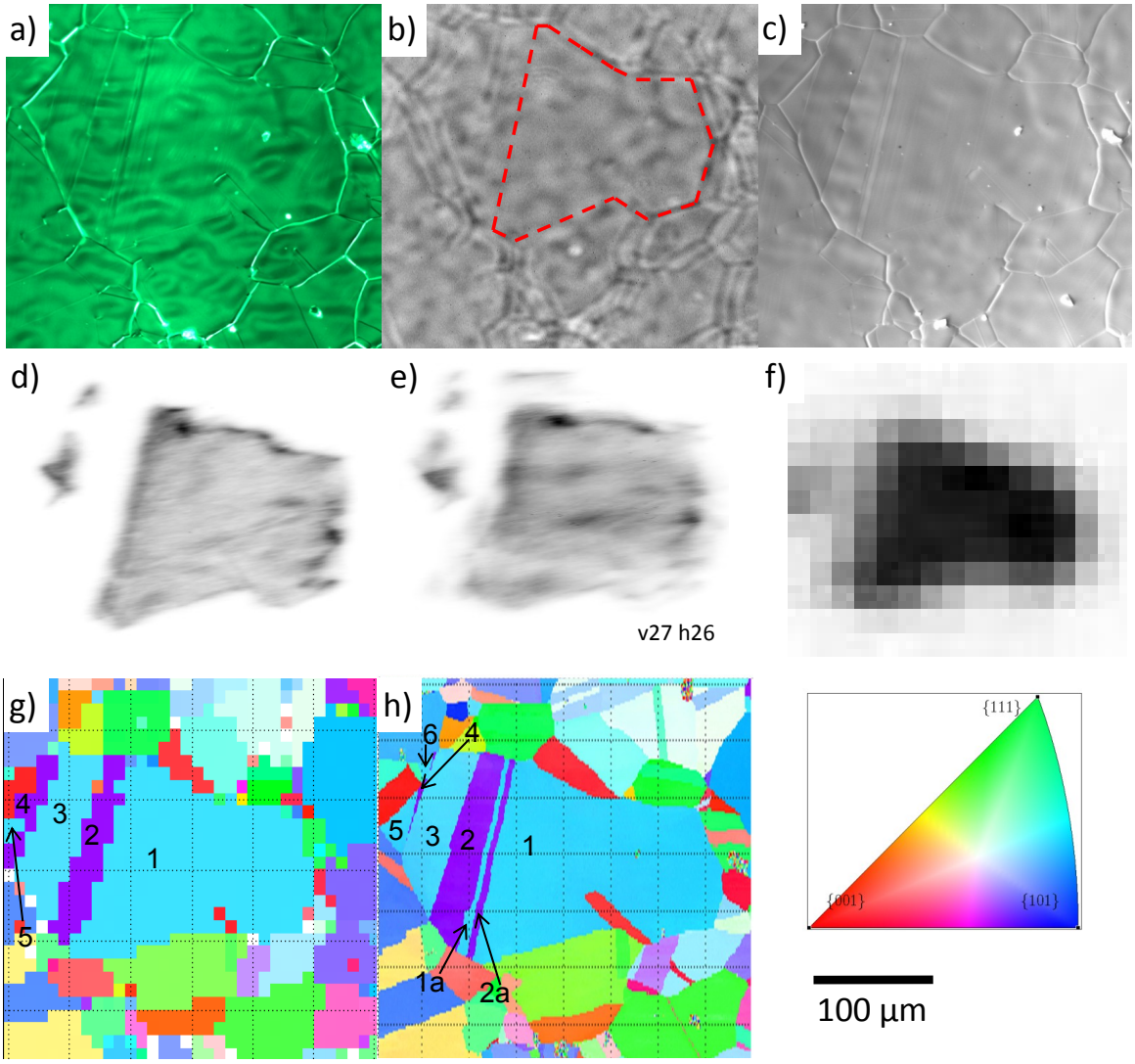

Figure 3.16: Multiple method characterisation of the grain of interest before deformation. a) Optical polarised light micrograph. b) Transmission radiograph, corrected for foreshortening in the horizontal direction. c) SEM micrograph. d) Remapped whole grain topograph. e) Compound scanning topograph. f) Integrated intensity map from scanning topographs. g) Micro-beam Laue orientation map. h) EBSD orientation map (note that common colour coding of orientations was used).

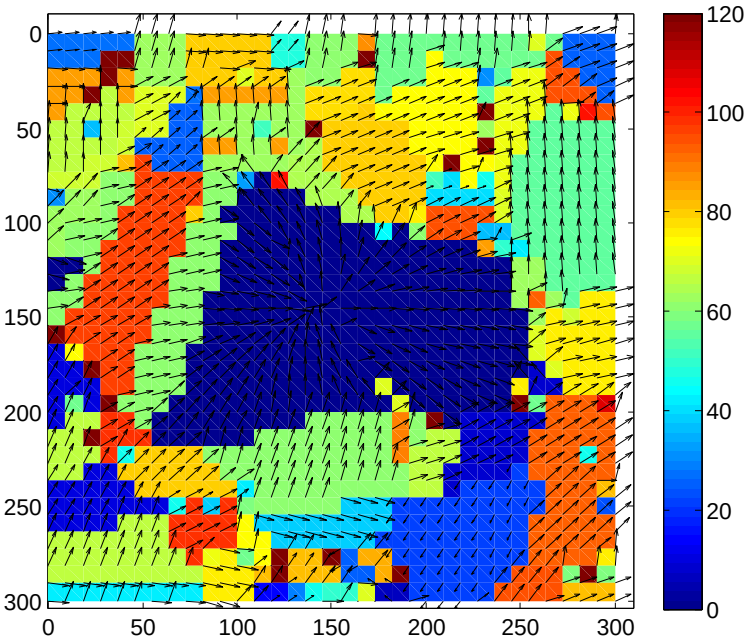

Figure 3.17: Variation of grain orientation with respect to grain 1 in lab coordinates. Colour scale is Rodriguez angle in degrees. Arrows are the in-plane, i.e. x and y, components of Rodriguez vector.

during the scan (figure 3.16 f)). The general shape of the high intensity region corresponds to grain 1, confirming the selection of a reflection from the correct region. The compound scanning topograph of the undeformed grain (figure 3.16 e)) is similar to the whole grain topograph (figure 3.16 d)). Its features are less sharp and different contrast is noted. The partially filled gauge volume edge effects can be clearly seen around the boundaries of the grain.

Comparing the whole grain topograph (figure 3.16 d)) to the micro-beam Laue and EBSD orientation maps (figure 3.16 g) and h)), it is interesting to note that only grains 1, 5 and 6 contribute to the topograph, although grain 3 shares the same out-of-plane direction. This can be explained considering figure 3.17, which shows a representation of the orientations of all grains in the mapping region relative to the orientation of grain 1 in lab coordinates. This rotation is described by $\mathbf{R}_{dif,l}$ (equation 3.4). For easier visualisation, the rotations were plotted in terms of the Rodriguez vector and angle. The colour scale corresponds to the Rodriguez angle in degrees. Superimposed are the in-plane, i.e. x and y, components of the unity Rodriguez vector. Grain 3 is rotated by 96.5° about the sample $(0.535, 0.832, -0.149)$

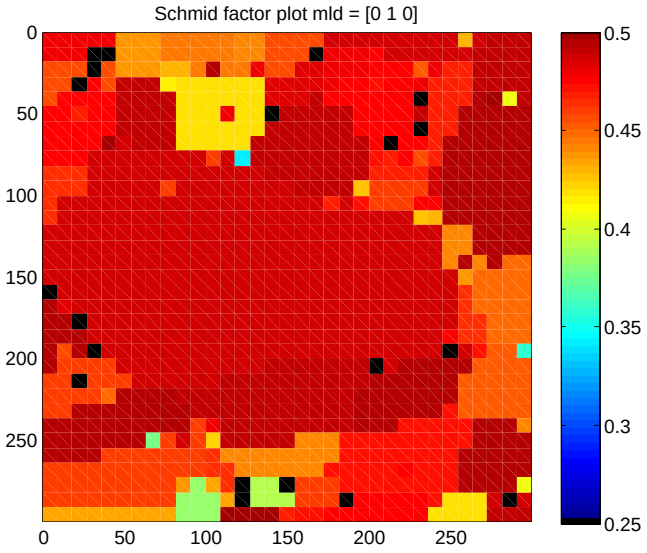

Figure 3.18: Plot of Schmid factor in the sampling region with respect to the macroscopic loading direction along the y-axis, i.e. $[010]$ sample direction.

direction, and hence does not have a $(0k0)$ reflection in the same position as grains 1, 5 and 6.

In crystal coordinates the rotation (i.e. $\mathbf{R}_{dif,c}$, equation 3.3) between grains 1 and 3 can be decomposed into two twinning rotations: from grain 1 to grain 2, $-60°$ rotation about $[111]$ axis, and from grain 2 to grain 3, $-60°$ about the $[11\bar{1}]$ direction. From grain 3 to grain 5, via grain 4, the reverse twinning rotations occur: $60°$ rotation about $[11\bar{1}]$ (grain 3 to grain 4) followed by $60°$ rotation about $[111]$ axis (grain 4 to grain 5). These twin boundaries can be identified as $\Sigma 3$ boundaries [174].

Figure 3.18 shows a plot of Schmid factor with respect to the macroscopic loading direction along the sample y-direction. Grains 1 to 5 share a very similar, high value of Schmid factor, ranging from 4.875 to 4.885. For grain 1, the highest Schmid factor occurs on the slip system with slip plane normal $\hat{\mathbf{n}} = (\bar{1}11)$ and slip direction $\hat{\mathbf{s}} = [110]$.

Evolution during deformation

Evolution of the raw and re-mapped whole grain topographs and of the compound scanning topographs is shown in figure 3.19. Up to total strain $\epsilon_t = 1.8\%$, the raw whole grain topographs show comparatively little distortion. After re-mapping based on the SEM micrograph, they capture well the shape and size of grain 1.

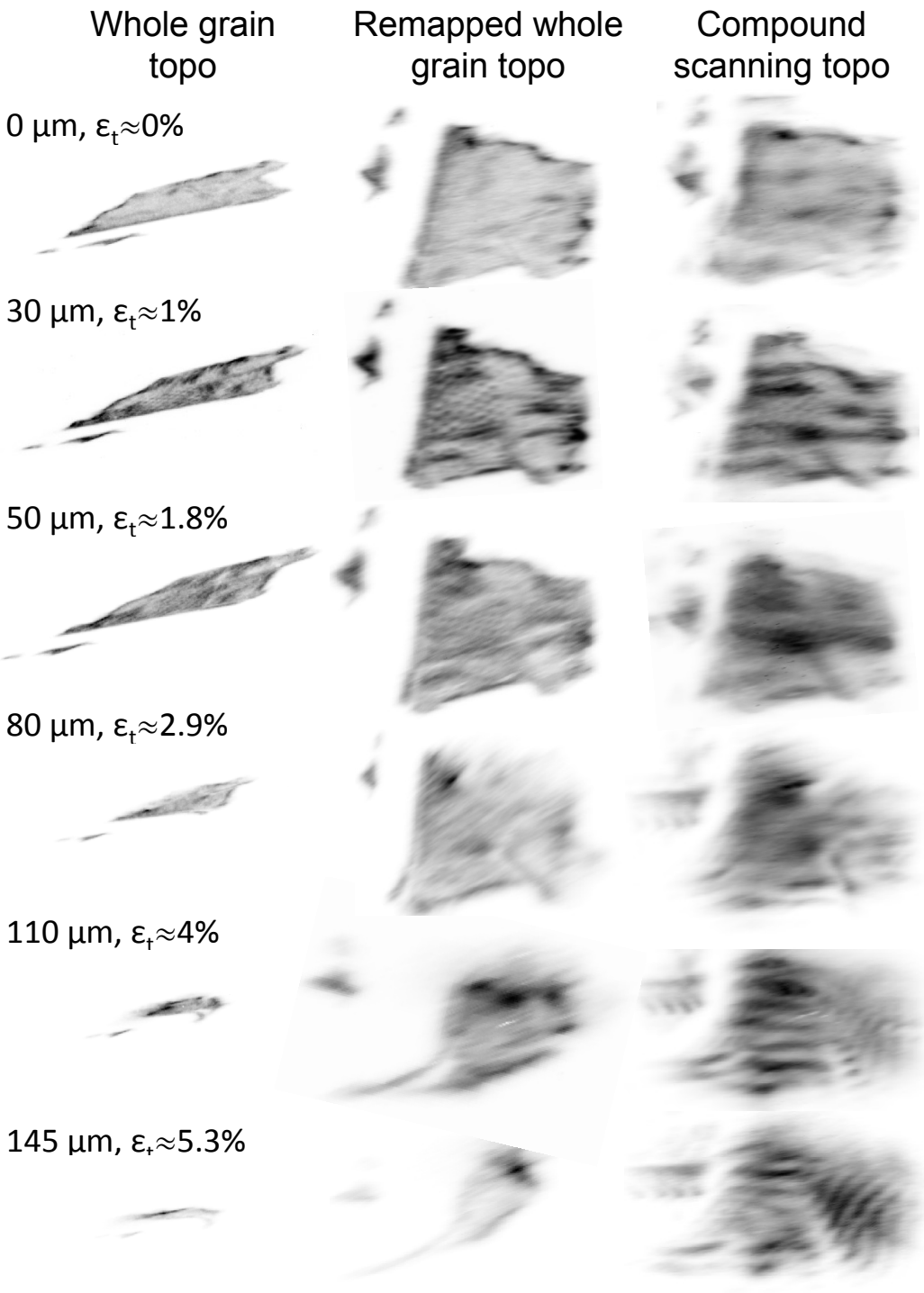

Figure 3.19: Evolution of raw and re-mapped whole grain topographs and compound scanning topographs at different stages during the deformation process.

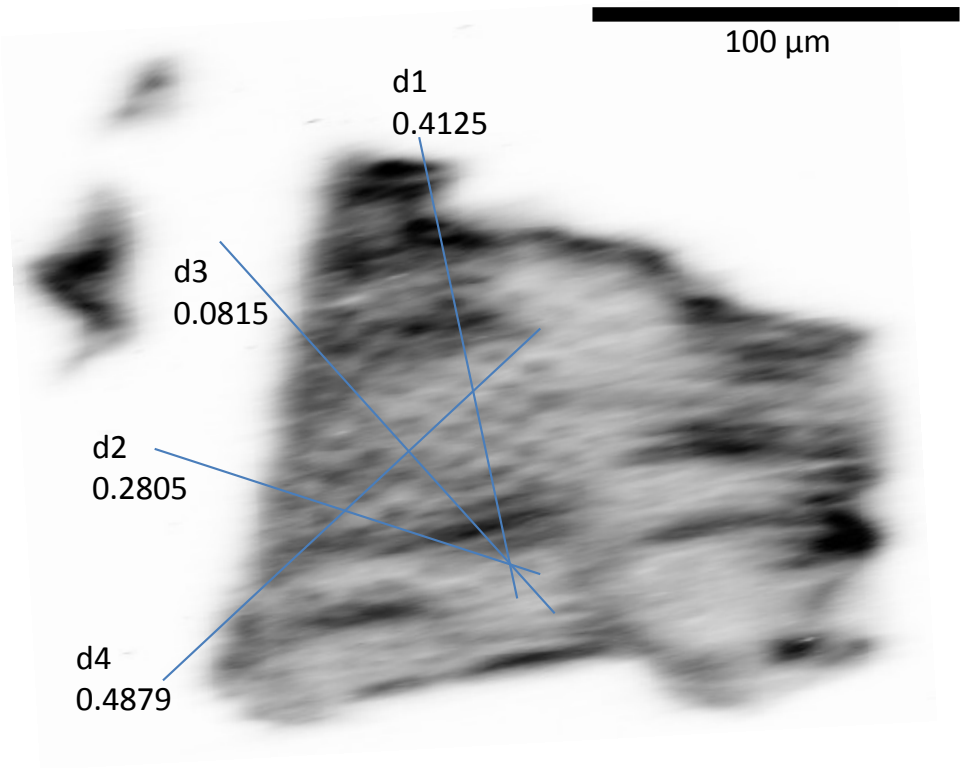

Figure 3.20: Re-mapped whole grain topograph at 1% total strain. Superimposed are the traces of the four slip planes.

Spatial features in the SEM micrograph can be easily related to the whole grain topograph. The compound scanning topographs are similar to the whole grain topographs. In the centre of grain 1 geometrical features are captured well. At the grain edges the previously discussed artefacts can be seen.

A number of whole grain topographs were collected at deformation increments between those in figure 3.19. It was noted that at $\epsilon_t \sim 0.4\%$ the formation of a "chequer" pattern started at the twin boundary between grains 1 and 2. This pattern progressively spread across grain 1 to the distribution shown in the enlarged topograph at $\epsilon_t = 1\%$ (figure 3.20). The individual partitions in the chequer pattern are lozenge shaped. Their side length was estimated as $\sim 6 - 8\mu\mathrm{m}$. With increasing deformation no further spreading of the chequer pattern across the grain could be observed. The extent shown in figure 3.20 was maintained. From $\epsilon_t = 1.5\%$ the chequer pattern faded in intensity, and at $\epsilon_t \sim 2\%$ it could no longer be observed. The size of the individual partitions in the chequer pattern decreased slightly with deformation to $\sim 4 - 6\mu\mathrm{m}$ at $\epsilon_t = 1.8\%$. The compound scanning topographs in

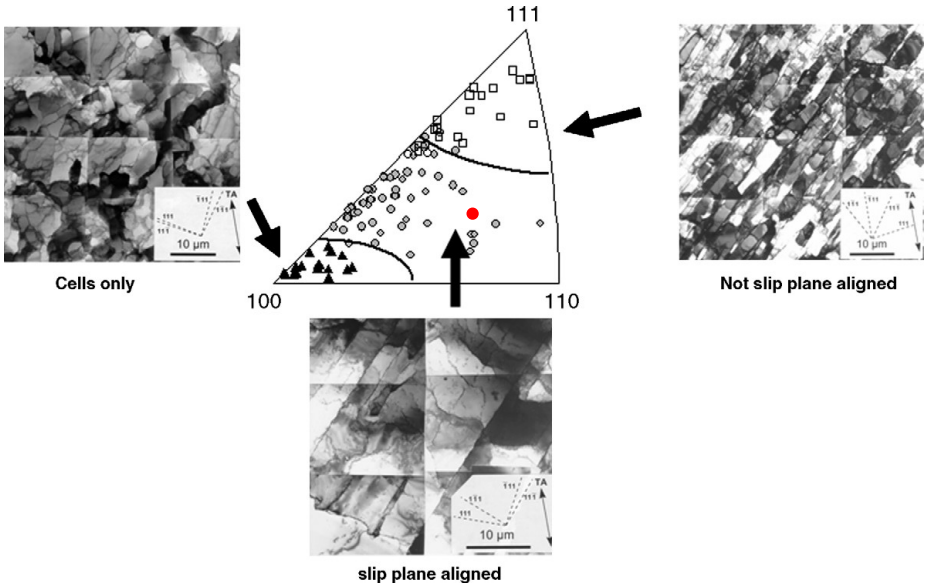

Figure 3.21: Formation of different dislocation substructures as a function of loading axis orientation in aluminium. Superimposed in red is the loading axis of grain 1. Figure from Winther [175]

figure 3.19 for $\epsilon_t = 1\%$ and $\epsilon_t = 1.8\%$ show the same chequer pattern as the whole grain topographs.

Superimposed on the whole grain topograph at $\epsilon_t = 1\%$ (figure 3.20) are the traces formed by the four slip planes and the sample surface. Noted next to each trace is the highest Schmid factor of any slip direction in the plane. Trace d4 corresponds to the slip plane with normal $\hat{\mathbf{n}} = (\bar{1}11)$ and has the highest Schmid factor. It is aligned with one of the chequer pattern directions.

The chequer pattern might arise from the formation of a dislocation cell/wall type structure at low deformation strains. Based on TEM studies Winther [175, 176] reported the establishment of different dislocation substructures during the tensile deformation of aluminium single crystals as a function of crystallographic orientation with respect to the loading axis. The behaviour can be captured by splitting the stereographic triangle into three regions (figure 3.21). Crystals orientated such that the loading direction lies close to the $\langle 111 \rangle$ axis tend to form dislocation structures which are not aligned with the slip planes. If the loading axis is close to the $\langle 100 \rangle$ direction, a dislocation cell-wall structure is formed in which only some of the dislocation walls are aligned with the slip systems. In the region between these extremes, dislocation structures form geometrically necessary boundaries (GNBs)

which are aligned with the highest Schmid factor slip system. Plotting the orientation of the macroscopic loading axis of Ni grain 1 (red dot) alongside the data presented by Winther [175, 176] confirms that one would indeed expect any GNBs to be aligned with the highest Schmid factor slip system (figure 3.21). The dislocation micro-structures formed in FCC aluminium and nickel are indeed similar, as confirmed by Bay [177]. For slip system aligned GNBs in aluminium, the spacing between GNBs has been estimated to be of the order of $4 - 10\mu\mathrm{m}$ based on TEM micrographs [175, 178]. This magnitude agrees approximately with the spacing of GNBs observed in grain 1. No clear indication could be found as to how the size of the dislocation structure might evolve with increasing plastic deformation. The trend for decreasing GNB spacing observed here seems plausible, providing increased overall lattice curvature with deformation.

With increasing deformation, the whole grain topographs start to fragment and become difficult to interpret even with re-mapping. At $\epsilon_t = 2.9\%$, the overall shape of grain 1 can still be recognised in the re-mapped topograph, however the top right hand corner of the topograph is already severely distorted. From $\epsilon_t = 4\%$ onwards whole grain topographs are too distorted for interpretation. The compound topographs remain interpretable to higher deformation. At $\epsilon_t = 2.9\%$ some horizontal streaking, parallel to the loading direction can be seen in the right hand half of grain 1. With increasing deformation these streaks become inclined at 45° to the loading direction and increase in intensity to a maximum in the last topograph at $\epsilon_t = 5.3\%$. On the left hand side of the grain some horizontal streaks form at $\epsilon_t = 4\%$, but their intensity is reduced again at $\epsilon_t = 5.3\%$.

Unfortunately even at modest deformations beyond $\epsilon_t = 2.9\%$ individual scanning topographs become severely distorted due to lattice orientation spread within the gauge volume. Their shape is no longer dominated by the real space of the sampling volume. This becomes particularly clear when considering mosaics of scanning topographs assembled with $vspace$ and $hspace$ such that individual scanning topographs are well separated spatially, but can be viewed as an ensemble. Figure 3.22 shows the evolution of these mosaics with deformation. Scanning topographs in the centre of the undeformed grain 1 are of square shape, replicating

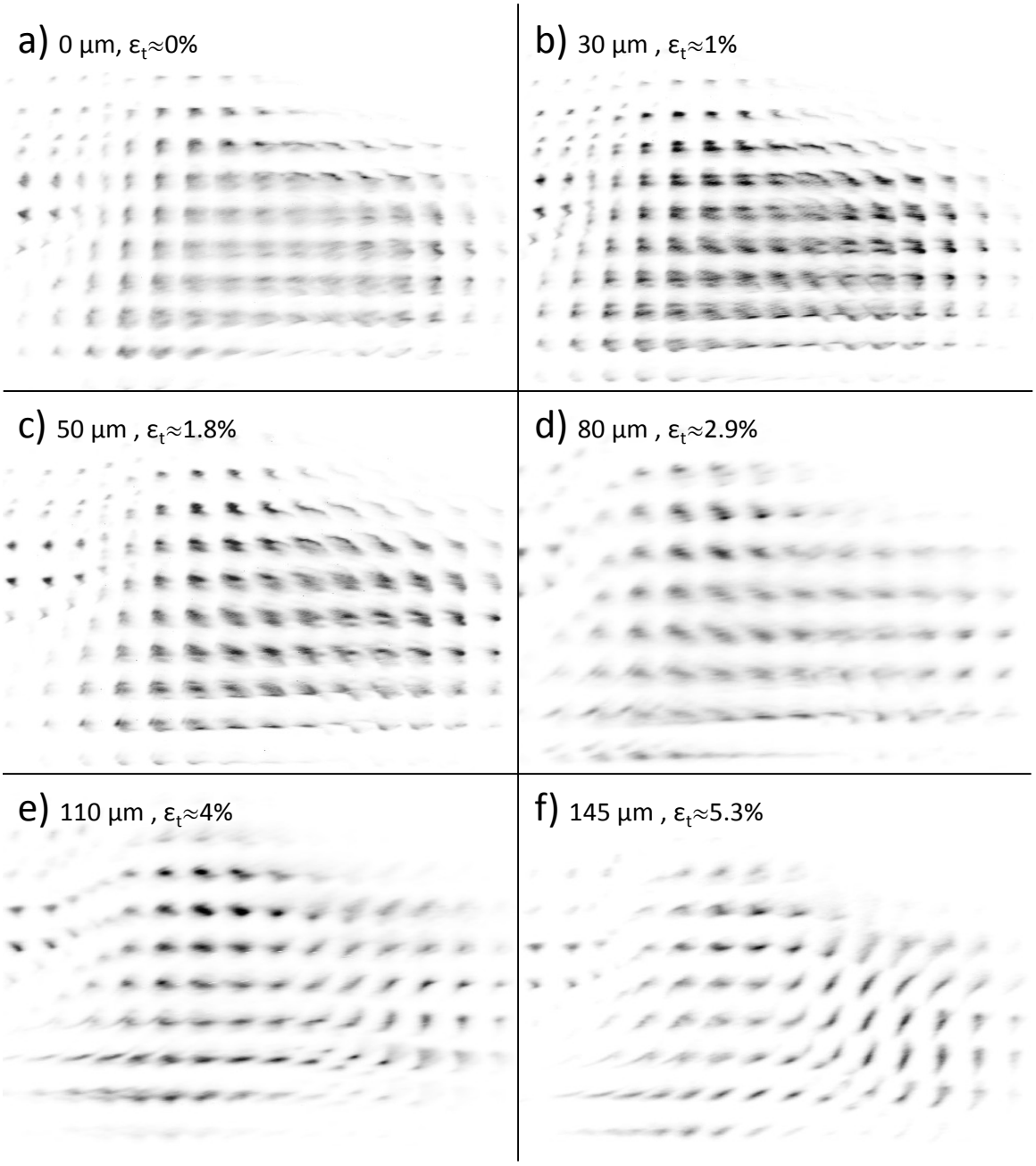

Figure 3.22: Mosaics of scanning topographs at increasing deformation assembled with $hspace$ and $vspace$ sufficiently large to avoid any overlap.

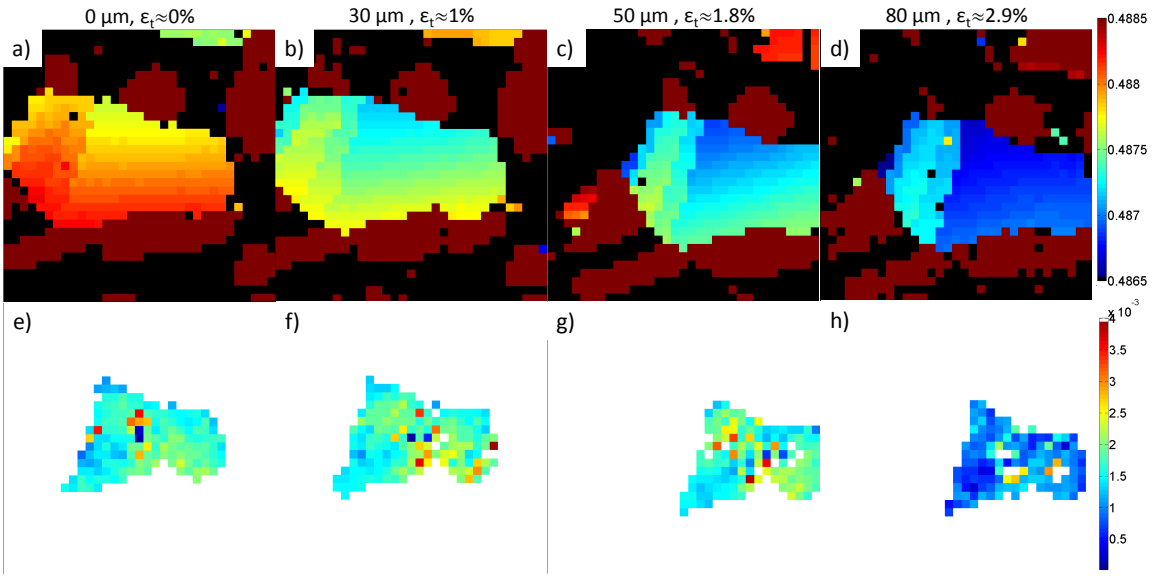

Figure 3.23: Schmid factor a) to d) and Rodriguez rotation angle gradient e) to h) evolution with deformation. Rotation angle colour scale is given in degrees per μm.

the shape of the illuminated sampling area. In the mosaic topographs at $\epsilon_t = 1\%$ and 1.8% the formation of the chequer pattern observed in the whole grain topographs can be clearly made out, whilst the topographs retain the approximately square shape of the illuminated sampling volume. From $\epsilon_t = 4\%$ onwards, significant deformation of the scanning topographs can be seen. At $\epsilon_t = 5.3\%$ the assembly of the compound scanning topograph becomes difficult due to severe distortion. Displaying them in the form of a mosaic makes it possible to visualise the different deformation types in separate areas of the grain.

To compare observations of lattice rotation patterning with the information which can be derived from micro-beam Laue diffraction, the evolution of Schmid factor in grain 1 was plotted as a function of deformation. Figures 3.23 a) to d) show maps of Schmid factor at deformation increments of $\epsilon_t = 0\%$, 1%, 1.8% and 2.9% respectively. From the colour scale it is clear that Schmid factor only evolves over a very small range from 0.4885 to 0.4865. It decreases with increasing deformation as the grain rotates under the influence of single slip.

Figures 3.23 e) to h) show the evolution of Rodriguez angle gradient at deformations of $\epsilon_t = 0\%$, 1%, 1.8% and 2.9% respectively. The Rodriguez angle gradient was plotted by taking the Rodriguez angle computed with respect to lattice orientation at the centre of grain 1 as a scalar field. To this the grad operator was

applied and the total magnitude of the gradient at each point computed in units of $\mathrm{degrees}/\mu\mathrm{m}$. In neither the plots of Schmid factor evolution, nor the plots of rotation gradient can the formation of the fine "chequer" board rotation structures be observed. This illustrates the need for the combined use of micro-beam Laue diffraction and scanning beam topography. Laue measurements provide high angular resolution measurements of average lattice orientation within the scattering volume under study, whilst the white beam topographs provide information about lattice orientation at higher spatial resolution than the probe size.

3.1.5 Discussion

The combined micro-beam Laue and scanning beam topography setup offers interesting insight but also shows up a number of difficulties. Through the choice of a parallel beam setup in combination with pinhole collimation, photon flux throughout the measurements was low. This resulted in lengthy measurement times, whilst still only a fairly modest spot size of $\sim 5\mu\mathrm{m}$ FWHM could be achieved on the sample. This combination made the frequent collection of large Laue maps impossible and also severely limited the spatial resolution. There is no obvious gain to using a low divergence beam for micro-beam Laue diffraction.

For the scanning topographs the incident beam was collimated to a size of $\sim 30 \times 30\mu\mathrm{m}^2$, using slits a long distance $(4.5\mathrm{m})$ upstream of the sample. This meant that the size of the incident beam at the sample position was not exactly known. Unfortunately it was not characterised by wire scans. As a result, the stepsize between adjacent scanning topographs could not be matched to the illuminated area and an unknown overlap existed between adjacent topographs. In the ideal case, the spacing between scanning topographs would be matched such that only a small, well defined overlap exists between adjacent points.

The use of a parallel beam for the collection of scanning and whole grain topographs meant that there was only negligible magnification of the topograph with increasing distance. In an ideal crystal the spatial resolution of a parallel beam topograph is limited by the detector resolution. Any additional divergence of the topograph is due to misorientation in the sampling volume. Even for small rota-

tions and small sampling volumes, this leads to the topograph being dominated by reciprocal, rather than real space effects, as shown in the scanning topograph mosaics (figure 3.22).

This situation could be improved by using a divergent (focused) beam, e.g. as provided by KB mirrors. For the collection of micro-beam Laue diffraction patterns, the obvious benefits are the increased photon flux and the smaller spotsize, allowing reduced measurement times and higher spatial resolution.

For topographs, the benefits of a divergent beam are more subtle. In classical topography, where a monochromatic beam is used, use of a parallel beam is essential to maintain all parts of the crystal with the same lattice orientation in diffraction condition at the same time. In white beam topography this is not the case, since the availability of a spread of wavelengths means that all parts of a single crystalline sampling volume with small lattice misorientation should remain in diffraction condition. Divergence would geometrically magnify the topograph, the further the detector is placed from the sample. Hence the scale of features which can be resolved is no longer limited by the detector pixel size. Topograph shape will be dominated by the scattering volume dimensions in real space, as long as the misorientation in the sampling volume is smaller than the beam divergence.

Following the notation of Nye [179], the angular change in lattice orientation, α_{GND}, in a volume of side length L arising from a density, ρ_{GND}, of parallel, geometrically necessary edge dislocations sharing the same Burgers vector b is given by:

$$\alpha_{GND} = \rho_{GND} L b. \tag{3.5}$$

The greatest Rodriguez angle gradient in grain 1 can be estimated as $4 \times 10^{-3}\mathrm{deg}/\mu\mathrm{m}$ or $70\,\mu\mathrm{rad}/\mu\mathrm{m}$ (figure 3.23). Burgers vector b in Ni is 2.49Å. Hence the maximum GND density, ρ_{GND}, in grain 1 can be estimated to be of the order of $0.280\mu m^{-2}$ or $2.8\times10^{11}m^{-2}$. This is lower than the total dislocation density, ρ_0, measured by TEM in nickel micro pillars during deformation, which varied from $10^{12}m^{-2}$ before deformation to $10^{14}m^{-2}$ after severe plastic deformation [180]. The difference might be explained by only a small number of all dislocations being unpaired and hence contributing to lattice curvature. Hence ρ_{GND} is lower then ρ_0.

The distinction between GNDs and SSDs is scale dependant, as previously pointed out [181]. One can imagine a thought experiment in which the probe size can be varied seamlessly from the nm to the mm size. If we zoom in to observe a single dislocation, this dislocation will appear as geometrically necessary, as it is not counterposed by any others. In this case one might argue that at the very local scale, every dislocation is geometrically necessary, by virtue of the fact that it introduces some lattice rotation. Now, if one imagines sampling the same dislocation structure at a next higher scale, than some of the dislocations will be counterposed by others and not contribute to overall lattice rotation. The conclusion is that the observed GND density decreases as sampling size is increased, provided there is no overall, externally imposed lattice curvature present in the sample. Understanding and quantifying these sampling-scale dependant effects is vital in the comparison of experimental measurements to numerical simulations. For comparison the same sampling scale should be used. Experimentally the spatial sampling when using a divergent focused beam can be easily varied by selecting different distances from the focal spot. Whilst beam divergence remains the same, the size of the illuminated area can be varied, and hence the effects associated with different length scales selectively observed.

The divergence introduced by KB focusing optics can be estimated as $\sim 1 - 2mrad$. Provided the orientation spread in the sampling volume, α_{GND} is smaller than the incident beam divergence, spatial features in the sampling volume should dominate the shape of the topograph. Substituting α_{GND} equal to an incident beam divergence of $1mrad$ and $\rho_{GND} = 10^{12}m^{-2}$ into expression 5.5, provides an estimate of the largest sampling volume dimension, L, of $\sim 4\mu m$. A further complication is that the sampling volume extends through the thickness of the Ni foil (here $15\mu\mathrm{m}$). Which dimension of the sampling volume should be used to compute misorientation within the sampling volume based on ρ_{GND} depends on the line direction and Burgers vector of the dislocation distribution in the sampling volume.

During a recent experiment in collaboration with Brian Abbey, [162], a Ni foil sample similar to the one studied here was mapped at two deformation increments ($\epsilon_t \approx 4\%$ and $\approx 8\%$) by focused scanning beam topography on beamline ID22

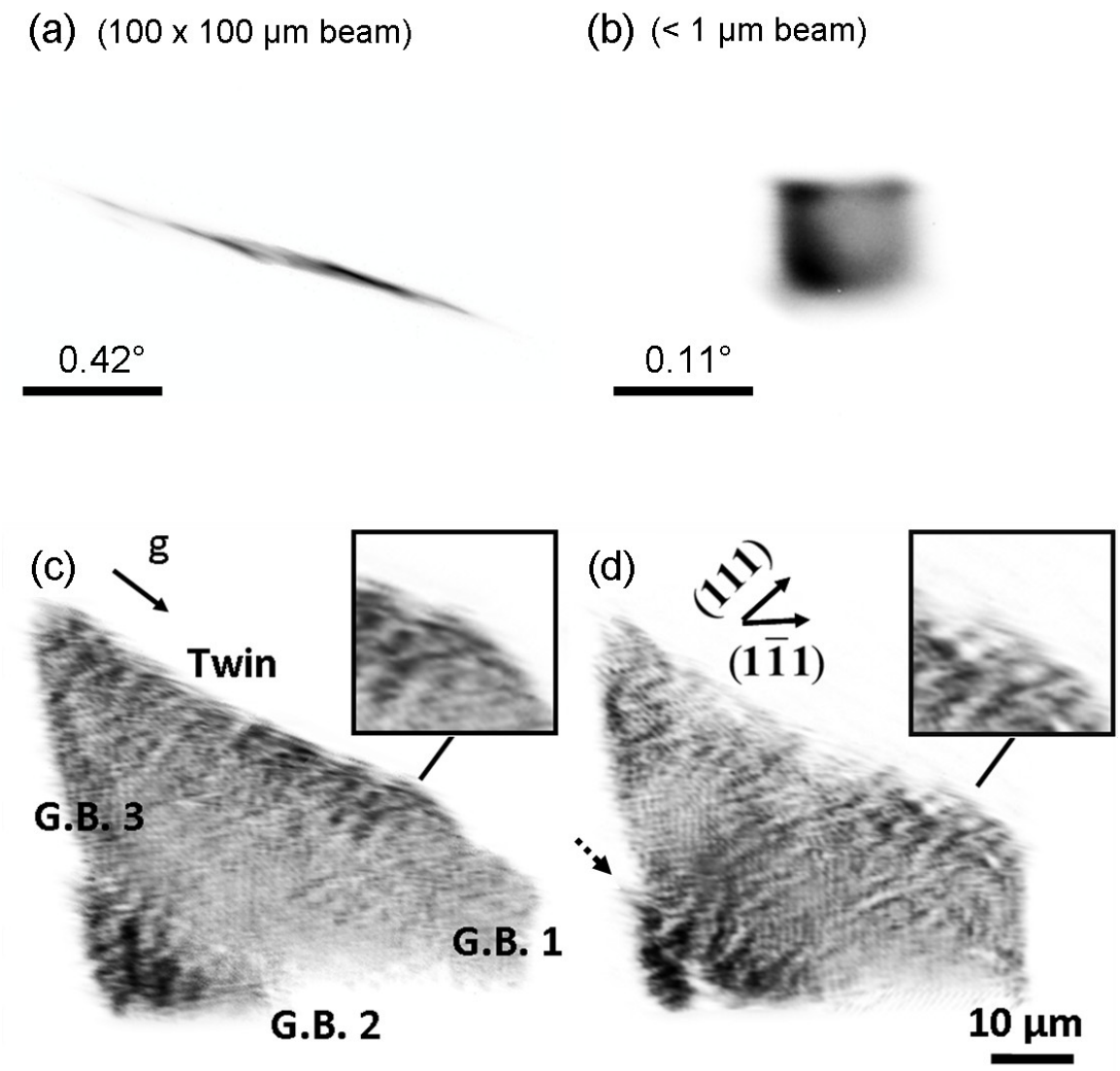

Figure 3.24: ID22 focused beam scanning topographs. a) Whole grain, box beam illumination topograph. b) Individual typical scanning topograph. c) Compound scanning topograph at $\epsilon_t \approx 4\%$. d) Compound scanning topograph at $\epsilon_t \approx 8\%$.

(ESRF). The incident X-ray beam, produced from the second undulator harmonic, had variable peak photon energy between 15 and 18 keV with $\triangle E/E \approx 1 - 2\%$. Focusing was achieved with KB mirrors to a focal spot size of $0.6 \times 0.6 \mu\mathrm{m}^2$. The scanning step was matched to the focal spotsize and scanning topographs were collected from a $\{220\}$ sample reflection. The scanning topographs were assembled into compound topographs as described above.

Figure 3.24 a) shows the uncorrected whole grain topograph. It is clearly too distorted for analysis due to lattice rotations. However, individual scanning topographs, due to the small sampling volume size and the divergence of the incident

beam, reproduce well the shape of the illuminated gauge volume of the sample, with some internal contrast due to variations of lattice orientation in the gauge volume (figure 3.24 b)). Compound scanning topographs for the two deformation states $\epsilon_t \approx 4\%$ and $\epsilon_t \approx 8\%$ (figures 3.24 c) and d) respectively) could be easily assembled due to limited distortion of the scanning topographs. At both deformation stages, fine features of lattice rotations can be identified. This illustrates the power of scanning beam topography when combined with a focused, divergent beam.

3.1.6 Future developments on B16 (DLS)

The key benefit of the setup on beamline B16 (DLS) is the flexibility it offers. New combinations of techniques can be easily tested and refined. The next logical step is the establishment of a combined micro-beam Laue diffraction and white beam scanning topography setup, but using a focused, divergent incident beam. This would allow much finer spatial sampling, provide greater photon flux to reduce measurement times, and enable more successful reconstruction of the scanning topographs to greater deformation levels. To this end, a set of KB focusing mirrors has been recently acquired and installed on the beamline. Their testing and commissioning is currently in progress.

3.2 Strain measurements and error estimation, BM32 (ESRF)

In the micro-beam Laue measurements on beamline B16 (DLS) it was not possible to measure elastic lattice strains reliably and repeatably. Lattice rotations on the other hand could be determined satisfactorily. This situation is to some extent reflected in the literature. Only a small number of publications mention elastic strain measurements. In general, the reported strains measured tend to be large, of the order of a few thousand micro-strain, e.g. in thin films [110, 117], metal matrix composites [141] or Si wafers under bending [133, 137]. Smaller strains have been

reported in pure FCC metal thin films exposed to cyclic thermal loading [106, 107] and in Sn whiskers during growth [114].

Very few of these investigations provide any estimate of the strain errors in the experimental measurements. The most widely quoted strain errors are of the order of 10^{-4} [97, 117, 122, 133, 137], though some estimates are as low as 5×10^{-5} [114]. Comparison of the macroscopic load with experimental strains measured in tungsten during in situ loading confirms the approximate strain error of 100 microstrain [182]. Tungsten is particularly suitable as it has a relatively wide elastic strain range ($\epsilon_y \approx 1400$ microstrain) and grains are close to elastically isotropic. Hence a uniform macroscopic stress field will generate an approximately uniform microscopic stress field. The strain error level of 100 microstrain is comparable to powder diffraction estimates [183, 184] and is acceptable for solid mechanics stress analysis. None of the investigations above discuss in any detail the sources of errors. However, in order to control and improve the experimental accuracy and perform reliable measurements proper understanding of the error sources in micro-beam Laue diffraction is vital.

One possible way of tackling this problem is to use a simulation-based approach. Laue diffraction patterns from a perfect, unstrained single crystal must be generated first. Then into the simulation of these patterns a small, known geometrical perturbation is introduced. The patterns are indexed and refined using XMAS software, assuming that no geometrical perturbation was present. The resulting elastic deviatoric strain computed from the refinement represents the strain error arising from the geometrical perturbation imposed in the simulation. This approach allows the analysis of the influence of individual geometrical perturbations on the overall strain error. Furthermore, it becomes possible to estimate the expected strain error of a measurement if the geometrical stability of the instrument is known. Refinement of the experimental setup can then concentrate on improving those factors which yield the greatest benefit in terms of strain accuracy.

As a basis for this study, the well-established micro-beam Laue diffraction setup on beamline BM32 (ESRF) was chosen. The beamline and setup will first be presented. Then the error estimation framework will be introduced and predictions of

$dd = \|\mathbf{D}\|$	$70\mathrm{mm}$
Energy	$5 - 25$ keV
CCD size	$165 \times 165\mathrm{mm}^2$ (2048×2048 pixels)
x centre - $xcent$	pixel 1024
y centre - $ycent$	pixel 1024
detector roll (α)	0°
detector pitch (β)	0°
detector yaw (γ)	0°

Table 3.1: Ideal micro-beam Laue diffraction geometrical parameters at beamline BM32 (ESRF).

the expected strain error made based on the stability of the instrument. These can be compared with the actual strain errors observed in our measurements on silicon and copper single crystal beams under four point bending.

3.2.1 Beamline BM32 (ESRF)

Beamline BM32 (ESRF) is a bending magnet beamline dedicated to surface diffraction under vacuum, high resolution monochromatic powder and single crystal diffraction and polychromatic micro-beam Laue diffraction. The bending magnet source has a size of $0.4 \times 0.3\mathrm{mm}^2$ FWHM and produces a smooth spectrum of photon energies in the range from 5 to 25 keV. For the dedicated micro-beam Laue diffraction setup, the beam is focused by a set of mirrors at $26\mathrm{m}$ and $30\mathrm{m}$ from the source to a secondary source for the final Kirkpatrick-Baez (KB) focusing optics. The secondary source at $35\mathrm{m}$ has a size of $20 \times 20\mu\mathrm{m}^2$ and is defined by a set of slits. Fine focusing of the beam onto the sample is carried out by KB mirrors at $60\mathrm{m}$ from source. Spot sizes of $0.5 \times 0.7\mu\mathrm{m}^2$ (H x V) FWHM on the sample can be achieved routinely. The sample is mounted such that its surface forms a 40° angle with the incident beam. Vertically above the sample at $2\theta = 90^\circ$, a MAR CCD detector with a tapered optics coupled scintillator is used to collect the diffraction patterns. The detector was originally designed for protein crystallography applications. Its distortion correction is hardwired and guarantees low pixel position errors.

The exact experimental parameters vary from measurement to measurement. Table 3.1 provides an overview of the "target" values of the setup. These were used

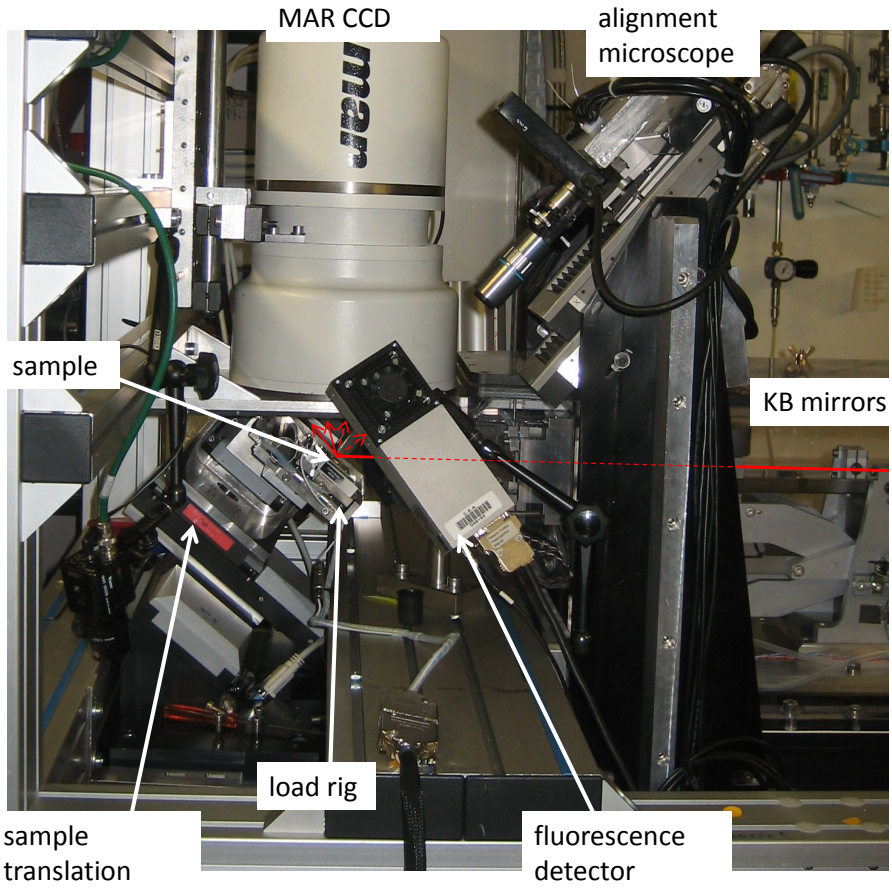

Figure 3.25: Photograph of the experimental micro-beam Laue diffraction setup at BM32 (ESRF). The incident beam is superimposed as a red line (dashed where obscured by other components).

as the basis for the simulation-based error analysis. Calibration of the experimental geometry was carried out based on the refinement of Ge or Si strain free single crystals. A high resolution optical microscope mounted at 90° to the sample surface allowed repeatable sample positioning (figure 3.25).

3.2.2 Error estimation framework for micro-beam Laue experiments

The geometry of the experimental setup can be described by six experimental parameters. Three describe the positioning of the detector with respect to the sample and the incident beam ($xcent$, $ycent$ and dd) and three describe the detector tilts (α, β and γ). Using the vector framework for micro-beam Laue ray tracing described in appendix A.3, $xcent$ and $ycent$ give the pixel position at which the

vector $\mathbf{D}$ meets the CCD active area along the $\hat{\mathbf{d}}_1$ and $\hat{\mathbf{d}}_2$ directions respectively (figure A.5). dd refers to the length of vector $\mathbf{D}$. The detector tilts correspond to detector roll, α, (rotation about the $\hat{\mathbf{d}}_2$ axis), detector pitch, β, (rotation about the $\hat{\mathbf{d}}_1$ axis) and detector yaw, γ (rotation about the $\hat{\mathbf{d}}_s$ axis, equation A.8). Errors in beam or sample position leading to relative changes of the scattering volume position to the detector do not need to be considered separately. They can be lumped into the detector position changes. Perturbations of the geometrical parameters are denoted by a $\triangle$, e.g. a perturbation of $xcent$ is denoted by $\triangle xcent$.

Using the ray tracing framework (appendix A.3) diffraction patterns were generated that would be observed from a single silicon crystal in the geometrically perturbed setup. These simulated perturbed Laue patterns were indexed and refined assuming ideal geometry (table 3.1). Since the simulated patterns were generated for a strain-free crystal, any elastic strain determined during the refinement is equivalent to the strain error arising from the geometrical perturbation introduced into the simulated Laue patterns.

Using micro-beam Laue diffraction setup without additional information derived from monochromatic diffraction, it is only possible to measure deviatoric elastic strains, i.e. lattice distortion. The hydrostatic component (lattice expansion or contraction) is not accessible (§ 2.2.4). Hence the appropriate measure of the perturbation-induced error is the deviatoric elastic strain found for the perturbed pattern:

$$\bar{\epsilon} = \sqrt{\frac{2}{3}\epsilon : \epsilon}, \tag{3.6}$$

where ϵ is the deviatoric strain tensor computed from XMAS refinement and the $:$ operator is the Frobenius inner product ($\mathbf{A} : \mathbf{B} = \sum_{i,j} \mathbf{A}_{ij}\mathbf{B}_{ij}$). Initially, the detector position and tilt errors were imposed separately to determine the isolated effect of each error source. Then, combinations of error sources were considered to find the compound effect of the individual contributions.

Individual detector position perturbations

Individual detector position perturbations of up to $50\mu\mathrm{m}$ were introduced to $xcent$, $ycent$ and dd. All other elements of the geometry were maintained at their ideal

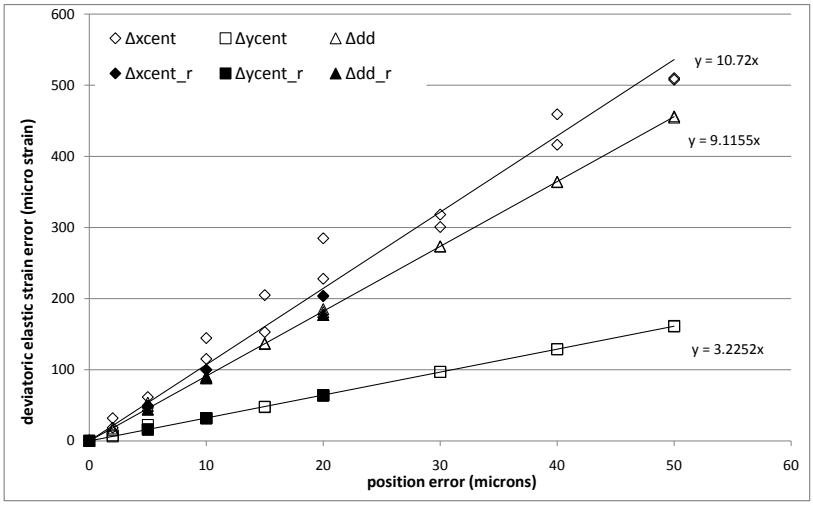

Figure 3.26: Plot of deviatoric elastic strain error introduced by perturbations $\triangle xcent$, $\triangle ycent$ and the sample-to-detector distance $\triangle dd$. The legend shows the symbols used to depict the errors arising from each type of perturbation.

values (table 3.1). Figure 3.26 (open symbols) shows the deviatoric elastic strain error, $\bar{\epsilon}$, introduced by each perturbation in turn. Positive and negative perturbations of each parameter gave very similar results. Hence only the magnitude of each perturbation was plotted.

The errors introduced by $xcent$ and dd perturbations appear to be be significantly larger than those introduced by $ycent$ perturbations. The reason is that the y direction ($\hat{\mathbf{d}}_2$) is aligned with the variation of 2θ angle. The factor of 2 introduces a demagnification effect of $ycent$ perturbations on diffraction peak position in reciprocal space.

Patterns for a different lattice orientation were simulated for each perturbation to confirm the independence of strain errors from lattice orientation (figure 3.26, filled symbols). Agreement of the errors from both orientations is good, confirming that strain error is a function of the experimental geometry.

As expected, simulated patterns with no geometrical perturbations produced zero strain error.

Individual detector tilt perturbations

Next, individual perturbations of detector roll (α), pitch (β) and yaw (γ) were considered of up to $\pm 0.05^{\circ}$. Figure 3.27 shows the resulting errors (open and filled

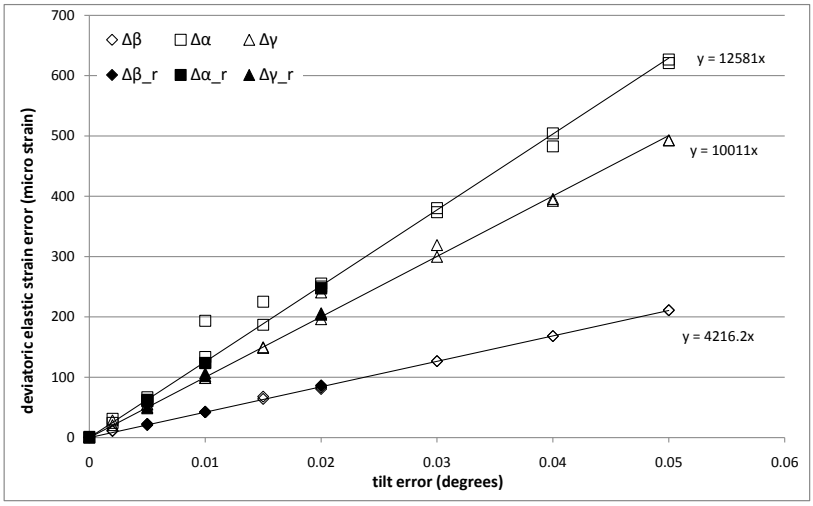

Figure 3.27: Plot of deviatoric elastic strain error arising from perturbations to the detector tilts: roll ($\triangle\alpha$), pitch ($\triangle\beta$) and yaw ($\triangle\gamma$). The legend shows the symbols used to depict the errors arising from each type of perturbation.

markers), corresponding to two different lattice orientations. The strain errors increase linearly with increasing tilt. Strain errors arising from errors in detector pitch ($\triangle\beta$) are significantly smaller than those associated with detector roll ($\triangle\alpha$) or detector yaw ($\triangle\gamma$) perturbations. The reason is that the detector pitch (β) rotation is aligned with the 2θ diffraction angle variation. The factor of 2, just as in the case of $ycent$ perturbations, introduces a demagnification effect of pitch errors on the error of reflection position in reciprocal space.

Pixel errors

A further source of errors is the uncertainty in the exact pixel position on the area detector. Most X-ray cameras used for Laue experiments consist of a scintillator coupled to a CCD chip by an optical taper (Image star 9000 on B16 (DLS) - § 3.1.1, MAR CCD on BM32 (ESRF) - § 3.2.1, Frelon camera on ID15 (ESRF) - § 5.2.1. The optical taper acts as a waveguide and is required to match the size of the available CCD to the scintillator size. During manufacture of the optical taper, some distortion occurs from the regular relationship between position on the scintillator and position on the CCD. Large scale distortions and undulations can be corrected by the application of a re-mapping function (§ 5.2.3). However, there is also a local

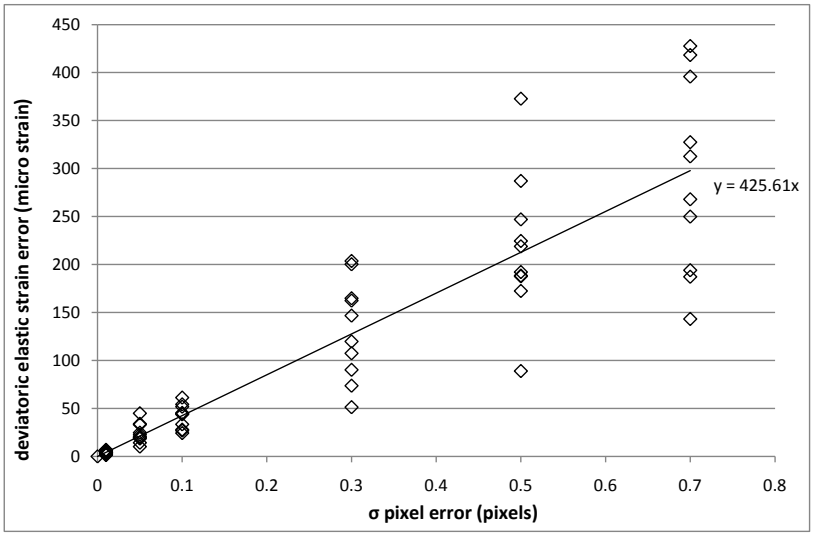

Figure 3.28: Plot of the deviatoric elastic strain error arising from errors in the pixel position. Pixel errors are randomly allocated, following a zero-centred Gaussian distribution with variance σ.

"jitter" of pixel positions, giving a random deviation of the centre position of each pixel from the global re-mapping function.

This local jitter was simulated by imposing a random error with a zero-centred Gaussian distribution of variance σ on the simulated peak positions. Rather than in terms of μm, σ was specified as a fraction of a pixel. Figure 3.28 shows the deviatoric elastic strain errors arising from different levels of pixel position error. The spread of strain errors increases significantly with σ.

There is also an intimate link between the number of peaks present in the diffraction pattern and the influence of local pixel jitter on the strain error. Consider a thought experiment with a diffraction pattern with an infinite number of peaks. In this experiment, one would expect the local pixel jitter to have no effect at all since overall the errors cancel out. The silicon diffraction patterns simulated here generally contained between 150 and 170 peaks that could be indexed, depending on the crystal orientation.

Combining error sources

To make quantitative predictions of the errors arising in an experimental setup with known stability limits, it is necessary to combine the strain errors from individual geometric perturbations. From figures 3.26 and 3.27, it is evident that strain error

f_{xcent}	f_{ycent}	f_{dd}	
$10.72\mu\mathrm{m}^{-1}$	$3.26\mu\mathrm{m}^{-1}$	$9.12\mu\mathrm{m}^{-1}$	
f_{α}	f_{β}	f_{γ}	f_{pix}
$12581\mathrm{deg}^{-1}$	$4216\mathrm{deg}^{-1}$	$10011\mathrm{deg}^{-1}$	$425.6\mathrm{pix}^{-1}$

Table 3.2: Coefficients linking individual perturbations of geometrical parameters to the resulting strain errors. Perturbations of $xcent$, $ycent$ and dd, $\triangle xcent$, $\triangle ycent$ and $\triangle dd$ in microns give rise to strain errors $\bar{\epsilon}_{xcent}$, $\bar{\epsilon}_{ycent}$ and $\bar{\epsilon}_{dd}$ in microstrain respectively. Detector tilt perturbations in roll (α), pitch (β) and yaw (γ), $\triangle\alpha$, $\triangle\beta$ and $\triangle\gamma$ in degrees, give rise to strain errors $\bar{\epsilon}_{\alpha}$, $\bar{\epsilon}_{\beta}$ and $\bar{\epsilon}_{\gamma}$ in microstrain respectively. On average a pixel positioning error of σ gives rise to strain error of $\bar{\epsilon}_{pix}$ in microstrain.

varies linearly with the perturbation giving rise to it. The data can be fitted with a linear function:

$$\bar{\epsilon}_x = f_x \triangle x, \tag{3.7}$$

where $\bar{\epsilon}_x$ is the strain error arising due to perturbation $\triangle x$, and f_x is the coefficient linking the two quantities. For the evolution of pixel error in figure 3.28, the situation is more difficult, due to the random nature of the pixel position error distribution. Still, a linear fit is appropriate to link the mean strain error $\bar{\epsilon}_{pix}$ to a given σ of pixel position error distribution. Table 3.2 shows the linear coefficients for the individual perturbations.

Combining detector position errors: Several possible ways of combining the strain errors from perturbations $\triangle xcent$, $\triangle ycent$ and $\triangle dd$ were explored. The best fit of predicted deviatoric elastic strain error versus the actual deviatoric elastic strain error found from XMAS refinement of the simulated Laue patterns was achieved using a sum of squares approach:

$$\bar{\epsilon}_{pos} = \sqrt{\bar{\epsilon}^2_{xcent} + \bar{\epsilon}^2_{ycent} + \bar{\epsilon}^2_{dd}} \tag{3.8}$$

where $\bar{\epsilon}_{pos}$ is the combined deviatoric elastic strain error predicted from the combination of individual detector position errors ($\triangle xcent$, $\triangle ycent$ and $\triangle dd$) . 33 Si patterns were simulated with randomly generated $\triangle xcent$, $\triangle ycent$ and $\triangle dd$ perturbations of up to $\pm 20\mu\mathrm{m}$. For each pattern, a random crystal lattice orientation was chosen. Figure 3.29 shows the errors $\bar{\epsilon}_{pos}$ predicted using the sum of squares

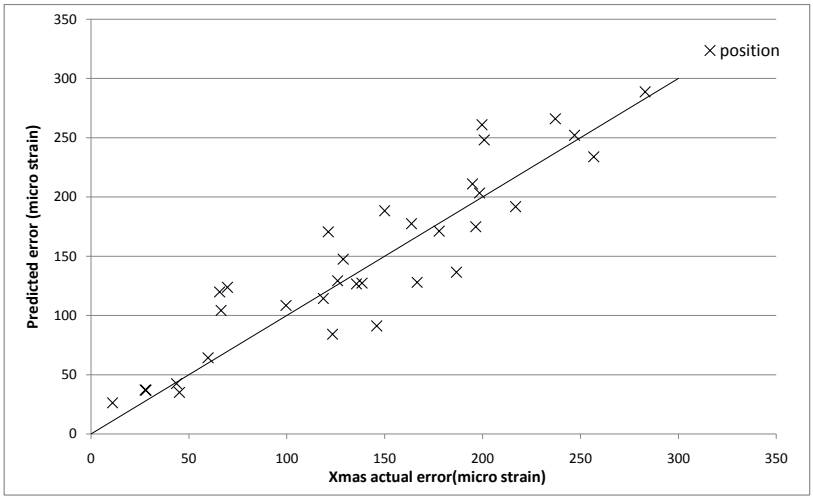

Figure 3.29: Combination of detector position deviatoric elastic strain errors $\bar{\epsilon}_{pos}$, plotted against strain error found from XMAS fitting of perturbed Laue patterns.

approach, plotted against the actual deviatoric elastic strain errors determined by XMAS refinement. Although the data points show some scatter, they lie approximately on a straight line of unit slope, confirming the appropriateness of equation 3.8.

Combining detector tilt errors: For detector tilt perturbations in roll ($\triangle\alpha$), pitch ($\triangle\beta$) and yaw ($\triangle\gamma$), the best fit of predicted strain error, $\bar{\epsilon}_{tilt}$, versus actual XMAS refined strain error was found using a sum of quartics approach:

$$\bar{\epsilon}_{tilt} = (\bar{\epsilon}_{\alpha}^{4} + \bar{\epsilon}_{\beta}^{4} + \bar{\epsilon}_{\gamma}^{4})^{\frac{1}{4}}. \tag{3.9}$$

28 Si patterns were simulated with random combinations of detector tilt perturbations up to $\pm 0.02^{\circ}$. Figure 3.30 shows the predicted errors computed for these patterns using equation 3.9 plotted against the actual strain errors from XMAS fitting of the patterns. The data points lie on a straight line with the gradient of unity, suggesting that equation 3.9 provides a suitable way of combining strain errors due to detector tilt perturbations. The scatter is less than that observed for the combination of detector position errors (figure 3.29).

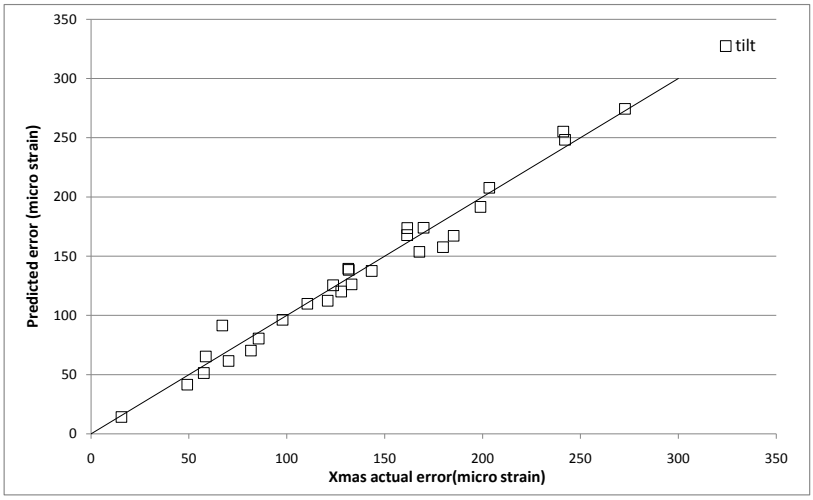

Figure 3.30: Predicted detector tilt perturbation induced strain errors, plotted against strain error found from XMAS fitting of perturbed Laue patterns.

Combining multiple tilt and positioning errors: Finally, both detector position and tilt errors must be combined to estimate the overall strain error for a setup with known stability limits. 40 Si patterns were computed for randomly orientated crystals with randomly assigned shift and tilt errors. The maximum position perturbations $\triangle xcent$, $\triangle ycent$ and $\triangle dd$ allowed were $\pm 20 \mu\mathrm{m}$, the maximum perturbations of detector roll ($\triangle\alpha$), pitch ($\triangle\beta$) and yaw ($\triangle\gamma$) were $\pm 0.02^{\circ}$. The most suitable error combination rule was found to be a sum of squares approach applied to $\bar{\epsilon}_{pos}$ and $\bar{\epsilon}_{tilt}$, to find the total deviatoric elastic strain error $\bar{\epsilon}_{total}$:

$$\bar{\epsilon}_{total} = \sqrt{\bar{\epsilon}_{pos}^2 + \bar{\epsilon}_{tilt}^2} = \sqrt{\bar{\epsilon}_{xcent}^2 + \bar{\epsilon}_{ycent}^2 + \bar{\epsilon}_{dd}^2 + \sqrt{\bar{\epsilon}_{\alpha}^4 + \bar{\epsilon}_{\beta}^4 + \bar{\epsilon}_{\gamma}^4}}. \tag{3.10}$$

Figure 3.31 shows a plot of the predicted values of $\bar{\epsilon}_{total}$, computed from individual perturbations, versus the actual strain errors from XMAS refinement of the simulated perturbed Laue patterns. Although the data points show significant scatter about a straight line with a gradient of unity though the origin, the proposed combination rule (equation 3.10) captures the overall trend well.

Pixel position perturbations were not included in the combined error calculation approach, since their random nature and the link between the influence of pixel position error and the number of peaks indexed, would add significant further scatter to the data.

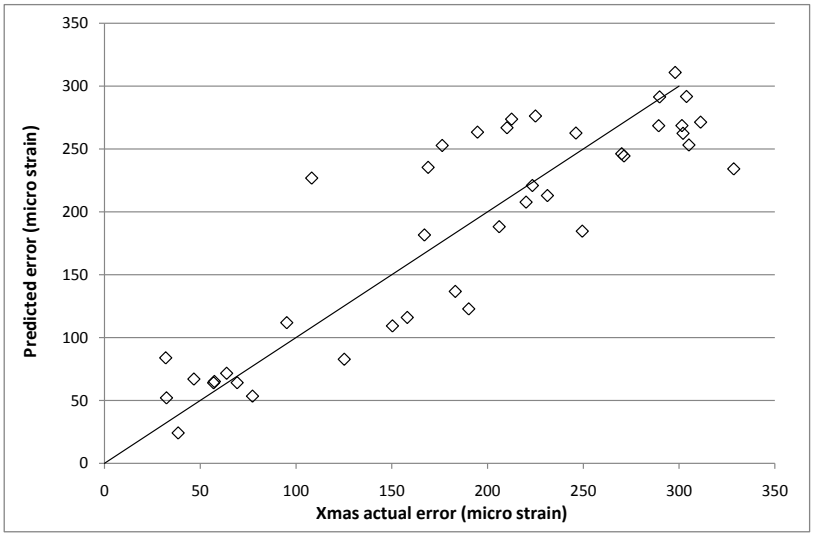

Figure 3.31: Plot of the combined strain errors $\bar{\epsilon}_{total}$ predicted based on the errors arising from individual perturbations, plotted against the actual strain errors found by XMAS refinement of the simulated perturbed Laue patterns.

Using the simulation based error analysis approach, the deviatoric elastic strain errors arising from individual geometrical perturbations can be quantified. The individual contributions can be combined using an empirical recipe to give the overall expected experimental error. Other positional error sources, e.g. sample surface roughness can be added into the present approach. It should be noted that the coefficients (f_x), linking a given geometrical perturbation to the strain error are specific to the experimental setup. If any parameter of the experimental setup were to be changed significantly, they must be recomputed.

It should also be possible to analytically compute the coefficients as derivatives of the total strain error $\bar{\epsilon}_{total}$, e.g. $f_{xcent} = \frac{\partial \bar{\epsilon}_{total}}{\partial xcent}$. This would be an interesting avenue to pursue for further treatment of micro-beam Laue errors.

3.2.3 Measurements

To validate the simulation-based error estimation technique, measurements were performed on single crystal bars under four point bending on beamline BM32 (ESRF). Figure 3.32 a) shows a sketch of the loading setup. The four point bend samples were aligned so that the illuminated sampling volume was at a constant distance from the neutral axis. If through-thickness variations of strain are assumed to be small, this means that the strain field in the sampling volume was the same

along the beam direction. Loading was applied by displacement of the inner set of pins B and C. The nominal displacement of these pins will be referred to as pd.

The four point bend configuration is highly suitable for the study of the tensile and compressive material response. It has been used extensively to study macroscopic deformation behaviour [185]. In the central area of the sample (between pins B and C), pure bending moment loading is present. Kinematics prescribe that the total strain component in the sample axial direction (y-direction) has to vary linearly along a line across the bar in the transverse (x-direction). Figure 3.32 b) shows a schematic of variation in the transverse direction of axial elastic strain (ϵ_{yy}) within an elastic-perfectly plastic material sample with no pre-existing residual stresses. When the sample is only deformed elastically, ϵ_{yy} varies linearly (red line). The elastic strain achievable is limited by plasticity. As plasticity sets in, the elastic strain shows a plateau associated with the plastic zone. With increasing loading, this plateau extends inwards from the sides of the sample towards the neutral axis (green line). Total strain ϵ_t can be decomposed into elastic, ϵ_e, and plastic strain, ϵ_p, as follows: $\epsilon_t = \epsilon_e + \epsilon_p$. In the central elastic section of the sample, total strain ϵ_t remains equal to the elastic strain ϵ_e. Since total strain must vary linearly, the plastic strain, ϵ_p, in the plastically deformed regions of the beam can be found simply as the difference between the total and elastic strains.

Next, unloading of the plastically deformed sample can be considered. Due to the plastically deformed regions of the specimen, an inverted "N" profile of residual elastic strain is set up (solid blue line). In the central region of the sample which was only deformed elastically, the elastic strain, ϵ_e, remains equal to total strain, ϵ_t, which still varies linearly (broken blue line). The difference between ϵ_t and ϵ_e, the plastic strain, ϵ_p, in the plastically deformed regions of the sample can thus be determined. A deformed four point bend sample in effect contains a permanently locked in record of the full characterisation of the material's monotonic tensile and compressive deformation response [185].

To determine the reliability of elastic strain measurements by micro-beam Laue diffraction, a number of line measurements were carried out in a single crystal Si bar under four point bending. Due to the brittle nature of Si at room temperature,

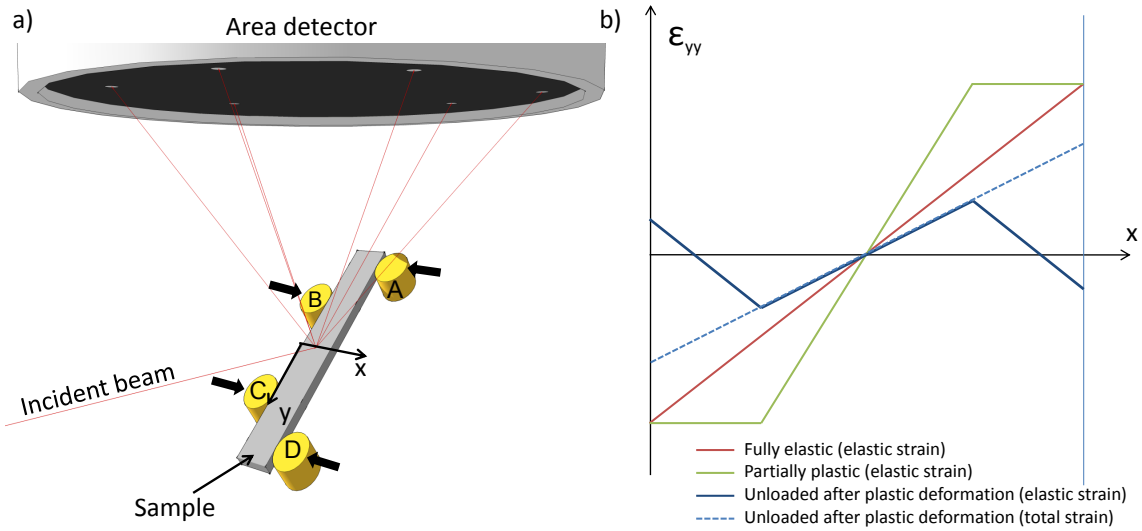

Figure 3.32: a) Schematic sample arrangement and orientation for the micro-beam Laue four point bend measurements. Deformation was imposed by displacing pins B and C a distance pd in the positive x direction. b) Illustration of the evolution of elastic strain profiles in a bar sample with increasing bending followed by unloading.

only elastic deformation was imposed on the bar. The results and the observed experimental strain errors are reported in § 3.2.5. This was followed by the measurement of axial elastic strain profiles in a Cu single crystal bar (§ 3.2.6).

3.2.4 Estimated strain errors associated with setup instability

At the start and end of each line measurement in the Si four point bend sample ten Ge calibration patterns were collected. These were used to determine the exact geometrical parameters for the refinement of the Si patterns. Refinement of the Ge patterns also makes it possible to evaluate the extent of geometrical perturbations during the measurements.

For each Si scan line across the sample the corresponding Ge calibration patterns (20-40 depending on the measurement) were refined, assuming a perfect Ge crystal, to find the geometrical parameters of the experimental setup. For the ith Si line measurement, the jth Ge pattern yields a geometrical parameter set $\mathbf{g}_{ij}$. The mean of these geometrical parameters, $\bar{\mathbf{g}}_i$, describes the set of geometrical parameters which should be used for the refinement of the ith Si line scan. The standard deviation of the geometrical parameters gives a measure of the geometrical

a)

$\triangle xcent_{exp}$	$\triangle ycent_{exp}$	$\triangle dd_{exp}$	$\triangle \alpha_{exp}$	$\triangle \beta_{exp}$	$\triangle \gamma_{exp}$
0.22μm	1.94μm	2.39μm	0.0024°	0.0017°	0.0011°

b)

$\bar{\epsilon}_{xcent,exp}$	$\bar{\epsilon}_{ycent,exp}$	$\bar{\epsilon}_{dd,exp}$	$\bar{\epsilon}_{\alpha,exp}$	$\bar{\epsilon}_{\beta,exp}$	$\bar{\epsilon}_{\gamma,exp}$
2.4	6.3	22.8	29.8	7.1	11.0

Table 3.3: a) Experimentally measured standard deviations of the geometrical parameters. b) Individual experimental strain errors that individual geometrical perturbations give rise (microstrain (10^{-6})).

perturbations of each parameter. It is equivalent to the geometrical perturbations discussed above and will be referred to as $\triangle \mathbf{g}_i$.

It was found that the mean of the geometrical parameters for each Si line measurement, $\bar{\mathbf{g}}_i$, showed quite significant variation between line scans. This variation arises as the detector has to be raised and lowered at every loading increment when the alignment microscope is used. The standard deviations of the geometrical parameters $\triangle \mathbf{g}_i$ were relatively consistent over the ensemble of Si line scans. Table 3.3 a) shows the measured standard deviations of detector $xcent$, $ycent$, dd, roll (α), pitch (β) and yaw (γ), averaged over all the Ge measurements from all Si lines, $\triangle xcent_{exp}$, $\triangle ycent_{exp}$, $\triangle dd_{exp}$, $\triangle \alpha_{exp}$, $\triangle \beta_{exp}$ and $\triangle \gamma_{exp}$ respectively. In total, 180 Ge patterns were considered.

It is interesting to note that the largest geometrical errors are $\triangle ycent_{exp}$ and $\triangle dd_{exp}$. These two parameters are coupled, as a vertical shift of the incident beam would change dd, $ycent$ by the same amount for a sample in 45° reflection geometry. Such changes in beam height could be caused by slight variations in slope of the vertically focusing KB mirror.

Substituting the geometrical error standard deviations (table 3.3 a)) into equation 3.7 with the coefficients given in table 3.2, the individual contributions to the elastic deviatoric strain error of each geometrical perturbation can be estimated (table 3.3). Substituting these into expression 3.10, the expected standard deviation of deviatoric total elastic strain error, $\bar{\epsilon}_{total,exp}$, can be found to be 38 microstrain.

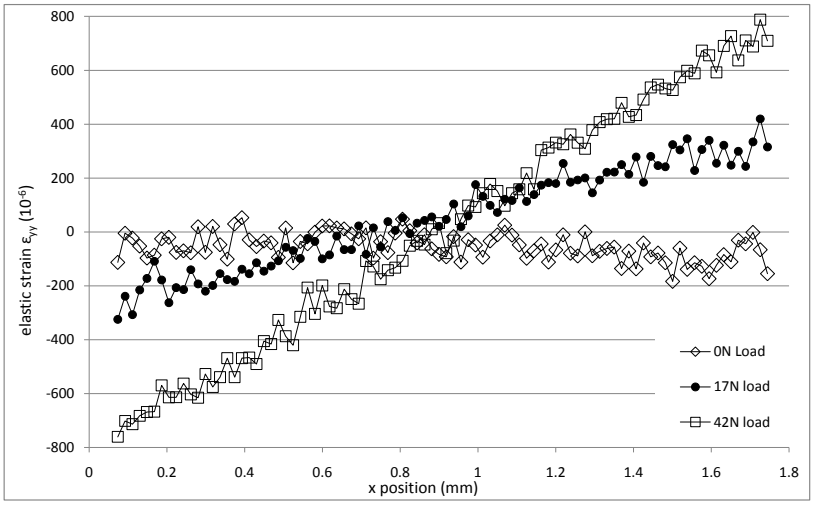

Figure 3.33: Profiles of elastic strain in the axial direction, ϵ_{yy}, along a line scan in the x-direction across the Si bar under four point bending with loads of $0\mathrm{N}$, $17\mathrm{N}$ and $42\mathrm{N}$.

3.2.5 Actual strain errors - Si bar four point bending

Four point bending measurements were carried out on a single crystal Si bar of length $10\mathrm{mm}$. The width of the bar (x-direction) was $1.820\mathrm{mm}$ with a greatest deviation of $\pm 1\mu\mathrm{m}$ over the $10\mathrm{mm}$ length. The thickness of the bar (z direction) varied linearly from $0.683\mathrm{mm}$ at one end to $0.671\mathrm{mm}$ at the other. The crystal was oriented, so that the $[101]$ direction was approximately aligned with the sample x-axis, the $[12\bar{1}]$ direction with the y-axis and the $[\bar{1}11]$ direction with the sample z-axis. Flatness of all faces was better than $1\mu\mathrm{m}$ and the surfaces were polished to a mirror finish with negligible roughness.

Loading was applied according to the schematic diagram in figure 3.32 a). The distance between loading pins A and D was $8\mathrm{mm}$ and between pins B and C $3\mathrm{mm}$. In the y-direction, the measurement line was centred between pins B and C. Two measurements were made at $0\mathrm{N}$ load. Then incremental loading steps were applied from $2\mathrm{N}$ to $42\mathrm{N}$ in steps of $5\mathrm{N}$.

Refinement of the diffraction patterns from the ith Si line scan was based on the geometrical parameters $\bar{\mathbf{g}}_i$ found from the Ge calibration patterns. Figure 3.33 shows the elastic strain profiles in the y-direction, ϵ_{yy}. The strains varied linearly across the section of the sample.

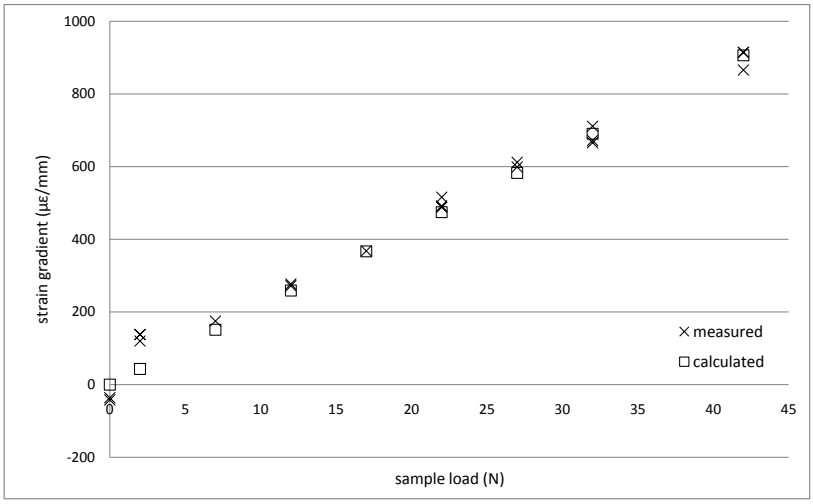

Figure 3.34: Transverse (x-direction) gradients of axial (y-direction) strain in the Si four point bend sample at different loads. Comparison is shown of measured gradients and those found from simple beam bending theory.

The experimental, ϵ_{yy}, profiles were fitted with straight lines. The resulting strain gradients in the x-direction of ϵ_{yy} are shown in figure 3.34. To verify the correctness of these measurements, a comparison with simple beam bending theory was made. For a bent bar:

$$\frac{M}{I} = \frac{\sigma}{x} = \frac{E}{R}, \tag{3.11}$$

where M is the moment carried by the bar at the point of interest, I is the second moment of area, σ the stress at distance x from the neutral axis, E Young's modulus and R the radius of curvature of the neutral axis. Rearranging gives an expression for the strain gradient $\frac{\epsilon}{x}$:

$$\frac{\epsilon}{x} = \frac{M}{IE}, \tag{3.12}$$

where M is defined by the loading and I by the sample cross-section, shape and dimensions. The elastic modulus along the $[12\bar{1}]$ axis, $E_{12\bar{1}}$ can be found by interpolation from the 3D anisotropic elastic constants for Si as ~ 170 GPa [186]. Based on this simple model, the expected strain gradients for the different loads were computed. Agreement between the experimentally measured values and the predictions is excellent (figure 3.34).

By subtracting the linear fit from the experimental strain values and computing the standard deviation, the experimental strain error can be evaluated. Here

only the strain error of the ϵ_{yy} measurements was considered. Ideally, linear fitting should be applied to all strain components and then the deviatoric elastic strain error computed. However, since the elastic strain response is dominated by the ϵ_{yy} component, one can assume that the strain error is dominated by this component. The standard deviations of the strain errors of the Si line profiles was 45 microstrain.

This is slightly larger than the predicted strain error, $\bar{\epsilon}_{total,exp}$, of 38 micro-strain (based on the refinement of Ge patterns). The difference may be accounted for by the pixel positioning errors which were assumed to be small for the MAR detector on BM32 (ESRF) and were not included in the strain error prediction thus far. Now assume that the pixel error induced strain errors can be simply included in the $\bar{\epsilon}_{total,exp}$ sum of squares in expression 3.10:

$$\bar{\epsilon}_{total} = \sqrt{\bar{\epsilon}^2_{pos} + \bar{\epsilon}^2_{tilt} + \bar{\epsilon}^2_{pix}}. \tag{3.13}$$

From the above, $\bar{\epsilon}_{pix}$ can be estimated as 24 microstrain. Refering to table 3.2, this gives a standard deviation of pixel position error of 0.056 pixels or $\sim 4.5\mu\mathrm{m}$. This is comparable to the manufacturer quoted pixel positioning errors, in which maximum values can reach $10 - 20\mu\mathrm{m}$ [187].

3.2.6 Actual strain errors - Cu single crystal four point bending

Next, in situ four point bending was applied to a $10\mathrm{mm}$ long single crystal copper bar. Copper is difficult material to measure owing to its low yield stress which results in small elastic strains of $\sim 2.5 \times 10^{-4}$ at yield. The mean width of the bar (x-direction) was $1.740\mathrm{mm}$, with a linear deviation of $\pm 4\mu\mathrm{m}$ from one end to the other. Thickness of the bar (z-direction) varied linearly from $0.565\mathrm{mm}$ at one end to $0.573\mathrm{mm}$ at the other. The crystal was oriented so that the $[1\bar{1}\bar{1}]$ axis was approximately aligned with the z-direction (figure 3.32). Misorientation between the two axes was 4°. The $(0.5316, -0.5670, -0.6292)$ lattice vector was exactly aligned with the z-axis. The $(-0.7330, 0.0642, -0.6772)$ lattice vector was aligned with the x-direction, which can be approximated to the crystal $[\bar{1}0\bar{1}]$ axis with a 4.3° mis-

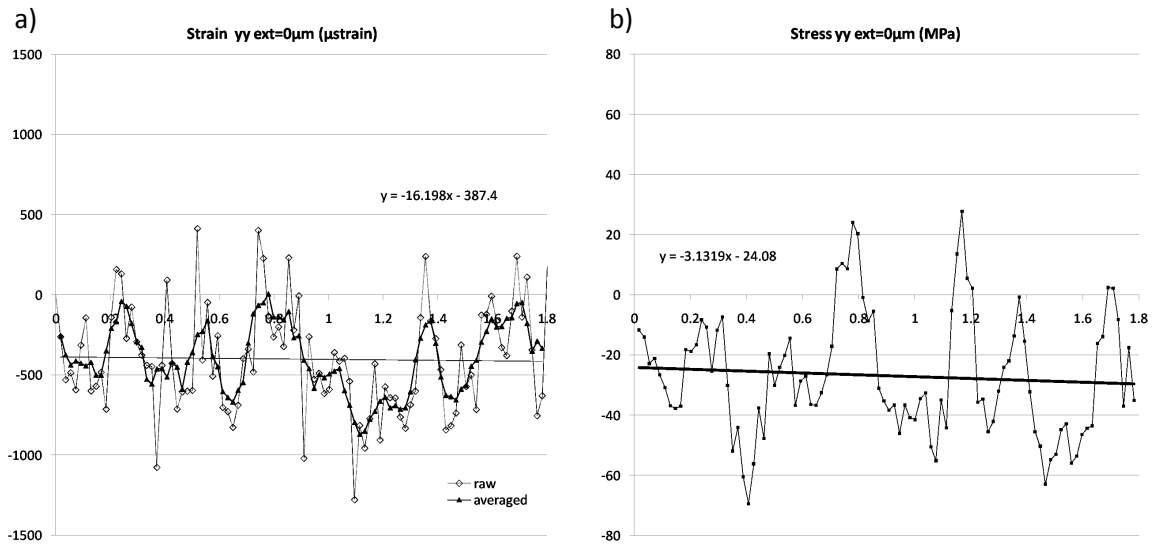

Figure 3.35: Micro-diffraction measurement results along a line in the x-direction across the unloaded Cu bar. a) Axial strain, ϵ_{yy}, in units of microstrain (10^{-6}), plotted as raw data and smoothed with a moving average filter over 5 measurement points ($90\mu\mathrm{m}$). b) Axial stress σ_{yy} (MPa), smoothed with a 5 point moving average filter.

orientation. Finally, the $(0.4244, 0.8212, -0.3814)$ lattice vector was aligned with the y-direction, the axial direction of the sample. With a misorientation of 1.8° this corresponds to the $[12\bar{1}]$ axis. The sample was prepared by sectioning with a diamond saw, followed by a sequence of grinding and polishing steps. In the as-polished state, the flatness of the specimen surfaces was better than $1\mu\mathrm{m}$, with negligible roughness.

Initial measurements of the sample in the as-polished state showed significant streaking of diffraction peaks. This was thought to arise from deformation of the sample surface during the polishing procedure. The damaged surface layer was removed by chemical polishing with a solution of $50\%\mathrm{HNO_3}(63\%)$ in $50\%\mathrm{H_2O}$ (balance) for 5 minutes. Subsequent diffraction measurements showed less streaked peaks, indicating the partially successful removal of the deformed surface layer. Analysis of the sample in an optical profilometer after the diffraction measurements showed an increased surface roughness with a standard deviation of $1.8\mu\mathrm{m}$.

Micro-beam Laue diffraction measurements were collected along a line in the x-direction across the centre section of the sample. Before indexation and refinement, the images were processed by background subtraction (appendix A.2).

Fitting was carried out with the XMAS software [99], based on Ge single crystals calibration patterns collected before and after every line measurement.

Figure 3.35 a) shows the profile of the elastic deviatoric strain, ϵ_{yy}, plotted with respect to the position in the x-direction in the unloaded sample. The as-measured, raw strain profile is very noisy, with a standard deviation of 333 microstrain about the linear fit. When the increased sample roughness and the resulting increased perturbation of $ycent$ is taken into account, the error prediction framework based on the stability limits of the instrument (§ 3.2.4) estimates a strain error standard deviation of 47 microstrain. The reason for this significant difference is not immediately clear. The key difficulty appears to lie in the challenge of accurately fitting diffraction spot centres that arises as soon as even a small amount of streaking is present. Fitting of diffraction spots was carried out with a 2D Gaussian function. Trials using a 2D Lorentzian or the spot centroid resulted in very similar strain error levels.

To reduce the level of noise, a moving average filtering was applied to the ϵ_{yy} data, averaging measurements over $90\mu\mathrm{m}$ which correspond to 5 measurement points. The resulting profile (bold in figure 3.35 a)) shows a reduced level of noise. A linear fit to this data shows only a small strain gradient, as expected for the unloaded sample. It also shows an offset of -387 microstrain, whereas one would expect the strain profile to have a zero mean.

Deviatoric stress tensor was computed based on the anisotropic stiffness constants $c_{11} = 176.4$ GPa, $c_{12} = 129.2$ GPa and $c_{44} = 75.2$ GPa for single crystal copper [188, 189]. A similar offset as in the strain profile can be seen in the profile of deviatoric stress, σ_{yy} (figure 3.35 b) . For equilibrium in the sample y-direction, the mean stress should be zero. The systematic offset in stress and strain is likely to be due to a systematic error in the detector calibration parameters. However, it was felt that refinement of the geometrical parameters to remove this offset should not be carried out, as this would essentially correspond to an "analysis towards a known result".

After the initial measurements on the unloaded sample, the Cu bar was loaded in four point bending to a pin displacement (pd) of $80\mu\mathrm{m}$. The measured load

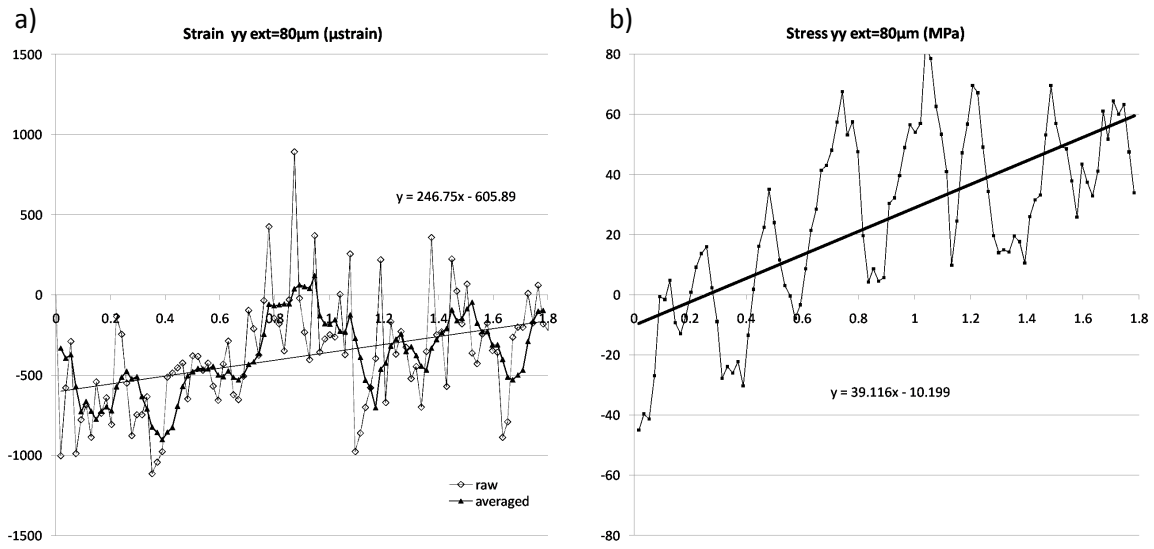

Figure 3.36: Micro-diffraction line measurement in the Cu four point bent bar at a pin displacement (pd) of $80\mu\mathrm{m}$ and a load of $10.45\mathrm{N}$, plotted along a line in the x-direction across the sample. a) Axial strain, ϵ_{yy}, in units of microstrain (10^{-6}), plotted as raw data and smoothed with a moving average filter over 5 measurement points ($90\mu\mathrm{m}$). b) Axial stress, σ_{yy}, (MPa) smoothed with a 5 point moving average filter.

was $10.5\mathrm{N}$. Figure 3.36 a) shows the measured profile of the axial strain, ϵ_{yy}. As before, the data is noisy with a standard deviation of 322 microstrain about a straight line. This is consistent with the strain error level in the unloaded sample. Based on the beam bending assumption that plane sections remain straight, a line was fitted to the 5 point average filtered data (figure 3.36 a)), giving a strain gradient of $247 \times 10^{-6}/\mathrm{mm}$. Based on simple beam bending theory (expression 3.12), the expected strain gradient is $239.9 \times 10^{-6}/\mathrm{mm}$, using $E_{121} = 131$ GPa [189]. Given the level of noise in the experimental strain measurement, the agreement between measured and predicted strain gradient is very good. Figure 3.36 b) shows the variation of σ_{yy}. The stress gradient also compares well with the moment loading applied to the Cu beam.

Figures 3.37a) and c) shows profiles of ϵ_{yy} for pin displacements, pd, of $800\mu\mathrm{m}$ (load 24.4 N) and $1500\mu\mathrm{m}$ (load 50 N) respectively. To overcome the high noise in the data, a moving average filter was applied over $90\mu\mathrm{m}$ (11 measurement points). The smoothed strain tensor was used to compute the deviatoric stress tensor. The axial component, σ_{yy}, is shown in figures 3.38b) and d) for $800\mu\mathrm{m}$ and $1500\mu\mathrm{m}$ pin displacement respectively.

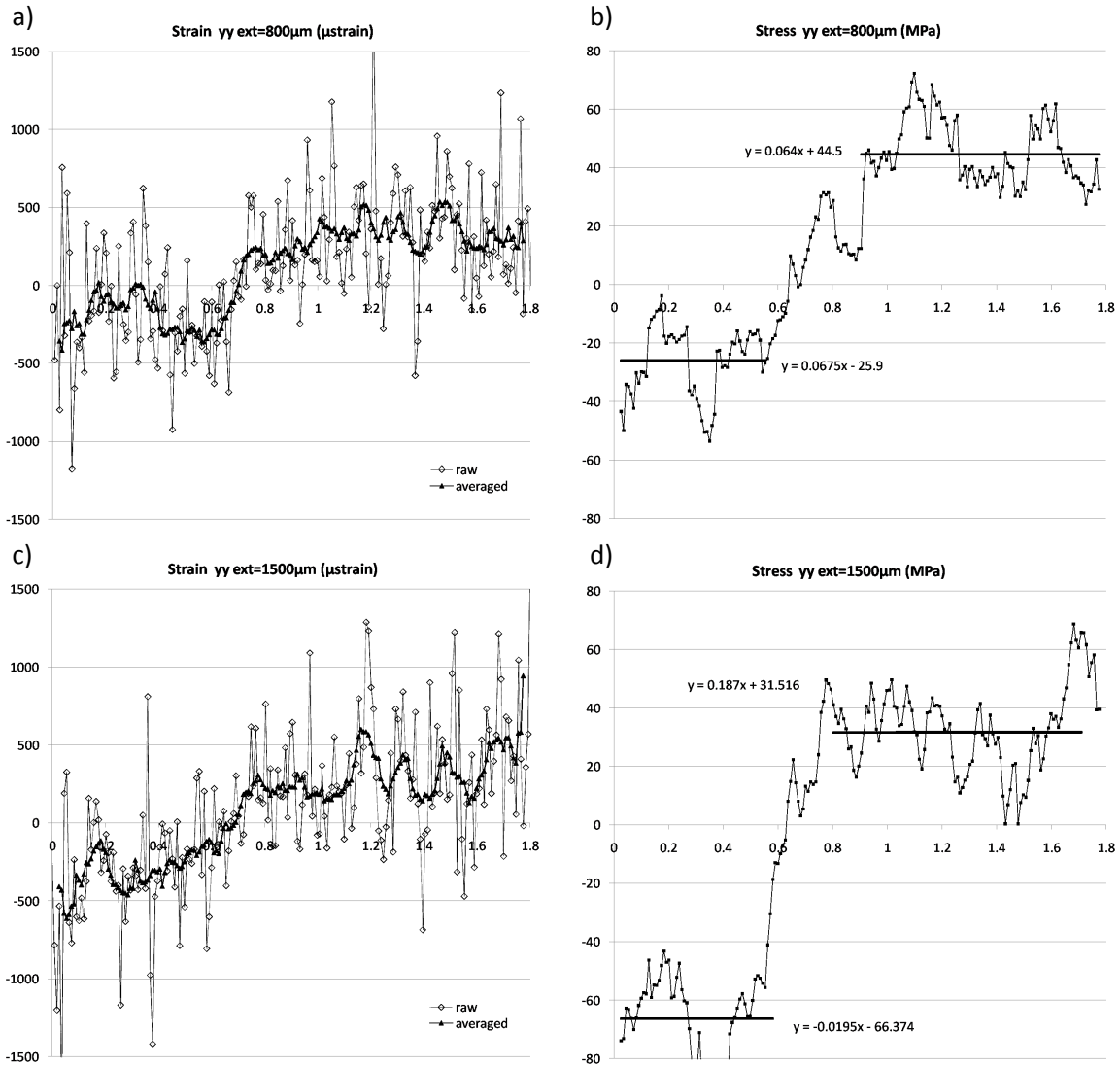

Figure 3.37: Micro-diffraction line measurement in the Cu bar under four point bending at pd of $800\mu\mathrm{m}$ (load $24.4\mathrm{N}$), a) and b), and at pd of $1500\mu\mathrm{m}$ (load $50\mathrm{N}$), c) and d), plotted along a line in the x-direction across the sample. a) and c) Axial strain ϵ_{yy} (microstrain (10^{-6})), plotted as raw data and smoothed with a moving average over 11 measurement points $(90\mu\mathrm{m})$. b) and d) Axial stress σ_{yy} (MPa), smoothed with an 11 point moving average filter.

As discussed above, once the strain at the edge of the beam, furthest from the neutral axis exceeds the yield strain, plastic deformation progresses from the specimen edge inwards. This can be clearly seen in figures 3.37b) and d). In the central region of the profile where total strain is equal to elastic strain, linear variation of stress can be seen. In the plastic zones towards the edges of the sample, the stress profile appears flat. Yield has occurred in compression and tension on the left and right hand side respectively. By fitting a straight line profile to the plastically deformed regions, the yield stress of copper can be estimated. At pd of $800\mu\mathrm{m}$, the difference between maximum and minimum stress is 70.4 MPa. Assuming yield occurs symmetrically in tension and compression, this suggests a flow stress of 35 MPa. At pd of $1500\mu\mathrm{m}$, the difference in stress between the two plateaus reaches 97.8 MPa, giving a flow stress of 49 MPa. Based on micro-bending, tension and compression tests, Kiener [190] gives an expression for the critical resolves shear stress (CRSS) in copper, τ, as a function of the size of the deforming volume, d ($\mu\mathrm{m}$):

$$\tau = 140 d^{-0.3}. \tag{3.14}$$

In the case of a beam under four point bending it is difficult to decide which value of d should be used, given that a non-uniform deformation state is imposed upon the sample. Here $d = 870\mu\mathrm{m}$ was chosen, corresponding to the half width of the Cu bar. The Schmid factor for loading along the sample y-axis can be determined to be 0.486. This leads to an estimated yield stress of 37.8 MPa, i.e. a reasonable match for the value of ~ 35 MPa estimated from the stress profile at pd of $800\mu\mathrm{m}$. The higher yield stress of ~ 49 MPa observed in the stress profile at pd of $1500\mu\mathrm{m}$ is likely to arise as the transition occurs between single slip and multiple slip, required to accommodate the imposed deformation. This may also be due to the extra constraints present in the four point bending case compared to a uniaxial tension experiment. The Schmid factor for the second slip system which would be activated is 0.435. Hence the yield stress can now be estimated to exceed 42.2 MPa. The presence of cross-slip is likely to provide additional hardening, increasing the actual shear stress required for slip beyond the prediction of equation 3.14. Unfortunately no reliable data could be found in the literature for the evolution of

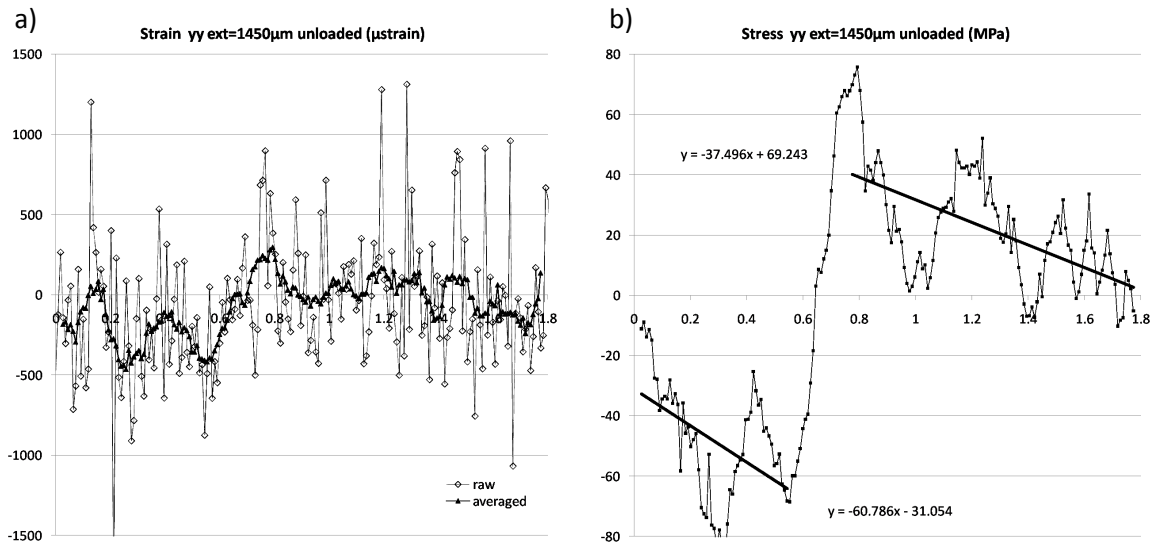

Figure 3.38: Micro-diffraction line measurement in the unloaded Cu bar after four point bend loading, plotted along a line in the x-direction across the sample. a) Axial strain, ϵ_{yy}, (microstrain (10^{-6})), plotted as raw data and smoothed with a moving average over 11 measurement points $(90\mu\mathrm{m})$. b) Axial stress σ_{yy} (MPa) smoothed with a 11 point moving average filter.

CRSS under cross-slip to provide a further quantitative comparison for the values measured here.

At pd of $800\mu\mathrm{m}$, the elastic zone close to the neutral axis of the beam has a width of $\sim 400\mu\mathrm{m}$ (figure 3.38b)). At pd of $1500\mu m$, its width reduces to $\sim 200\mu m$ (figure 3.38d)), as expected with increasing plastic bending.

After pd of $1500\mu\mathrm{m}$, the sample was unloaded and another line measurement in the x-direction across the sample carried out.The resulting elastic deviatoric strain and stress profiles are shown in figures 3.38 a) and b) respectively. The sample now shows an inverse "N" residual stress profile known from synchrotron studies of macroscopic residual stress in polycrystalline bars deformed in four point bending [185]. By integrating the residual stress in the y-direction, equilibrium of the sample can be confirmed. However, taking moments about the neutral axis, the sample does not appear equilibrated.

3.2.7 Future developments on BM32 (ESRF)

In this section it has been demonstrated that a simulation-based approach can be used to quantifying the elastic strain error due to randomly fluctuating geometrical

error sources. The analysis was successfully applied to beamline BM32 (ESRF). Under ideal conditions measurements with mean strain error below 5×10^{-5} can be achieved. The largest positioning errors occurred in $ycent$ and dd, most likely due to slight changes in the vertical KB focusing mirror tilt. At the micro-beam Laue diffraction beamline 34 IDE (ALS) the use of nested Montel optics is currently being tested [103]. These optics reduce the number of degrees of freedom required by the focusing mirrors to two tilts and would provide increased stability. On BM32 (ESRF) the small sample-to-detector distance of $70\mathrm{mm}$ makes the setup very sensitive to geometrical perturbations. Use of a larger area detector placed further away from the sample would reduce this sensitivity.

The large elastic strain errors found in the Cu bar under four point bending are most likely due to uncertainties in the fitting of diffraction peak centres. Lattice misorientation in the sampling volume causes streaking and fragmentation of the Laue peaks. The simple fitting with a 2D Gaussian or Lorentzian function no longer matches the diffraction peak sufficiently well to accurately find the peak centre position representative of the sampling volume average. Conceptually there are two avenues to tackling this problem. More advanced fitting functions could be used to better match the experimentally observed diffraction peaks. This approach is instructive in terms of understanding local deformation mechanisms in specific cases. However it is difficult to generalise for an arbitrary sample. Alternatively the sampling volume and hence lattice orientation spread could be reduced (e.g. smaller focal spot size and depth resolution by DAXM), so that analysis of diffraction spots using simple 2D fitting functions becomes more feasible again. This latter approach is currently being pursued with the developments of the DAXM technique at beamline BM32 (ESRF).

3.3 Chapter Conclusions

In this chapter the development work on micro-beam Laue diffraction at photon energies in the range from 5 to 30 keV at beamlines B16 (DLS) and BM32 (ESRF) has been presented.

On beamline B16 (DLS), the first UK-based micro-beam Laue diffraction setup was developed. The following key points can be noted:

- Initially evolution of lattice orientation with tensile deformation was mapped within a large-grained, polycrystalline nickel sample (§ 3.1.2). Grains could be successfully identified at successive load increments and showed different deformation behaviour depending on their lattice orientation.

- It was verified that the same information about lattice misorientation within the scattering volume can be deduced from high resolution micro-beam Laue, energy scanning and RSM measurements (§ 3.1.3). If no resolution in the radial direction of reciprocal space is required, high resolution micro-beam Laue measurements provide equivalent data to RSM in a fraction of the time.

- Combining micro-beam Laue diffraction and white scanning beam topography opens up interesting opportunities for the study of lattice orientation in the scattering volume. By partial deconvolution of real and reciprocal space contributions it becomes possible to apply traditional topography principles to more highly deformed samples. The use of a focused beam would be very beneficial in future measurements.

- In thin nickel foil the formation of a "chequer board" pattern of lattice rotation was observed at low strains. The spatial distribution agreed well with TEM observations in the literature [175, 176].

The next logical step for the further development of the micro-beam Laue setup on B16 (DLS) is the installation of KB focusing mirrors. Work to this end is currently under way.

The inability to successfully extract lattice strains at B16 (DLS) was addressed by studying the experimental errors which can arise during micro-beam Laue diffraction, based on measurements at beamline BM32 (ESRF). The main conclusions are:

- A simulation-based framework for the assessment of error sources in micro-beam Laue measurements makes it possible to assess the individual contributions of geometrical error sources to the total measurement error. This

allows the targeted refinement of the experimental setup to maximise the gain in terms of strain accuracy.

- Predictions of the expected strain error based on stability measurements of the experimental setup agree well with the errors from an "ideal" silicon sample under four point bending. Accuracy of strain measurements on BM32 (ESRF) is better than 5×10^{-5} under optimum conditions.

- For a "difficult" copper sample strain errors are significantly larger $(\sim 3 \times 10^{-4})$. This is most likely due to inaccuracies in determining diffraction spot centre positions. Overall trends and salient material properties (e.g. strain gradient and flow stress) could still be extracted successfully.

To improve the handling of samples with high gradients of lattice orientation in the sampling volume, the development of DAXM technique is under way on BM32 (ESRF). The lessons learnt from the strain error measurements on BM32 (ESRF) provide an important stepping stone for the further development of combined micro-beam Laue and scanning beam topography at B16 (DLS).

Chapter 4

Dislocation-based modelling of reciprocal space maps and diffraction peak shape

4.1 Motivation

The discussion of the micro-beam Laue diffraction measurements on beamlines B16 (DLS) and BM32 (ESRF) (§ 3.3) showed that, whilst lattice orientation can be found reliably, measurement of elastic lattice strains is much more challenging. This suggests that the validation of any numerical crystal plasticity or dislocation dynamics simulations should concentrate on linking experimentally observed and numerically predicted lattice rotations and their evolution with deformation. Lattice rotation in itself is closely linked to the presence of local elastic and plastic strain gradients and GND distribution. As discussed in § 3.1.4, it can be split into two parts: Large lattice rotations (rigid body), which cause a net change of the scattering volume lattice orientation and a shift in the diffraction spot positions, and changes of the orientation spread in the scattering volume, which change diffraction spot shape. How a given distribution of lattice orientations in the crystal is perceived depends on the probe size.

Changes in micro-beam Laue diffraction peak shape have been previously interpreted in terms of the local active slip systems [124, 125, 127] (§ 2.2.4). Reciprocal

space mapping (§ 2.2.3) provides the same misorientation information as micro-beam Laue diffraction, although at higher angular resolution and resolved in the radial direction of reciprocal space (§ 3.1.3). Jakobsen and co-workers interpreted the evolution of reciprocal space maps in terms of the formation of local dislocation sub-structures [91–93] (§ 2.2.3).

The question is how best to compare the experimentally measured lattice orientation spread in the scattering volume with numerical predictions. One approach is to predict the diffraction patterns a "virtual" scattering experiment on the simulated material volume would give rise to. Good agreement of experiment and simulation suggests that the mechanical model correctly captures behaviour of the sampling volume. This approach was recently applied to the study of the large grained Ni sample deformed in situ during micro-beam Laue measurements on beamline B16 (DLS) (§ 3.1.2). Song et al [191] showed that Laue diffraction patterns predicted based on crystal plasticity simulations correctly captured the evolution of Laue spot position and shape. An alternative to strain gradient crystal plasticity finite element models for the simulation of deformation at the single crystal level is provided by dislocation dynamics modelling (§ 2.1.4).

Classical solutions of dislocation problems in two and three dimensions have long been available (see for example Bilby and Eshelby [192]). These are mainly concerned with dislocation statics, i.e. the equilibrium arrangements reached by ensembles of dislocations or the motion of individual dislocations. Only with the advent of modern high performance computing have numerical simulations of the large scale motion of many dislocation become feasible [5]. A number of different approaches can be chosen: Van der Giessen, Needleman and co-workers [4] (detailed overview in § 2.1.4) developed a two dimensional framework where edge dislocations lie perpendicular to the simulation plane and glide on predetermined slip systems. They nucleate from randomly distributed sources, and their motion and propagation in response to externally applied stress is governed by a set of constitutive laws. The boundary value problem is solved by a superimposed elastic finite element computation. The attractions of this approach are its comparative simplicity and ease of implementation, whilst still being able to reproduce many

experimentally observed phenomena. A recent implementation of this framework was presented by Gaucherin et al [56] and shown capable of capturing orientation dependance of yield, Hall-Petch behaviour and cyclic hardening .

A more general, three-dimensional, framework was proposed by Arsenlis, Cai, Bulatov et al. [5–7] (detailed overview in § 2.1.4). They model dislocations by discretisation into straight segments linked by nodes. Their motion in response to external stress is computed in an incremental manner, considering the motion of the dislocation nodes. Behaviour and dislocation interactions are prescribed by a set of constitutive rules. This framework was implemented in the ParaDiS simulation code. Simulations captured in detail the deformation response of single crystals and elucidated the role played by dislocation junctions in strain hardening [76]. The key benefits of this approach are the physical accuracy of the dislocation representation and its generality. However the increased complexity of three dimensions means that only simple boundary conditions can currently be implemented. The high computational cost limits the computations feasible on lab computers to small, simple examples.

An important aspect of sophisticated dislocation dynamics simulation codes is that they should be able to reproduce successfully the equilibrium solutions of classical, analytically solved problems of dislocation statics. In this chapter (§ 4.2) this is confirmed for the problem of $(n-2)$ edge dislocations trapped between two sessile dislocations [192]. The analytical solution is compared with the dislocation positions predicted by the ParaDiS code.

The remainder of this chapter focuses on the post-processing of dislocation models to provide the diffraction patterns which would be observed in a virtual scattering experiment on the simulation volume. First, reciprocal space maps collected from a lightly deformed Aluminium crystal on beamline I16 (DLS) are presented (§ 4.3). Simulated patterns from a "naive" model of a two-dimensional dislocation cell/wall structure capture some of the experimentally observed features.

To overcome the restrictions of two-dimensions, a framework for the computation of diffraction patterns based on three-dimensional dislocation dynamics simulations is introduced. The fundamental building blocks for this are the lattice rota-

tions arising from a triangular dislocation loop. As a demonstration, maps of lattice rotations arising during the emission of a dislocation loop from a Frank-Read source are computed based on a ParaDiS simulation.

4.2 The parallel dislocation problem

A classical problem in dislocation statics is that of a line of $(n-2)$ parallel edge dislocations with the same Burgers vector, trapped on the same glide plane between two sessile dislocations (figure 4.1). A comparison is made between the equilibrium dislocation positions predicted by ParaDiS, and the analytical solution [192].

4.2.1 Analytical solution

The analytical solution follows the treatment by Bilby and Eshelby [192]. The displacement field due to an edge dislocation, $\perp_{zx}$, lying at the origin, parallel to the z axis, with Burgers vector b_x parallel to the x-axis, is given by:

$$u_{x,\perp_{zx}}(x,y) = \frac{b_x}{2\pi}\left[\arctan(\frac{y}{x}) + \frac{yx}{2(1-\nu)(x^2+y^2)}\right], \tag{4.1}$$

$$u_{y,\perp_{zx}}(x,y) = -\frac{b_x}{2\pi}\left[\frac{(1-2\nu)}{4(1-\nu)}\ln(y^2+x^2) + \frac{x^2-y^2}{4(1-\nu)(x^2+y^2)}\right], \tag{4.2}$$

$$u_{z,\perp_{zx}}(x,y) = 0. \tag{4.3}$$

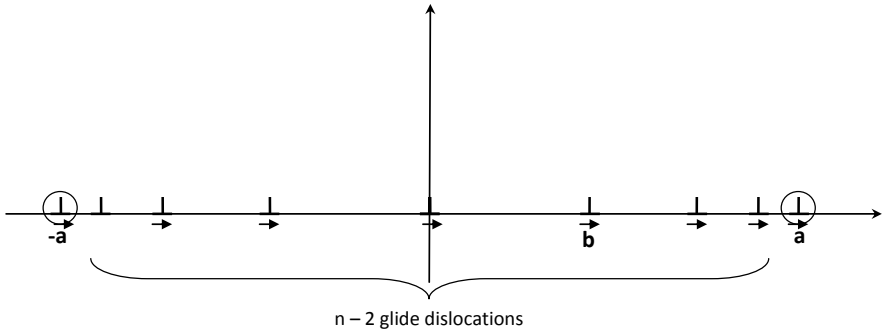

Figure 4.1: Diagram of n-2 parallel edge dislocations of Burgers vector b lying in the same glide plane blocked between two fixed dislocations at a and $-a$.

Shear stress τ_{xy} is then:

$$\tau_{xy}(x,y) = \mu\gamma_{xy} = \mu\left(\frac{\delta u_{y,\perp_{zx}}}{\delta x} + \frac{\delta u_{x,\perp_{zx}}}{\delta y}\right) = \frac{\mu b x(x^2-y^2)}{2\pi(x^2+y^2)^2(1-\nu)}. \tag{4.4}$$

Considering shear only along the x-axis, i.e. $y=0$, this simplifies to:

$$\tau_{xy}(x,0) = \frac{\mu b}{2\pi x(1-\nu)} = \frac{A}{x}. \tag{4.5}$$

where $A = \frac{\mu b}{2\pi(1-\nu)}$ for an edge dislocation. The shear stress acting on a single dislocation at position x_j due to other n dislocations in the line at positions x_i, where $i \neq j$, is:

$$\tau_{xy}(x_j) = \tau_{xy,ext}(x_j) + \sum_{\substack{i=1 \\ i\neq j}}^{n} \frac{A}{x_j - x_i}, \tag{4.6}$$

where $\tau_{xy,ext}$ is the externally applied shear stress.

Now, if the dislocation at x_j is in equilibrium (which here is a necessary condition since we are considering a static dislocation arrangement) then $\tau_{xy}(x_j) = 0$. Also one can now define $p(x) = \frac{\tau_{xy,ext}(x)}{A}$ and then:

$$\sum_{\substack{i=1 \\ i\neq j}}^{n} \frac{1}{x_j - x_i} + p(x_j) = 0; \qquad j = 1,2,3,...n \tag{4.7}$$

Next,define a polynomial $f(x)$ and note the logarithmic derivative $\frac{f'(x)}{f(x)}$:

$$f(x) = \prod_{i=1}^{n}(x - x_i), \tag{4.8}$$

$$\frac{f'(x)}{f(x)} = \sum_{i=1}^{n}\frac{1}{x - x_i}. \tag{4.9}$$

It follows that the first term of equation 4.7 can be written as:

$$\sum_{\substack{i=1 \\ i\neq j}}^{n} \frac{1}{x_j - x_i} = \left(\frac{f'(x)}{f(x)} - \frac{1}{x - x_j}\right)\Bigg|_{x=x_j} = \frac{(x-x_j)f'(x) - f(x)}{f(x)(x-x_j)}\Bigg|_{x=x_j}. \tag{4.10}$$

Now to evaluate this equation at $x = x_j$, l'Hôpital's rule must be used:

$$\lim_{x\to x_j}\left(\frac{(x-x_j)f'(x)-f(x)}{f(x)(x-x_j)}\right) = \lim_{x\to x_j}\left(\frac{f'(x)+(x-x_j)f''(x)-f'(x)}{f(x)+f'(x)(x-x_j)}\right) \quad (4.11)$$

$$= \lim_{x\to x_j}\left(\frac{f''(x)+(x-x_j)f'''(x)}{f'(x)+f'(x)+f''(x)(x-x_j)}\right) \quad (4.12)$$

$$= \frac{f''(x_j)}{2f'(x_j)}. \quad (4.13)$$

Substituting this into equation 4.7, we get the equilibrium condition:

$$\frac{f''(x_j)}{2f'(x_j)} + p(x_j) = 0. \quad (4.14)$$

Directly from equation 4.8 we get:

$$f(x_j) = 0; \qquad j = 1, 2, 3, ...n \quad (4.15)$$

Combining these equations gives:

$$f''(x_j) + 2p(x_j)f'(x_j) + q(n, x_j)f(x_j) = 0. \quad (4.16)$$

It can then be said that it is sufficient for $f(x_j)$ to be a solution of equation 4.16 for equilibrium, provided $q(n, x_j) \neq 0$ if $f(x_j) = 0$.

Now let us turn to the specific case of $n - 2$ edge dislocations, with Burgers vector b, which are held in a glide plane between two fixed dislocation at positions $-a$ and a. For simplicity take $a = 1$. Then for the stress contributions coming from the pinned dislocations, one can write:

$$p(x) = \frac{1}{x-1} + \frac{1}{x+1} = \frac{2x}{x^2-1}. \quad (4.17)$$

Substituting this into equation 4.16, we get:

$$(1-x^2)f''(x) - 4xf'(x) + (1-x^2)q(n, x)f(x) = 0. \quad (4.18)$$

Compare this with the equation for the mth derivative $u = \frac{d^m P_v}{dx^m}$ of the Legendre polynomial $P_v(x)$ as given in Kreyszig [193]:

$$(1-x^2)u''(x) - 2(m+1)xu'(x) + [v(v+1) - m(m+1)]u(x) = 0. \tag{4.19}$$

Now, if we choose $v = n-1$ and $m = 1$ and substitute these into equation 4.19 then we get:

$$(1-x^2)u''(x) - 4xu'(x) + [n(n-1) - 2]u(x) = 0, \tag{4.20}$$

where now $u(x) = P'_{n-1}(x)$. Hence one can choose:

$$q(n,x) = \frac{n(n-1)-2}{1-x^2}, \tag{4.21}$$

$$f(x) = P'_{n-1}(x). \tag{4.22}$$

Thus the equilibrium positions of the $n-2$ dislocations are given by the roots of the first derivative of the Legendre polynomial $P_{n-1}(x)$, i.e. by the roots of:

$$f(x) = P'_{n-1}(x) = 0. \tag{4.23}$$

4.2.2 Model setup in ParaDiS

The ParaDiS model was setup for an FCC lattice structure. Slip occurs on the (111) planes. Figure 4.2 shows a view of the (111) plane looking along the $[111]$ axis. For convenience a separate coordinate system cde was introduced in the (111) plane (figure 4.2), with the e-axis aligned with the $[111]$ axis. Two sessile dislocations were introduced parallel to the d-axis at $-ca$ and $+ca$ which correspond to $-a$ and $+a$ respectively in the analytical example. Between the two sessile dislocations $(n-2)$ straight edge dislocations with Burgers vector $\mathbf{b}$ aligned in the c-direction were introduced. In the ParaDiS code a mobile dislocation can only exist as a loop or as a line between two immobile nodes. Hence the nodes at the ends of the mobile dislocations were fixed. This procedure fixes the free dislocation ends. However, provided da is significantly larger than ca, one can assume that in the

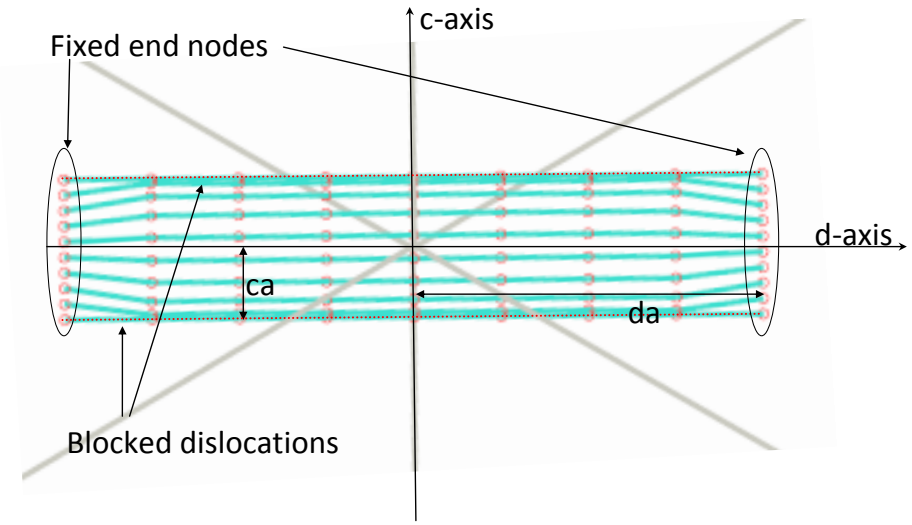

Figure 4.2: Diagram of n-2 parallel edge dislocations of Burgers vector $\mathbf{b}$ lying in the same glide plane blocked between two fixed dislocations at a and $-a$.

simulation cube side length	60000 units
ca	5000 units
da	25000 units
Burgers vector	1.225 units

Table 4.1: Parameters used in the bound dislocation model in ParaDiS.

centre, along the c-axis, the scenario assumed for the analytical solution (figure 4.1) is reproduced.

Three simulation scenarios were considered in which the number of mobile dislocations was varied but all other parameters were kept the same (table 4.1). To minimise errors, a Matlab script was written to generate the ParaDiS input files. The ParaDiS simulation was assumed to have reached equilibrium after 1000 cycles. To prevent dislocation climb, which is not accounted for in the analytical model, dislocation climb mobility was set to zero.

4.2.3 Results

Figure 4.3 shows a plot of predicted dislocation positions where the x-axis of the graph displays distance along the c-axis as shown in figure 4.2 with fixed dislocations at -1 and 1. The square markers represent the positions predicted by ParaDiS. Blue, red and green markers represent the cases of $n = 5$, $n = 10$ and $n = 20$

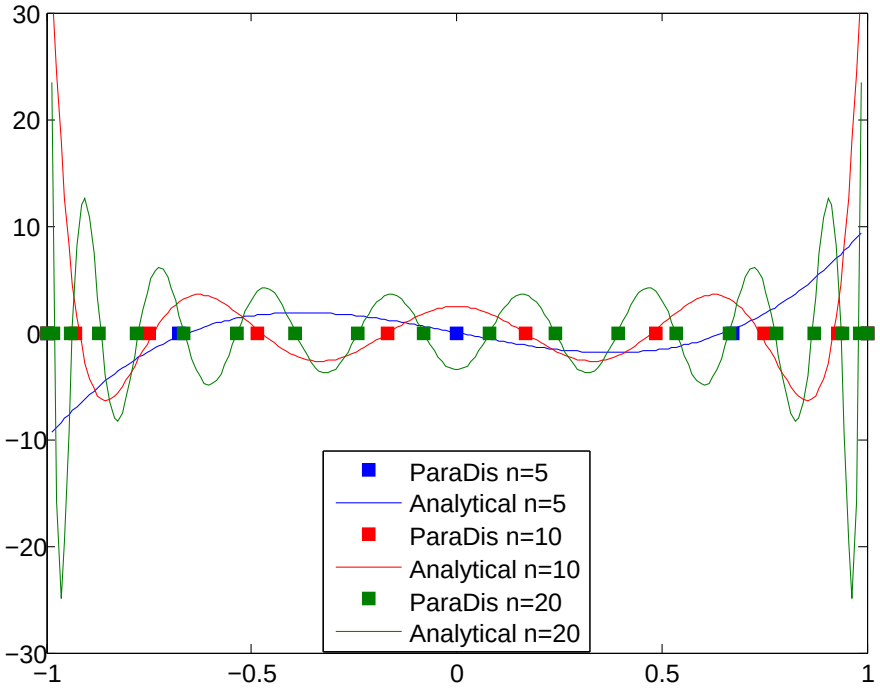

Figure 4.3: Comparison of ParaDiS predicted dislocation equilibrium position with analytically predicted dislocation positions.

respectively. On the same plot, the analytically predicted dislocation locations are shown as the x-axis intercepts of the blue, red and green lines (representing $n = 5$, $n = 10$ and $n = 20$ respectively). Agreement of the ParaDiS predicted and analytically calculated positions is very good. This confirms that ParaDiS computations converge to the analytically found dislocation equilibrium positions in this particular case and constitutes a partial validation of the ParaDiS code which is used latter in this chapter (§ 4.4.4).

4.3 Forward simulation of reciprocal space mapping - the "naive" model

In this section, reciprocal space maps we have collected on beamline I16 (DLS) from a lightly deformed ($\sim 4\%$ total strain), large grained aluminium alloy sample are presented. For comparison, a "naive" model of a two dimensional dislocation cell/wall type structure is postulated. Predicted orientation maps for this model

Al	Mg	Si
99 %	0.5 %	0.5 %

Table 4.2: Composition of 6063 aluminium alloy by weight [194].

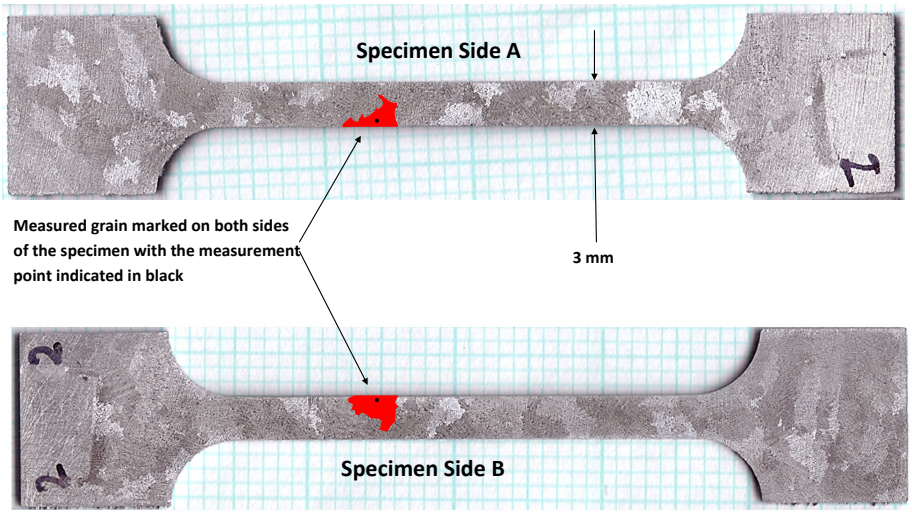

Figure 4.4: Front and back face macrographs of the aluminium alloy specimen. The grain of interest is highlighted in red and the measurement location marked by a black dot.

capture some of the experimentally observed features and allow the exploration of the effects of GNDs and SSDs.

4.3.1 Sample

A dogbone-shaped sample was machined from an aluminium alloy ingot. The ingot was cast from AA6063 stock material and furnace cooled to encourage grain growth. The nominal composition, neglecting any trace elements, is shown in table 4.2. Etching with Tuckers reagent [194] was used to reveal the ingot microstructure and to confirm the presence of large grains. A specimen thickness of $0.5\mathrm{mm}$ was chosen to minimise through-thickness grain variation. Given the large grain sizes (up to several mm), the specimen's microstructure could be treated as pseudo two-dimensional to a first approximation. After machining, the sample was ground in stages to a fine finish and etched to reveal the microstructure.

Figure 4.4 shows the grain structure of the specimen under investigation. Grains up to several millimeters in size are clearly visible. A grain was selected which

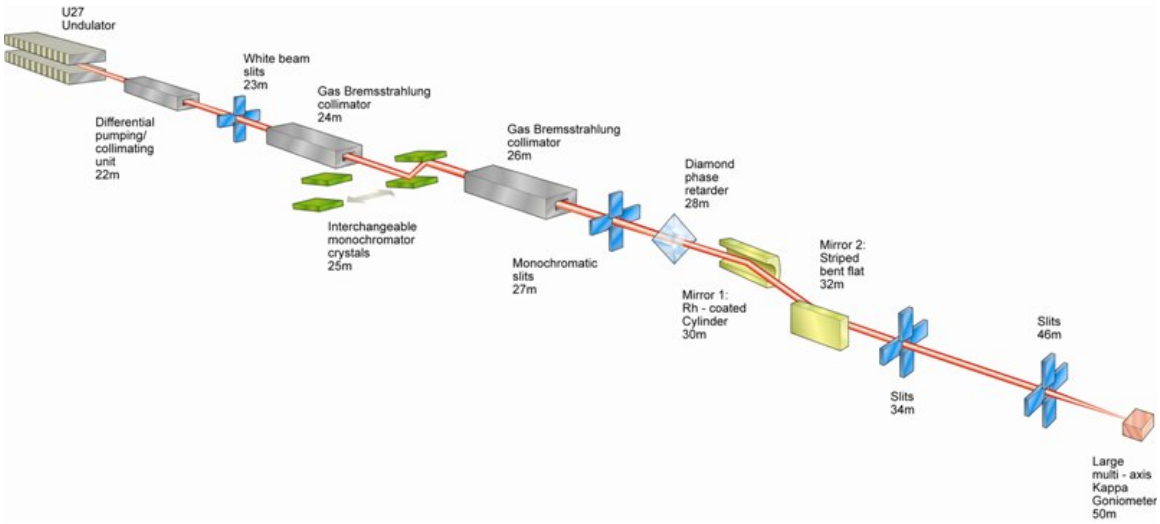

Figure 4.5: Schematic of the optics layout on beamline I16 (DLS).

could be identified through the thickness of the specimen (highlighted in red in figure 4.4). Three small solder spheres were attached to the specimen surface to aid alignment. Before the diffraction measurements, tensile deformation corresponding to $\sim 4\%$ total strain was applied to the sample.

4.3.2 Experimental setup on beamline I16 (DLS)

General beamline layout

Diffraction measurements were carried out on the Materials and Magnetism beamline I16 (DLS). I16 (DLS) is an undulator beamline equipped with a Si (111) or (311) DCM, designed to provide monochromatic light at photon energies between 2.5 and 25 keV. From 2.5 to 15 keV, a set of focusing mirrors can be used to provide a focused beamsize of $200 \times 50 \mu m^2$. The recent addition of a set of KB focusing mirrors now also provides the capability to deliver micron-sized, focused X-ray beams. The experimental hutch is equipped with a high accuracy, heavy duty Kappa-geometry goniometer. A schematic of the optics layout is shown in figure 4.5.

A number of different detectors are available. In this experiment, an avalanche photo diode (APD) was used as a point detector for calibration reciprocal space maps. Mounted above the ADP is a Pilatus area detector (figure 4.6) with a matrix of 195×487 pixels and a pixel size of $170 \mu \mathrm{m}$. It was used for rapid acquisition of

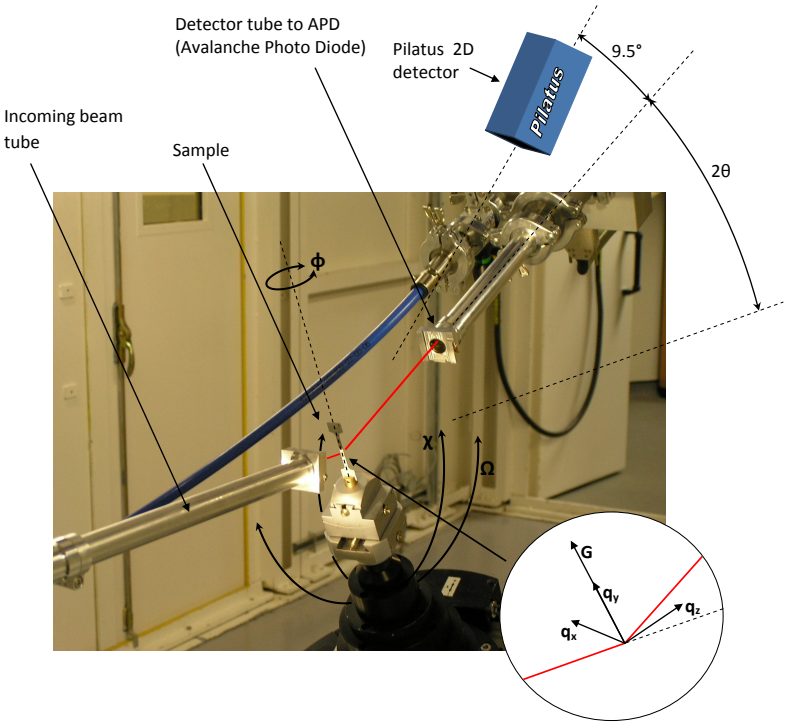

Figure 4.6: Experimental setup on beamline I16 (DLS) showing sample positioning, sample axes and detector arrangements.

reciprocal space maps. Figure 4.6 shows the sample positioning arrangement and the sample axes used.

Sample alignment

The sample was mounted in transmission geometry and an incident, monochromatic photon beam with energy of 15keV used. Alignment was carried out in stages. First, the goniometer and the incident beam were aligned on a pin to $30\mu\mathrm{m}$ accuracy, which corresponds to the diffractometer sphere of confusion. Then the sample was mounted and visually aligned with a theodolite. Alignment of the measurement point was completed by scanning for the reference solder spheres with the direct beam. Lattice orientation at the measurement point was found by placing the Pilatus detector at the correct 2θ angle for the (200) reflection and rotating the sample in Ω, χ and ϕ until a reflection was found. The reflection was centred using the APD and stored in a reflection file. The next (200) reflection was sought more systematically by rotating the sample about the plane normal of the first (200) reflection. The scattering vector precesses in a ring at 90° to the established $[200]$

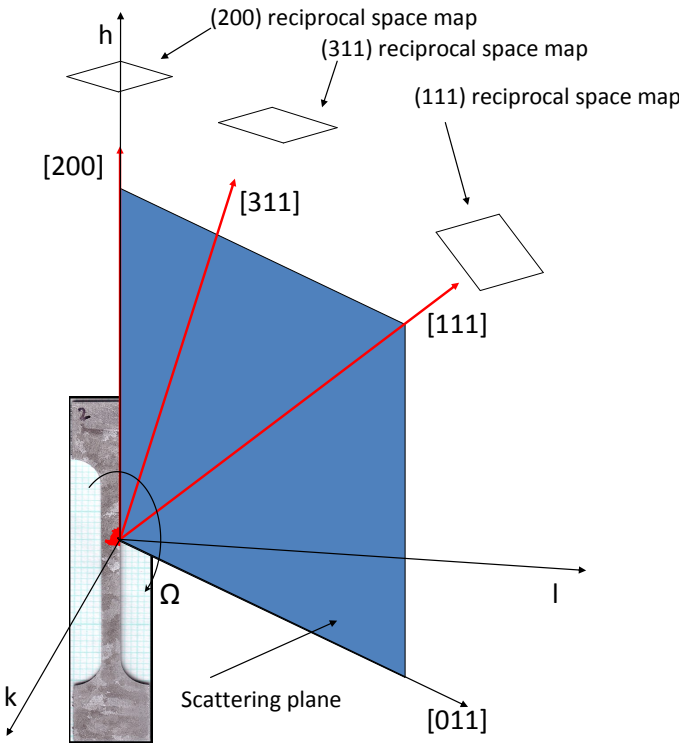

Figure 4.7: Scattering plane alignment with the $[200]$, $[311]$ and $[111]$ lattice directions.

crystal axis. Once two reflections were found, the UB matrix [98] was established and the presence of other reflections verified and used to refine the UB matrix. For the measurements the sample was aligned such that the scattering plane coincided with the plane formed by the $[200]$ and $[011]$ crystal directions (figure 4.7). This plane also contained the $[311]$ and $[111]$ lattice directions .

Measuring the reciprocal space maps

Reciprocal space maps were acquired using the 2D Pilatus detector, oriented with the larger image dimension in the 2θ direction and the shorter dimension corresponding to rotation in χ angle (figures 4.8 and 4.6). For each reciprocal space map 401 images were collected as the sample was tilted 400 steps in ω from -4° to $+4^\circ$ from the reflection centre. To plot maps in the q_x, q_z plane, i.e. the tangential plane of reciprocal space, each pixel position was mapped from detector coordinates to its position in χ , Ω angle space. The image was then summed in the 2θ direction, i.e. integrated in the radial direction of reciprocal space, to give a profile of intensity variation with χ angle at a given Ω angle. The profiles were stacked up

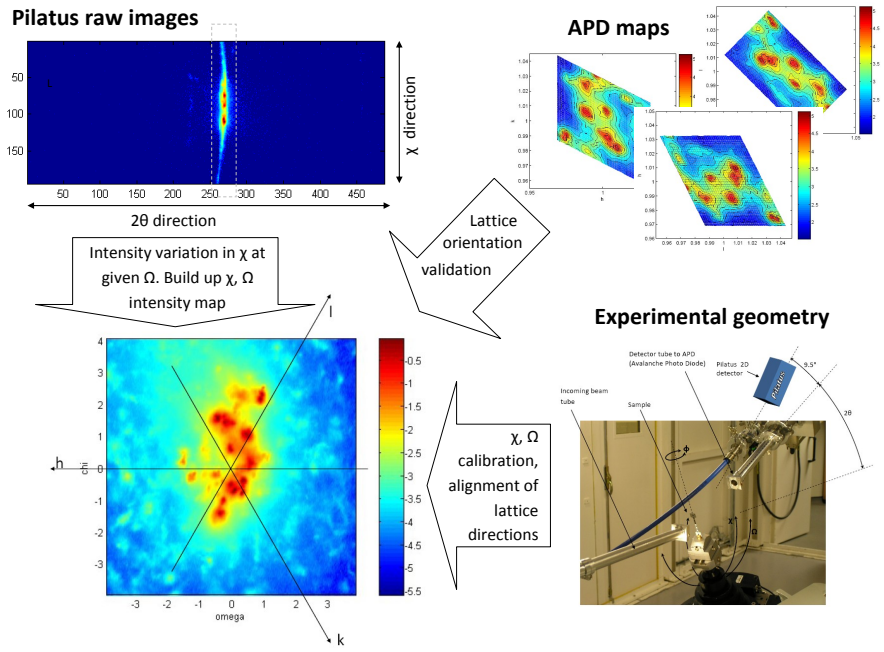

Figure 4.8: Schematic of the use of Pilatus detector images, diffraction geometry information and APD maps in the assembly of the reciprocal space maps.

(figure 4.8) to give a 2D tangential reciprocal space map of the reflection in terms of χ and Ω angles with respect to the reflection centre. To visualise maps within the crystal lattice coordinates, the projections of the crystal axes have been superimposed, as they would be seen looking along the radial direction of reciprocal space towards the origin. Some small reciprocal space maps were also collected with the APD to provide a comparison for the maps collected with the Pilatus detector.

4.3.3 Experimental results

Figures 4.9, 4.10 and 4.11 show the reciprocal space maps in the q_x, q_z plane for the (200), (311) and (111) reflections respectively. Intensity was normalised to the highest intensity present and plotted on a log scale.

All three maps show a number of sharp peaks superimposed on a cloud of enhanced intensity, as discussed by Jakobsen et al. [91]. The number of peaks visible in each map varies between 11 and 13, probably due to the change in gauge volume as the sample is rotated to map different reflections. The angular spread of sharp peaks is larger than previously reported for oxygen-free high thermal conductivity (OFHC) copper deformed to a strain of 2% in tension [92].

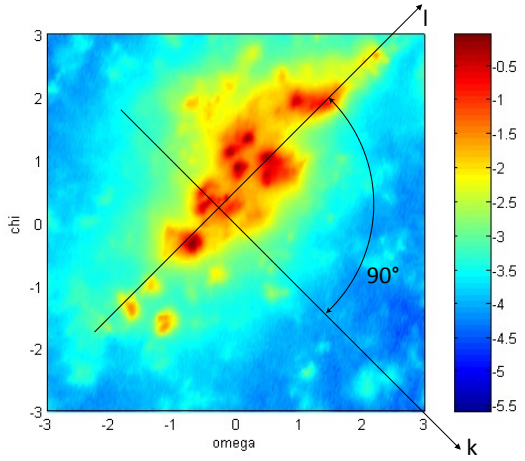

Figure 4.9: (200) reflection reciprocal space map in the q_x, q_z plane.

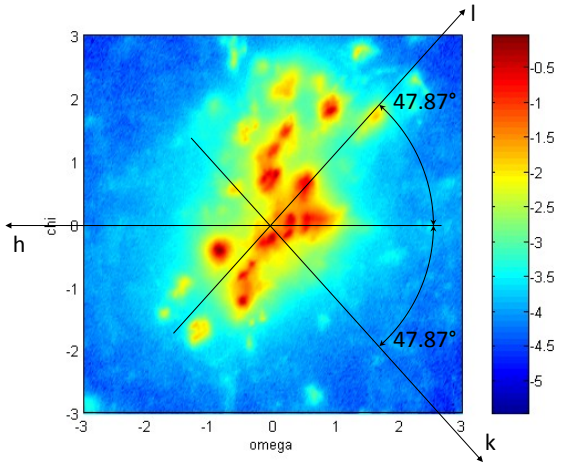

Figure 4.10: (311) reflection reciprocal space map in the q_x, q_z plane.

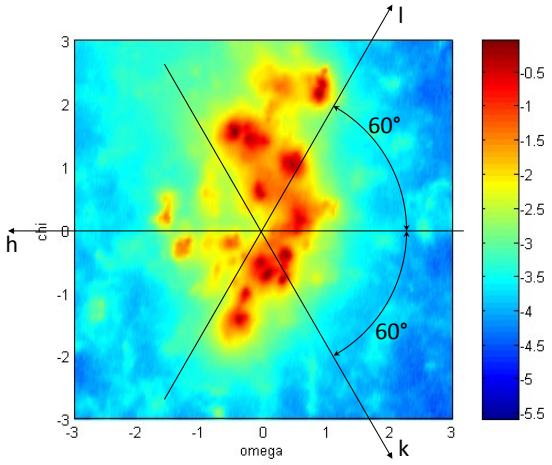

Figure 4.11: (111) reflection reciprocal space map in the q_x, q_z plane.

4.3.4 The "naive" model

The experimentally observed dislocation cell/wall structures reported in the literature (§ 2.2.3) are thought to give rise to the fragmentation of tangential reciprocal space maps. This section presents a first, "naive" modelling attempt at reproducing these structures numerically and predicting the reciprocal space maps they would give rise to in the q_x, q_z plane of reciprocal space.

General model concept

The "naive" model considers a two dimensional material section in the scattering plane (figure 4.7). For simplicity, only the dislocation lines perpendicular to the section are represented. The model's dislocation cell/wall structure consists of n vertical and m horizontal dislocation walls of width w separating rectangular dislocation-free regions (figure 4.12). A grid of equispaced measurement points at which lattice rotations are computed is superimposed on the simulation area. Assuming the reciprocal space map is composed of individual, small Gaussian contributions from every point in the scattering volume, the simulated reciprocal space map is built up by summing up the contributions from all measurement points to give the overall intensity profile.

Computation of local lattice rotation

Local lattice rotation is dependent on the displacement field associated with each dislocation and the spatial distribution of dislocations. It is convenient to adopt a notation where a subscript $\perp_{ij}$ indicates a quantity associated with an edge dislocation parallel to the i axis and Burgers vector along the j axis. Similarly the subscript S_i indicates a quantity associated with a screw dislocation along the i axis.

Analogous to equations 4.1 - 4.3, the displacement field of an edge dislocation parallel to the x-axis and passing through the origin, with Burgers vector b_z parallel to the z-axis is:

$$u_{x,\perp_{xz}}(y,z) = 0, \tag{4.24}$$

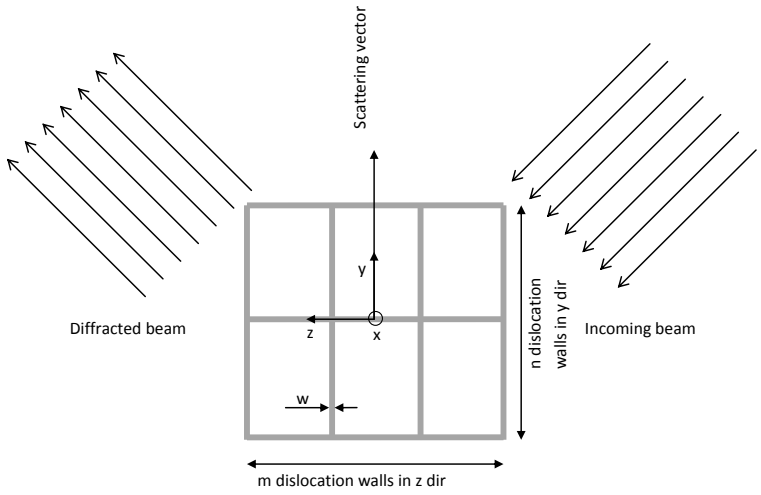

Figure 4.12: Overview of the "naive" dislocation cell/wall model layout

$$u_{y,\perp_{xz}}(y,z) = -\frac{b_z}{2\pi}\left[\frac{(1-2\nu)}{4(1-\nu)}\ln(y^2+z^2) + \frac{z^2-y^2}{4(1-\nu)(y^2+z^2)}\right], \tag{4.25}$$

$$u_{z,\perp_{xz}}(y,z) = \frac{b_z}{2\pi}\left[\arctan\left(\frac{y}{z}\right) + \frac{yz}{2(1-\nu)(y^2+z^2)}\right], \tag{4.26}$$

where $u_{x,\perp_{xz}}$,$u_{y,\perp_{xz}}$ and $u_{z,\perp_{xz}}$ are the displacement components in the x,y and z directions respectively, b_z is Burgers vector in the z-direction, and ν is Poisson's ratio. The displacement field of a screw dislocation along the x-axis and passing through the origin is given by:

$$u_{x,S_x}(y,z) = \frac{b_x}{2\pi}\arctan\left(\frac{z}{y}\right), \tag{4.27}$$

$$u_{y,S_x}(y,z) = 0, \tag{4.28}$$

$$u_{z,S_x}(y,z) = 0. \tag{4.29}$$

Provided the rotations are small, rigid body rotations ω_x, ω_y and ω_z are given by:

$$\omega_x = \frac{1}{2}\left(\frac{\delta u_z}{\delta y} - \frac{\delta u_y}{\delta z}\right) = \Omega, \tag{4.30}$$

$$\omega_y = \frac{1}{2}\left(\frac{\delta u_x}{\delta z} - \frac{\delta u_z}{\delta x}\right), \tag{4.31}$$

$$\omega_z = \frac{1}{2}\left(\frac{\delta u_y}{\delta x} - \frac{\delta u_x}{\delta y}\right) = \chi. \tag{4.32}$$

Since the scattering vector is aligned with the y-axis, rotations ω_y about the y-axis are of no interest (Figure 4.12). ω_x and ω_z correspond to experimental rotations Ω and χ respectively (figures 4.6 and 4.7). Substituting expressions 4.24 - 4.26 into equations 4.30 - 4.32, rotations $\Omega_{\perp_{xz}}$ and $\chi_{\perp_{xz}}$ due to an edge dislocation along the x-axis with Burgers vector b_z aligned with the z-axis are given by:

$$\Omega_{\perp_{xz}} = \omega_{x,\perp_{xz}} = -\frac{b_z}{2\pi}\frac{z}{y^2+z^2}, \tag{4.33}$$

$$\chi_{\perp_{xz}} = \omega_{z,\perp_{xz}} = 0. \tag{4.34}$$

Similarly, rotations $\Omega_{\perp_{xy}}$ and $\chi_{\perp_{xy}}$ due to an edge dislocation along the x-axis with Burgers vector b_y along the y-axis are:

$$\Omega_{\perp_{xy}} = \omega_{x,\perp_{xy}} = -\frac{b_y}{2\pi}\frac{y}{y^2+z^2}, \tag{4.35}$$

$$\chi_{\perp_{xy}} = \omega_{z,\perp_{xy}} = 0. \tag{4.36}$$

For a screw dislocation aligned with the x-axis, rotations Ω_{S_x} and χ_{S_x} are:

$$\Omega_{S_x} = \omega_{x,S_x} = 0, \tag{4.37}$$

$$\chi_{S_x} = \omega_{z,S_x} = \frac{b_x}{4\pi}\frac{z}{y^2+z^2}. \tag{4.38}$$

Net lattice rotation in the χ direction is caused by the GND element of the screw dislocations in the dislocation walls, whilst net lattice rotation in the Ω direction arises from the GND element of the edge dislocations. In the "naive" model this distinction is possible as only one dislocation line direction, i.e. parallel to the x-axis is considered. In a real crystal the situation is more complex.

SSDs do not provide any net lattice rotation, but increase the local lattice orientation spread.

Equations 4.33 - 4.38 are singular at the origin. For computational studies of the fields generated by clusters of dislocations it is desirable to remove this singularity,

which is done here using a multiplicative "blunting" function of the form:

$$f(r) = \left(\frac{2 \arctan{(Cr)}}{\pi} \right)^2, \tag{4.39}$$

where $r = \sqrt{y^2 + z^2}$ and C is a constant determining the strength of blunting. Pre-multiplying equations 4.33, 4.35 and 4.38 by equation 4.39, the "blunted" rotation expressions are:

$$\Omega_{\perp_{xz},b} = -\left(\frac{2 \arctan{(Cr)}}{\pi} \right)^2 \frac{b_z}{2\pi} \frac{z}{y^2 + z^2}, \tag{4.40}$$

$$\Omega_{\perp_{xy},b} = -\left(\frac{2 \arctan{(Cr)}}{\pi} \right)^2 \frac{b_y}{2\pi} \frac{y}{y^2 + z^2}, \tag{4.41}$$

$$\chi_{S_x,b} = \left(\frac{2 \arctan{(Cr)}}{\pi} \right)^2 \frac{b_x}{4\pi} \frac{z}{y^2 + z^2}. \tag{4.42}$$

These equations can be combined for a given dislocation with line direction along the x-axis, position vector $\mathbf{x}$ in the y-z plane, and Burgers vector $\mathbf{b}$, into the form:

$$\mathbf{R}(\mathbf{x}, \mathbf{b}) = \begin{bmatrix} \Omega \\ \chi \end{bmatrix} = \begin{bmatrix} \Omega_{\perp_{xz},b} + \Omega_{\perp_{xy},b} + \Omega_{S_x,b} \\ \chi_{\perp_{xz},b} + \chi_{\perp_{xy},b} + \chi_{S_x,b} \end{bmatrix} \tag{4.43}$$

$$= \begin{bmatrix} -\left(\frac{2 \arctan{(Cr)}}{\pi} \right)^2 \frac{b_z}{2\pi} \frac{z}{y^2+z^2} - \left(\frac{2 \arctan{(Cr)}}{\pi} \right)^2 \frac{b_y}{2\pi} \frac{y}{y^2+z^2} \\ \left(\frac{2 \arctan{(Cr)}}{\pi} \right)^2 \frac{b_x}{4\pi} \frac{z}{y^2+z^2} \end{bmatrix}. \tag{4.44}$$

In a cloud of N dislocations parallel to the x-axis, where the ith dislocation has Burgers vector $\mathbf{b}_i$ consisting of components b_x, b_y and b_z and is at position $\mathbf{d}_i$, the lattice rotation $\mathbf{R}_p$ at a point p with coordinates $\mathbf{P}$ is given by:

$$\mathbf{R}_p = \sum_{i=1}^{N} \mathbf{R}(\mathbf{P} - \mathbf{d}_i, \mathbf{b}_i). \tag{4.45}$$

Model dislocation micro-structure

We postulate a model dislocation structure which consists of m dislocation walls in the z-direction and n dislocation walls in the y-direction, evenly spaced in a square simulation area of side length $2L$ (figure 4.12). Dislocation walls are described by their dislocation density ρ_0 and wall thickness w. They each contain $2Lw\rho_0$

dislocations at randomly generated positions. Each dislocation can only have one non-zero Burgers vector component, i.e. it can either be a pure edge dislocation with Burgers vector either in the z or y-direction, or a pure screw dislocation. Each type was assigned to one third of the dislocations within each wall.

This is a much simplified setup. In a real material dislocations will be orientated according to the slip plane in which they propagate. However, since any real dislocation Burgers vector orientation can be constructed from a linear combination of the orthogonal basis Burgers vectors, the representation in the "naive" model is adequate at this stage.

Two different strategies were used to assign Burgers vectors to the randomly generated dislocation positions:

1. Burgers vectors are randomly assigned to all dislocations within each wall, with equal probability of having positive or negative sign. This corresponds to only SSDs being present. Hence no overall lattice rotation should occur between dislocation cells.

2. A random bias is introduced for each dislocation type in each dislocation wall, such that the probability of a dislocation of a given species having positive sign is equal to the bias. In this case a GND component is introduced to each dislocation type. Macroscopically, considering a large number of dislocation walls, the net rotation averages to zero, i.e. no overall large scale lattice curvature is introduced into the crystal.

Diffraction peak generation

Lattice rotation at each measurement point is computed using equation 4.45. The predicted reciprocal space map in the q_x, q_z plane is then assembled by summing up the scattered intensity contributions from all measurement points p:

$$M(\Omega, \chi) = \sum_p G(\mathbf{R}_p, \Delta_{inst}, 1). \tag{4.46}$$

$G(\mathbf{R}_p, \Delta_{inst}, 1)$ is a 2D Gaussian function, centred on the elements of vector $\mathbf{R}_p$, Ω and χ, with full width at half maximum (FWHM) of Δ_{inst} , corresponding to the

instrumental broadening and a peak height of unity. The reciprocal space map $M(\Omega, \chi)$ is normalised to give $M_n(\Omega, \chi)$:

$$M_n(\Omega, \chi) = \frac{M(\Omega, \chi)}{\max(M(\Omega, \chi))}. \tag{4.47}$$

The computed reciprocal space map is a map of misorientation within the simulation volume, imaged in terms of rotations about the x-axis (Ω) and z-axis (χ). In a full 3D simulation, taking into account crystal orientation, dislocation positions should be physically based and not randomly generated. They should be placed in accordance with the crystal slip systems, in which case the generation of hkl direction specific misorientation maps would be useful. In the case of the naive model, the arrangement of dislocations is rather contrived, precluding a direct quantitative comparison with experimental measurements. Instead it should be viewed as a tool that helps to elucidate the underlying physics of the problem and to provide qualitative understanding. For this purpose the (020) peak reciprocal space maps computed below are sufficient.

4.3.5 Modelling results

Computational details

The following simulation results were generated using the dislocation cell/wall model parameters listed in table 4.3. The parameters are specified in arbitrary units.

Unbiased wall example

Initially a reciprocal space map was computed for a dislocation cell/wall structure with unbiased dislocation walls. All dislocations present, screw and edge alike, act as SSDs. Each dislocation has a counterpart of opposite sign near it and GNDs are absent. Hence there should be no net rotation between any of the dislocation depleted regions.

As expected, the predicted reciprocal space map in the q_x, q_z plane shows a single, unfragmented, but broadened, peak. It is centred ($\chi = 0$ and $\Omega = 0$) and intensity falls off evenly to all sides.

Dislocation parameters		
Simulation area side-length	$2L$	6 units
Dislocation wall width	w	0.05 units
Number of walls in y-direction	n	4
Number of walls in z-direction	m	4
Wall dislocation density	ρ_0	1650
Burgers vector	b	2×10^{-4} units
Measurement grid parameters		
Sampling grid side-length	$2sg$	6 units
Number of sampling points in y-direction	Np_y	701
Number of sampling points in z-direction	Np_z	701
Instrumental broadening	Δ_{inst}	$0.04°$

Table 4.3: Parameters used in the dislocation cell model.

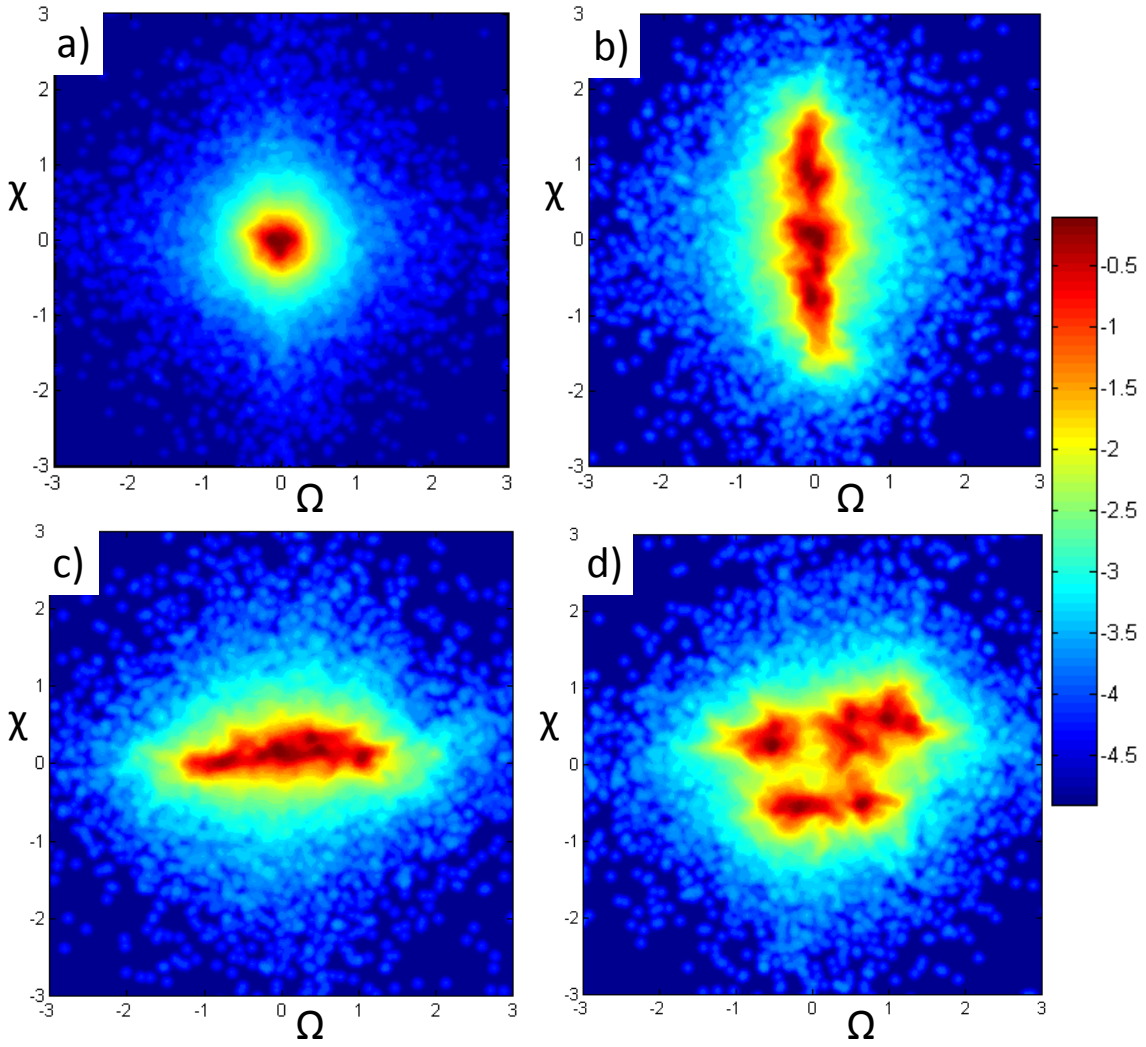

Figure 4.13: Simulated reciprocal space maps: a) With no dislocation wall bias. b) With biased screw dislocations. c) With biased edge dislocations. d) With biased edge and screw dislocations. The colour scale is the logarithm of normalised counts, $M_n(\Omega, \chi)$.

Screw biased wall example

To illustrate the fragmentation of the reciprocal space peak as biasing is introduced to the dislocation walls, a random bias was assigned to the screw dislocations in each wall. Edge dislocations were not biased. Since screw dislocations in the "naive" model only produce rotation in χ, the predicted peaks in reciprocal space are broadened in the χ direction. In the Ω direction, since all edge dislocations are SSDs, the peaks are expected to remain at zero tilt. This behaviour is confirmed by the predicted reciprocal space map (figure 4.13 b)).

Edge biased wall example

Next the previous scenario was altered and screw dislocations were left unbiased, whilst edge dislocations in each wall were assigned a random bias. As expected, figure 4.13 c) shows a spreading of the peaks in the Ω direction and little variation from zero in the χ direction.

Edge and screw biased example

In the final simulation both edge and screw dislocation biasing were activated. Diffraction peaks are now spread out both in the χ and Ω direction (figure 4.13 d)), due to GNDs being present in both the edge and screw dislocation populations.

4.3.6 Discussion

Considering figures 4.9 - 4.11 and figure 4.13, qualitatively similar features can be clearly identified in the experimental and numerical reciprocal space maps. In particular in figure 4.13 d) the structure of sharp peaks superimposed on a background of enhanced intensity is clearly present. This suggests that the experimentally observed patterns indeed arise from a structure similar to that considered in the simulation, with regions of relatively uniform lattice orientation being separated by misorientation walls. We have interpreted these as dislocation walls which contain GNDs, leading to misorientation between dislocation-depleted regions. It is interesting to note that the intensity ratio between the sharp diffraction peaks and

the enhanced background is approximately 2.5 orders of magnitude in the experimental and simulated reciprocal space maps. Both also show a similar angular spread.

By fine-tuning of the parameters of the “naive” model, a much better match of simulation to experiment could be achieved. From this some of the sample parameters such as the cell size to wall thickness ratio, the average misorientation between cells etc. could be determined. However, RSM offers very high reciprocal space resolution, but no information about the real space distribution of features within the scattering volume. Hence, there is no unique solution to the inverse problem of going from a reciprocal space map to the real sample microstructure. Even in terms of absolute sizes of dislocation depleted regions only guesses can be made based on the absolute size of the scattering volume. Because of this non-uniqueness of solution and the need to postulate an arbitrary dislocation structure within the scattering volume, no further quantitative interpretation of the experimental results based on the "naive" model was attempted here. It was rather used to provide a fundamental qualitative understanding of the problem and as an approximate numerical check of the experimentally observed RSMs.

The "naive" model provides a very good tool to explore and illustrate the influence of GNDs and SSDs on single crystal diffraction patterns. SSDs cause a general broadening of the peak in reciprocal space (figure 4.13 a)). However, they do not result in the fragmentation of the peak. GNDs, on the other hand, introduce net lattice rotations. These lead to a more pronounced, directionally specific broadening of the diffraction peak. This type of streaking could be seen in the microbeam Laue diffraction measurements of grain 3 in figure 3.7 (§ 3.1.2). If GNDs are non-uniformly distributed - e.g. dislocation cell-wall structure or arrangement into geometrically necessary boundaries (GNBs) - they lead to the fragmentation of the diffraction peak in reciprocal space, as previously reported by Barabash et al. [124, 125].

To provide improved physicality of the modelling setup, the prediction of diffraction pattern should be based on a mechanical model of the deformation processes taking place within the scattering volume. Dislocation dynamics simulations or

strain gradient crystal plasticity models are ideally suited to provide this input. A further limitation of the "naive" model lies in its confinement to two dimensions. A two dimensional model can only ever be a coarse approximation of the real three-dimensional phenomenon. It is reasonable to expect that this simplification means that certain aspects of plastic deformation by dislocation slip and interaction are not reflected correctly. This is addressed in the next section with the development of the tools required for diffraction post-processing of three-dimensional dislocation structures, such as those which might be simulated using the ParaDiS dislocation dynamics framework.

4.4 Diffraction post-processing of three-dimensional discrete dislocation dynamics simulations

ParaDiS is a three-dimensional dislocation dynamics simulation code, based on the framework proposed by Arsenlis, Cai, Bulatov et al. [5–7] (detailed description in § 2.1.4). Crucially, it deals with the computation of the motion of non-straight dislocation lines by discretising them into straight dislocation segments linked by nodes. Computations of dislocation motion are carried out at nodes. A set of constitutive rules governs dislocation behaviour and interaction.

To compute the diffraction patterns arising from such a discretised three-dimensional dislocation structure, a solution for the lattice rotation field arising from a dislocation segment is needed. In this section a solution for the lattice rotations due to a triangular dislocation loop is presented (developed in collaboration with Sinéad Keegan). It is based on the displacement field for isotropic elasticity given by Barnett and Balluffi [195, 196], which is an adaptation of the solution given by Hirth and Lothe [197]. For the purposes of validation and illustration, the rotation solution is applied to the simple example of a triangular dislocation loop consisting of one edge dislocation segment, one screw dislocation segment and one mixed dislocation segment. Comparison of the edge and screw dislocation rotation fields with the analytical solutions for the rotation fields due to an infinite edge and an infinite screw dislocation respectively shows excellent agreement. By superposi-

tion of individual dislocation triangle solutions, the rotation fields arising from more complex, multi-segment three-dimensional dislocation loops can be evaluated.

Ultimately the aim is to apply the diffraction post-processing to dislocation positions simulated using the ParaDiS simulation code. As a first example, the evolution of a Frank-Read source at different stages during the emission of a dislocation loop was modelled using ParaDiS. Based on the predicted dislocation segment positions, the lattice rotations were evaluated. Misorientation plots, similar to tangential reciprocal space maps in that they depict the local orientation spread, show streaking similar to that observed in diffraction measurements, and which can be interpreted in terms of the active slip system(s). Unfortunately more complex simulations using ParaDiS were not possible due to the limited computational resources available.

4.4.1 Lattice rotation from a triangular dislocation loop

Following the notation of Barnett and Balluffi [195, 196], let ABC be a triangular dislocation loop and P be a field point. $\mathbf{R}_A$, $\mathbf{R}_B$, $\mathbf{R}_C$ denote the vectors from P to the vertices A, B, C respectively. Ω denotes the solid angle associated with the triangle ABC, as seen by an observer at P. Then the displacement field at P due to the loop is

$$\mathbf{u}(P) = -\frac{\mathbf{b}\Omega}{4\pi} + \mathbf{F}_{AB} + \mathbf{F}_{BC} + \mathbf{F}_{CA}, \tag{4.48}$$

where

$$\begin{aligned} \mathbf{F}_{AB} &= -\frac{(1-2\nu)}{8\pi(1-\nu)}\left(\mathbf{b}\times\mathbf{t}_{AB}\right)\ln\left(\frac{R_B+\mathbf{R}_B\cdot\mathbf{t}_{AB}}{R_A+\mathbf{R}_A\cdot\mathbf{t}_{AB}}\right) \\ &+ \frac{1}{8\pi(1-\nu)}\left(\mathbf{b}\cdot\mathbf{n}_{AB}\right)\left(\boldsymbol{\lambda}_B-\boldsymbol{\lambda}_A\right)\times\mathbf{n}_{AB}, \end{aligned} \tag{4.49}$$

and

$$\mathbf{n}_{AB} = \frac{\boldsymbol{\lambda}_A\times\boldsymbol{\lambda}_B}{|\boldsymbol{\lambda}_A\times\boldsymbol{\lambda}_B|}. \tag{4.50}$$

Cyclic interchange of A, B, C in equations 4.49 and 4.50 results in expressions for $\mathbf{F}_{BC}$ and $\mathbf{F}_{CA}$. R_A, R_B, R_C denote the magnitudes of $\mathbf{R}_A$, $\mathbf{R}_B$, $\mathbf{R}_C$ respectively, and $\boldsymbol{\lambda}_A$, $\boldsymbol{\lambda}_B$, $\boldsymbol{\lambda}_C$ denote unit vectors in the $\mathbf{R}_A$, $\mathbf{R}_B$, $\mathbf{R}_C$ directions respectively. $\mathbf{t}_{AB}$,

$\mathbf{t}_{BC}$, $\mathbf{t}_{CA}$ denote unit tangents along $\mathbf{AB}$, $\mathbf{BC}$, $\mathbf{CA}$ respectively. ν is Poisson's ratio and $\mathbf{b}$ the loop Burgers vector.

The solid angle Ω is given by the equation

$$\Omega = -\mathrm{sgn}\left(\boldsymbol{\lambda}_A \cdot \mathbf{N}\right) E, \tag{4.51}$$

where $\mathbf{N}$ is a unit normal to the ABC plane, chosen such that an observer looking in the direction $-\mathbf{N}$ sees ABC in an anti-clockwise direction. In our calculations we define

$$\mathbf{N} = \frac{\mathbf{t}_{AB} \times \mathbf{t}_{BC}}{|\mathbf{t}_{AB} \times \mathbf{t}_{BC}|}. \tag{4.52}$$

The quantity E is computed using the equation

$$E = 4 \arctan \sqrt{\tan\left(\frac{s}{2}\right) \tan\left(\frac{s-a}{2}\right) \tan\left(\frac{s-b}{2}\right) \tan\left(\frac{s-c}{2}\right)}, \tag{4.53}$$

where a is defined by

$$a = \arccos\left(\boldsymbol{\lambda}_B \cdot \boldsymbol{\lambda}_C\right), \tag{4.54}$$

and b and c are obtained by cyclic interchange in equation 4.54. The quantity s is defined as

$$s = \frac{1}{2}\left(a + b + c\right). \tag{4.55}$$

We wish to calculate the derivatives of the loop displacement field $\mathbf{u}(P)$ with respect to x, y, and z respectively, so that the small rotation angles can be computed. In the following equations ξ can be replaced by either x, y or z.

The derivative of $\mathbf{F}_{AB}$ is given by

$$\begin{aligned}
\frac{\partial \mathbf{F}_{AB}}{\partial \xi} &= -\frac{(1-2\nu)}{8\pi(1-\nu)}\left(\mathbf{b} \times \mathbf{t}_{AB}\right)\left(\frac{\frac{\partial R_B}{\partial \xi} + \frac{\partial \mathbf{R}_B}{\partial \xi} \cdot \mathbf{t}_{AB}}{R_B + \mathbf{R}_B \cdot \mathbf{t}_{AB}} - \frac{\frac{\partial R_A}{\partial \xi} + \frac{\partial \mathbf{R}_A}{\partial \xi} \cdot \mathbf{t}_{AB}}{R_A + \mathbf{R}_A \cdot \mathbf{t}_{AB}}\right) \\
&+ \frac{(\mathbf{b} \cdot \mathbf{n}_{AB})}{8\pi(1-\nu)}\left((\boldsymbol{\lambda}_B - \boldsymbol{\lambda}_A) \times \frac{\partial \mathbf{n}_{AB}}{\partial \xi} + \left(\frac{\partial \boldsymbol{\lambda}_B}{\partial \xi} - \frac{\partial \boldsymbol{\lambda}_A}{\partial \xi}\right) \times \mathbf{n}_{AB}\right) \\
&+ \frac{1}{8\pi(1-\nu)}\left(\mathbf{b} \cdot \frac{\partial \mathbf{n}_{AB}}{\partial \xi}\right)\left((\boldsymbol{\lambda}_B - \boldsymbol{\lambda}_A) \times \mathbf{n}_{AB}\right),
\end{aligned} \tag{4.56}$$

where

$$\frac{\partial \mathbf{R}_A}{\partial x} = (-1, 0, 0), \tag{4.57}$$

$$\frac{\partial \mathbf{R}_A}{\partial y} = (0, -1, 0), \tag{4.58}$$

$$\frac{\partial \mathbf{R}_A}{\partial z} = (0, 0, -1), \tag{4.59}$$

$$\frac{\partial R_A}{\partial \xi} = \frac{\xi - A_\xi}{R_A}, \tag{4.60}$$

$$\frac{\partial \boldsymbol{\lambda}_A}{\partial \xi} = \frac{R_A \frac{\partial \mathbf{R}_A}{\partial \xi} - \frac{\partial R_A}{\partial \xi}\mathbf{R}_A}{(R_A)^2}, \tag{4.61}$$

and A can be replaced by B or C as appropriate. In equation 4.60, A_ξ denotes the ξ^{th} component of A. The following derivatives also appear in equation 4.56.

$$\frac{\partial \left|\boldsymbol{\lambda}_A \times \boldsymbol{\lambda}_B\right|}{\partial \xi} = \mathbf{n}_{AB} \cdot \frac{\partial \left(\boldsymbol{\lambda}_A \times \boldsymbol{\lambda}_B\right)}{\partial \xi}, \tag{4.62}$$

$$\frac{\partial \left(\boldsymbol{\lambda}_A \times \boldsymbol{\lambda}_B\right)}{\partial \xi} = \boldsymbol{\lambda}_A \times \frac{\partial \boldsymbol{\lambda}_B}{\partial \xi} + \frac{\partial \boldsymbol{\lambda}_A}{\partial \xi} \times \boldsymbol{\lambda}_B, \tag{4.63}$$

$$\frac{\partial \mathbf{n}_{AB}}{\partial \xi} = \frac{1}{\left|\boldsymbol{\lambda}_A \times \boldsymbol{\lambda}_B\right|} \frac{\partial \left(\boldsymbol{\lambda}_A \times \boldsymbol{\lambda}_B\right)}{\partial \xi} - \frac{\left(\boldsymbol{\lambda}_A \times \boldsymbol{\lambda}_B\right)}{\left|\boldsymbol{\lambda}_A \times \boldsymbol{\lambda}_B\right|^2} \frac{\partial \left|\boldsymbol{\lambda}_A \times \boldsymbol{\lambda}_B\right|}{\partial \xi}. \tag{4.64}$$

The derivatives of $\mathbf{F}_{BC}$ and $\mathbf{F}_{CA}$ are obtained by the cyclic interchange of A, B, C in the above equations.

To compute the derivative of $\mathbf{u}(P)$ it is also necessary to differentiate the quantity E. This is done as follows:

$$\begin{aligned}
\frac{\partial E}{\partial \xi} = & \left[\sec^2\left(\frac{s}{2}\right)\tan\left(\frac{s-a}{2}\right)\tan\left(\frac{s-b}{2}\right)\tan\left(\frac{s-c}{2}\right)\frac{\partial s}{\partial \xi}\right. \\
& + \sec^2\left(\frac{s-a}{2}\right)\tan\left(\frac{s}{2}\right)\tan\left(\frac{s-b}{2}\right)\tan\left(\frac{s-c}{2}\right)\frac{\partial (s-a)}{\partial \xi} \\
& + \sec^2\left(\frac{s-b}{2}\right)\tan\left(\frac{s}{2}\right)\tan\left(\frac{s-a}{2}\right)\tan\left(\frac{s-c}{2}\right)\frac{\partial (s-b)}{\partial \xi} \\
& \left. + \sec^2\left(\frac{s-c}{2}\right)\tan\left(\frac{s}{2}\right)\tan\left(\frac{s-a}{2}\right)\tan\left(\frac{s-b}{2}\right)\frac{\partial (s-c)}{\partial \xi}\right] \\
& \div \sec^2\left(\frac{E}{4}\right)\tan\left(\frac{E}{4}\right),
\end{aligned} \tag{4.65}$$

where

$$\frac{\partial a}{\partial \xi} = \frac{-1}{|\boldsymbol{\lambda}_B \times \boldsymbol{\lambda}_C|}\left(\frac{\partial}{\partial \xi}\left(\boldsymbol{\lambda}_B \cdot \boldsymbol{\lambda}_C\right)\right), \tag{4.66}$$

$$\frac{\partial b}{\partial \xi} = \frac{-1}{|\boldsymbol{\lambda}_C \times \boldsymbol{\lambda}_A|}\left(\frac{\partial}{\partial \xi}\left(\boldsymbol{\lambda}_C \cdot \boldsymbol{\lambda}_A\right)\right), \tag{4.67}$$

$$\frac{\partial c}{\partial \xi} = \frac{-1}{|\boldsymbol{\lambda}_A \times \boldsymbol{\lambda}_B|}\left(\frac{\partial}{\partial \xi}\left(\boldsymbol{\lambda}_A \cdot \boldsymbol{\lambda}_B\right)\right), \tag{4.68}$$

$$\frac{\partial s}{\partial \xi} = \frac{1}{2}\left(\frac{\partial a}{\partial \xi} + \frac{\partial b}{\partial \xi} + \frac{\partial c}{\partial \xi}\right), \tag{4.69}$$

and

$$\frac{\partial}{\partial \xi}\left(\boldsymbol{\lambda}_A \cdot \boldsymbol{\lambda}_B\right) = \boldsymbol{\lambda}_A \cdot \frac{\partial \boldsymbol{\lambda}_B}{\partial \xi} + \boldsymbol{\lambda}_B \cdot \frac{\partial \boldsymbol{\lambda}_A}{\partial \xi}. \tag{4.70}$$

The derivative of Ω is given by

$$\frac{\partial \Omega}{\partial \xi} = -\mathrm{sgn}\left(\boldsymbol{\lambda}_A \cdot \mathbf{N}\right)\frac{\partial E}{\partial \xi} - 2\delta\left(\boldsymbol{\lambda}_A \cdot \mathbf{N}\right)\left(\frac{\partial \boldsymbol{\lambda}_A}{\partial \xi} \cdot \mathbf{N}\right)E, \tag{4.71}$$

where δ denotes the Dirac delta function. Finally, the derivative of $\mathbf{u}(P)$ is given by

$$\frac{\partial}{\partial \xi}\mathbf{u}(P) = -\frac{\mathbf{b}}{4\pi}\frac{\partial \Omega}{\partial \xi} + \frac{\partial \mathbf{F}_{AB}}{\partial \xi} + \frac{\partial \mathbf{F}_{BC}}{\partial \xi} + \frac{\partial \mathbf{F}_{CA}}{\partial \xi}, \tag{4.72}$$

where ξ denotes either x or y or z. The lattice rotations at field point P due to the presence of dislocation loop ABC are:

$$\omega_x = \frac{1}{2}\left(\frac{\partial u_z}{\partial y} - \frac{\partial u_y}{\partial z}\right), \tag{4.73}$$

$$\omega_y = \frac{1}{2}\left(\frac{\partial u_x}{\partial z} - \frac{\partial u_z}{\partial x}\right), \tag{4.74}$$

$$\omega_z = \frac{1}{2}\left(\frac{\partial u_y}{\partial x} - \frac{\partial u_x}{\partial y}\right), \tag{4.75}$$

where ω_x, ω_y and ω_z correspond to small rotations about the x, y and z axes respectively. u_x, u_y and u_z denote respectively the x, y and z components of $\mathbf{u}$. The

elastic strains at field point P are given by:

$$\epsilon_{xx} = \frac{\partial u_x}{\partial x}, \quad \epsilon_{xx} = \frac{\partial u_x}{\partial x}, \quad \epsilon_{xx} = \frac{\partial u_x}{\partial x}, \tag{4.76}$$

$$\gamma_{xy} = \frac{\partial u_y}{\partial x} + \frac{\partial u_x}{\partial y}, \quad \gamma_{yz} = \frac{\partial u_z}{\partial y} + \frac{\partial u_y}{\partial z}, \quad \gamma_{zx} = \frac{\partial u_x}{\partial z} + \frac{\partial u_z}{\partial x}, \tag{4.77}$$

where ϵ_{xx}, ϵ_{yy} and ϵ_{zz} denote the direct elastic strains in the x, y and z directions respectively, and γ_{xy}, γ_{xy} and γ_{xy} give the shear strains.

The remainder of this section focuses on the lattice rotations induced by the presence of dislocations, as this quantity is most readily measured using high angular resolution synchrotron X-ray diffraction measurements (§ 3.2).

4.4.2 Comparison with two-dimensional solutions

To validate the correctness of the solution for ω_x, ω_y and ω_z, comparisons with some simple, two-dimensional analytical solutions are made. Analogous to equations 4.33 and 4.34 in § 4.3.4, the lattice rotations induced by an infinitely long edge dislocation in an isotropic elastic medium, running along the z-axis, with Burgers vector of magnitude b_x along the x-axis are given by:

$$\omega_{x,\perp_{zx}} = 0, \tag{4.78}$$

$$\omega_{y,\perp_{zx}} = 0, \tag{4.79}$$

$$\omega_{z,\perp_{zx}} = -\frac{b_x}{2\pi}\frac{x}{x^2+y^2}, \tag{4.80}$$

where $\omega_{x,\perp_{zx}}$, $\omega_{y,\perp_{zx}}$ and $\omega_{z,\perp_{zx}}$ are the lattice rotations about the x, y and z axes respectively. Similarly the lattice rotations resulting from an infinitely long screw dislocation along the x-axis as previously given by equations 4.37 and 4.38 in section 4.3.4 (here repeated for completeness) are given by:

$$\omega_{x,S_x} = 0, \tag{4.81}$$

$$\omega_{y,S_x} = \frac{b}{4\pi}\frac{y}{y^2+z^2}, \tag{4.82}$$

$$\omega_{z,S_x} = \frac{b}{4\pi}\frac{z}{y^2+z^2}, \tag{4.83}$$

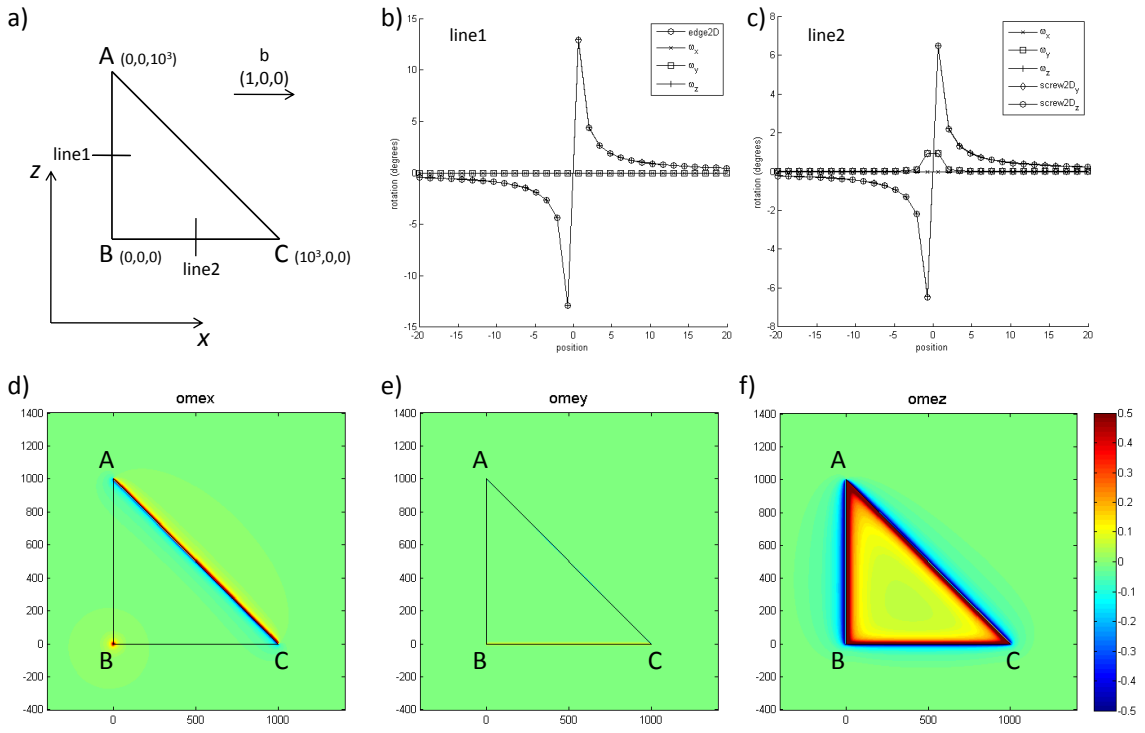

Figure 4.14: Consideration of a simple triangular dislocation loop ABC with Burgers vector $\mathbf{b}$. a) Diagram of the dislocation loop. b) Line plot of rotation along "line 1", showing ω_x, ω_y, ω_z and $\omega_{z,\perp_{zx}}$. c) Line plot of rotation along "line 2", showing ω_x, ω_y, ω_z, ω_{y,S_x} and ω_{z,S_x}. d), e) and f) Maps of ω_x, ω_y and ω_z rotations respectively for the dislocation loop in the x, z plane, computed at $y = 0.1$.

where ω_{x,S_x}, ω_{y,S_x} and ω_{z,S_x} are the lattice rotations about the x, y and z axes respectively.

To test and validate the rotation expressions for a dislocation triangle ABC, it is instructive to consider a simple example in which pure edge, pure screw and mixed dislocation elements are present. A simple structure for which this can be achieved is the dislocation triangle shown in figure 4.14 a). Here the dislocation loop consists of the three vertices A, B and C, placed at $[0, 0, 1000]$, $[0, 0, 0]$ and $[1000, 0, 0]$ respectively. Assigning a Burgers vector $\mathbf{b}$ of $[1, 0, 0]$ means that the segment AB is a pure edge dislocation, segment BC a pure screw dislocation, and segment CA a mixed dislocation with both a screw and an edge component. Poisson's ration ν was taken to be 0.3.

The length of segment AB is 1000 units, which is large compared to the Burgers vector magnitude of 1 unit. Hence the rotation field in the centre of segment AB should be comparable to the rotation field of an infinite edge dislocation running

along the z axis, with Burgers vector in the x direction (equations 4.78 - 4.80). This comparison was carried out along a line from $[-20, 0.1, 500]$ to $[-20, 0.1, 500]$ - "line 1" in figure 4.14 a). Figure 4.14 b) shows the variation of ω_x, ω_y and ω_z along this line, plotted with the corresponding $\omega_{z,\perp_{zx}}$ variation for an infinite edge dislocation. Clearly ω_z and $\omega_{z,\perp_{zx}}$ show very good agreement, as anticipated. ω_x and ω_y are both zero which is consistent with the values of $\omega_{x,\perp_{zx}}$ and $\omega_{y,\perp_{zx}}$ respectively, as expected for an infinite edge dislocation.

Similarly, the length of segment BC of 1000 units is large compared to the Burgers vector. Hence the rotation field in the middle of segment BC should be well matched to the rotation field of an infinite screw dislocation along the x axis (equations 4.81 - 4.83).The rotation field was probed along a line from $[500, 0.1, -20]$ to $[500, 0.1, 20]$, marked as "line 2" in figure 4.14 a) . Figure 4.14 c) shows the variation of ω_x, ω_y and ω_z along this line. Plotted alongside are ω_{y,S_x} and ω_{z,S_x}, the rotations about the y and z axes respectively, for an infinite screw dislocation running along the x axis. ω_z and ω_{z,S_x} show very good agreement. Likewise ω_y and ω_{y,S_x} agree very closely. The rise at the centre of the ω_y and ω_{y,S_x} profiles occurs as "line 2" passes not right through the core of the dislocation at $y = 0$, but rather runs at $y = 0.1$. The ω_x rotation is zero, which is consistent with the solution for an infinite screw dislocation along the x axis.

Figures 4.14 d), e) and f) show maps of ω_x, ω_y and ω_z rotation respectively, computed for the dislocation triangle ABC on an xz plane intersecting the y-axis at 0.1. The map of ω_x rotation, figure 4.14 d) , shows that no rotation about this axis is present in the edge dislocation segment AB or in the screw dislocation segment BC. This is as expected from the infinite edge and screw dislocation solutions, equations 4.78 - 4.80 and 4.81 - 4.83 respectively. It is interesting to note that the mixed dislocation segment on the other hand has some ω_x rotation component. Also a local maximum of ω_x rotation is present at point B.

The map of ω_y rotation (figure 4.14 e)) shows (as expected from the infinite, two-dimensional edge dislocation solution) that no ω_y rotation is present in the AB pure edge dislocation segment. In the pure screw dislocation segment BC, small positive rotations in ω_y are present close to the dislocation core. This is in good

agreement with the line plot in figure 4.14 c) and is a result of the mapping plane crossing the y-axis at $y = 0.1$, whilst the plane of the dislocation loop ABC crosses the y-axis at $y = 0$. In the mixed dislocation segment CA it is interesting to note that no ω_y rotation is present.

For this particular dislocation triangle the greatest lattice rotations occur in the ω_z rotation direction (figure 4.14 f)). As would be expected from the expressions for $\omega_{z,\perp_{zx}}$ and ω_{z,S_x}, equations 4.80 and 4.83 respectively, the rotation field about the edge segment AB is a factor of two greater that the ω_z rotation field of the screw segment BC. It is reassuring to note that the rotation field remains well confined to the dislocation triangle and there do not appear to be any spurious rotations present. Interestingly the area inside the dislocation triangle experiences exclusively positive ω_z rotation, whilst the area outside the triangle experiences exclusively negative ω_z rotation. This observation is consistent with the expected behaviour of the individual dislocation segments when each is considered separately and compared to the two-dimensional solution for an infinite dislocation.

4.4.3 Lattice rotations from multi-segment three-dimensional dislocation structures

Based on the lattice rotations arising from a dislocation triangle, the rotation fields for more complicated dislocation structures arising in $3D$ can be determined. Since the material was assumed to be linearly elastic, superposition can be used to evaluate the total rotation field ω_ξ arising from n dislocation triangles, each giving rise to lattice rotations $\omega_{i\xi}$, where ξ denotes either x, y or z.

$$\omega_\xi = \sum_{i=1}^{n} \omega_{i\xi}. \tag{4.84}$$

Figure 4.15 a) shows a dislocation loop, discretised into segments and with vertices A, B, D, E, F, G and H. Each dislocation segment has a line direction, indicated by the arrows in figure 4.15 a), and a Burgers vector, common to all the segments in the loop due to conservation of Burgers vector. To evaluate the lattice rotations ω_x, ω_y and ω_z for this dislocation loop, one possible strategy is

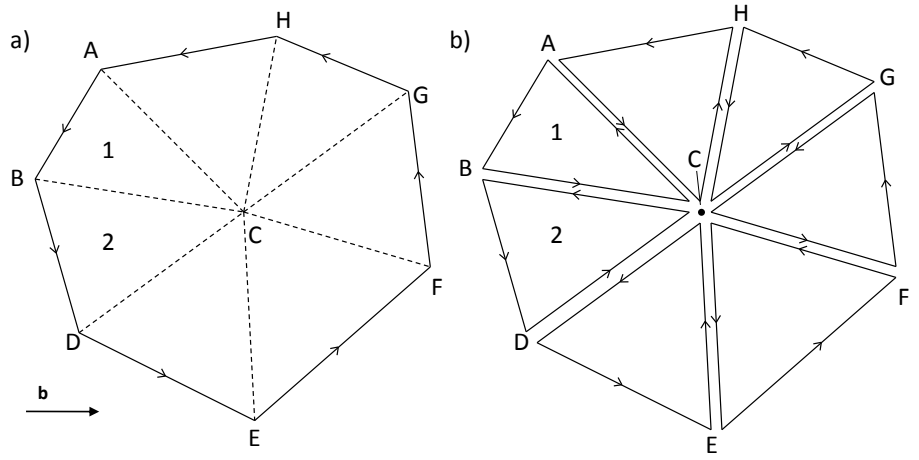

Figure 4.15: Schematic of a dislocation loop. a) The loop is discretised into dislocation segments. b) For the computation of rotation each dislocation segment is linked to a virtual point C by two virtual segments to give a triangular dislocation loop.

to introduce a virtual node C. Linking each vertex of the loop to point C allows the generation of a triangular dislocation loop for each segment. See for example dislocation segment AB in figure 4.15 a), which is shown as dislocation triangle ABC in figure 4.15 b). Summing up the rotation fields from the dislocation triangles arising from each segment and node C provides the total lattice rotation field for the dislocation loop. The contributions from the virtual dislocation lines linking the loop vertices to C cancel out. This can be seen clearly in figure 4.15 b), by considering triangles ABC and BDC. Dislocation line BC in triangle ABC and dislocation line CB in triangle BDC have opposite line directions. Since both have the same Burgers vector, their net rotations cancel out. This highlights the importance of closed contours in dislocation loops. Physically a dislocation cannot end inside the lattice. It must terminate at a boundary of the lattice, for example a free surface, a grain boundary or some other obstacle. Computationally, a non-closed dislocation loop would lead to the virtual dislocation segments from the ends of the loop not cancelling out, thus introducing an artificial closure of the loop. Obviously this is not admissible. Hence any dislocation loop should always be closed.

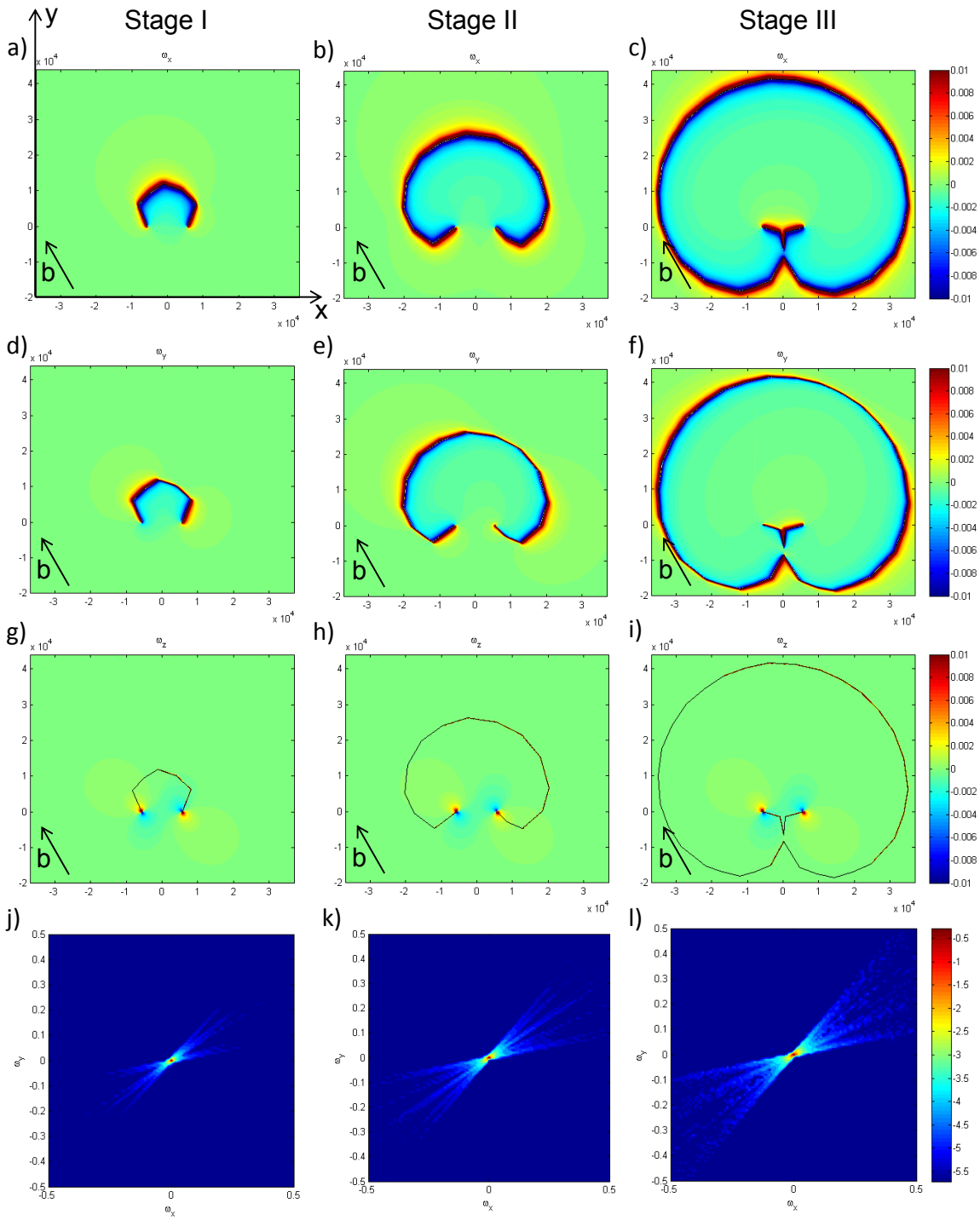

Figure 4.16: Plots of lattice rotation computed in the plane of a Frank-Read source on the (111) plane, with Burgers vector $[01\bar{1}]$ direction. The x-axis lies along the $[1\bar{1}0]$ crystal direction and the y-axis along the $[11\bar{2}]$ crystal direction. The $[111]$ axis is normal to the plane. a), b) and c) show plots of ω_x lattice rotation, corresponding to rotation about the $[1\bar{1}0]$ axis, for three stages of the Frank-Read loop formation. d), e) and f) show plots of ω_y rotation, i.e. rotation about the $[11\bar{2}]$ crystal direction. g), h) and i) are maps of ω_z rotation, about the $[111]$ crystal axis. The plotting plane was located 0.5 units below the plane of the Frank-Read source. j), k) and l) show maps of misorientation in ω_x and ω_y for the three evolution stages of the Frank-Read loop. The colour coding is in degrees in a) to i) and in $\log$ of normalised intensity in j) to l).

4.4.4 Lattice rotations due to a Frank-Read source

As an example of dislocation-induced, three-dimensional lattice rotations, the rotation field arising from a Frank-Read source was considered. The computations to determine the spatial distribution of dislocation segments were carried out using the ParaDiS discrete dislocation dynamics code [5]. An FCC crystal was simulated, which is loaded under uniaxial tension along the $[001]$ crystal axis. A dislocation segment with $[1\bar{1}0]$ line direction (10^4 units length) and Burgers vector direction $[01\bar{1}]$ (1 unit length) was introduced on the (111) slip plane. Snapshots were taken of the simulation just as the dislocation line is starting to bow out (figures 4.16 a), d) and g)), as the dislocation loop curves around the two fixed points (figures 4.16 b), e) and h)) and as a complete dislocation loop has been formed and the process is about to repeat itself for the emission of the next dislocation loop (figures 4.16 c), f) and i)). These three stages will be referred to as I, II and III respectively.

An obvious difficulty is that in the conventional picture of a Frank-Read source, the source segment does not form a closed loop. It is rather assumed that the ends of the dislocation segment are somehow pinned (e.g. by an obstacle), preventing them from moving. In our simulations, a dislocation segment running in the $[\bar{1}\bar{1}\bar{1}]$ direction was attached to each end of the Frank-Read source segment. At a large distance from the simulation plane, a linking segment was introduced. This closes the dislocation loop, whilst, by virtue of being far away from the simulation volume, not disturbing the pattern of lattice rotations produced by the Frank-Read source.

Lattice rotations were computed in a plane parallel to the (111) crystal plane, according to expression 4.84. For figures 4.16 a) - i) the plotting plane was aligned such that the x-axis was along the $[1\bar{1}0]$ direction and the y-axis along the $[11\bar{2}]$ direction. Furthermore, the plane on which rotations were considered was offset by 0.5 units along the $[\bar{1}\bar{1}\bar{1}]$ direction from the plane of the Frank-Read source to avoid problems of singularity of solution which arise in the plane of the dislocation loop.

Figures 4.16 a), b) and c) show a maps of lattice rotation (in degrees) in the ω_x direction, i.e. about the $[1\bar{1}0]$ lattice axis. A number of interesting features can be noticed. No artifacts are evident from the "virtual" dislocation segments

which were introduced for the computations of "dislocation triangle" rotation fields. Lattice rotation outside the loop is positive, whilst inside the loop it is consistently negative. At the fixed ends of the Frank-Read source loop, where the dislocation line runs perpendicular to the plotting plane, the rotation field decays as expected. In figure 4.16 c), with one dislocation loop complete, it can be seen that a similar rotation field is established for the next dislocation loop, with positive lattice rotation outside and negative inside the loop. This is as expected from the Burgers vector and line direction configuration. Figures 4.16 d), e) and f) show maps of lattice rotation in the ω_y direction, i.e. about the $[11\bar{2}]$ crystal direction. In this direction lattice rotation is also positive outside the dislocation loop and negative inside. Figures 4.16 g), h) and i) show maps of lattice rotation in the ω_z direction, i.e. about the crystal $[111]$ direction. As expected, since we are close to the plane of the dislocation loop, only little rotation is present in this direction. Interestingly, when zooming into the fixed ends of the Frank-Read source segment, which are linked to the long dislocation segments in the $[\bar{1}\bar{1}\bar{1}]$ direction for loop closure, the typical edge dislocation rotation field can be seen. The positioning of the positive and negative rotation lobes is as expected from the Burgers vector and dislocation line directions. These edge dislocation fields are the same in figures 4.16 g), h) and i). Their presence confirms the correct functioning of the implementation.

In X-ray diffraction measurements it is difficult to resolve the exact spatial distribution of lattice rotations, due to the limited probe sizes available. Spot sizes of 300nm have become routinely achievable [103] and it is anticipated that smaller beamsizes (sub-100nm) will be available in future. Hence it is not possible at present to measure the exact spatial distribution of lattice orientation; rather only the spread of lattice orientations present within the probed gauge volume can be assessed.

It is instructive to look at the spread of lattice orientations introduced by the Frank-Read source. Figures 4.16 j), k) and l) show two-dimensional histograms of ω_x and ω_y orientation at stages I, II and III respectively of the Frank-Read source loop formation. Each bin in the histogram has a width of 0.01° in both orientation directions. To highlight the contributions from areas of larger lattice rotation, the

number of counts per bin was normalised against the bin with the highest number of counts and then plotted on a log scale. This misorientation map corresponds essentially to the orientation spread which would be seen when projecting a $[111]$ reflection reciprocal space map for this system onto the tangential reciprocal space directions.

A number of interesting features can be seen in the misorientation maps. The orientation spread shows distinct streaking, i.e. elongation in the $+\omega_x/+\omega_y$ to $-\omega_x/-\omega_y$ direction. In fact, the streak consists of a number of individual sub-streaks. The number of sub-streaks increases with the number of dislocation segments as one moves from stage I of the Frank-Read loop to stage II. This suggests that the sub-streaks are in fact an artifact of the discretisation of the dislocation loop into discrete segments. If infinitesimal dislocation segments were used for the representation of the Frank-Read loop, the sub-streaks should merge into one. It can also be noted that the streaking direction is the same figures 4.16 j), k) and l). If the Frank-Read loop were replaced by straight infinite edge dislocations, with line direction along the $[2\bar{1}\bar{1}]$ direction, and the same Burgers vector, they would give rise to lattice rotation about the $[2\bar{1}\bar{1}]$ axis. The resulting streaking would be in the same direction in the ω_x, ω_y rotation space as for the Frank-Read source. This result supports the validity of the methodology used in the literature to determine the active slip system from streaking by considering lattice rotations from a population of infinite, straight edge dislocations on a slip plane [123]. Finally, it can be noted that, as the Frank-Read loop formation progresses, the spread of lattice orientations in the considered volume increases, which is as expected due to the increase in dislocation density.

4.4.5 Outlook

The method described in this section makes it possible to compute the lattice rotation fields from any three-dimensional dislocation structure discretised into segments. The positioning of individual segments can be computed using discrete dislocation dynamics codes, such as ParaDiS. At the moment the solution is limited to elastically isotropic media, however, given elastic anisotropy at the crystal scale

of most engineering metals, an extension to elastically anisotropic media would be a worthwhile challenge. The resulting rotation fields can be used to compute predicted diffraction patterns for direct comparison with experimental diffraction measurements using ray tracing techniques (e.g. as outlined in appendix A.3 for micro-beam Laue diffraction). This would be particularly useful for the investigation of phenomena like dislocation substructure formation, where, due to the limits of spatial resolution, comparison with simulations should play an essential role in ensuring correct interpretation and understanding of experimental results. Lattice rotations could also be used to inform discrete dislocation dynamics codes of the local reorientation of slip planes. In three-dimensional simulations this effect has thus far been assumed to be small, but it was shown to be of importance in two dimensions [40, 46, 47].

A limitation of the framework is the time required for the point by point sampling of rotation fields. A much more efficient approach would be to find an integral expression for the misorientation spread arising in a volume of limited size due to a dislocation segment or a triangular dislocation loop. This would make the misorientation analysis of much larger dislocation ensembles feasible and significantly reduce computation time. Work with this objective is planned for the near future.

4.5 Chapter conclusions

In this chapter some advances in the diffraction post-processing of dislocation structures in two and three dimensions were presented. The aim was to make a direct comparison with experimentally collected diffraction patterns possible.

Initially reciprocal space maps collected from a large grained, slightly deformed aluminium sample were considered. In the tangential directions of reciprocal space they showed a number of sharp peaks superimposed on a background of enhanced intensity. To explain this structure a "naive", two-dimensional, model was postulated, with several dislocation depleted regions separated by high dislocation density walls. Diffraction post-processing of lattice orientation from this model made it possible to capture some of the experimentally observed features. In par-

ticular the different influences of GNDs and SSDs could be explored. GNDs lead to anisotropic broadening (streaking) and fragmentation of diffraction peaks in the tangential directions of reciprocal space. SSDs on the other hand resulted in a uniform broadening.

For improved physicality the positioning of dislocations should be computed by dislocation dynamics simulations, and the method should be extended to three-dimensional dislocation structures. To this end a solution for lattice rotations arising from arbitrary three-dimensional dislocation structures, discretised into dislocation segments, was developed. It was based on the rotation fields arising from a triangular dislocation loop. Comparison of the triangular dislocation loop solution with analytical, two-dimensional lattice rotation solutions showed excellent agreement. The lattice rotations from more complex, multi-segment dislocation loops can be computed by superposition of multiple triangular dislocation loop solutions.

As a demonstration, the lattice rotations due to a Frank-Read source at different stages of the emission of a dislocation loop were evaluated. Dislocation segment positions were computed using the ParaDiS dislocation dynamics code. In maps of orientation spread, anisotropic broadening was observed. It could be linked to the streaking of reflections observed in micro-beam Laue diffraction measurements.

The proposed framework provides an important step towards the diffraction post-processing of full, three-dimensional dislocation dynamics simulations. It also lends itself to the incorporation of lattice rotations into discrete dislocation dynamics simulation codes such as ParaDiS. An important next step would be the development of an integral solution for the orientation spread arising from a dislocation triangle. This would remove the need for point-by-point sampling and make the computations of lattice rotations from larger three-dimensional dislocation structures feasible.

Chapter 5

High energy transmission micro-beam Laue diffraction

5.1 Motivation and chapter overview

The Laue diffraction methods discussed so far are limited to the study of near-surface regions. This is due to the photon energies used, e.g. in Ni, the attenuation length at 20 keV is $\sim 36\mu\mathrm{m}$, although in Al at 20 keV, the attenuation length is $\sim 1.17\mathrm{mm}$. 3DXRD and DCT methods operate at higher photon energies, and hence offer greater penetration depths (§ 2.2.5). However, the need for sample rotation can be a limiting factor, especially for samples of complex shape and with limited access.

A more useful experimental tool would allow the penetration deep into the bulk of real engineering components, where path lengths might reach up to several mm, without the need for sample rotation. One way of achieving this non-destructively is to extend the micro-beam Laue diffraction technique to higher photon energies.

The idea of extending existing diffraction methods to higher photon energies for enhanced penetration into thick samples is commonly used in the powder diffraction community. Examples include the use of both monochromatic [198, 199] and energy dispersive [183, 200] high energy x-ray diffraction setups for the determination of lattice strains, micro-strains, microstructure and texture evolution. High energy micro-beam Laue diffraction would allow the study of material buried deep

within the bulk and through-thickness characterisation of intragranular orientation and elastic strain in real engineering components.

Bragg's law dictates that as the energy of the incident photon beam is increased, reflections occur at lower 2θ angles, i.e. the stronger, lower order reflections will be forward scattered. This makes transmission geometry with the area detector centre placed at $2\theta = 0^\circ$ the natural choice.

This chapter reports the first successful high energy transmission micro-beam Laue (HETL) diffraction setup established on beamline ID15 (ESRF). It was used to study the evolution of lattice orientation through-thickness within a $300\mu\mathrm{m}$ thick CP Ni sheet sample as a function of in situ deformation. A detailed overview of the technique, the setup and the analysis methods is given.

Three-dimensional, intragranular characterisation of lattice orientation and elastic strain is essential to fully understand and analyse deformation at the micro-scale. In HETL measurements, the collected diffraction patterns are integrated through the sample thickness. To achieve through-thickness resolution, two extensions of the HETL setup were developed:

Laue Orientation Tomography (LOT): Line scans of HETL measurements are collected from a sample slice at different angular orientations around a fixed vertical axis of rotation. Tomographic reconstruction techniques are used to determine the position and shape of individual grains within the selected sample slice.

High Energy Differential Aperture X-ray Microscopy (HEDAXM): An extension of the DAXM technique (§ 2.2.4) to higher photon energies was developed. A set of wires was scanned through the diffracted beam and triangulation was used to determine the position of the scattering volume that gave rise to each reflection.

Both techniques are presented here in detail, along with the first implementations of the reconstruction methods for each. Their application to simple samples and their potential and limitations are discussed. Finally, some suggestions for future developments are made and conclusions drawn.

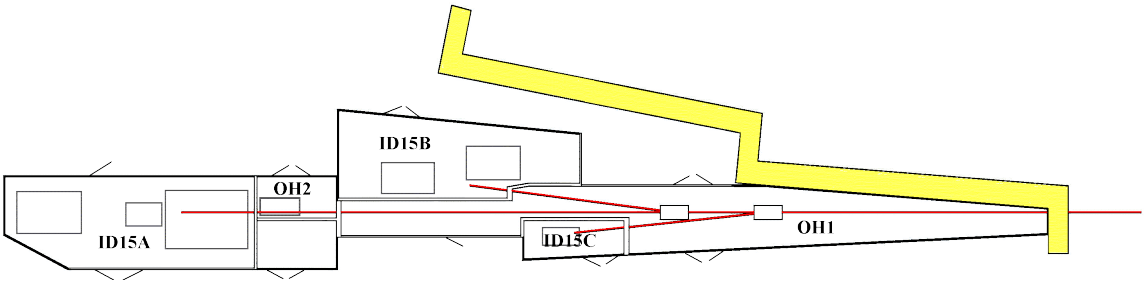

Figure 5.1: layout of the ID15 beamline, showing experimental hutches A, B and C

5.2 High energy transmission Laue (HETL) diffraction, ID15 (ESRF)

5.2.1 Experimental configuration

Beamline ID15 (ESRF) is dedicated to experiments using very high energy X-ray radiation. Three separate end stations are available (figure 5.1). ID15A can take either polychromatic or monochromatic radiation, whilst ID15B and ID15C are both equipped with monochromatic instruments. ID15A (ESRF) is ideally suited for HETL measurements.

Two different insertion devices (IDs) are available as sources on ID15, a 7 pole 1.84T asymmetric multipole wiggler (AMPW) and an in-vacuum undulator (U22). Figure 5.2 shows a plot of the flux provided by these two IDs. Due to its smooth spectrum the AMPW is the most suitable source for HETL measurements. Its critical energy is 44keV and its spectrum extends to over 600keV.

The ID15A hutch has a very flexible experimental setup with several large, heavy duty translation stages, on top of which smaller translation stages are mounted for fine adjustment. This arrangement is ideal for experimental development.

In the experiments described here, the incident beam was collimated to a size of $25 \times 25 \mu\mathrm{m}^2$ by a set of precision slits mounted in OH2. A double shutter arrangement was positioned at the entrance to the ID15A hutch to attenuate the beam between exposures. To minimise stray scatter, an anti-scatter guard was placed downstream of the shutters. The sample was mounted in a purpose-built tensile rig to allow the application of in situ loading. It is particularly important that care

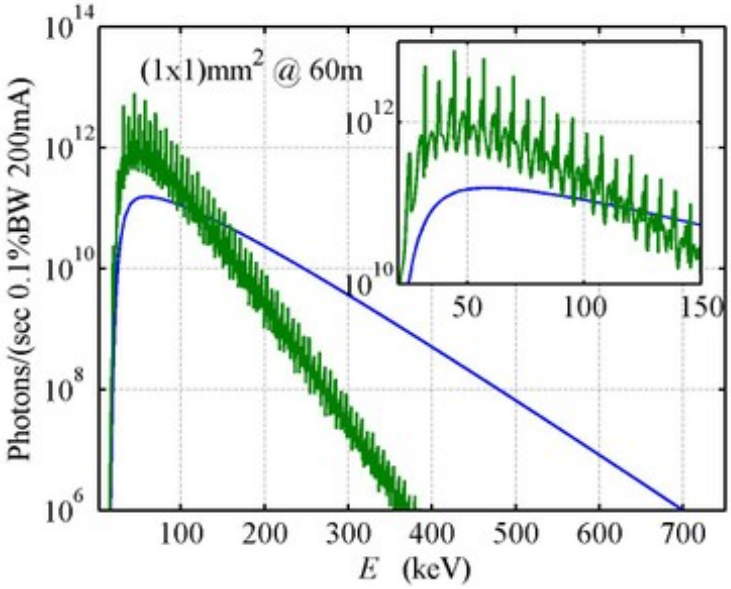

Figure 5.2: Flux from AMP wiggler (blue, smooth) and U22 undulator (green, multi-peaked) through a $1 \times 1\mathrm{mm}^2$ pinhole $60\mathrm{m}$ from the source.

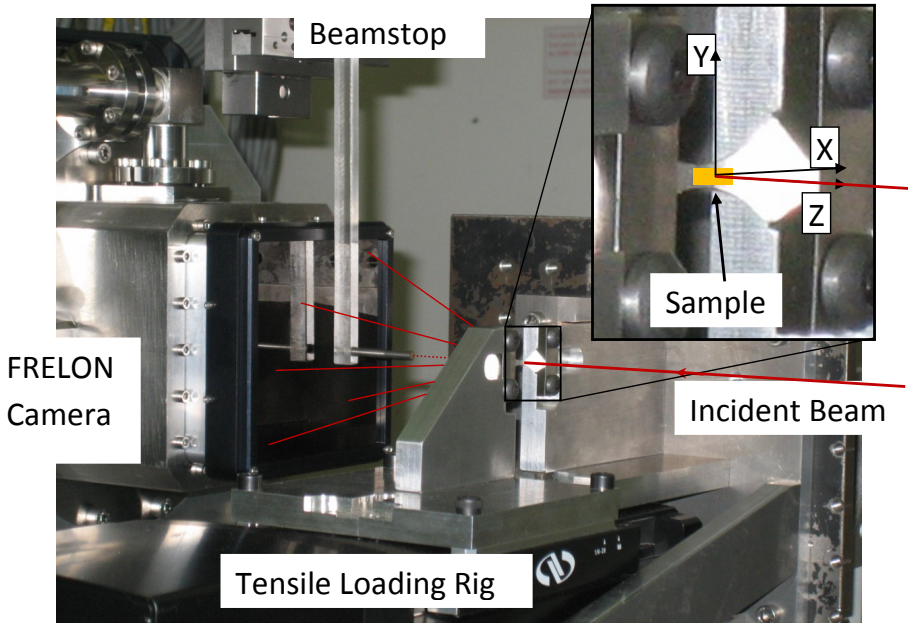

Figure 5.3: detailed view of the sample and detector arrangement during the HETL measurements on ID15 (ESRF).

be taken in the alignment of the rig and the translations, to minimise movement of the sample along the beam as it is translated horizontally or vertically across the beam.

A scintillator of $96.64\mathrm{mm}$ side length, coupled to a FReLoN camera by a fibre optic taper was mounted in transmission geometry $106.7\mathrm{mm}$ downstream of the sample. The greatest angular acceptance of this detector was $32.6°$. A tungsten rod was mounted close to the detector as a direct beamstop.

5.2.2 Sample and loading

A Ni dogbone sample was cut from a $300\mu\mathrm{m}$ thick, rolled, commercial purity Ni sheet. After machining, the sample was annealed to induce re-crystallisation and grain growth (following the procedure in appendix A.1.2). Grains in the sample ranged in diameter from $0.2\mathrm{mm}$ to $1\mathrm{mm}$, with most grains extending through the thickness of the specimen. Hence, to a first approximation, the sample could be treated as having a two-dimensional microstructure with only small variations through thickness. Figure 5.6 c) shows an optical micrograph of the central gauge region of the sample. A number of growth twins are clearly visible, that are typical of highly annealed CP Ni.

Three load increments were applied to the sample. Macroscopically they corresponded to the elastic limit, 1.2% and 2.4% plastic strain.

5.2.3 Calibration and data interpretation

Distortion correction

X-ray area detectors with scintillators coupled to a CCD by a fibre optic taper generally have a certain amount of distortion. It is vital that this is accounted for and corrected. Distortions arise due to the imperfect mapping of positions on the scintillator to position on the CCD by the fibre optic taper. In the FReLoN camera pixel positions in some regions of the detector were as far as 20 pixels or $0.94\mathrm{mm}$ removed from their nominal position. Distortion correction was carried out based on detector images of an absorbing mask with circular apertures of $0.75\mathrm{mm}$ diameter,

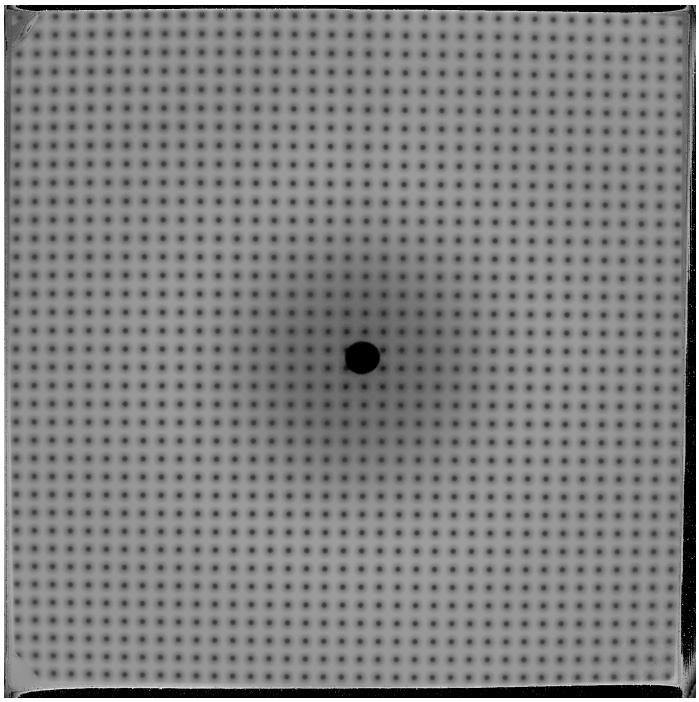

Figure 5.4: Detector image of the absorbing mask used to correct for detector distortion. The image was normalised against the flux present in the absence of the absorbing mask.

precisely positioned in a regular array with a spacing of $2.5\mathrm{mm}$. This mask was positioned directly in front of the scintillator and illuminated by a point source $1.5m$ upstream of the detector. Figure 5.4 shows a detector image of the absorbing mask, normalised against the incident intensity without the mask. A fourth order polynomial was used to re-map the recorded aperture positions to their nominal positions. In the centre of the image a circular shadow from the primary beam-stop can be seen. Here the distortion correction was interpolated between the surrounding aperture positions. This is acceptable since in the HETL images this region of the detector will be shadowed by the beamstop.

Calibration of geometrical parameters

Calibration of the experimental geometry was based on the Laue patterns of a $300\mu\mathrm{m}$ thick Si wafer placed at the sample position. Initially a coarse estimate of the geometrical parameters was found by triangulation using different detector positions. Then the detector and sample position were fixed and the geometrical parameters successively refined until a good match was found. Figure 5.5 shows

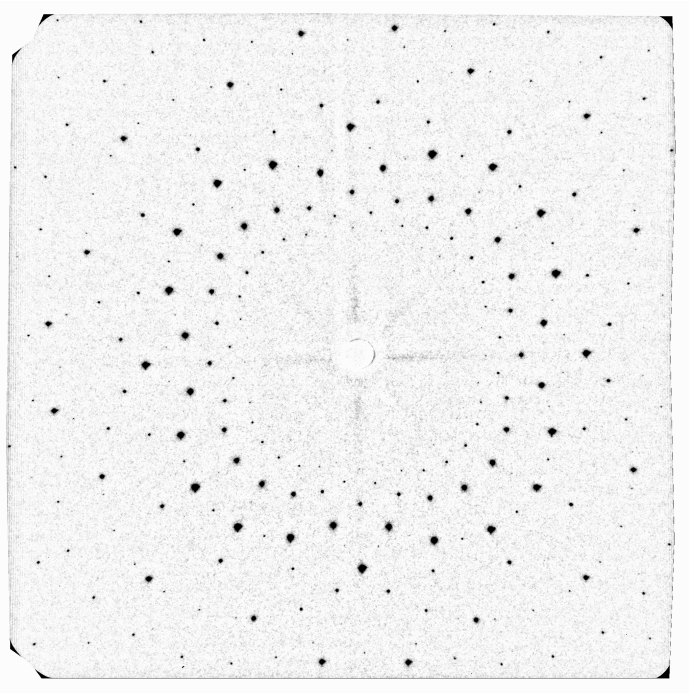

Figure 5.5: Si single crystal wafer calibration pattern. 205 reflections were indexed for the photon energy range from 50 to 150 keV.

the background-subtracted Si calibration pattern. In the photon energy range from 50 to 150 keV a total of 205 reflections could be indexed. The greatest positional deviation of any Laue peak from the predicted position was 2.2 pixels. The mean deviation from the ideal position was 0.833 pixels. Assuming the Si crystal to be perfect, the largest peak deviation provides an estimate of the quality of the distortion correction. It suggests that the maximum deviation of any pixel from its nominal position is 2.2 pixels or $100\mu\mathrm{m}$. Given the rather coarse procedure used for distortion correction, this is an acceptable value. However, this is still significantly higher than the value of $15\mu\mathrm{m}$ quoted for the MarCCD used on beamline BM32 (ESRF) (§ 3.2.5). For future HETL experiments on ID15 (ESRF) some time should be dedicated to a more careful distortion correction, especially since this characterisation procedure would only have to be carried out once for a given detector and should then remain the same.

Data interpretation

The transmission Laue detector images were processed in a number of steps. First each image was re-mapped and distortion corrected as described above.

Then background subtraction was applied to each image by median filtering (appendix A.2). Indexation and refinement of the Laue images was carried out using the XMAS software [99]. The geometrical parameters for the refinement of the patterns were taken to be those found from refinement of the Si single crystal wafer patterns. The sample-to-detector distance (dd) was adjusted at every load step to get the best agreement. This is the only parameter of the setup that can vary with sample positioning, assuming that the beam and detector positions remain the same throughout the measurement. For indexation purposes it was assumed that the photon energy spectrum extended from 50 to 150 keV. The actual incident beam spectrum in fact extends to significantly higher photon energies. However, it was found that beyond 150 keV indexation became instable. Plotting of orientation, stress and strain was carried out using dedicated Matlab scripts, as well as the MTEX Matlab toolbox [173].

5.2.4 Comparison with optical and EBSD micrographs

To validate the orientation and microstructure determined by the HETL measurements, a comparison was made with optical images of the sample microstructure and surface lattice orientation determined by EBSD. Figure 5.6 a) shows a coarse ($100\mu\mathrm{m}$ point spacing) HETL orientation map of the central region of the undeformed sample. In figure 5.6 b) a higher spatial resolution ($50\mu\mathrm{m}$ point spacing) HETL orientation map of the central $2 \times 4\mathrm{mm}$ gauge region is shown. Grain orientations in the coarse and fine HETL maps agree well. The same crystallographic features, such as grain boundaries and twin boundaries, can be identified in both maps.

Figure 5.6 c) shows an optical micrograph of the undeformed gauge region. Grain boundaries and twins are clearly visible. Comparison with the fine HETL map (figure 5.6 b)) makes it possible to identify similar features in both. The locations of grain boundaries and twin boundaries show good agreement. This is interesting, since the optical micrograph represents an image of the sample surface, whilst the HETL map corresponds to an integral measurement through the sample thickness. The comparatively close agreement confirms that, to a first approximation, it is rea-

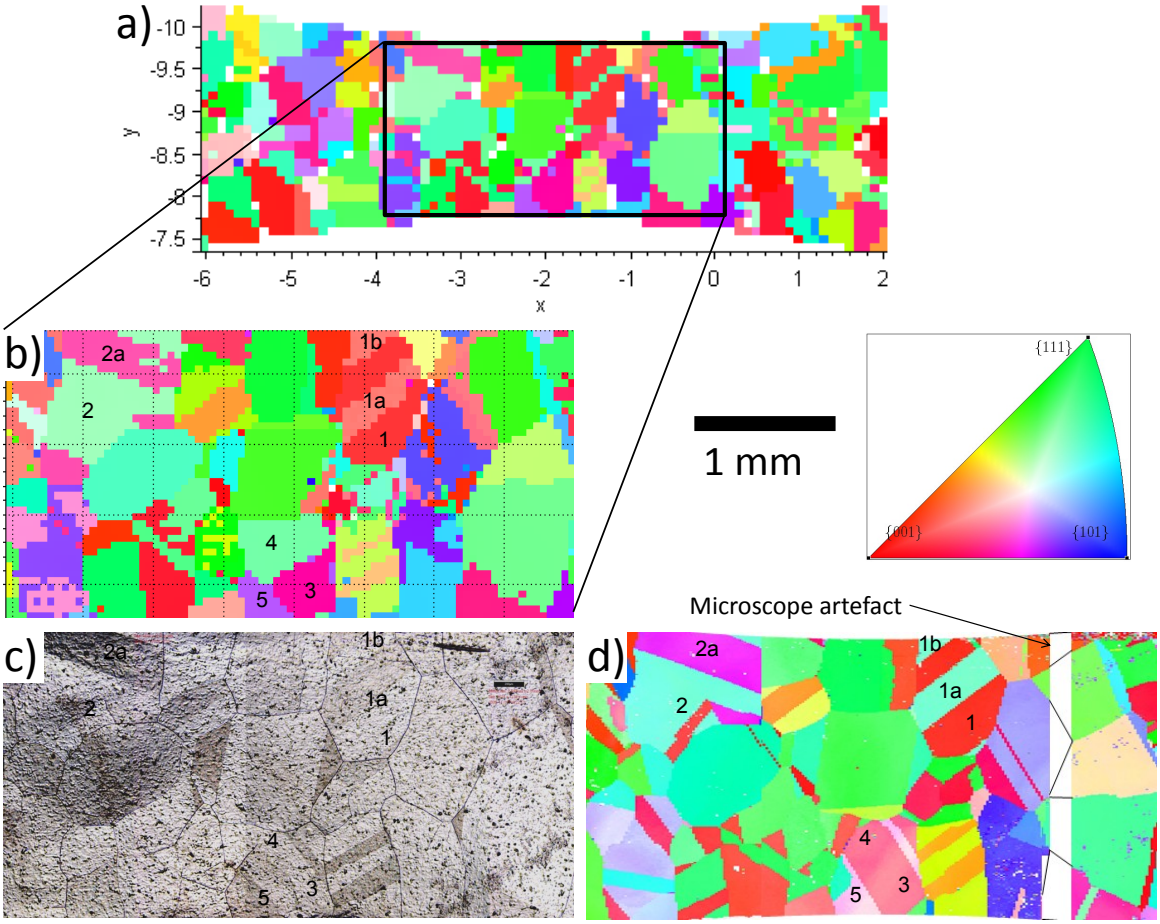

Figure 5.6: Illustration of the microstructure at the sample surface and in the bulk. a) Coarse (100μm step size) HETL orientation map of sample central region before deformation. b) Fine (50μm step size) HETL orientation map of sample gauge region before deformation. c) Optical micrograph of the sample before deformation. d) EBSD orientation map (20μm step size) of the sample gauge region after deformation. The scale bar applies to b), c) and d) and the same colour coding is used for all orientation maps.

sonable to assume that the sample has a pseudo two-dimensional microstructure with most grains extending through thickness.

Unfortunately, no facilities for EBSD measurements were available before the diffraction measurements. Figure 5.6 d) shows an EBSD map collected *after* the last deformation increment with a $20\mu\mathrm{m}$ point spacing. The missing line of data in the EBSD map was due to a microscope malfunction. Since only a modest amount of plastic deformation was imposed upon the sample, plasticity induced lattice rotations can be assumed to be sufficiently small to allow a comparison with maps of the undeformed gauge region. Agreement of the microstructure observed by EBSD and optical microscopy is excellent, as expected, given that the same sample surface was imaged. In general the grain microstructure found by EBSD agrees well with the distribution shown in the fine HETL map. In particular, the positioning of grain boundaries is consistent in both maps, whilst twin boundaries appear shifted in some of the grains. This can be explained by noting that the EBSD map reflects lattice orientation at the sample surface, whilst the HETL map shows the predominant orientation through the sample thickness. FIB sectioning of $15\mu\mathrm{m}$-thick Ni foil samples showed that grain boundaries generally run close to perpendicular to the sample surface (appendix A.1.3). Hence they have approximately the same position in both maps. Twin boundaries, on the other hand, are often inclined to the sample surface. Hence, their position in the sample plane depends on the through-thickness position considered.

For most grains the lattice orientations found by HETL and EBSD agree well, especially considering the former was recorded in the undeformed sample and the latter after the last deformation increment. In some grains, however (e.g. grain 1 and its twins 1a and 1b), a mismatch between the lattice orientations found by the two methods can be seen. Similarly, the structure of grains 3, 4 and 5 that can be clearly made out in the HETL orientation map can not be found in the EBSD map. Instead, a different grain with significantly different shape and lattice orientation is seen in their place. These differences are attributed to microstructural variations through the sample thickness.

5.2.5 Evolution of orientation and stress with deformation

Next, the evolution of lattice orientation in the gauge area measured by HETL at different deformation increments was considered. Figures 5.7 a) - d) show HETL orientation maps of the undeformed sample, deformation to the elastic limit, 1.2% and 2.4% macroscopic plastic strain respectively. In figures 5.7 e) to h) the corresponding maps of the XMAS indexation fitting errors at different deformation stages are shown. The fitting error is the average distance in pixels of the experimental peak centre position from the ideal, fitted peak centre position. In general a value of below 3 indicates an acceptable quality of indexation and a value below 1 a good indexation.

In the orientation maps, the same grains can be identified reliably at consecutive deformation increments, and lattice orientations remain very similar. This is expected, given the modest amount of plastic strain imposed upon the sample. The number of un-indexed patterns (plotted in white in the orientation maps and black in the stress maps) only increased very slightly with deformation.

It is interesting to note, that the orientations of twins 1a and 1b of grain 1 are significantly different in the undeformed sample to the other deformation steps. In fact the orientations of twins 1a and 1b shown in maps b) to d) of figure 5.7 agree well with those found by EBSD. The fitting error map for the undeformed sample shows high fitting errors for twins 1a and 1b, whilst the error is much lower for the rest of grain 1. This suggests that the observed difference in orientation is due to an incorrect indexation by XMAS in the first sample map. Incorrect orientations can generally be identified easily by considering the fitting error and the number of fitted reflections, which, in the present setup, should be in excess of 50 for nickel. The orientations of grains 2 to 10 are very similar for all deformation increments.

Figures 5.7 e) to h) show a general increase of the fitting error with deformation. This was largely due to changes in Laue spot shape and fragmentation of Laue spots with increasing spread of lattice orientation within the gauge volume. These made accurate fitting of the Laue spot centre positions more difficult. This effect was previously discussed for reflection geometry Laue measurements, § 3.1.2.

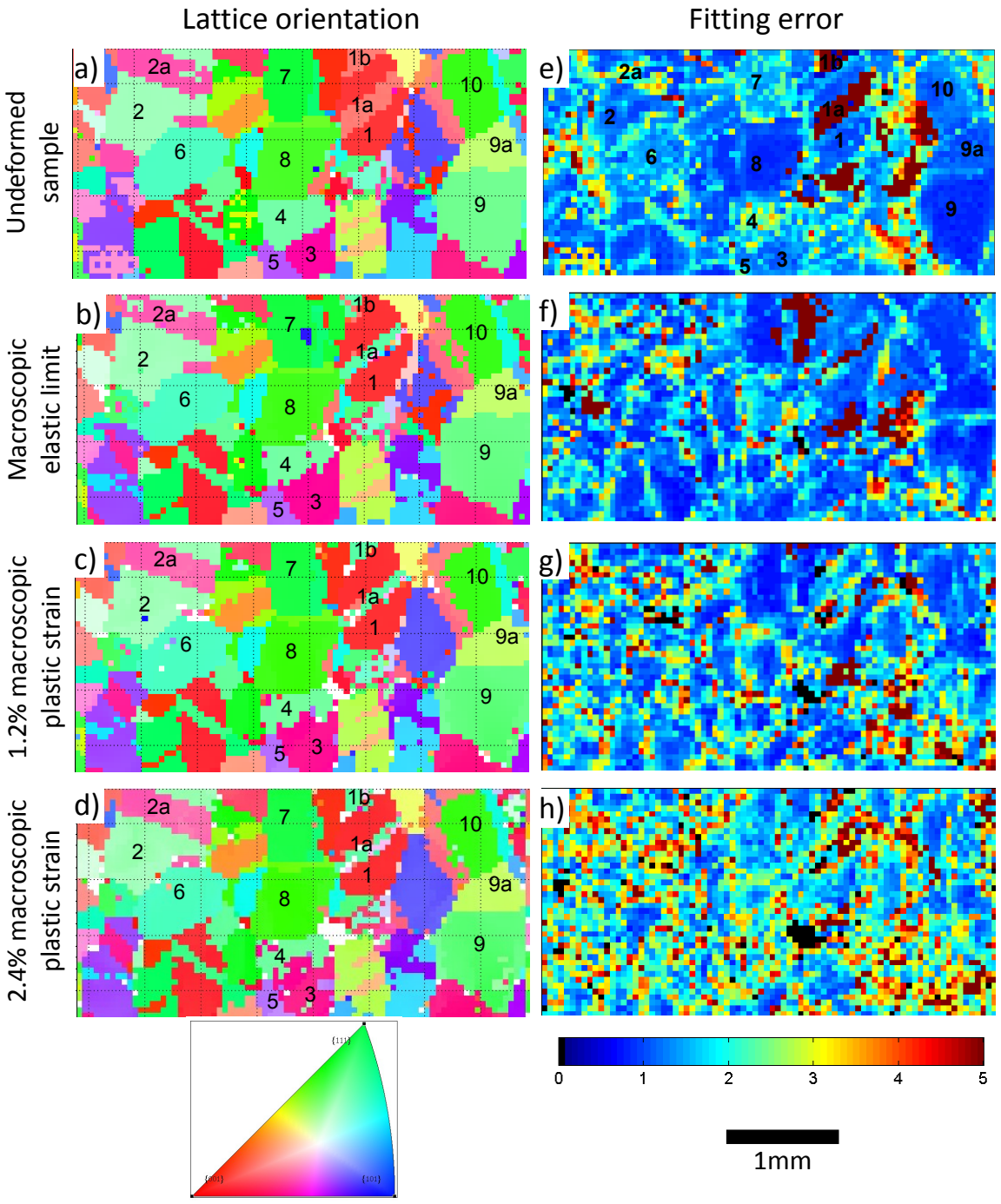

Figure 5.7: Lattice orientation in the sample gauge volume of the undeformed sample, at the macroscopic elastic limit and at 1.2% and 2.4% macroscopic plastic strain, a), b), c) and d) respectively. Fitting error in terms of the experimental peak position compared to the predicted peak position (in pixels) for the undeformed sample, at the macroscopic elastic limit and at 1.2% and 2.4% macroscopic plastic strain, e), f), g) and h) respectively.

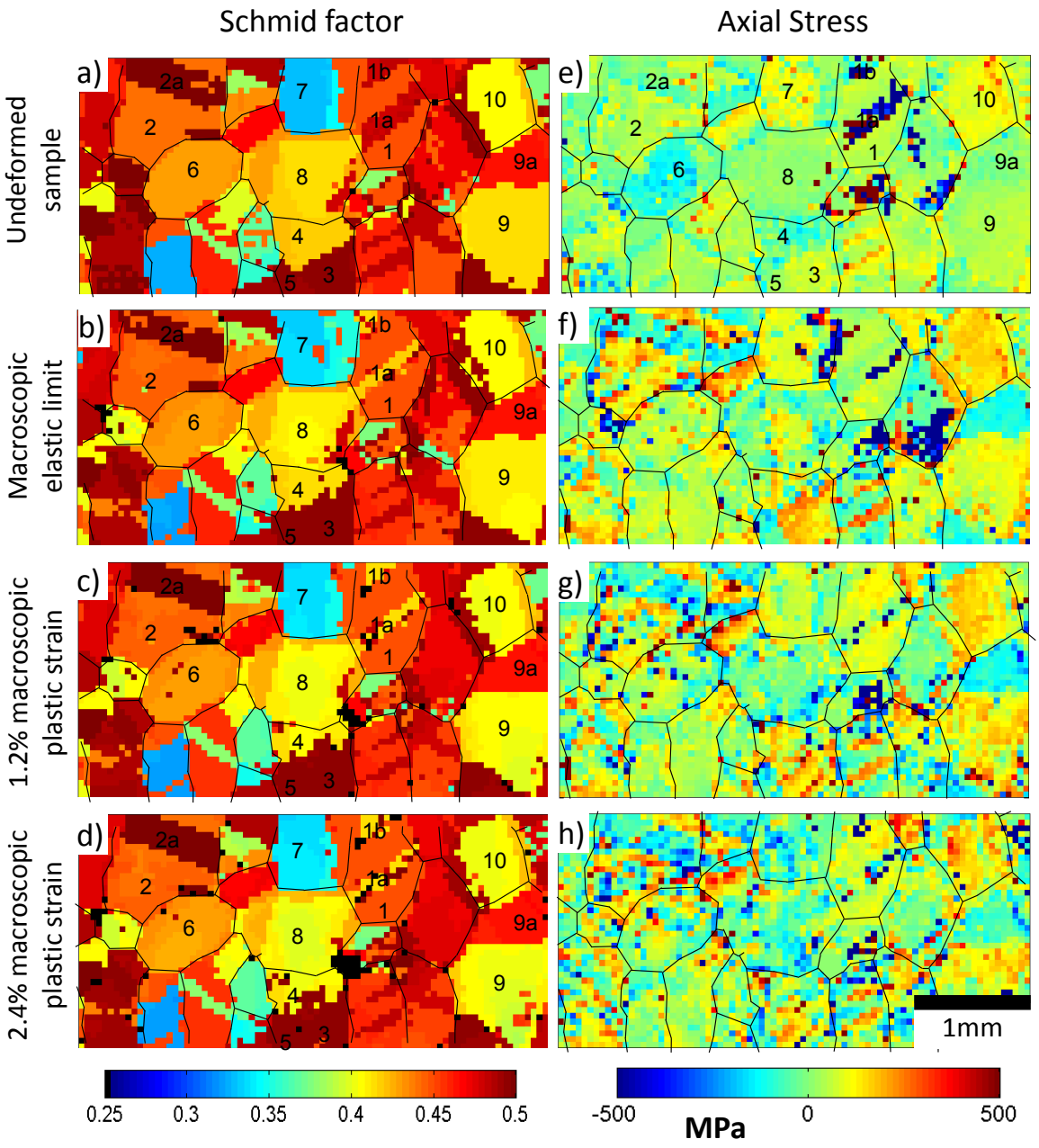

Figure 5.8: a) to d): Schmid factor maps with respect to the macroscopic loading direction for the undeformed sample, at the macroscopic elastic limit and at 1.2% and 2.4% macroscopic plastic strain respectively. e) to h): Axial stress (MPa) from XMAS refinement for the undeformed sample, at the macroscopic elastic limit and at 1.2% and 2.4% macroscopic plastic strain respectively.

Figures 5.8 a) to d) show Schmid factor maps with respect to the horizontal macroscopic loading direction. A high Schmid factor indicates that a grain is oriented favourably for slip and should appear "soft" for this loading direction. A low Schmid factor means that the grain is not favourably oriented for slip and should appear "hard". Since "hard" grains are expected to deform less readily, one would expect the lattice orientation spread within these grains to be smaller after deformation than in grains with "high" Schmid. This was previously confirmed by considering the variation of Laue reflection shape in grains with different Schmid factors (§ 3.1.2). In figure 5.8, grain 7 has a low Schmid factor. Considering the maps of fitting error in figures 5.7 e) to h), it can be seen the area corresponding to grain 7 shows a consistently lower value than the map average.

Figures 5.8 e) to h) show maps of axial deviatoric stress at the different loading increments. Superimposed are the approximate grain contours to provide an indication of the distribution of stresses with respect to the sample microstructure. The key question is whether the computed stresses are physically reasonable. Macroscopically the uniaxial yield stress for the large grained Ni samples was found to be of the order of ~ 35 MPa and the ultimate tensile stress of the order of ~ 65 MPa [191]. This suggests that the high stresses measured by HETL in some parts of the sample are not correct. Another way of assessing whether the measured stresses are reasonable is by considering equilibrium. The integrated load carried by any vertical sample section in the axial direction should correspond to the macroscopically applied load. No measurements of the externally applied load were possible in this experiment. Still, in the central, approximately parallel, gauge region of the sample, the average stress carried by each vertical sample slice in the axial direction should be the same.

Figure 5.9 shows the average stress in axial direction for vertical sample slices as a function of position along the x-axis. The blue line corresponds to the sample at the elastic limit. The red and green curves correspond to 1.2% and 2.4% macroscopic plastic strain respectively. Given that variations in the sample cross-section are comparatively small, one would expect the average stress to be approximately constant. However, it is clear that there are significant variations, with stress in

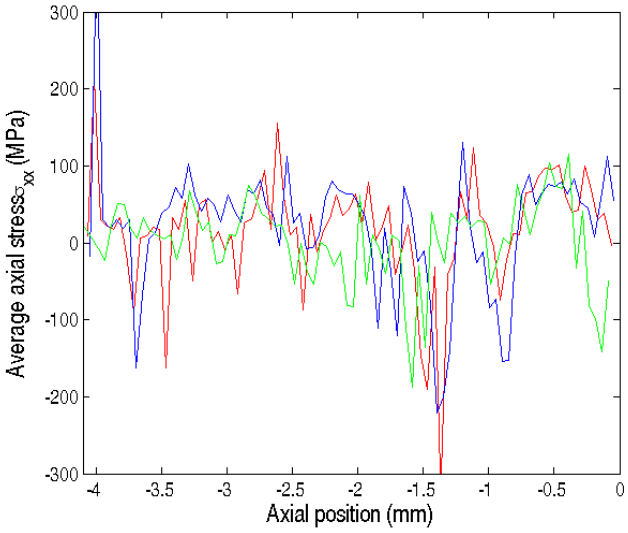

Figure 5.9: Plot of average axial stress of different samples slices in the vertical direction as a function of position in the axial direction for the first deformation step (blue line), the second deformation step (red line) and the last deformation step (green line).

some sections becoming negative. This is not consistent with the macroscopically applied tensile loading and equilibrium. Similar peaks and troughs can be identified in the stress profiles at different loading steps, suggesting that the stress determined in sample coordinates is geometry-dependant. This should certainly not be the case.

It is interesting, nonetheless, that in some cases the relative differences in the axial stress between adjacent grains appear to make physical sense. A simplistic model would suggest that during axial plastic deformation, grains with a high Schmid factor should show lower stresses than grains with low Schmid factor. In the maps in figure 5.8 this appears to be the case for the sample cross-section containing grains 9, 9a and 10. Grains 9 and 10 have a medium Schmid factor of ~ 0.4, whilst twin 9a has a higher Schmid factor of ~ 0.47. Axial stress in grains 9 and 10 is significantly higher than in twin 9a. Whilst this apparent qualitative physical agreement is encouraging, the absolute stress values measured in this experiment cannot be seen as reliable. This is most likely due to the only rather coarse detector distortion correction that was possible in the time available. A more accurate determination of the distortion correction should improve the stress accuracy significantly. It has to be acknowledged that CP Ni is a particularly difficult

candidate material for the measurement of elastic stresses, given its low yield and ultimate tensile stress.

5.2.6 Intragranular variation of orientation after deformation

Nye [179] established the direct link between local variation of lattice orientation and the density of GNDs (discussed in § 3.1.4). For the HETL measurements, a simple scheme for comparison of lattice orientation at a point to its nearest neighbours was used.

Any indexed measurement point i is characterised by a rotation matrix $\mathbf{R}_i$ that maps any vector in the crystal reference frame to the sample (laboratory) reference frame. This measurement point will have N nearest neighbours in the measurement grid, each associated with a rotation matrix $\mathbf{R}_{i,n}$. Misorientation between the measurement point and the n^{th} nearest neighbours can be captured by a reorientation matrix $\mathbf{R}_{dif,i,n}$, defined as:

$$\mathbf{R}_{dif,i,n} = \mathbf{R}_{i,n}^{-1}\mathbf{R}_i. \tag{5.1}$$

$\mathbf{R}_{dif,i,n}$ maps any direction in crystal coordinates of the measurement point i to the crystal reference frame of the n^{th} nearest neighbour. By expressing $\mathbf{R}_{dif,i,n}$ in terms of the Rodriguez vector, $\hat{\omega}_{dif,i,n}$ and Rodriguez angle, $\theta_{dif,i,n}$ (see appendix A.4 for definition), the angular orientation change between the measurement point i and its n^{th} nearest neighbour can be easily assessed.

A simple means of defining the misorientation of the measurement point with respect to all its neighbours is as follows:

$$\bar{\theta}_{dif,i} = \frac{\sum_{n=1}^{N} f_{i,n}\theta_{dif,i,n}}{\sum_{n=1}^{N} f_{i,n}}, \tag{5.2}$$

where $f_{i,n}$ is an indicator flag that is 1 if the n^{th} neighbouring measurement point is suitable for the computation of local misorientation and 0 if it is not. Two cases for $f_{i,n} = 0$ can be considered:

- If the n^{th} neighbouring measurement positions could not be indexed, it should be disregarded. This is particularly the case for measurement points at the edge of the map.

- If the change in orientation, $\theta_{dif,i,n}$ is greater than a certain threshold, θ_{thr}, it should be disregarded. This makes it possible to distinguish between the large rotations which occur at grain boundaries due to different lattice orientations in the two grains and the small misorientations which occur within grains during plastic deformation. Generally the latter are of greater interest.

Two cases can occur where it is not possible to compute local misorientation:

- If a given measurement point does not have any nearest neighbours suitable for the computation of lattice misorientation, i.e. $\sum_{n=1}^{N} f_{i,n} = 0$.

- The diffraction pattern at the reference point could not be indexed, i.e. $\mathbf{R}_i$ is not available.

In both these cases the points were marked as outliers (black in figure 5.10).

In the HETL measurements the measurement points were placed on a square grid, i.e. each measurement point in the map had four nearest neighbours. Figure 5.10 shows a map of $\bar{\theta}_{dif,i}$ after 2.4% macroscopic plastic strain. The acceptance threshold was set to $\theta_{thr} = 4^{\circ}$, which should be sufficiently large to include any intragranular rotations for the modest plastic strain applied, but discriminate against different orientations of neighbouring grains. The colour scale is given in degrees. Points at which $\bar{\theta}_{dif,i}$ exceeded the maximum value of the colour scale are plotted in white, whilst any points where $\bar{\theta}_{dif,i}$ could not be computed are shown in black. Superimposed are approximate grain boundaries.

Figure 5.10 clearly shows the presence of a number of bands of high misorientation between measurement points. The orientation of these bands varies from being almost perpendicular (grain 8) to forming an angle of $\sim 30^{\circ}$ (grain 2) with the macroscopic loading direction. Interestingly, the presence of high lattice misorientation does not seem to be confined to high Schmid factor grains (figure 5.8 a) to d)). Grain 7, with a low Schmid factor, shows only little intragranular misorientation.

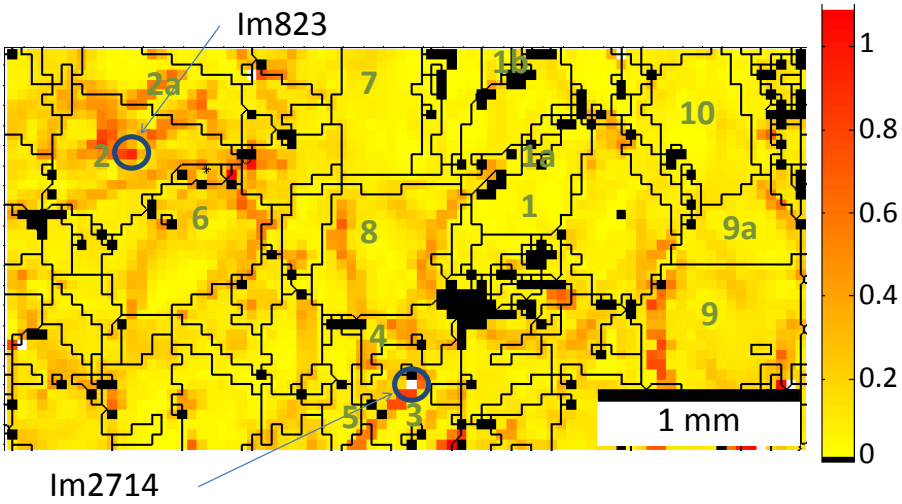

Figure 5.10: Plot of local average misorientation $\bar{\theta}_{dif,i}$ after the last deformation increment. The colorbar shows misorientation in degrees. Two measurement points of particularly high misorientation are highlighted. In grain 2 this corresponds to diffraction pattern "Im823" and in grain 3 to pattern "Im2714".

This is consistent with the very sharp Laue peaks found in the diffraction patterns from this grain. Grains 8 and 9 have a medium Schmid factor of 0.41. Both show significantly higher degrees of lattice misorientation than for example the higher Schmid factor twin 9a. This suggests that the formation of high local orientation gradients not only depends on lattice orientation, but also importantly on the local grain neighbourhood [107, 201].

One can also note, considering grain 2 and its twin 2a, that bands of high misorientation can be transmitted across twin boundaries and, to a lesser extent, across grain boundaries (grains 2 and 6).

By computing the rotation gradient within individual grains, the Nye dislocation density tensor could be found [202]. However, because the measurements presented here are two-dimensional, only three components of the total of six components of the dislocation tensor could be found. Furthermore, the Nye tensor determined this way would be an average through the sample thickness. Although the potential exists to find the Nye tensor by comparing misorientations, it was viewed to be beyond the scope of this particular study. Note that the broadening and deformation of the collected Laue patterns provides in itself information about lattice misorientation. This is discussed in the next section.

5.2.7 Misorientation within the scattering volume after deformation

In some areas of the local misorientation map in figure 5.10, particularly high local misorientations of neighbouring patterns with $\bar{\theta}_{dif,i} > 1^{\circ}$ could be seen. Two of these areas were selected for closer study of the orientation spread within the scattering volume. In figure 5.10 they are marked as "Im823" and "Im2714" in grains 2 and 3 respectively. This corresponds to the filenames of the Laue diffraction patterns collected in these locations in the map of the sample after the last deformation increment.

Gupta et al. [203] described a template-matching approach for the indexation of low quality Laue patterns. Experimental Laue patterns are indexed by matching to a set of predicted Laue spot positions, the template. Once the experimental pattern has been indexed, a least squares refinement of the experimental and predicted Laue spot positions can be used to find the exact orientation of the sample crystal. To study the local misorientation within the scattering volume, they propose the matching of templates generated on a fine grid of angular variation about the average lattice orientation found from indexation.

For the HETL measurements, initial indexation and refinement of the microbeam Laue patterns was carried out using the XMAS software. This provides the average crystal orientation of each sampling volume, $\mathbf{R}_i$. To map the misorientation within the scattering volume, small rotations θ_x, θ_y and θ_z about the x, y and z crystal axes respectively were applied to the crystal axes before rotation $\mathbf{R}_i$. Then, the forward computation of predicted Laue diffraction spot positions was carried out and the match with the experimental pattern assessed. Hence, an intensity map of the Laue pattern match in terms of the three small rotations was built up.

Given that for small rotation angles Rodriguez vector is additive (as shown in appendix A.4), the compound Rodriguez vector due to θ_x, θ_y and θ_z was $\hat{\omega}_{xyz} = (\theta_x, \theta_y, \theta_z)/|(\theta_x, \theta_y, \theta_z)|$. The Rodriguez angle, θ_{xyz}, was given by $\theta_{xyz} = |(\theta_x, \theta_y, \theta_z)|$. Using $\hat{\omega}_{xyz}$ and θ_{xyz} the compound rotation matrix, $\mathbf{R}_{xyz}$ capturing small rotations θ_x, θ_y and θ_z was determined. The overall rotation matrix, $\mathbf{R}$ of the crystal was

given by:

$$\mathbf{R} = \mathbf{R}_i \mathbf{R}_{xyz}. \tag{5.3}$$

Based on $\mathbf{R}$, the Laue ray tracing framework presented in appendix A.3 was used to predict the Laue diffraction spot positions, $\mathbf{P}$, in detector pixel coordinates. The geometrical parameters used for the ray tracing were found from refinement of silicon calibration patterns. Next, a correlation coefficient C was defined as:

$$C(\theta_x, \theta_y, \theta_z) = \sum \mathbf{I}(\mathbf{P}). \tag{5.4}$$

Here the sum was taken over all reflections for which the forward prediction was carried out, and $\mathbf{I}(\mathbf{P})$ was the intensity value of the pixel at position $\mathbf{P}$ within the Laue image. The correlation coefficient was evaluated over a range of θ_x, θ_y and θ_z values.

Initially this scheme was applied to the background-subtracted Laue images. However, it was found that the correlation coefficient in this case could be dominated by a small number of very bright peaks, i.e. if the bright peaks were well matched a high correlation coefficient was achieved, even if the majority of lower intensity peaks were not well matched. A similar difficulty was reported by Gupta et al. [203]. To avoid this problem they binarised the images, setting pixels within a reflection to 1 and outside to 0. However, with this approach some of the orientation details are lost. As a compromise an upper cut-off was imposed on the reflection intensity. This was here chosen as 50 counts. Any pixels with higher counts were assigned the cut-off value of 50.

Figure 5.11 a) shows the experimentally collected Laue pattern "Im823". Reflections in the pattern show a dumbell type structure, consisting of a two intense spots linked by a weaker streak. The four-dimensional plot of lattice orientation spread for "Im823" is shown in figure 5.11 b). In this plot the spatial position of each point indicates the corresponding θ_x, θ_y and θ_z values. The colour coding reflects the magnitude of $C(\theta_x, \theta_y, \theta_z)$ at this location. This "cloud" provides a means of displaying the four-dimensional dataset. For each angle, the angular range from -3° to $+3^\circ$ was explored.

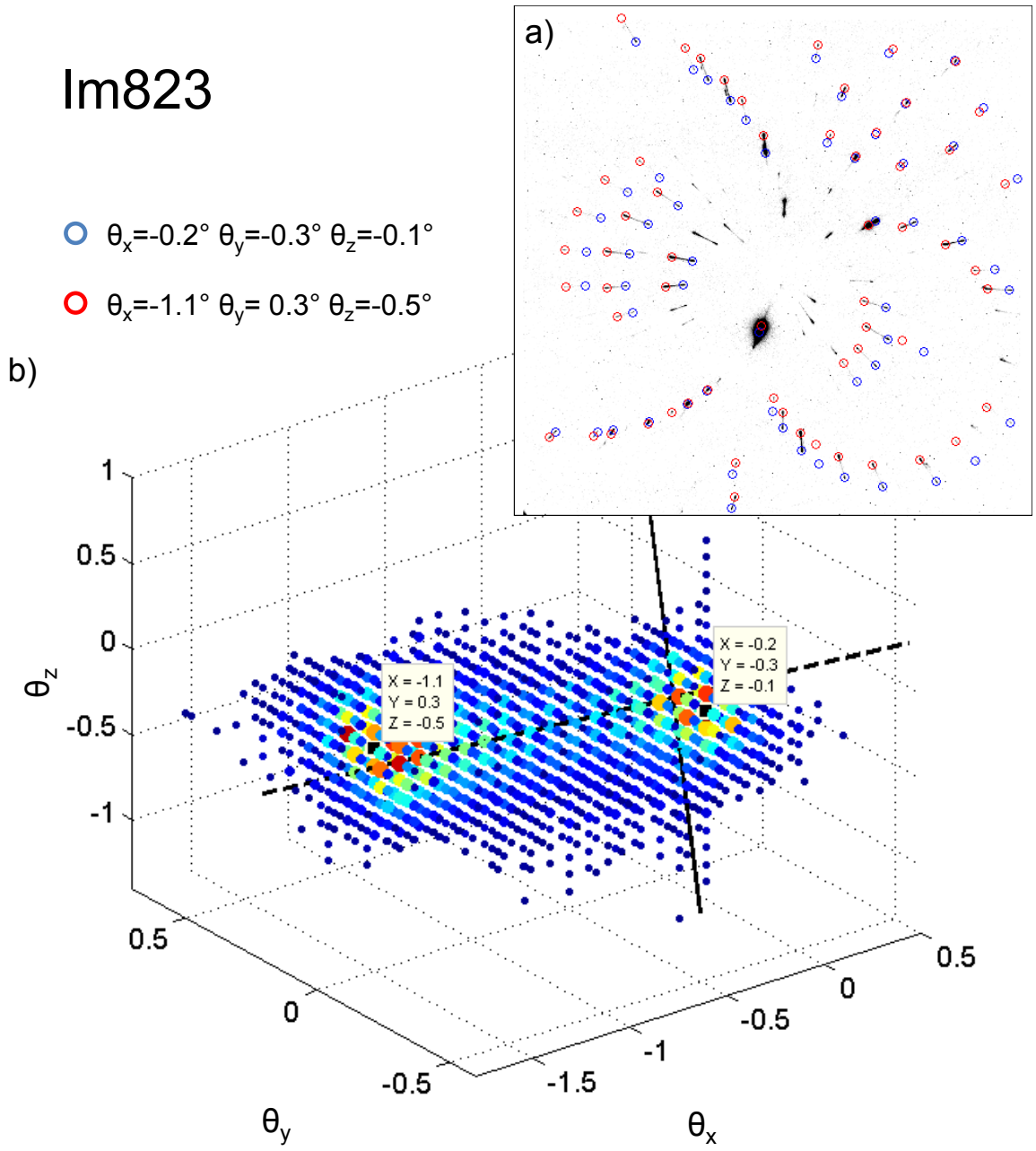

Figure 5.11: Illustration of the misorientation spread in the scattering volume at position "Im823" after the last deformation increment. a) Experimentally collected Laue diffraction pattern with superimposed predicted reflection positions. b) Four-dimensional orientation plot of "Im823". Small rotation angles θ_x, θ_y and θ_x are given in degrees. Superimposed are the predicted rotation axes for the highest Schmid factor slip system $(\bar{1}\bar{1}1)[\bar{1}10]$ (solid line) and for the $(\bar{1}\bar{1}1)[0\bar{1}\bar{1}]$ slip system (dashed line).

The orientation plot clearly reflects the dumbell shape of the reflection in the experimental Laue pattern. It has two maxima of correlation coefficient, one at $\theta_x = -0.2°$, $\theta_y = -0.3°$ and $\theta_z = -0.1°$ and the other at $\theta_x = -1.1°$, $\theta_y = 0.3°$ and $\theta_z = -0.5°$. Here rotations θ_x, θ_y and θ_z are given in the crystal coordinates and with respect to the indexed lattice orientations. The predicted Laue diffraction spot positions for these two maxima were computed and then superimposed on the experimental Laue pattern in figure 5.11 a). As expected, the predicted Laue spot positions lie on the two intense spots at either end of the experimentally found Laue streaks. This forward calculation provides a useful check of the correctness of the four-dimensional orientation plot.

The angular separation between the two correlation coefficient maxima is $1.2°$ about the $[-0.9, 0.6, -0.4]$ crystal axis. This axis could be approximated as $[\bar{2}1\bar{1}]$ (dashed line in figure 5.11 b)). Assuming that GND distribution is dominated by edge dislocations propagating on the active slip system [125, 127], the expected rotation axis can be found by taking the cross product of the slip plane normal, $\hat{\mathbf{n}}$, and the slip direction, $\hat{\mathbf{s}}$. In this case the observed streaking with rotation about the $[\bar{2}1\bar{1}]$ axis corresponds to lattice rotation due to an active slip system with plane normal $\hat{\mathbf{n}} = (\bar{1}\bar{1}1)$ and slip direction $\hat{\mathbf{s}} = [0\bar{1}\bar{1}]$. Given the macroscopic $[100]$ loading direction in lab coordinates, the Schmid factor for this slip system can be evaluated as 0.33. However, this is only the second largest Schmid factor slip system for this particular crystal orientation. The highest Schmid factor of 0.436 is achieved for the same slip plane normal $\hat{\mathbf{n}} = (\bar{1}\bar{1}1)$, but combined with a slip direction $\hat{\mathbf{s}} = [\bar{1}10]$. The expected rotation axis due to GNDs in this case is the $[112]$ axis (solid line in figure 5.11 b)). It is clear that it does not agree with the orientation of the of the greatest correlation factor cloud.

A similar analysis of orientation spread within the scattering volume was performed for "lm2714". Figure 5.12 a) shows the experimental diffraction pattern collected at this position. Compared to the experimental pattern "lm823" (figure 5.11 a)), a much more uniform streaking of reflections can be seen. This is confirmed by the four-dimensional orientation plot for "lm2714" (figure 5.12 b)), which shows an elongated cloud with a central core/streak of high correlation coefficient. Two

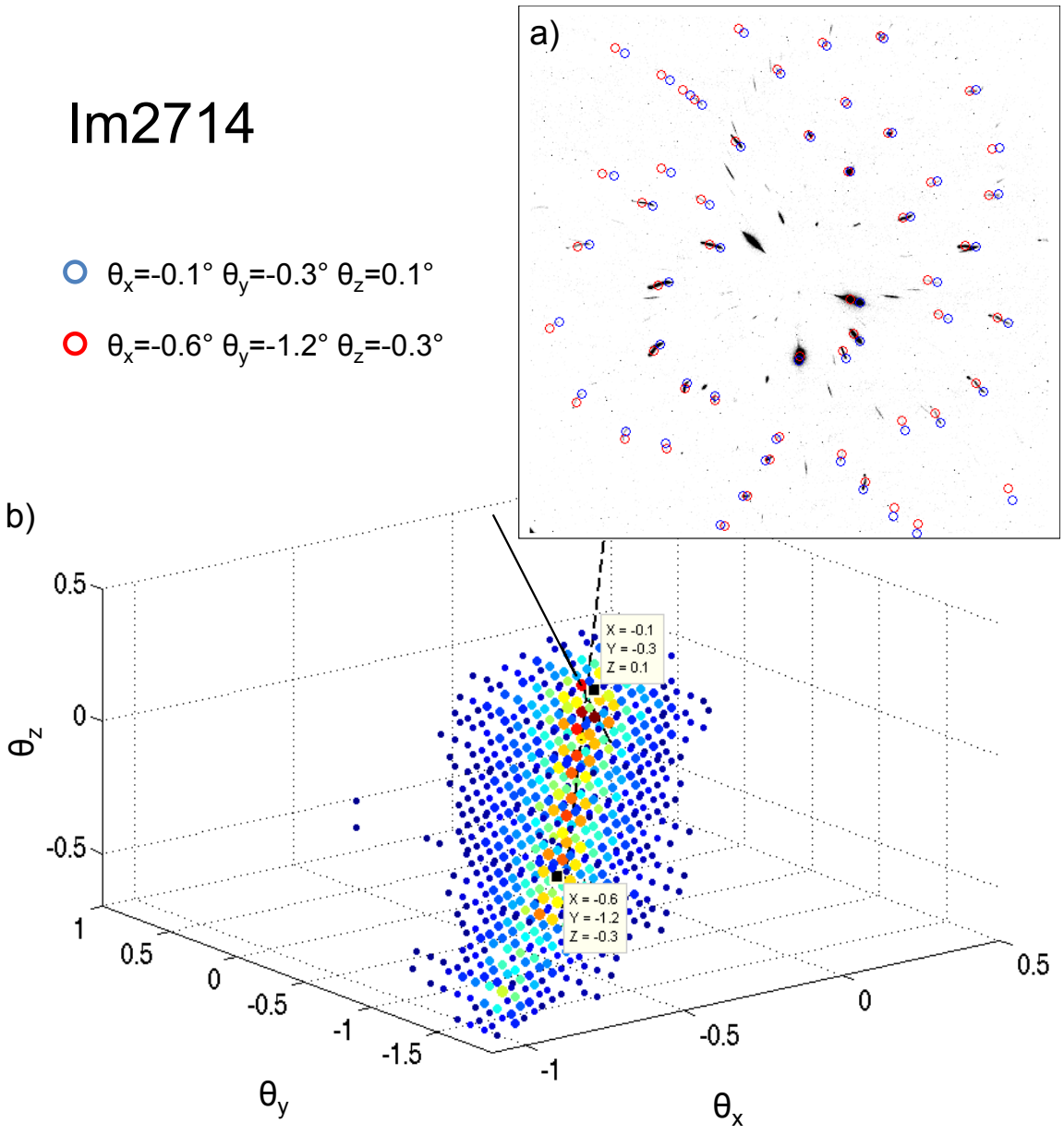

Figure 5.12: Illustration of the misorientation spread within scattering volume at position "Im2714" after the last deformation increment. a) Experimentally collected Laue diffraction pattern with superimposed predicted reflection positions. b) Four-dimensional orientation plot of "Im2714". Small rotation angles θ_x, θ_y and θ_x are given in degrees. Two slip systems have the same high Schmid factor of 0.492. The predicted rotation axes for each are superimposed; $(\bar{1}1\bar{1})[\bar{1}01]$, with $[121]$ rotation axis (dashed line) and $(\bar{1}11)[\bar{1}0\bar{1}]$, with $[\bar{1}\bar{2}1]$ rotation axis (solid line)

points in θ_x, θ_y and θ_z coordinates, one at either end of the cloud, were selected. Their positions were $\theta_x = -0.1°$, $\theta_y = -0.3°$ and $\theta_z = 0.1°$ for the first point and $\theta_x = -0.6°$, $\theta_y = -1.2°$ and $\theta_z = -0.3°$ for the second. The predicted Laue reflection positions were computed for both points and superimposed on the experimental Laue pattern (figure 5.12 a)). The predicted Laue spot positions captured well the locations of the experimental Laue streaks. The angular separation between the two selected points of interest was $1.1°$ and corresponded to a rotation about the $[0.5, 0.9, 0.4]$ crystal axis. This rotation axis could be approximated as $[121]$.

Grain 3 at "Im2714" was oriented for double slip. It had two slip systems with equally high Schmid factor of 0.492, $(\bar{1}1\bar{1})[\bar{1}01]$ and $(\bar{1}11)[\bar{1}0\bar{1}]$. GNDs on the first slip system would cause lattice rotations about the $[121]$ crystal axis (dashed line in figure 5.12 b)). GNDs on the second slip system would cause rotations about the $[\bar{1}\bar{2}1]$ crystal axis (solid line in figure 5.12 b)). The orientation cloud in figure 5.12 b) is clearly aligned with the dashed line, suggesting that the increased presence of GNDs on the first, $(\bar{1}1\bar{1})[\bar{1}01]$ slip system, and hence that this is the primary, active slip system. No spreading of the reflection was seen along the solid line, suggesting that the $(\bar{1}11)[\bar{1}0\bar{1}]$ slip system was not active.

It is interesting to consider the deformation behaviour of grains 2 and 3. In grain 2 ("Im823") slip occurred on the slip system with the second highest Schmid factor. The slip system with the highest Schmid factor was not active. In grain 3 ("Im2714"), which was aligned for double slip, only one slip systems was activated. In both grains, just considering the loading applied remotely, as is the case of simple Schmid factor analysis, does not fully capture the local deformation response. Rather the active slip system is selected as a function of the local loading conditions. These turn out to be different to the macroscopically applied loading. This is likely to be due to the additional constraints provided by the grain neighbourhood. It would be interesting to see if this behaviour and the activated slip systems could be captured by a crystal plasticity model of the sample. The present data set would be eminently suitable for a such a comparison. For example a similar approach could be chosen to that used by Song et al. [191] for the modelling of the

deformation of a polycrystalline nickel sample studied by conventional micro-beam Laue diffraction (§ 3.1.2).

Based on the lattice orientation spread found from the four-dimensional orientation plots, the GND density, ρ_{GND}, on the active slip systems could be estimated using the following expression given by Nye [179]:

$$\rho_{GND} = \frac{\hat{\alpha}_{GND}}{Lb}, \tag{5.5}$$

where $\hat{\alpha}_{GND}$ is the angular change in lattice orientation in radians, L is the side length of the considered volume and b the burgers vector. In the present case it is not actually clear which dimension L should be used for the computation, given that the gauge volume has a high aspect ratio of $15 : 1$, due to the the incident beam size of $20 \times 20\ \mu\mathrm{m}^2$ and the sample thickness of $300\ \mu\mathrm{m}$. If misorientation occurred primarily perpendicular to the incident beam, the required dislocation density would be 15 times higher, than if misorientation occurred primarily through the sample thickness. This uncertainty highlights the need for the knowledge of three-dimensional distribution of lattice misorientation within the sample. The development of experimental methods for the characterisation of three-dimensional misorientation is described in § 5.3.

5.2.8 Summary

In this section, the first demonstration study of micro-beam High Energy Transmission Laue (HETL) was described. The method was applied to the investigation of a polycrystalline, $300\ \mu\mathrm{m}$ thick Ni sheet sample during in situ deformation. A number of key points can be noted:

- HETL measurements were successfully performed to study the deformation response within individual grains of thicker, polycrystalline nickel samples.
- Careful calibration and detector distortion correction were essential for the successful analysis of HETL diffraction patterns.

- Analysis of the experimental data could be carried out using well-established lower energy micro-beam Laue diffraction tools, e.g. the XMAS software package.

- Lattice orientation was successfully mapped and followed during deformation. Agreement with EBSD surface maps was very good. Errors were marginally too high for successful measurement of stresses. The most likely error source was the low quality of the detector distortion correction. This could be improved by using a detector with lower distortion and a greater sample-to-detector distance.

- Post-processing of lattice orientations in terms of intragranular misorientation between measurement points highlighted the presence of bands of increased lattice misorientation within individual grains of the Ni sample. The presence of these bands was not limited to high Schmid factor grains.

- Matching of predicted Laue patterns computed for a range of small rotation steps allowed the study of misorientation within the scattering volume. Rotation spread and the active slip system were determined. The study of two particular locations highlighted the differences in active slip system selection between grains, depending on the local grain neighbourhood. This phenomenon should be studied by comparison of the experimental dataset with crystal plasticity or discrete dislocation dynamics simulations.

5.3 Development of HETL methods for 3D characterisation

5.3.1 Motivation

In the thus far presented Laue measurements, both in the reflection and the high energy transmission case, the collected diffraction patterns provided integrated information over the sampling volume. Whilst scanning of the beam typically provides good spatial resolution in the two directions perpendicular to the beam, achieving

spatial resolution in the third direction, along the incident beam, is much more challenging.

Three-dimensional resolution is vital however, to be able to map the microstructure in the bulk of the sample and to determine the full distribution of GNDs in the volume under study (i.e. the full Nye tensor [202]). It is also needed to map the variation of the full stress and strain tensors in three dimensions. Grain shape and orientation in the bulk can be mapped using the monochromatic 3DXRD and DCT techniques (§ 2.2.5). However, both these methods rely on complex reconstruction techniques and intragranular resolution is difficult to achieve, particularly for heavily deformed samples.

In this section two different white beam approaches are proposed that constitute an extension to the HETL technique. Laue Orientation Tomography (LOT) is based on the recording of HETL line measurements at different sample rotations about a vertical axis. Considering grain specific diffracted intensity, tomographic reconstruction techniques can be used to determine the shape of the grains in the scattering volume.

High Energy Differential Aperture X-ray Microscopy (HEDAXM) is an extension to higher photon energies of the well-established DAXM method (§ 2.2.4). It uses a set of scanning wires, that are translated through the diffracted beam, to triangulate the position of the scattering volume giving rise to each reflection. Both techniques were developed at beamline I12 (DLS). In the following an overview of both methods is given and simple, illustrative applications are described. The advantages and limitations of each technique are discussed.

5.3.2 Beamline I12 (DLS)

The I12 Joint Engineering, Environmental and Processing (JEEP) beamline is a recently commissioned high energy instrument at the DLS. It is designed to deliver intense monochromatic and polychromatic X-ray beams with photon energies ranging from 50 to beyond 200 keV for powder and single crystal diffraction, imaging, tomography and small angle scattering. A particular emphasis is placed on in situ and engineering studies. This is reflected in the twin experimental hutch de-

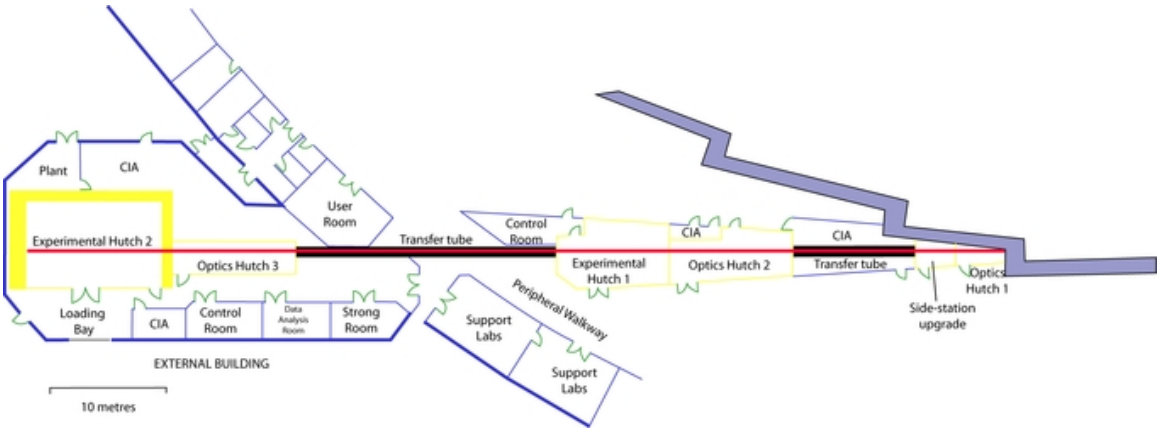

Figure 5.13: Floor plan of the I12 beamline at the DLS [204].

sign of the beamline (figure 5.13). The first experimental hutch, EH1, is located in the main DLS experimental hall. Due to its proximity to the source it provides high flux for diffraction and tomography on smaller scale samples. The second experimental hutch, EH2, is located in a separate external building. It provides space for the study of large engineering structures that could not be accommodated in EH1 and is fitted with translation stages that offer high load capacity and long travel.

The I12 source is a 4.2T super-conducting multipole wiggler. Figure 5.14 shows the predicted photon flux through a $1\times1\mathrm{mm}^2$ aperture placed at the sample position in EH1. In the unfiltered wiggler spectrum, high photon flux is present from 10 keV to well above 200 keV. To reduce heat loading on the optical elements and to provide beam hardening, a set of low energy filters (primary: two $1.1\mathrm{mm}$ chemical vapor deposited (CVD) diamond windows, secondary: $4\mathrm{mm}$ CVD SiC filter) are permanently installed at the entrance to the first optics hutch, $23\mathrm{m}$ from the source (figure 5.15). These provide significant reduction of flux at energies below 30 keV. Further attenuation of medium energies can be achieved by the introduction of copper filters, $41\mathrm{m}$ from the source, which are available in a range of different thicknesses. Their effect on the flux available at the sample position is illustrated in figure 5.14.

Further downstream at $44\mathrm{m}$ from the source a Laue monochromator is installed (figure 5.15). This will not be further discussed here, given that only white beam mode was used. Collimation of the incident beam for EH1 is achieved by a set of entrance beam slits at $17\mathrm{m}$ (BS1) and a second pair of slits at $46\mathrm{m}$ (BS2) (fig-

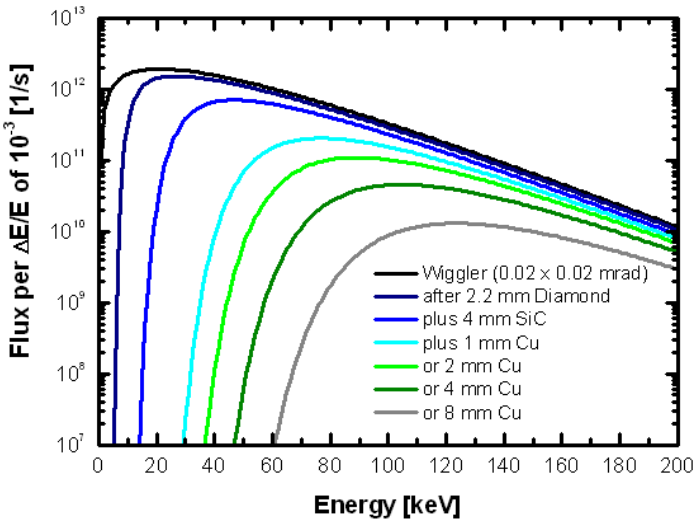

Figure 5.14: Calculated photon flux at the EH1 sample table on beamline I12 (DLS) [204].

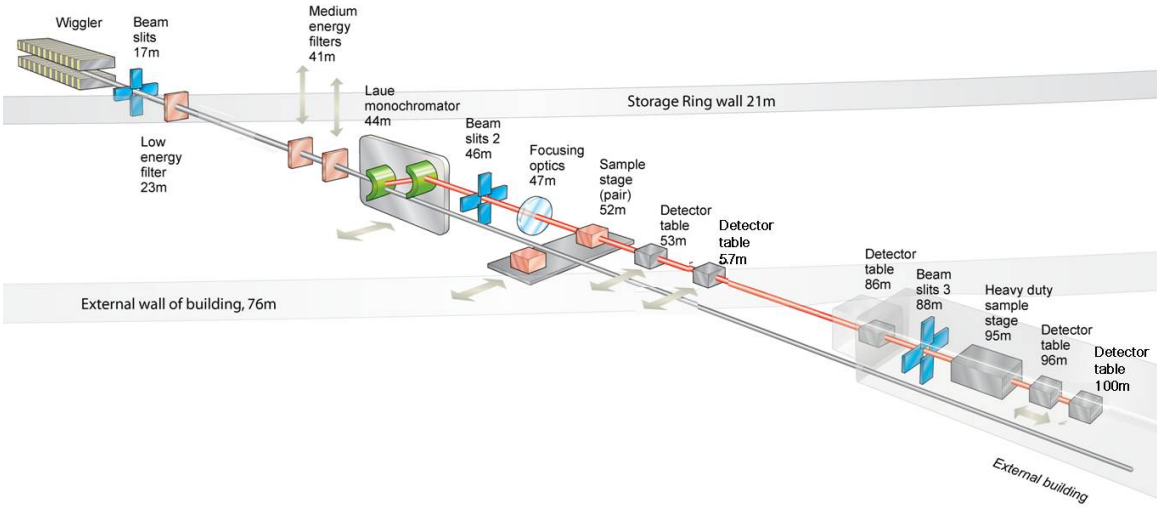

Figure 5.15: Schematic of the optics layout on beamline I12 (DLS) [204].

ure 5.15). Most of the heat loading is carried by BS1. BS2 provide final collimation with a repeatability of $2\mu\mathrm{m}$. All beam sizes quoted for I12 refer to the opening size of the of the BS2 slits. In the experiments on I12 (DLS) no focusing optics were used. To eliminate the scattering from the BS2 edges, an anti-scatter guard was mounted close to the sample.

A number of different detectors are available on I12:

- Canberra 23-element Germanium energy dispersive X-ray diffraction detector for polychromatic powder measurements.
- PCO 4000 camera for high-resolution monochromatic X-ray imaging.

- Vision Research Phantom v7.3 CMOS high speed white beam imaging detector.
- Trixel Pixium RF 4343, large area 2D detector.

The Trixel Pixium RF 4343 detector is of particular interest for micro-beam Laue diffraction. It has a large active area of $426.24 \times 426.388\mathrm{mm}^2$ which is subdivided into 2880×2881 pixels. Each pixel consists of a CsI scintillator bonded directly onto an amorphous Si substrate. This construction removes the need for tapered optics coupling of the scintillator and thereby removes the main source of detector distortion. As a result the Pixium detector has excellent pixel positioning accuracy. At present readout rates of only $0.2\mathrm{Hz}$ are achievable, due to bottlenecks that exist in the data transfer and storage system. The detector itself is capable of readout frequencies up to $30\mathrm{Hz}$ [205].

5.3.3 Laue Orientation Tomography (LOT)

In conventional absorption tomography it is not possible to distinguish between individual grains, as different lattice orientations do not provide sufficient absorption contrast. The newly proposed technique of Laue Orientation Tomography (LOT) uses tomography-style measurements. However, rather than basing reconstruction on absorption contrast, grain orientation sensitive diffracted intensity is considered. In Laue measurements, each lattice orientation gives rise to a distinct pattern of Laue spots. For a constant incident flux, the intensity of a Laue spots in the transmission configuration depends on the sample path length within the scattering crystal. Absorption reduces peak intensity, i.e. the thicker the sample the less intensity, whilst increasing the proportion of the total path length which is in the scattering crystal increases scattered intensity. In the high energy case, i.e. photon energies greater than 50keV, one can assume that scattering intensity is governed mainly by the path length of the scattering crystal, rather than the absorption effects. If this assumption is valid, then the integrated intensity of diffraction patterns from a certain orientation (measured as a line scan across the sample) provides a measure of the length of material with this lattice orientation at each point in the line

scan. This is analogous to the information about sample slice absorption provided by a detector line in the case of conventional tomography, but now with orientation sensitivity. Hence the morphology of individual grains can be reconstructed simply by using normal filtered back projection algorithms.

In the following, the details of the experimental setup and the reconstruction technique will be given. As a first trial, the method was applied to the reconstruction of grains within a polycrystalline, large-grained Ni sample. Based on this a number of refinements and improvements to the method are suggested.

Experimental setup and measurements

The experimental LOT setup was established in EH1 of beamline I12 (DLS). A schematic of the setup is shown in figure 5.16 a). The sample was mounted $573\mathrm{mm}$ upstream of the Pixum area detector in transmission geometry. The incident beam was collimated to a size of $20 \times 20 \mu\mathrm{m}^2$ using BS2 slits. Lower photon energies were filtered out by $12\mathrm{mm}$ copper filters. The direct, transmitted beam was captured by a tungsten rod beam stop mounted just upstream of the area detector. Underneath the sample, a high precision tomography rotation stage was mounted to provide ϕ rotation. On top of the rotation stage, two smaller, linear translation stages were mounted to allow the alignment of the sample with the centre of rotation. For clarity, these two translations are not shown in figure 5.16 a). Underneath the ϕ rotation stage, a linear stage aligned with the x direction was mounted to allow translation across the beam. This whole assembly was mounted on a vertical translation, aligned with the y direction (not shown in figure 5.16 a) for clarity).

Alignment of the setup was carried out in two stages. First, a single crystal Si wafer calibration sample was placed in the approximate sample position. Calibration patterns collected from this were used to determine the spatial parameters of the setup. All parameters, apart from the sample-to-detector distance, were defined by the positioning of the incident beam and the detector, and did not change during a change of sample. Next, the Ni sample under study was mounted, the slice of interest in the y direction selected, and the sample aligned with the centre of the ϕ rotation. Laue images from the sample were then recorded at different

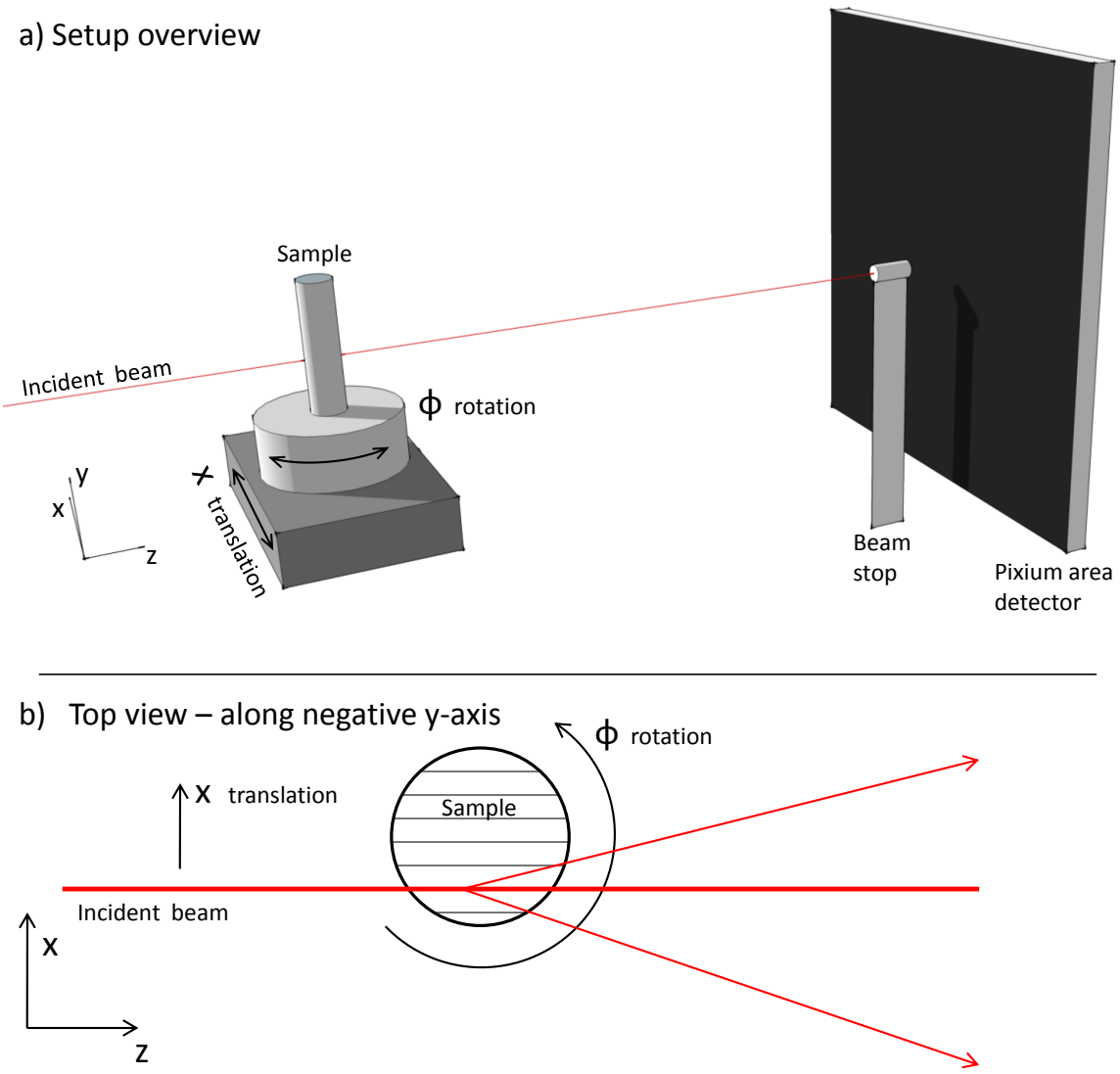

Figure 5.16: LOT setup on I12. a) Three dimensional schematic of the setup. b) Top view illustrating sample translation and rotation.

detector distances, and the exact sample-to-detector distance determined by triangulation.

In total 91 projections were considered, with ϕ angles from $0°$ to $180°$, spaced at $2°$ intervals. In the following, the notation ϕ_j will be used to refer to the sample angular position where $\phi = j°$. At each ϕ_j, a line scan of 56 measurements in the x-direction was carried out, at positions x_i, spanning a range of 1.1mm, with a spacing of $20\mu\text{m}$, that corresponded to the nominal beam size.

Reconstruction Technique

The aim of the simple reconstruction scheme described here was to recover the spatial extent and morphology of each individual grain within the measured sample slice. First, all Laue diffraction patterns at positions x_i were indexed for the line measurement at ϕ_0. Using the Rodriguez vector formulation, the angular misorientation between adjacent patterns was computed. If the angular change was greater than a certain threshold value, θ_{thr}, then the orientation was counted as belonging to a new grain. If the angular change was smaller than θ_{thr}, the orientation was counted as belonging to the same grain. With this filtering routine, a list of grain orientations, $\mathbf{R}_g$ present in the sample was computed, where g refers to the index of the grain. $\mathbf{R}_g$ maps the crystal directions in grain g to the laboratory reference frame at rotation ϕ_0.

For each grain g, it was necessary to find the diffraction spots that it produces at different rotations ϕ_j. The rotation ϕ_j about the y-axis was captured by the rotation matrix $\mathbf{R}_{\phi_j}$. Hence, the rotation matrix $\mathbf{R}_{g,j}$ which gives the orientation of grain g at angular position ϕ_j was given by:

$$\mathbf{R}_{g,j} = \mathbf{R}_{\phi_j}\mathbf{R}_g. \tag{5.6}$$

Using the Laue ray tracing framework from appendix A.3, the predicted Laue spot positions $\mathbf{P}_{g,j}$ were computed for grain g at angular position ϕ_j. The sum scattered intensity, $I_{g,j,i}$, was found as:

$$I_{g,j,i} = \sum \mathbf{I}_{j,i}(\mathbf{P}_{g,j}), \tag{5.7}$$

where $\mathbf{I}_{j,i}(\mathbf{P}_{g,j})$ denotes the intensity value of the detector image $\mathbf{I}_{j,i}$ evaluated at $\mathbf{P}_{g,j}$. The sum was carried out over all reflections from grain g.

However, it is important to note that even small misorientations within the scattering volume lead to a change in reflection position. Reading out just the intensity at a single pixel position in the diffraction image, especially if the crystal is strained or deformed, might mean that the reflection is missed altogether. For the purpose of reconstruction it is best if the entire intensity of a reflection is available. This can

be done by specifying a mask radius, r_{mask}, around each predicted pixel position within which the intensity is integrated.

Normalisation of the measurements within each line at an angle ϕ_j is essential, given that the number of reflections and thereby the absolute intensity will vary as a function of ϕ. At each projection, the total illuminated area of grain g, A_g, is constant and proportional to the line sum of the scattered intensity from grain g, i.e. $A_g \propto \sum_i I_{g,j,i}$. The normalised scattered intensity, $\bar{I}_{g,j,i}$, is hence:

$$\bar{I}_{g,j,i} = \frac{I_{g,j,i}}{\sum_i I_{g,j,i}}. \tag{5.8}$$

For grain g, $\bar{I}_{g,j,i}$ can be plotted as a three-dimensional plot of intensity as a function of ϕ and x position. This plot is analogous to the sinogram in conventional absorption tomography and will be referred to here as an origram. Taking the inverse radon transform of $\bar{I}_{g,j,i}$ for g returns the shape of the grain in the illuminated slice.

This reconstruction technique was applied to all grain orientations $\mathbf{R}_g$ identified in the indexation of Laue patterns at ϕ_0. By applying this method to the measurements of slices at different heights of the sample, the three-dimensional grain structure can be determined.

Sample

As a first trial, a highly annealed, polycrystalline nickel sample was considered. A $500\mu\mathrm{m}$ wide, $15\mathrm{mm}$ long strip was cut from a $300\mu\mathrm{m}$ thick nickel foil. It was then processed and heat treated as described in appendix A.1.2.

Figure 5.17 shows optical micrographs of the four sides of the sample. A number of grains were identified. Some extended through the thickness of the sample to give a bamboo-type structure.

Results and Discussion

Due to time constraints, only a single horizontal slice $1.92\mathrm{mm}$ below the top of the sample was measured. External micrographs of the sample at this position sug-

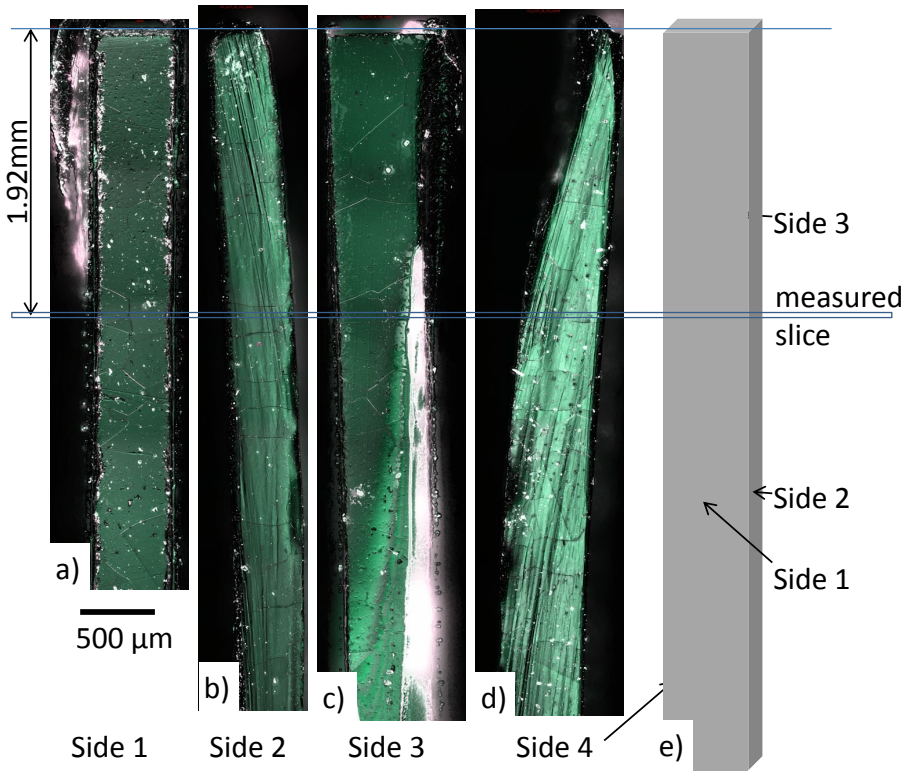

Figure 5.17: Optical micrographs recorded from four sides of the Ni sample used for the LOT demonstration. The measurement plane was located $1.92\mathrm{mm}$ below the top of the sample.

gested the presence of several grains through thickness. Based on the indexation of Laue patterns at the ϕ_0 line measurement, five grains were identified. The misorientation threshold for the recognition of a new grain was set to $\theta_{thr} = 2°$.

Figure 5.18 shows the mean orientation matrix, $\mathbf{R}_g$, at ϕ_0 for each grain, the corresponding origram and the reconstructed grain shapes. For the origram construction a radius r_{mask} of 20 pixels was used (angular acceptance of $\mp 0.28°$ in the χ direction and $\mp 0.14°$ in the θ direction). Only reflections between 2θ diffraction angles of $10°$ and $15°$ were considered. The grain shapes were computed using the inverse Radon transform function in MATLAB, "iradon", that contains an implementation of the filtered back projection algorithm.

The origram for grain 1 shows the expected smooth, half period sinusoidal variation. In some of the slices artefacts can be seen in the upper half of the origram, although these are few and faint. The reconstructed shape of grain 1 shows sharp features, with reasonably uniform intensity in the centre of the reconstructed grain shape. At the edges of the reconstruction, some blurring can be seen, with the

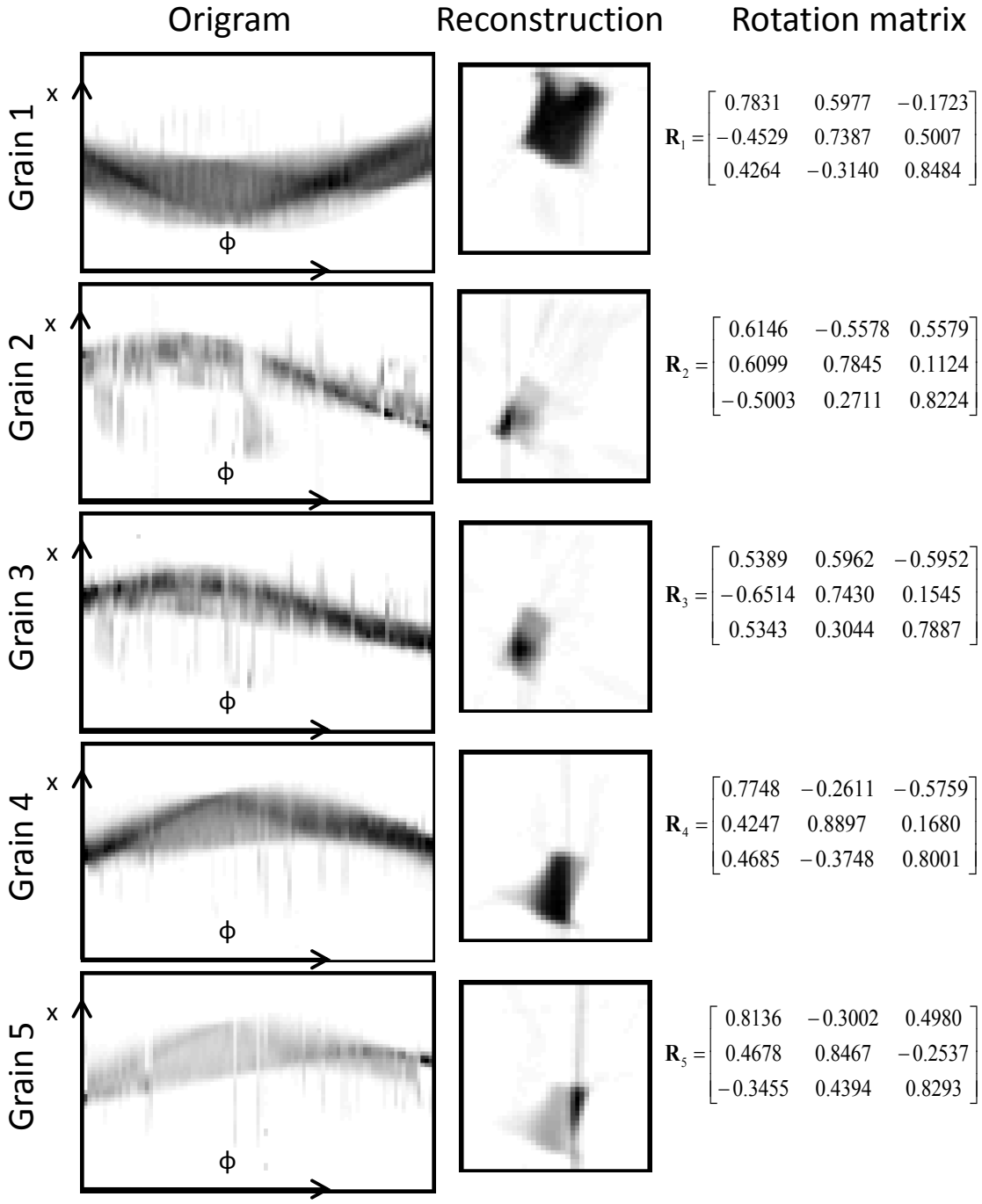

Figure 5.18: Origrams, reconstructed grain slices and rotation matrices $\mathbf{R}_g$ for grains 1 to 5.

edge spreading out over up to four pixels in places. Given the step size of $20\mu\mathrm{m}$, this corresponds to a blurring of up to $80\mu\mathrm{m}$. This might have been an artefact of the reconstruction, i.e. that reflections from the grain edge were not captured successfully due to lattice rotations. This possibility was excluded by checking the lattice rotations of indexed patterns of grain 1. They revealed that misorientation at any point within the grain was significantly below 0.1°. Alternatively, diffraction from the edges of the BS2 slits which were mounted $6\mathrm{m}$ upstream of the sample may have caused the addition of "tails" to the incident beam. An anti-scatter guard was mounted $1\mathrm{m}$ upstream of the sample to reduce these tails. However no knife edge scans were carried out to confirm the exact beam size at the sample. Origrams and reconstructions for grains 4 and 5 show similar characteristics to the grain 1 origram and reconstruction.

Grain 2 and 3 origrams showed significantly stronger artefacts. These arose from overlapping Laue peaks at some ϕ_j rotations. This was a particular problem for small grains which provided only comparatively weak Laue peaks. Even the intensity from a single, overlapping Laue peak due to a neighbouring grain was sufficient to skew significantly the intensity distribution in the origram. This explains why artefacts in the grain 2 origram are much more prominent than in the origram from grain 1 that is larger and provides a stronger diffraction signal. A possible way of reducing these difficulties would be to filter out any reflections which are close to reflections from other grains for any given ϕ_j rotation, and not to consider them in the reconstruction. Work to this end is in progress. Despite the artefacts in the origrams, the shapes of grains 2 and 3 were reasonably successfully reconstructed (figure 5.18).

Considering the reconstructions of grains 2 and 3, their complementary shape can be noticed. The high intensity area in the lower left hand corner of grain 2 fits well in shape the area of reduced intensity in the reconstruction of grain 3. Based on their orientation matrices, $\mathbf{R}_2$ and $\mathbf{R}_3$ respectively, the orientation change between grains 2 and 3 was found to correspond to a rotation by 109.5° about the $[011]$ crystal axis. This corresponds to one of the $\sum 3$ twin rotations for FCC materials [174]. Similarly, it can be found that grains 4 and 5 are twins: their orientation

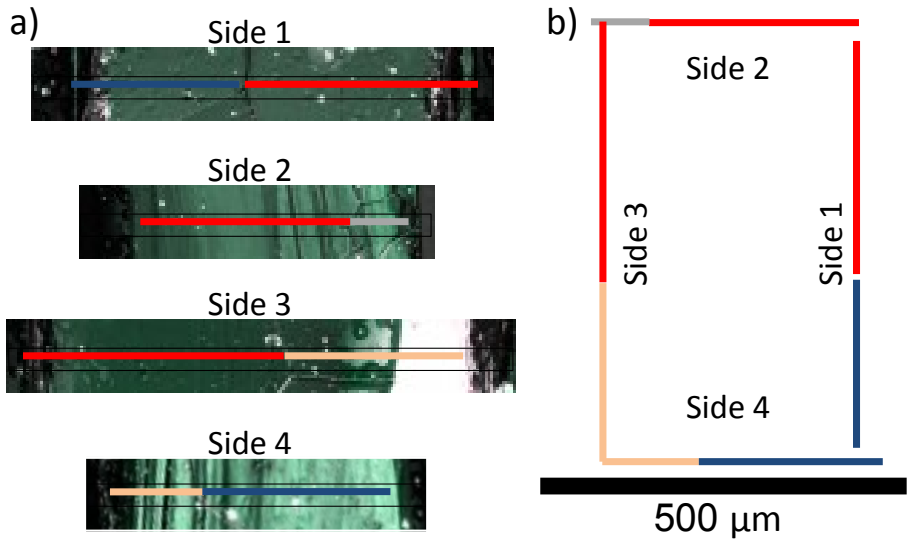

Figure 5.19: External grain shapes. a) Optical micrographs of the sample sides at the level of the reconstructed slice. Upper and lower limit of sampling volume are shown by a thin black line. b) Approximate positioning of grains at the sample surface in the measurement plane.

change corresponds to a rotation of $70.5°$ about the $[\bar{1}\bar{1}0]$ crystal axis, and their shapes are complementary. For full characterisation of the twin boundaries, the boundary normal vector is required. This could be found by the reconstruction of further sample slices at different heights.

The validation of the reconstructed grain shapes is difficult, since the reconstructed slice lies within the bulk of the material. One possibility would be to section the sample and carry out EBSD measurements on the mapped sample slice. However, technically such sectioning would be very difficult, especially without locally introducing plastic deformation which could modify the local crystal geometry and orientation.

Partial validation of the reconstructed grain shapes can be achieved by considering the externally visible grain boundaries in the optical micrographs of the sample sides. Figure 5.19 a) shows a magnified view of the micrographs at the height of the measurement plane. In each micrograph the approximate upper and lower limit of the illuminated slice are shown by a thin black line. Within these boundaries, coloured bars were fitted visually to the approximate extent of grains in each of the side views. Whilst this procedure is relatively straightforward for sides 1 and 3 that correspond to the flat, polished sides of the original Ni sheet,

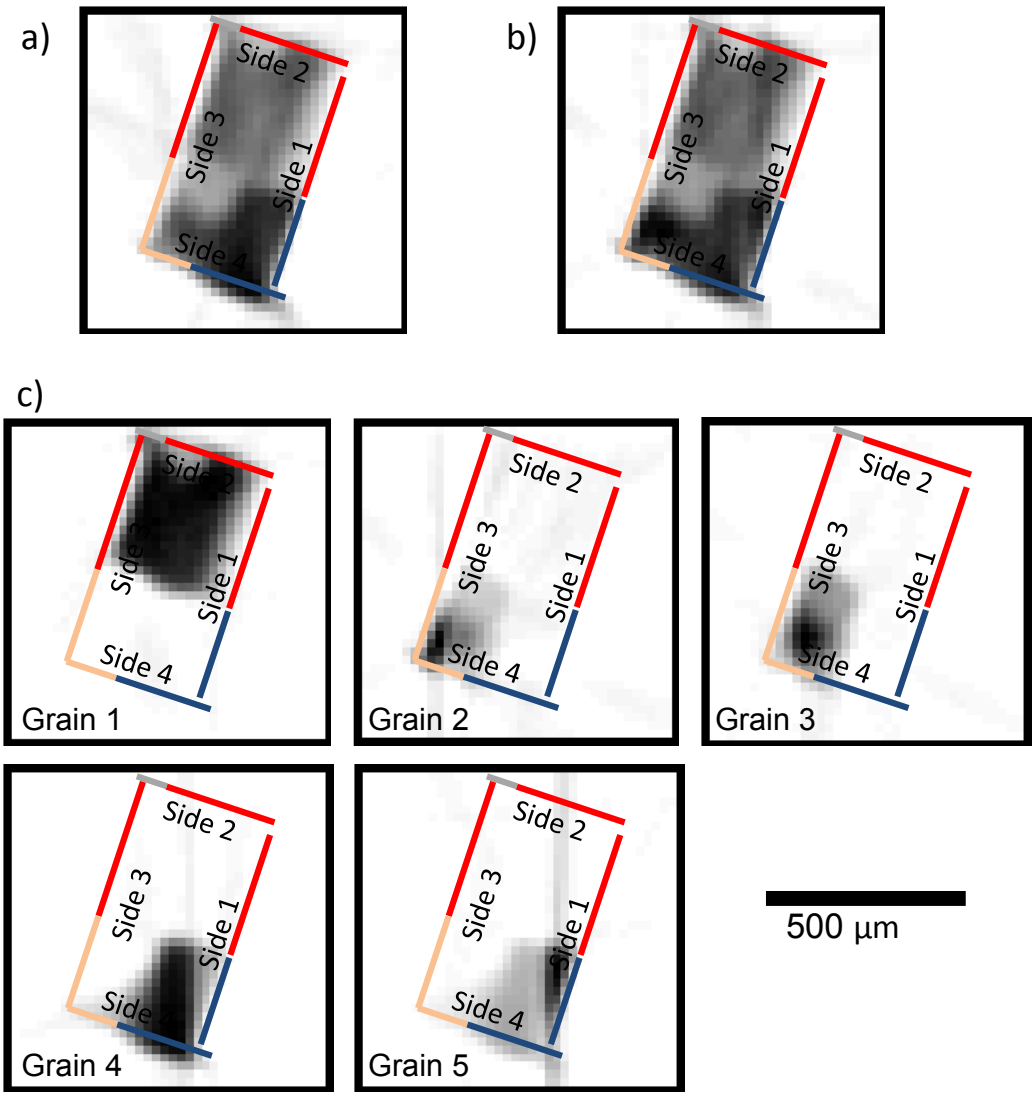

Figure 5.20: Sample and grain shape reconstructions with superimposed grain surface positions from optical micrographs. a) Whole slice reconstruction from summation of total diffracted intensity. b) Summations of the individual reconstructed grain shapes. c) Individual reconstructed grain shapes.

it is more difficult for sides 2 and 4, where additional contrast arises from grooves due to sample cutting. The colourbars can be assembled into an approximate map of grains on the sample surface (figure 5.19 b)).

Figure 5.20 a) shows a reconstruction of the sample slice, computed by the summation of the entire scattered intensity from all grains captured by the area detector. Superimposed is the grain surface position map determined from optical micrographs. The outer shape of the sample agrees reasonably well. Figure 5.20 b) shows a summation of the five reconstructed grains shown in figure 5.18. Agree-

ment with figure 5.20 a) is very good, suggesting that all the grains in the cross-section were successfully captured.

Next, the individual, reconstructed grain shapes were plotted and the optically determined surface grain positions superimposed (figure 5.20 c)). Grain 1 agrees well in terms of positioning and proportion with the red external grain shape. The combination of grains 2 and 3 (twins) fits with the location of the pink surface grain region and grains 4 and 5 (twins) occupy the blue region. This reasonable agreement of grain boundary positions at the sample surface allows partial validation of the reconstructed grain shapes. For complete validation, a comparison with a full two-dimensional map should be carried out. This could be done with a measurement just below the top surface of a polycrystalline sample. EBSD measurements on the top surface would provide a direct comparison and allow the validation of grain morphology and orientation. Based on the good agreement of previous HETL measurements with EBSD maps (§ 5.2.4), one can be reasonably confident that the lattice orientations were here determined correctly. It should be noted, that a working reconstruction in itself confirms a correct indexation, as otherwise Laue spots would not be found in their expected positions, and the scattered intensities could not be determined.

LOT limitations and refinements

In the present formulation, a number of limitations of the technique can be identified:

- Only grain shape can be determined, but not intragranular misorientation or elastic strain.
- The intragranular misorientation that the technique can cope with is limited by the angular acceptance prescribed by r_{mask}. The size of r_{mask} is limited by the need to discriminate against reflections from different grains.
- Reflection overlap causes artefacts in the origrams.
- A lengthy measurement time of 7 hours was required per slice (~ 5 s per point)

The first two points can be addressed by considering an alternative reconstruction scheme:

Rather than indexing patterns only at ϕ_0 and then forward predicting the diffraction spot positions, multi-grain indexation is performed on all collected patterns. For Laue patterns at $\phi_{j\neq 0}$, the indexed rotation matrices are rotated back to the ϕ_0 reference frame. Then a filtering of orientations is performed. Grain orientations which have a relative misorientation smaller than a given threshold are ascribed to the same grain. For the reconstruction of grain shape, the indexed reflections for each grain are used to determine diffracted intensities. This sidesteps the limited angular acceptance problem due to r_{mask}. Also each indexation will provide a measurement of the orientation and elastic strain tensor average along the line of the incident beam. Next these quantities are rotated back to the ϕ_0 reference orientation. By multiplying them by the sample path length, it should be possible to apply the inverse Radon transform, to reconstruct each component in turn. This is similar to the "strain tomography" method recently developed by Korsunsky et al. [206]. The implementation of this improved reconstruction framework is currently under way, but is beyond the scope of this thesis.

The time required by these measurements could be significantly reduced by improving data transfer and storage rates. Given the maximum detector frame rate of 30 frames/s and an exposure time of 0.1 s, a frame rate of 7.5 frames/s could be achieved. This would reduce the collection time per slice to 11 minutes, making the mapping of larger volumes feasible.

5.3.4 High Energy DAXM (HEDAXM)

An alternative approach to LOT for achieving three-dimensional spatial resolution in HETL measurements is to extend the differential aperture X-ray microscopy (DAXM) method to higher photon energies.

A detailed overview of the DAXM technique, the analysis routines required and its applications was given in § 2.2.4. The key concept is that a wire is scanned between the sample and the detector, close to the sample surface. By triangulating using the reflection position on the detector, the wire position when the reflection is

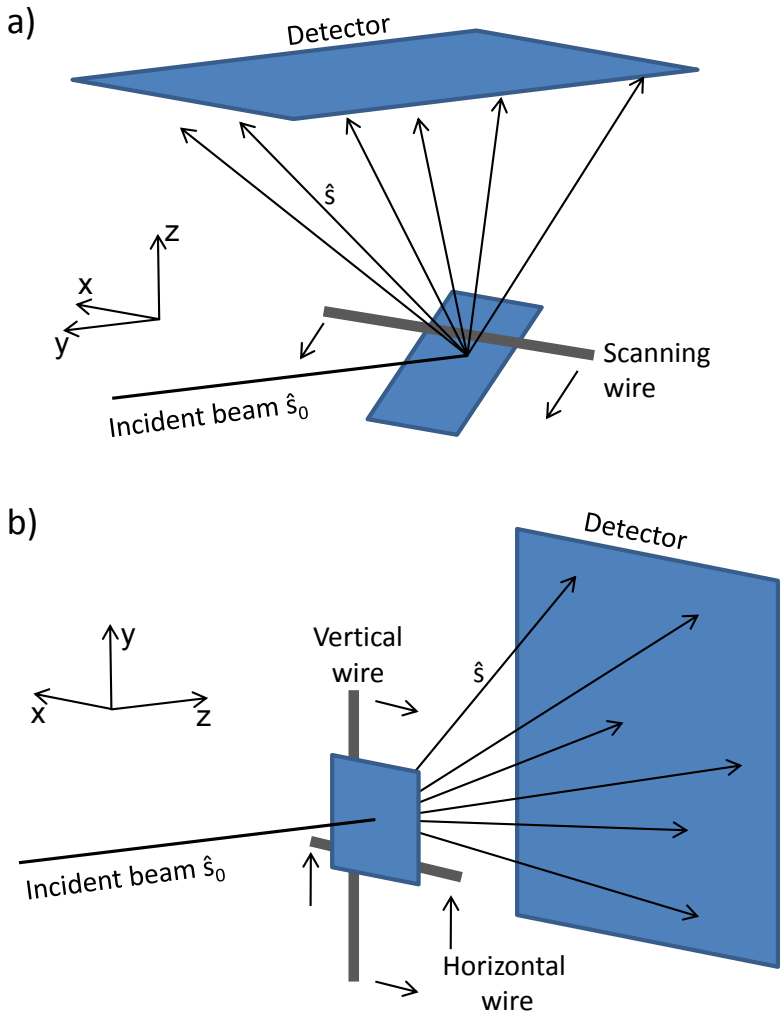

Figure 5.21: Comparison of a) conventional DAXM setup with single scanning wire and b) High energy DAXM setup with a vertical scanning wire and horizontal scanning wire. In both cases the incident beam is denoted by $\hat{s_0}$ and the scattered beam by $\hat{s}$.

obscured and the position of the incident beam, the exact portion of the illuminated volume giving rise to each reflection can be determined. Hence, three dimensional resolution can be achieved along the incident beam direction and depth resolved Laue patterns generated. This makes it possible to map grain structure, lattice rotation and elastic strain in three dimensions with intragranular resolution [207, 208].

Figure 5.21 shows the different geometrical arrangements for low energy, reflection geometry DAXM and high energy transmission DAXM (HEDAXM). Whilst in DAXM only a single scanning wire is required (figure 5.21 a)), two are necessary for the HEDAXM (figure 5.21 b)) configuration. This can be explained as follows.

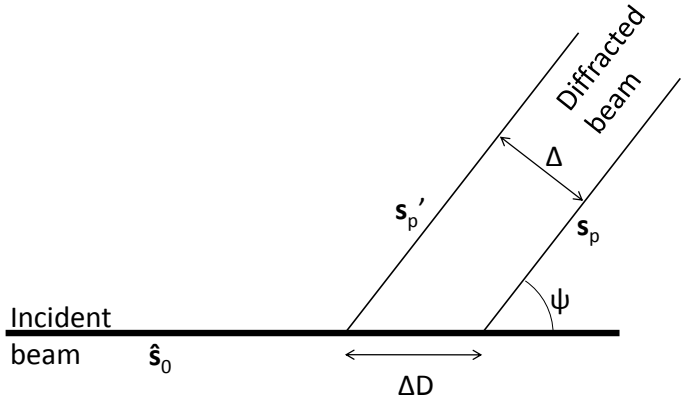

Figure 5.22: Illustration of the positional error $\Delta\mathbf{D}$ arising due to a positional error Δ in the determination of scattered ray position s_p. ψ is the angle between the incident beam $\hat{\mathrm{s}}_0$ and the component s_p of scattered ray $\hat{\mathrm{s}}$ perpendicular to the scanning wire $\hat{\mathbf{w}}$.

The wire triangulation is only sensitive to the change in spatial and angular position of the component, s_p, of the reflection direction vector, $\hat{\mathrm{s}}$, that lies in the plane perpendicular to the scanning wire, $\hat{\mathbf{w}}$:

$$\mathrm{s}_p = \hat{\mathrm{s}} - (\hat{\mathbf{w}} \cdot \hat{\mathrm{s}})\hat{\mathbf{w}}, \tag{5.9}$$

where $\hat{\mathbf{w}}$ is a unit vector along the axis of the scanning wire. One can now consider the positioning error $\Delta\mathbf{D}$ of the estimated sample position, that arises due to an error Δ in the determination of the position of $\hat{\mathrm{s}}$, which is reflected in the position of s_p. For simplicity only a parallel offset error of Δ from s_p to s_p' was considered, as this is sufficient to illustrate the need for two scanning wires (figure 5.22). The angle ψ is given by:

$$\psi = \arccos\left(\frac{\mathbf{s}_p \cdot \hat{\mathbf{s}}_0}{|\mathbf{s}_p||\hat{\mathbf{s}}_0|}\right). \tag{5.10}$$

The ratio of $\frac{\Delta\mathbf{D}}{\Delta}$ provides a measure of the geometrical magnification factor of any position errors in $\hat{\mathrm{s}}$ and is given by:

$$\frac{\Delta\mathbf{D}}{\Delta} = \frac{1}{\sin(\psi)} = \frac{|\mathbf{s}_p||\hat{\mathbf{s}}_0|}{\sqrt{(|\mathbf{s}_p||\hat{\mathbf{s}}_0|)^2 - (\mathbf{s}_p \cdot \hat{\mathbf{s}}_0)^2}}. \tag{5.11}$$

For a given diffraction geometry, $\frac{\Delta\mathbf{D}}{\Delta}$ can be plotted as a function of the angular position of a reflection on the detector. For conventional low energy DAXM with

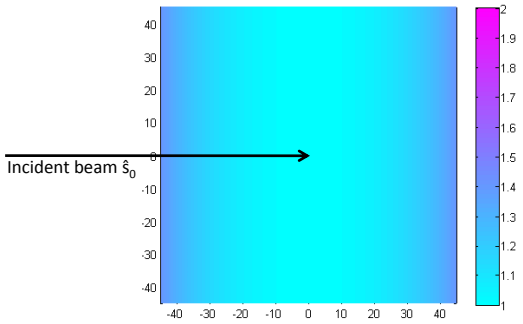

Figure 5.23: Plot of $\frac{\Delta D}{\Delta}$ for conventional DAXM setup. The axes on the plot show the angles spanned by the detector.

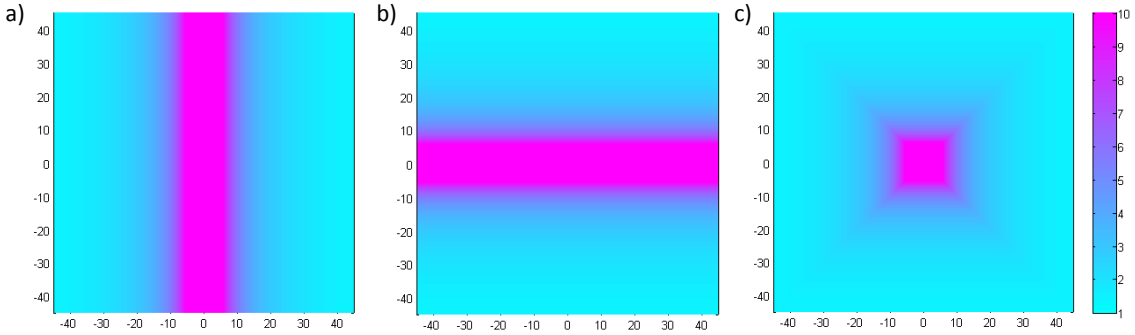

Figure 5.24: Plot of $\frac{\Delta D}{\Delta}$ for high energy transmission DAXM. The axes on the plot show the angle spanned by the detector. a) vertical wire only, b) horizontal wire only, c) combined use of vertical and horizontal wires.

a single scanning wire (as shown in figure 5.21 a)), this is plotted in figure 5.23. The plot corresponds to the detector viewed along the positive z direction. For illustration, the position of the incident beam is shown. The sampling volume is located at the end of the incident beam, beneath the centre of the detector along the negative z direction. The vertical and horizontal plot axes show the angle the scattered beam, $\hat{\mathrm{s}}$, forms with the y - z plane and x - z plane respectively. The colour coding indicates the value of $\frac{\Delta D}{\Delta}$ for each angular position on the detector. For the single wire DAXM setup the maximum value of $\frac{\Delta D}{\Delta}$ in the -45° to $+45^\circ$ angular range spanned by the detector is $\frac{1}{\sqrt{2}}$. The triangulation problem is well conditioned.

The corresponding plots for the transmission geometry are shown in figure 5.24. The detector area is viewed along the positive z direction. The horizonal and vertical axes of the plots correspond to the angle between the scattered beam $\hat{\mathrm{s}}$ and

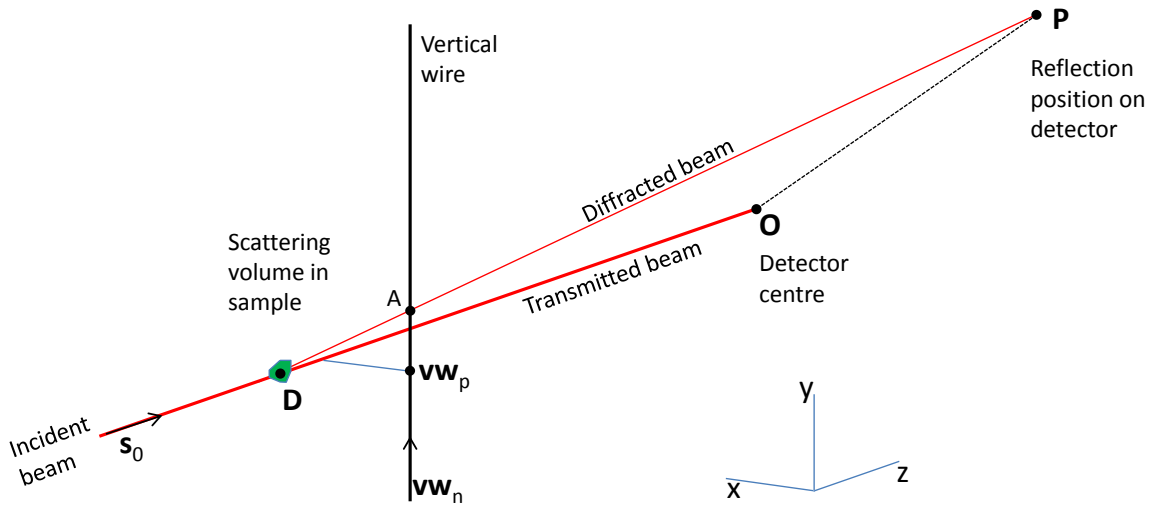

Figure 5.25: Triangulation framework for the vertical wire. Triangulation procedure for the horizontal wire is analogous.

the y - z and x - z plane respectively. For the vertical wire (figure 5.24 a)), $\frac{\Delta \mathrm{D}}{\Delta}$ increases rapidly as the angle between $\hat{\mathrm{s}}$ and the y - z plane (ψ) decreases. If only a vertical wire were used, a vertical section of reflections near the detector centre would become unusable for triangulation.

Now consider the case when only a horizontal scanning wire is used. Analogous to the vertical scanning wire, reflections in a horizontal section near the detector centre are now not usable for triangulation (figure 5.24 b)). However, by combining both a horizontal and a vertical scanning wire and selecting the wire for triangulation that provides the lowest value of $\frac{\Delta \mathrm{D}}{\Delta}$ for a given angular position, the area of the detector that is unusable for triangulation is reduced to a window in the detector centre of about $\pm 10^{\circ}$ (figure 5.24 c)).

Reconstruction technique

The reconstruction of depth-resolved HETL patterns is carried out by determining the distance from the detector centre to the scattering volume that gives rise to each recorded reflection. By binning reflections according to the scattering volume position, HETL patterns originating from different depths in the sample can be reconstructed.

Consider a given reflection on the detector, at position P that arises from the scattering volume at D (figure 5.25). Triangulation is carried out independently for

vertical and horizontal wire scans. Since the reconstruction procedure is the same for both wires, only the vertical wire is considered here. The direction of the vertical wire is given by the unit vector $\mathbf{vw}_n$. Reflection intensity varies as a function of the scanning wire position. When the vertical wire passes across the diffracted beam, the intensity is reduced. The point at which the vertical wire crosses the diffracted beam is marked by point $\mathbf{A}$ (figure 5.25). The position of point $\mathbf{A}$ is given by:

$$\mathbf{A} = \mathbf{vw}_p + N\ \mathbf{vw}_n, \tag{5.12}$$

where $\mathbf{vw}_p$ is a point on the wire and N is a constant to be determined. $\mathbf{vw}_p$ varies from reflection to reflection and captures the position of the vertical scanning wire at which it intersects the diffracted beam of a given reflection. Position $\mathbf{A}$ is also given by:

$$\mathbf{A} = \mathbf{P} - K\ \mathbf{s}, \tag{5.13}$$

where $\mathbf{s}$ is the scattered beam vector from $\mathbf{D}$ to $\mathbf{P}$ (see appendix A.3), and K is a constant to be determined. Two expressions can also be written for the position of the scattering volume $\mathbf{D}$:

$$\mathbf{D} = \mathbf{O} + M\ \hat{\mathbf{s}}_0, \tag{5.14}$$

$$\mathbf{D} = \mathbf{P} - \mathbf{s}, \tag{5.15}$$

where $\hat{\mathbf{s}}_0$ is the incident beam direction vector and M is a constant to be determined. As $\hat{\mathbf{s}}_0$ is a unit vector, M is the distance of the scattering volume $\mathbf{D}$ from the detector centre $\mathbf{O}$. From equations 5.15 and 5.15 the following expression for $\mathbf{s}$ can be found:

$$\mathbf{s} = \mathbf{P} - M\ \hat{\mathbf{s}}_0 - \mathbf{O}. \tag{5.16}$$

Combining equations 5.12 and 5.13 and then substituting in expression 5.16 gives:

$$N\ \mathbf{vw}_n - K\ M\ \hat{\mathbf{s}}_0 + K\ (\mathbf{P} - \mathbf{O}) = \mathbf{P} - \mathbf{vw}_p. \tag{5.17}$$

In this, all parameters are known, apart from constants N, K and M, that can be found by solving the three simultaneous equations.

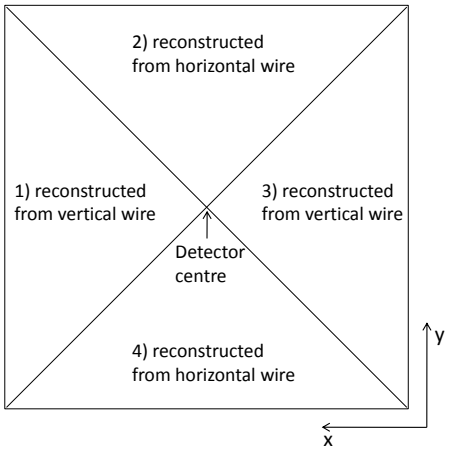

Figure 5.26: Reconstruction areas of the detector allocated to the horizontal and vertical wire.

In the current implementation the reflection position $\mathbf{P}$ is taken as the centre of gravity of a reflection. The components of the vertical wire position vector, $\mathbf{vw}_p$, when the wire crosses the diffracted beam can be found as follows: the first component (in the x direction) gives the distance of the wire to the transmitted, direct, beam. The second component (along the y direction) is zero. The third component (along the z direction), vw_d, is the distance from the vertical scanning wire to the detector plane.

For the horizontal scanning wire the triangulation routine is analogous. The wire direction vector in this case is given by $\mathbf{hw}_n$ and the wire position by $\mathbf{hw}_p$, with the third component hw_d, which captures the distance along the z axis from the horizontal wire to the detector plane.

Based on the plots of $\frac{\Delta \mathbf{D}}{\Delta}$ for the two-wire HEDAXM setup (figure 5.24 c)), the detector was divided into four areas (figure 5.26). Reflections within areas 1 and 3 were reconstructed based on triangulations from the vertical scanning wire, whilst triangulation for reflections in areas 2 and 4 was carried out based on the horizontal wire. Hence, the M value for each reflection was found.

Finally, the reflections were binned according to their M value, which corresponds to their depth within the sample. Hence depth-resolved Laue patterns were reconstructed.

Experimental configuration

An overview of the experimental HEDAXM setup established on beamline I12 (DLS) is shown in figure 5.27 a). Sample and detector were mounted on separate, high accuracy stages to allow translation in all three dimensions. The direct beamstop was positioned close to the detector surface to occupy as little as possible of the angle spanned by the detector. The horizontal and vertical scanning wires were mounted on a brass plate, supported by an aluminium arm connected to a set of translation stages. These stages provided three tilts and translation in three dimensions with a nominal repeatability of $\sim 2\mu\mathrm{m}$. The mounting of the scanning wires on such a "diving board" type arrangement is not ideal. It makes the scanning wire positions very sensitive to positioning inaccuracies due to differential thermal expansion and vibrations of the aluminium mounting arm. However, this was the only feasible mounting arrangement given the available translation stages on the beamline.

A more detailed view of the wire scanning plate and the sample holder is provided in figure 5.27 b). The wire scanning plate was machined to achieve high parallelity of the front and back faces, with semi-circular apertures to allow the passage of the diffracted beams. The scanning wires were cut from drawn, nominally straight, $100\mu\mathrm{m}$ diameter tungsten wire and glue-mounted in $100\mu\mathrm{m}$ deep, triangular crossection grooves. Positioning and straightness of the wires was checked using an optical profilometer with a nominal spatial resolution better than $0.5\mu\mathrm{m}$ in all three dimensions. For the vertical wire, the central $2\mathrm{mm}$ section of the total unsupported $10\mathrm{mm}$ length was considered. The maximum deviation of the wire from a straight line in the plane of the scanning plate, i.e. x - y plane was $\sim 4\mu\mathrm{m}$, and $\sim 2\mu\mathrm{m}$ in the y - z plane. For the central $2\mathrm{mm}$ section of the horizonal wire, the deviation from a straight line in the x - y plane was $\sim 3\mu\mathrm{m}$, and $< 1\mu\mathrm{m}$ in the x - z plane. Surface roughness for both wires and variations in the wire diameter were below the detection limit of the optical profilometer. The angle between the two wires was $89.9°$. Given the relatively small deviations of the wires from a straight line, they were treated as nominally straight for the purposes of the analysis.

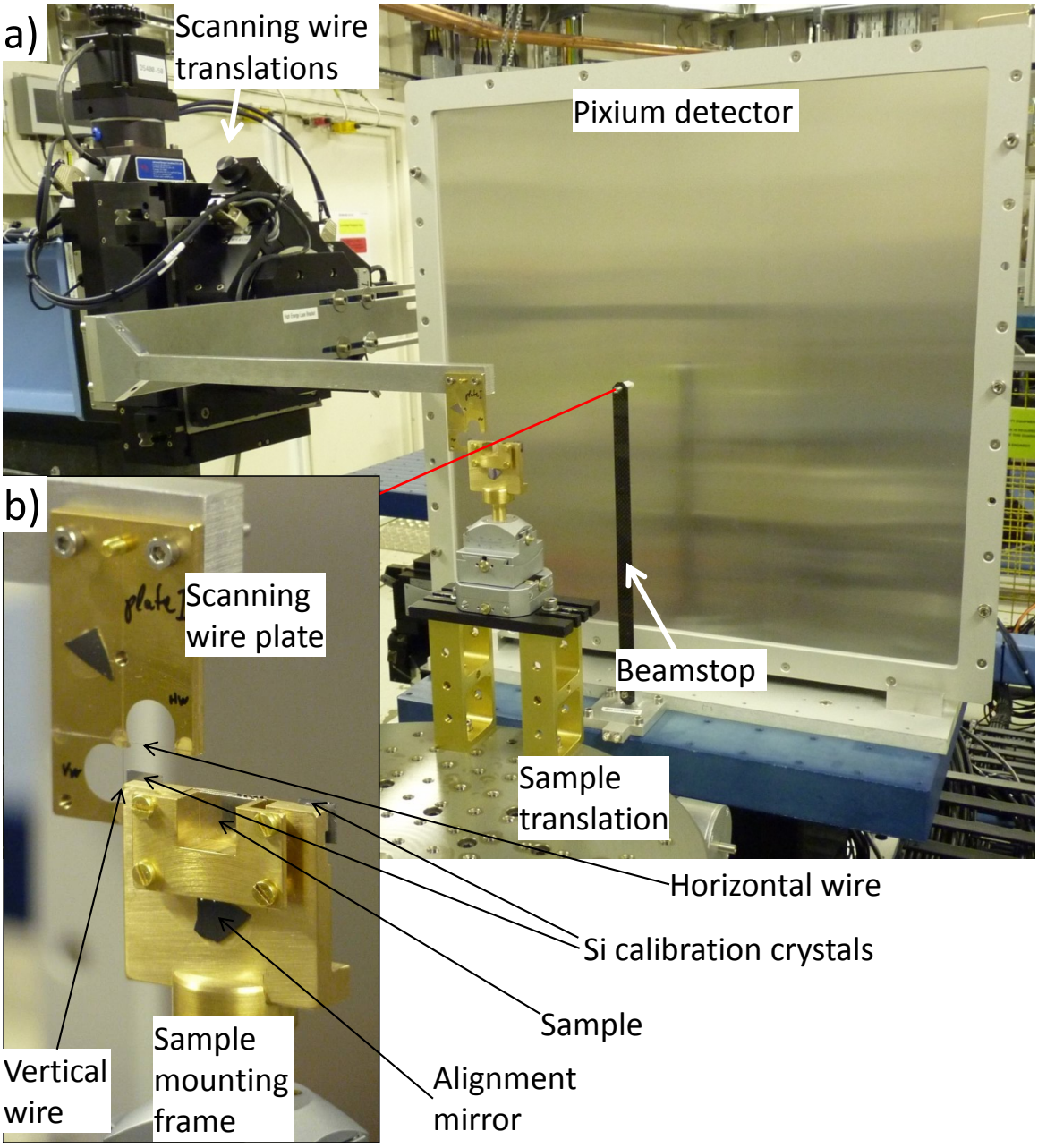

Figure 5.27: High Energy DAXM experimental setup on beamline I12 (DLS). a) Overview of the setup, showing the area detector, beamstop, sample holder and scanning wire plate. The incident direct beam is illustrated with a red line. b) Detailed view of the scanning wire plate and sample holder.

The sample holder was designed to accommodate flat, sheet-like samples of $10 \times 15\mathrm{mm}^2$ size and thickness up to several mm. To guarantee reliable sample positioning (essential as demonstrated in § 3.2), a "picture frame" type arrangement was chosen, where the sample is firmly pressed against a reference edge of the sample holder. The position of the sample holder can be determined accurately using two silicon calibration crystals mounted at either side. These were previously surveyed in using an optical profilometer. Finally, it is essential that the sample holder does not obscure any of the diffracted beams and allows access of the scanning wires close to the sample surface. In the present setup the scanning wires were mounted $\sim 1.4\mathrm{mm}$ downstream of the sample surface.

Setup alignment and calibration

To allow reliable measurements, accurate alignment and calibration of the experimental setup is vital. In particular, it is important that misalignment tilts of the scanning wires and the sample holder are minimised. For initial alignment, the beam of an alignment laser was positioned coaxially with the x-ray beam. On the scanning wire plate and the sample mount, small, highly polished and parallel pieces of silicon single crystal were mounted (figure 5.27 b)). These were used as back reflection mirrors for the alignment laser beam. The flight path of the laser beam was $\sim 4\mathrm{m}$ and alignment of the reflected laser spot to the incident laser spot was estimated to be better than $\sim 1\mathrm{mm}$. Hence perpendicularity of the scanning wire plate and the sample holder to the incident x-ray beam of better than 0.02° could be ensured.

The scanning wire positions relative to the incident beam and their tilts in the x - y plane were determined by scanning the wires through the direct beam. Hence the wire vectors $\mathbf{vw}_n$ and $\mathbf{hw}_n$ were found. Calibration of the detector position and tilts was carried out based on the measurement of one of the silicon single crystal calibration samples mounted on the side of the sample holder. After indexation of the pattern with XMAS, the detector parameters were optimised to give a best fit. In the photon energy range from 50 to 100 keV 186 reflections could be indexed. No distortion correction was necessary for the Pixium detector, as pixels were

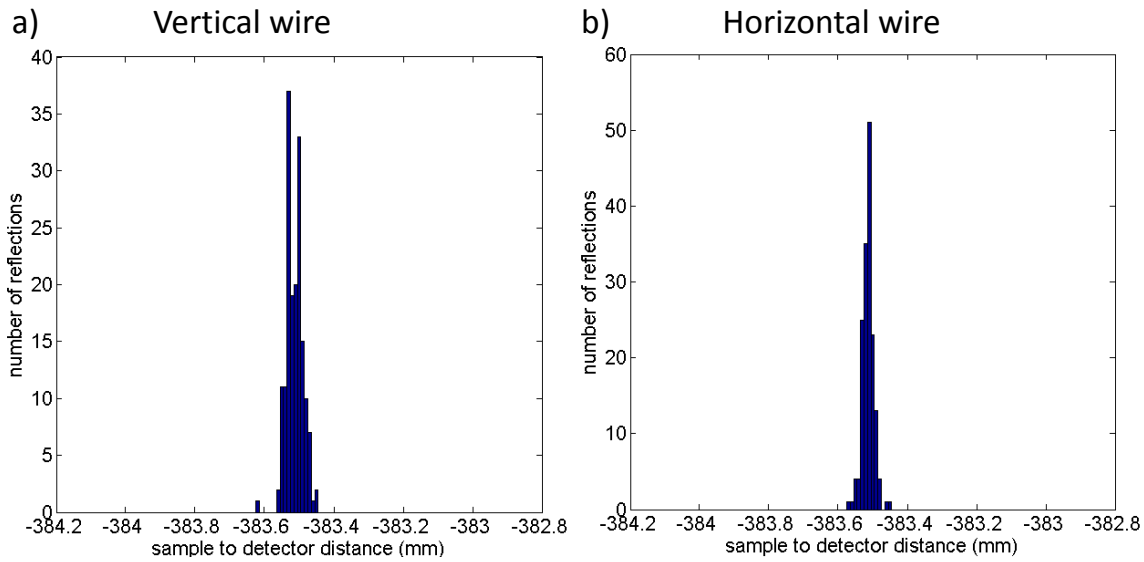

Figure 5.28: Histograms of reflection M values for the Si calibration crystal. a) based on triangulation using only the vertical scanning wire. b) based on triangulation using only the horizontal scanning wire.

positioned very accurately. The mean deviation of diffraction peaks from their ideal position was 0.32 pixels. From this refinement the sample-to-detector distance, dd, was found to be $383.513\mathrm{mm}$.

For the calibration of the vertical and horizontal wire distances along the z axis to the detector plane $\mathbf{O}$, vw_d and hw_d respectively, a single point measurement in the silicon calibration sample was considered. Initially, with the horizontal wire removed from the field of view, the vertical wire was scanned in the x direction from $-1.3\mathrm{mm}$ to $-0.1\mathrm{mm}$ and from $0.1\mathrm{mm}$ to $1.3\mathrm{mm}$ relative to the direct beam in steps of $15\mu\mathrm{m}$. Similarly, with the vertical wire removed from the field of view, the horizontal wire was scanned in the y direction from $-1.3\mathrm{mm}$ to $-0.1\mathrm{mm}$ and from $0.1\mathrm{mm}$ to $1.3\mathrm{mm}$ relative to the direct beam in steps of $15\mu\mathrm{m}$. At each wire position a diffraction image was recorded; a total of 324 images for this measurement point. For the triangulation of the reflection origin, initial guess values of $vw_d = hw_d = 382\mathrm{mm}$ were adopted. In the silicon diffraction patterns 231 reflections could be identified and triangulated. By taking the average of the M values predicted for all reflections, the sample-to-detector distance was be estimated. However, as vw_d and hw_d were only guessed initially, this result differed from the correct value of dd found by XMAS refinement. Next, the values of vw_d and hw_d were modified, until

the triangulation estimated sample-to-detector distance matched the estimate from XMAS.

Figure 5.28 a) shows a histogram of reflection M values computed by triangulation using only the vertical wire, with $vw_d = 382.243\mathrm{mm}$. A peak can be seen, centered on $M = 383.512\mathrm{mm}$. This agrees well with the XMAS determined value of $383.513\mathrm{mm}$ and confirms the correctness of the vw_d value. The peak shows a double peak structure. This is likely to be a result of noise in the data and reconstruction. The width at the base of the peak is $\sim 120\mu\mathrm{m}$, which gives an approximate indication of the current spatial resolution. In figure 5.28 b), a similar histogram of reflection M values is shown for triangulation using only the horizontal wire. It shows a peak centered on $M = 383.514\mathrm{mm}$. This is very close to the value of dd determined by XMAS and confirms the correctness of the calibrated hw_d value of $382.232\mathrm{mm}$.

For the following reconstructions, the experimental setup was assumed to be mechanically stable, so that the calibrated scanning wire parameters and detector position and tilt parameters could be used without modification.

Silicon multi-layer sample

An initial test sample was made up from three layers of $380\mu\mathrm{m}$ thick single crystal silicon wafer. Three individual pieces were cut at different orientations and then glued together to form a sandwich of $1.16\mathrm{mm}$ thickness. The additional thickness of $\sim 20\mu\mathrm{m}$ can be ascribed to the two glue layers. The silicon slice closest to the detector was referred to as $Si1$, the central Slice as $Si2$, and the most upstream slice as $Si3$.

A similar sandwich was constructed from three layers of $300\mu\mathrm{m}$ thick nickel foil described in appendix A.1. Analysis of this dataset is still under way and results will be reported at a later stage.

Results and Discussion

For the three-layer silicon sample, a single measurement point was considered. The same scanning wire positions as in the calibration scans were used, and a

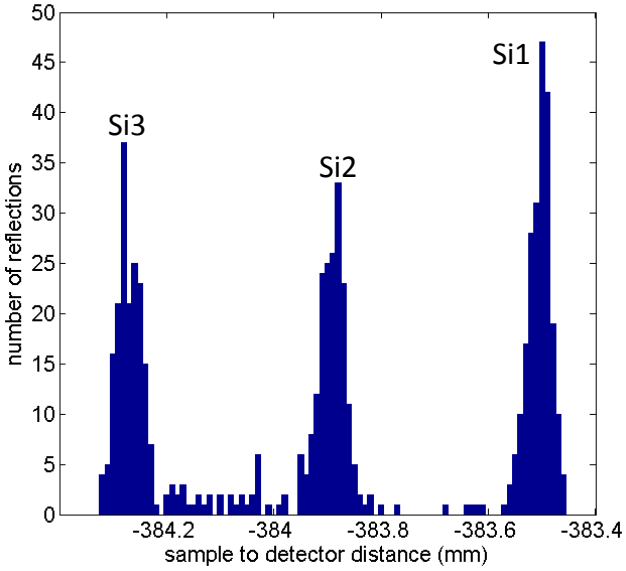

Figure 5.29: Histogram of sample-to-detector distance for the 619 reflections which could be triangulated in the 3 silicon crystal sample.

total of 324 images for different wire positions collected. The distance from the scattering volume giving rise to each reflection to the detector center, the M value, was determined based on triangulation from the vertical wire or the horizontal wire, depending on the reflection position on the detector (figure 5.26). Overall, 691 reflections were identified in the compound HETL pattern, of which 619 could be successfully triangulated.

Figure 5.29 shows a histogram (bin width $10\mu\mathrm{m}$) of the M values for the reflections that could be triangulated. They are clearly grouped into three peaks, corresponding to reflections from each of the three silicon layers ($Si1$, $Si2$ and $Si3$). The centre of the $Si1$ peak, closest to the detector, is at $383.505\mathrm{mm}$. As expected from the sample holder geometry this is close to the value found for the silicon calibration crystal. The mean M values for peaks due to $Si2$ and $Si3$ are $383.883\mathrm{mm}$ and $384.278\mathrm{mm}$ respectively. The thickness of the individual silicon slices can be estimated from the difference in position between the $Si1$, $Si2$ and $Si3$ peaks: $378\mu\mathrm{m}$ for the distance between $Si1$ and $Si2$, and $395\mu\mathrm{m}$ for the distance between $Si2$ and $Si3$. These thickness estimates are close to the actual, measured thickness of the Si wafer used to build up the sample of $380\mu\mathrm{m}$.

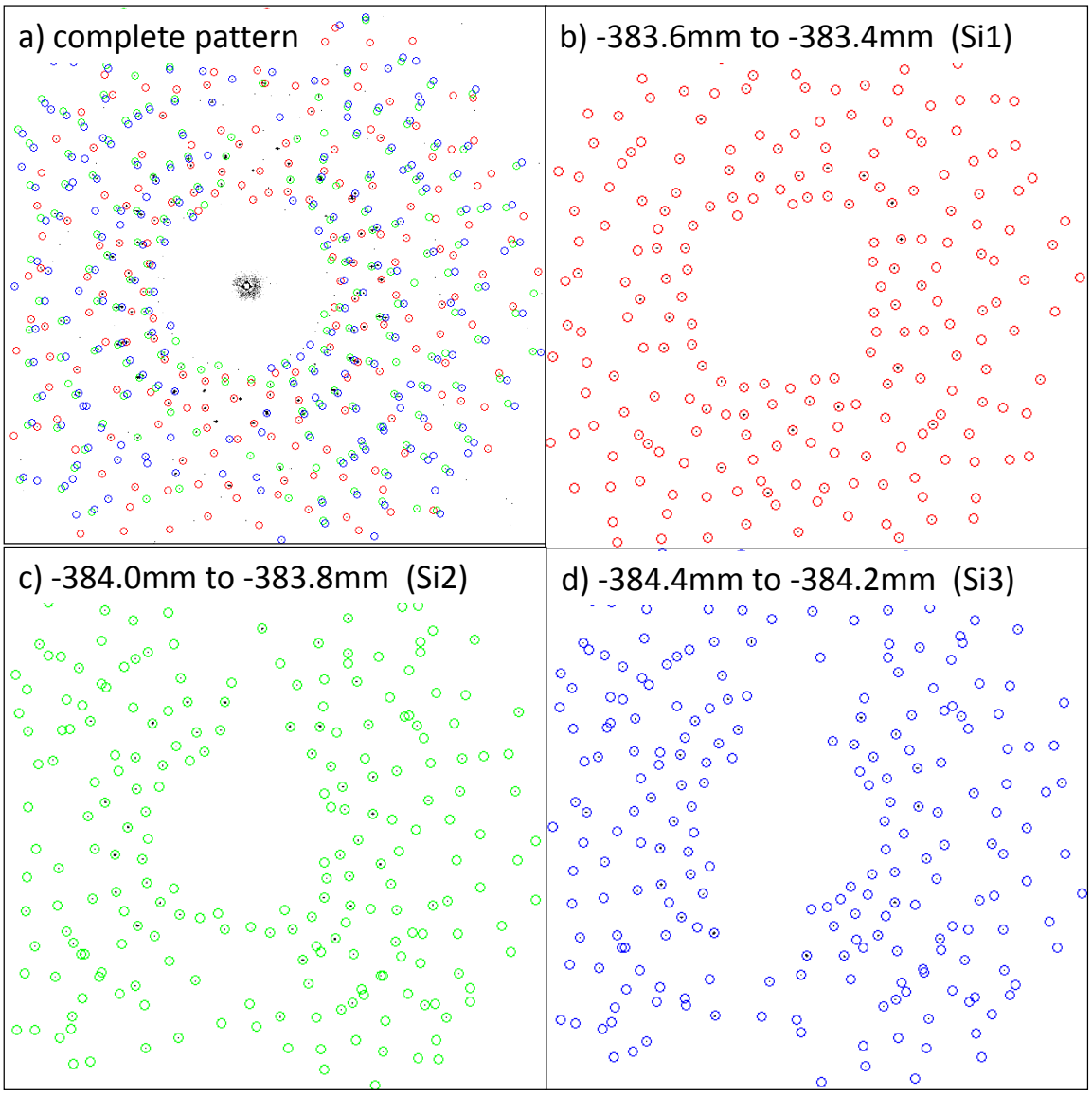

Figure 5.30: HETL diffraction patterns from the three-layer silicon crystal sample. a) Complete compound pattern. HEDAXM patterns reconstructed for different sample-to-detector distances binned over $200\mu\mathrm{m}$ depth: b) Between $-383.6\mathrm{mm}$ and $-383.4\mathrm{mm}$ ($Si1$). c) Between $-384.0\mathrm{mm}$ and $-383.8\mathrm{mm}$ ($Si2$). d) Between $-384.4\mathrm{mm}$ and $-384.2\mathrm{mm}$ ($Si3$).

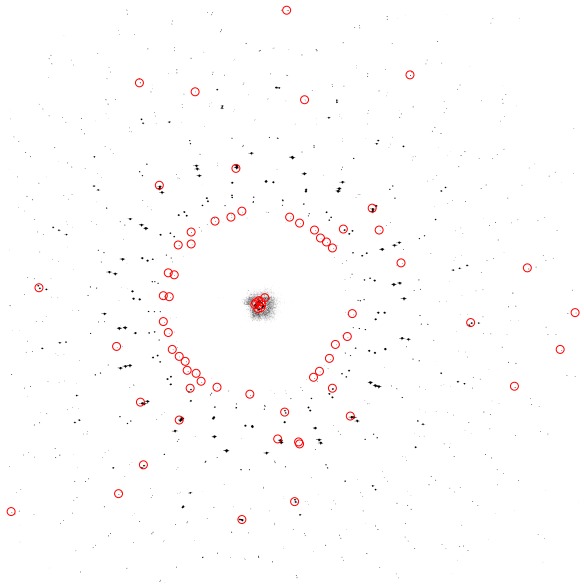

Figure 5.31: Three silicon crystal sandwich sample HETL diffraction pattern with 72 peak positions marked for which triangulation was not possible.

The complete HETL diffraction pattern before triangulation is shown in figure 5.30 a). By binning of the reflections in $200\mu\mathrm{m}$ increments between $383\mathrm{mm}$ and $385\mathrm{mm}$ according to their M value, depth-resolved Laue patterns were computed. In figures 5.30 b), c) and d), the depth-resolved diffraction patterns for sample-to-detector distances between $383.4\mathrm{mm}$ and $383.6\mathrm{mm}$, between $383.8\mathrm{mm}$ and $384.0\mathrm{mm}$ and between $384.2\mathrm{mm}$ and $384.4\mathrm{mm}$ are shown. They contain the diffraction peaks arising from the $Si1$, $Si2$ and $Si3$ silicon slices respectively. For illustration, the peak positions in figure 5.30 which belong to $Si1$, $Si2$ and $Si3$ were highlighted in red, green and blue colours respectively. The diffraction patterns reconstructed for other sample-to-detector distances have are not shown as they only contained few, stray peaks.

Of the total 691 reflections which were identified in the HETL diffraction pattern of the three-layer silicon sample, 619 could be triangulated. The positions of the remaining 72 reflections for which triangulation was not successful are shown superimposed on the full diffraction pattern in figure 5.31. They can be divided into two groups:

- Reflections close to the detector centre. These could not be triangulated successfully, as the wire range of travel was not sufficiently close to the trans-

Si slice	colour code	dd triangulation	dd XMAS
$Si1$	red	$383.505\mathrm{mm}$	$383.523\mathrm{mm}$
$Si2$	green	$383.883\mathrm{mm}$	$383.868\mathrm{mm}$
$Si3$	blue	$384.278\mathrm{mm}$	$384.240\mathrm{mm}$

Table 5.1: Comparison of the sample-to-detector distances dd computed for silicon slices $Si1$, $Si2$ and $Si3$ by triangulation and by XMAS refinement.

mitted beam to capture fully the absorption profile as the wire crossed each reflection. This could be improved upon by increasing the wire range of travel.

- Reflections in other parts of the detector that were excluded from triangulation because of insufficient signal to noise ratio. It was chosen that the absorption peak at the passage of the scanning wire should be at least 2.5 times as large as any noise in the reflection intensity signal. In particular this criterion was often not met by overlapping reflections.

The fact that some of the diffraction peaks in the HEDAXM diffraction patterns can at present not be successfully triangulated will be addressed in future versions of the reconstruction code. However, given the large number of diffraction peaks collected for each silicon slice for which triangulation was successful (>150), failure to triangulate some of the peaks ($\sim 10\%$) does not constitute a major limitation of the technique.

To validate the sample-to-detector distances determined for the three silicon slices, the reconstructed patterns for $Si1$, $Si2$ and $Si3$ (figure 5.30 b) , c) and d)) were indexed with the XMAS software and refined to determine the sample-to-detector distance dd in each case, assuming a perfect, undistorted crystal. The other geometrical parameters of the setup were not refined. The results are shown in table 5.1 alongside the predictions from triangulation. Overall agreement of the two techniques is reasonable, although a difference of $38\mu\mathrm{m}$ exists for $Si3$. This difference is most likely due to errors introduced during the fitting of reflection and wire positions in the triangulation routine. Some uncertainty in the wire positions also arises from the "diving board" wire mounting arrangement.

HEDAXM limitations and refinements

A number of limitations of the HEDAXM technique can be identified:

- Only the position of the centre of mass of a scattering volume giving rise to a particular set of reflections can be determined, but not the extent of the scattering volume along the incident beam.
- Grain level misorientation and elastic strain can be determined, but not intragranular variation of these quantities.
- Measurements are very time-intensive. Collecting the data from 364 wire positions at each measurement point required ~ 40 minutes.

In the low energy reflection geometry DAXM measurements described by Yang [132] and Larson [131], the first two points are addressed by carrying out triangulation of Laue patterns on a pixel by pixel basis, rather than for entire diffraction peaks. They use the scanning wire edge as a sharp knife edge. By subtracting images from subsequent wire positions, the intensity which would pass through a small aperture with the width of the wire scanning step is determined. Hence, depth resolved patterns with intragranular resolution could be computed.

The case of HEDAXM is more difficult, as transmission though the scanning wire is substantial. Hence the edge of the wire does not work as a sharp knife edge. Rather, as shown above, the centre of the scanning wire can be determined and hence the grain centre triangulated. A possible solution to this problem might be to deconvolve the wire shape from the absorption profile of the reflection at the passage of the wire. Hence the length of a scattering volume along the incident beam direction giving rise to each reflection could be determined. However, this would still not allow intragranular resolution. Alternatively, a larger scanning wire diameter could be used to reduce transmitted intensity and achieve a closer match to the sharp knife edge used in low energy DAXM. Work on both approaches is in progress.

As discussed previously, the time required for the measurements could be significantly reduced by improving the data transfer and storage rates. Frame rates of

7.5 frames/s should be achievable, and would reduce the time required per point measurement to below 50 seconds, making the mapping of larger volumes feasible.

5.3.5 LOT vs HEDAXM

Both LOT and HEDAXM present potential candidates for achieving three-dimensional resolution in HETL measurements. The key advantages of LOT are the comparatively faster data acquisition and the significantly simpler experimental setup, without the need for scanning wires. With further development of the reconstruction algorithm (§ 5.3.3), the determination of intragranular lattice orientation and elastic strain should be feasible in three dimensions. Potential limitations are the need for sample rotation that limits the viability of complex sample environments, and the need to index and refine Laue patterns from a large number of grains. Especially in samples with large orientation spread in the scattering volume, streaked reflections might lead to difficulties of indexation and refinement, potentially confining this technique to low deformation samples.

HEDAXM is an extension of the well-established DAXM technique to higher photon energies. The benefit of this technique is that it does not require sample rotation, making it more suited to complex sample environments and high aspect ratio samples. If the implementation of a reconstruction method to achieve intragranular resolution were successful (§ 5.3.4), it would be ideally suited to the measurement of samples with high misorientation within the illuminated volume (e.g. friction stir processed titanium [139]). On the other hand, the more complex experimental setup and longer experimental collection times of this method need to be considered.

Spatial resolution of both methods is dependant on the size of the incident beam. Achromatic focusing at higher photon energies is significantly more difficult than at lower energies. Ultimately a compromise must be found between large sample size and high spatial resolution. At the moment the spatial resolution of either LOT or HEDAXM at $\sim 50\mu\mathrm{m}$ is still fairly low compared with 3DXRD and DCT that are the alternative techniques for the measurement of grain shape and orientation in three dimensions (§ 2.2.5). With 3DXRD resolution of $\sim 7\mu\mathrm{m}$ can

be achieved [154], whilst DCT currently has a lower limit of $\sim 10\mu\mathrm{m}$ grain size that is accessible [160]. With some degree of focusing and/or collimation of the incident beam, albeit at the cost of reduced flux, similar spatial resolutions could be achieved with LOT or HEDAXM. The crucial advantage of both new techniques lies in the potential to provide intragranular measurements of lattice strain and of orientation at high angular resolution, which is currently difficult using either 3DXRD or DCT. The potential of HEDAXM to supply depth-resolved Laue patterns, from which orientation and strain could be determined in highly distorted samples, is unique.

5.4 Chapter Conclusions

In this chapter, the feasibility of High Energy Transmission Laue (HETL) diffraction for the study of individual grains in thick, polycrystalline samples has been demonstrated. Initial measurements performed on ID15 (ESRF) allowed the study of lattice orientation in a $300\mu\mathrm{m}$ thick nickel sample during deformation. Some key points can be noted from this:

- Careful detector distortion correction and calibration of the setup were vital for successful data analysis.
- Indexation and refinement could be carried out using well-established analysis tools, such as the XMAS software.
- Orientation maps agreed well with EBSD surface orientation maps.
- Misorientation within the scattering volume was studied using a patterns matching approach. The active slip system and orientation spread in the scattering volume were successfully deduced.

In these first measurements the recorded diffraction signal represented an average through the sample thickness. To understand fully the deformation mechanisms at work, resolution in three dimensions is essential. Two candidate techniques which make such measurements possible are Laue Orientation Tomography (LOT) and High Energy Differential Aperture X-ray Microscopy (HEDAXM).

The LOT technique involves the collection of line measurements of Laue patterns for different angular sample positions about a vertical rotation axis. By applying tomographic reconstruction principles to the grain specific scattered intensity, the grain morphology in the sample slice is determined. LOT was successfully applied to the measurement of grain shape in a two-dimensional, through-thickness slice of a large-grained nickel sample. The reconstructed grain shapes agreed well with external optical micrographs.

The HEDAXM technique is an extension to higher photon energies of the DAXM technique. Two wires were scanned through the diffracted beam. Using triangulation the position of the scattering volume giving rise to each reflection was found. This technique was successfully used to recover the centre of gravity positions of individual, coherently scattering volumes in a silicon multi-layer sample. Depth resolved Laue patterns were generated and could be analysed using well-established indexation and refinement codes, such as XMAS.

Both techniques have the potential to provide through-thickness, three-dimensional measurements of crystal orientation and elastic strain in thick, polycrystalline samples. In particular they offer the promise of intragranular resolution, that remains a challenge to alternative methods, such as 3DXRD or DCT. Further development steps identified for each technique are:

LOT: development of analysis routines to allow not only shape, but also intragranular lattice orientation and strain to be determined (§ 5.3.3).

HEDAXM: refinement of the analysis code to provide intragranularly resolved Laue patterns, rather than just the centroid of the scattering volume giving rise to each reflection.

Chapter 6

Conclusions

In this thesis several advances were presented in the synchrotron X-ray micro-diffraction study of grain-level deformation in polycrystalline engineering alloys. In this chapter the contributions made to the development of experimental techniques and data analysis, and the diffraction post-processing of discrete dislocation simulations will be reviewed first. Then the insights into material deformation at the micro-scale which were gained using these new techniques will be summarised.

For the experimental study of intra-granular deformation, a novel micro-beam Laue diffraction setup was developed at beamline B16 (DLS). In the first set of experiments, the deformation of individual crystallites in a large-grained, polycrystalline CP nickel sample was followed during in situ loading. Lattice rotations were extracted to high angular resolution. Specific grains could be reliably identified at successive load increments up to 14% macroscopic tensile strain. Depending on their lattice orientation, individual grains showed significant variations in their deformation response [209].

Next the combination of high angular resolution micro-beam Laue diffraction, reciprocal space mapping and energy scanning measurements was considered. Each technique was used to measure a $\{311\}$ reflection from a single grain in a polycrystalline, deformed CP nickel sample. Based on this, the information about lattice orientation spread in the sampling volume determined by each method was compared. Reciprocal space mapping and energy scanning provided resolution in the radial direction of reciprocal space (d-spacing). In micro-beam Laue diffraction

the diffraction peak corresponds to an integral in the radial direction of reciprocal space. Information about d-spacing cannot be extracted. If only misorientation information is required, high angular resolution micro-beam Laue diffraction provides the same information as reciprocal space mapping or energy scanning in a fraction of the time [210].

By combining micro-beam Laue diffraction with scanning white beam topography, misorientation within the scattering volume was studied at high angular resolution [211]. Using this technique, rotation features smaller than the size of the sampling beam were resolved. Compared to traditional topography the sampling volume was reduced by the use of a scanning beam. This limited the distortion of individual scanning topographs due to lattice rotations. The individual scanning topographs were assembled into a compound, whole-grain topograph. This procedure essentially corresponded to a partial deconvolution of the real and reciprocal space contributions to the whole-grain topograph. Using this approach, the application of classical topography techniques to deformed metallic samples becomes possible.

There are very significant benefits to using a focused divergent beam. Apart from the gain in flux, reduction in measurement time and increased spatial resolution, it makes it possible to maintain low distortion of individual scanning topographs to higher dislocation densities (§ 3.1.5). First measurements using this approach were successful [162] and allowed the mapping of fine rotation structure in nickel samples deformed up to 8% plastic strain.

Whilst lattice rotations were readily extracted from micro-beam Laue diffraction patterns, reliable measurements of elastic strain were much more challenging. For accurate elastic strain determination a quantitative understanding of the experimental errors in micro-beam Laue diffraction is essential. To this end a study of the error sources at the dedicated micro-beam Laue beamline BM32 (ESRF) was performed. A simulation-based error analysis framework was developed to assess the individual contributions of random geometrical errors to the overall strain measurement error. It highlighted that repeatable positioning of the sample and high geometrical stability of the experimental setup are critical for accurate mea-

surements. The random fluctuations of the geometrical parameters of the setup at BM32 (ESRF) were estimated using calibration diffraction patterns from a germanium single crystal. Based on the fluctuations, the expected strain errors were predicted. These agreed well with the experimental strain errors found in measurements of a single crystal silicon bar under four point bending. Under ideal conditions elastic strain measurements with an error standard deviation below 5×10^{-5} were demonstrated.

Next, a CP copper single crystal bar was loaded under four point bending and measured at several deformation increments. Copper was a particularly difficult material to study due to its low elastic strain at yield. Strain errors were significantly larger, with a standard deviation exceeding $\sim 3 \times 10^{-4}$. This was largely due to the inability to fit accurately the distorted reflections that arise as the result of lattice orientation spread in the sampling volume. Nevertheless, salient values, such as strain gradients and flow stress, were successfully extracted.

The proposed error analysis framework is a valuable tool for the rational refinement of experimental configurations, to maximise the benefit in terms of strain accuracy. The problem of the inadequate fitting of deformed diffraction peaks can be addressed by reducing the sampling volume size and hence lattice orientation spread. To this end, the development of DAXM measurements is under-way at BM32 (ESRF) [212].

To allow the validation of computational material deformation models, the direct comparison with experimental measurements must be made. Lattice orientations are particularly suitable for this purpose as they are more readily determined than elastic strains. One approach is to compute the diffraction patterns that a "virtual" scattering experiment on the simulation volume would give rise to. These predicted diffraction patterns provide a direct comparison to those collected experimentally. Crystal plasticity and discrete dislocation dynamics models are particularly powerful tools for the study of grain-level deformation. In this thesis methods for the diffraction post-processing of discrete dislocation models were developed.

First, a simple, two-dimensional "naive" model of a dislocation cell/wall structure was postulated for comparison with reciprocal space maps from a large grained,

lightly deformed aluminium alloy sample, measured at beamline I16 (DLS) [161]. Diffraction post-processing of the model captured some of the features observed experimentally. Simulated and measured reciprocal space maps both showed a pattern of sharp peaks superimposed on a background of enhanced intensity in the tangential directions of reciprocal space. Using the model, qualitative understanding of the different effects of SSDs and GNDs was gained. GNDs introduced net lattice curvature and hence led to anisotropic broadening of diffraction peaks. If GNDs were non-uniformly distributed, they caused a fragmentation of the diffraction peak. SSDs on the other hand introduced no long-range lattice curvature and led to a less pronounced, isotropic broadening of diffraction peaks. The distinction between SSDs and GNDs is dependant upon the scale under consideration. In diffraction measurements, the scale is prescribed by the sampling volume size.

To overcome the constraints of two-dimensional dislocation models, the solution for lattice rotations due to a three-dimensional, triangular dislocation loop was developed. Validation against two-dimensional solutions for edge and screw dislocations showed excellent agreement. The triangular dislocation loop solution was used as the fundamental building block to evaluate lattice rotations from three-dimensional dislocation structures discretised into dislocation segments.

By superimposing the solutions for individual triangular dislocation loops, the lattice orientation spread arising during the emission of a dislocation loop from a Frank-Read source was computed. Dislocation positions were simulated using the ParaDiS discrete dislocation dynamics code. Plots of orientation spread showed anisotropic broadening. This was compared to the broadening/streaking observed in micro-beam Laue diffraction experiments and could be linked to the technique used experimentally to determine the active slip system. The framework for the determination of lattice rotations from three-dimensional dislocation structures constitutes a key element from the diffraction post-processing of large, three-dimensional discrete dislocation dynamics simulations. It would also allow the consideration of lattice rotations, which have, thus far, been assumed to be small in these simulations.

To overcome the restriction of micro-beam Laue diffraction measurements to thin samples or the sample surface region (sub $100\mu\mathrm{m}$ depth), an extension of the technique to higher photon energies (50 - 150 keV) was developed on beamline ID15 (ESRF) [213]. This allowed the through-thickness measurement of a $300\mu\mathrm{m}$ thick CP nickel sample at different tensile loading increments. Transmission geometry, with the area detector centre placed at $2\theta = 0°$, was the natural choice for the high energy transmission Laue (HETL) measurements. Distortion correction of the area detector was found to be vital for successful data interpretation using well-established tools such as the XMAS software.

Individual grains were successfully identified at successive load increments. The microstructure and the measured lattice orientations agreed well with EBSD surface maps. This was expected, since most grains extended through the thickness of the sample. To study misorientation within the scattering volume, a pattern matching approach was used. From this the active slip systems were successfully determined.

To achieve the three-dimensional resolution in HETL measurements that is necessary to characterise fully local microstructure, lattice orientation and elastic strains, two different approaches were tested on beamline I12 (DLS):

Laue orientation tomography (LOT): HETL line measurements were collected from a horizontal sample slice at different angular positions about a fixed, vertical rotation axis. From indexation, peaks belonging to different grains were identified. Filtered back projection was then applied to the diffracted intensity from each grain to determine the grain morphology in the illuminated slice. This approach was successfully used to map the microstructure within a slice of a large-grained CP nickel sample. Agreement with external optical micrographs of the sample was good. The development of more refined analysis techniques to allow the mapping of intragranular lattice orientation and elastic strain is under-way.

High energy differential aperture X-ray microscopy (HEDAXM): In this extension of the DAXM technique to higher photon energies, two scanning wires were translated through the diffracted beams in a HETL measurement. When

a wire obscured a given reflection, triangulation was used to determine the position of the scattering volume along the incident beam which had given rise to the reflection. Hence depth resolution in the sample was achieved. This technique was successfully used to separate the diffraction patterns arising from three separate slices in a multi-layered silicon sample. The diffraction pattern from each individual slice could then be analysed using conventional tools such as the XMAS software. At the moment the technique is limited to finding the centroid of each coherently scattering volume. Work is underway to extend it, such that measurements with intragranular resolution along the incident beam direction become possible.

Both LOT and HEDAXM are promising methods for the three-dimensional, grain level characterisation of real, thick engineering components. They promise to allow intragranular resolution of lattice orientation and elastic strain, which would be difficult to obtain with competing methods. The potential of the HEDAXM technique to allow the study of thick samples with high orientation gradients is unique. Several experimental visits are scheduled in the near future to continue the development of both techniques.

In this thesis, polycrystalline, large-grained CP nickel samples were extensively studied. CP nickel was a particularly suitable candidate material due to its simple crystal structure (FCC) that made it an ideal object for the development of experimental techniques and micro-deformation models. The findings made in the course of this project must be considered in the context of the established views of the dislocation and grain level deformation behaviour of ductile polycrystals.

An approach to understanding the deformation behaviour of FCC single crystals has been provided by the Mughrabi composite model [86]. It considers the heterogenous evolution of dislocation density in the crystal in terms of dislocation-depleted regions (cells), which are separated by higher dislocation density regions (walls). Observed at the crystal level, the structure behaves as a composite, consisting of hard, high dislocation density walls and softer cells with lower dislocation density. Depending on the orientation of the dislocation walls, it can be imagined that either a Reuss (common stress) or a Voigt (common strain) approach is

appropriate. The complexity of real dislocation distributions means that the actual deformation response lies somewhere between these two extremes [88]. In the deformation of polycrystalline FCC material, further constraints are imposed upon the deformation of each individual grain by the presence of its neighbours. Ashby [18] describes this effect and the requirement for the deformation of neighbouring grains to be compatible. This compatibility is achieved by the local installation of geometrically necessary dislocation. It is taken into account numerically by strain gradient crystal plasticity models, as described previously (§ 2.1.3). The deformation response observed in individual grains, as loading is applied to a polycrystalline aggregate, is the compound result of the macroscopically applied loading, the local microstructure and deformation behaviour at the single crystal level.

In the course of this thesis the following observations were made and conclusions drawn:

- In topographs of a thin ($15\mu\mathrm{m}$) nickel foil sample, the formation of a regular lattice rotation pattern was observed at small strains ($1\% - 2\%$). It was ascribed to the formation of a dislocation cell/wall type structure. One of the axes of the rotation pattern was aligned with the trace of the highest Schmid factor slip system. The period of the structure was found to be $\sim 6 - 8\mu\mathrm{m}$ at 1% total strain.The orientation of the pattern and the approximate spacing were similar to TEM observations of dislocation cell/wall structures in aluminium single crystals reported by Winther [175]. With further deformation to 1.8% plastic strain, a decrease in the spacing of the rotation structure to $\sim 4 - 6\mu\mathrm{m}$ was observed. Seen in the context of the Mughrabi model, this seems reasonable. The reduced spacing caters for an increase in dislocation density as a result of plastic deformation. As total strain was increased further, the chequer pattern could no longer be observed. At $\sim 2.9\%$ total strain it was instead replaced by streaks of enhanced intensity aligned in the direction of the highest Schmid factor slip system. This suggests a change from a dislocation cell/wall type structure to a planar dislocation structure where slip occurs in discrete bands.

- Under imposed remote displacement of sample boundaries, individual grains showed significantly different deformation response. The evolution of lattice orientation depended strongly both on the initial lattice orientation and on the local grain neighbourhood. The latter should be understood to include both the orientation relationship between neighbouring grains, as well as their morphology (shape and size). In some cases it was found that deformation did not occur on the slip system predicted by Schmid factor analysis. A similar effect was reported in single crystal micro pillars by Maaß et al. [118–121]. They ascribed the selection of alternative slip systems, and not of the highest Schmid factor slip system, to initial defects of the micro-pillars. In a polycrystal the response of each grain depends strongly on the load transfer from its neighbours, but also the constraints provided by them. As a consequence the consideration of remote stress only (as Schmid factor does), is not sufficient. An efficient approach to studying these effects is to compare directly the simulations of the experimentally studied sample and the experimentally measured quantities. This was demonstrated by Song et al. [191] in a direct comparison of the sample studied in § 3.1.2 with strain gradient crystal plasticity simulations. In the numerical model the sample microstructure was replicated based on the experimentally measured lattice orientations. At a simulated sample extension of 2% plastic strain, a direct comparison of the model and experimental measurements showed good agreement of lattice rotations and local orientation spread.

- In HETL measurements of thicker $(300\mu\mathrm{m})$ nickel samples, discrete bands of increased local lattice misorientation were found. By the nature of the measurement, HETL diffraction patterns correspond to an integral through the thickness of the sample. The lattice orientation of a point in a grain derived from HETL measurements hence represents the average orientation along the beam direction of the grain at the measurement point. The high misorientation bands were generally not confined to high Schmid factor grains. They had a range of orientations from close to perpendicular to angles of 30° to the loading direction. Some of the misorientation bands were trans-

mitted across twin boundaries. Transmission across grain boundaries was less readily achieved. A comparison of the misorientation bands with crystal plasticity simulations would constitute an important extension to the work of Ohashi et al [136]. They compared lattice rotations near a grain boundary in a deformed nickel bi-crystal with crystal plasticity simulations and demonstrated good agreement. Capturing the more complex, detailed interactions of several grains would constitute the next natural step in the validation of the crystal plasticity approach.

The experimental observations made in this thesis reinforce the importance of heterogeneous deformation behaviour in FCC polycrystals both at the intra- and the inter-granular scale. The collected datasets provide a benchmark for the comparison with and validation of material deformation models at the micro-scale. Their use for the refinement of crystal plasticity simulations and discrete dislocation dynamics models is planned for the near future.

Bibliography

[1] Chui, S. *http://www.samchuiphotos.com/A380TripReport/A380TripReport.html* (2005).

[2] Belnoue, J. P., Garnham, B., Bache, M., and Korsunsky, A. M. *Engineering Fracture Mechanics* **77**(11), 1721–1729 (2010).

[3] Zhang, W. and Schwager, F. *Journal of The Electrochemical Society* **153**(5), 337–343 (2006).

[4] Van der Giessen, E. and Needleman, A. *Modelling and Simulation in Materials Science and Engineering* **3**, 689–735 (1995).

[5] Bulatov, V. V. and Cai, W. *Computer Simulations of Dislocations*. Oxford University Press, (2006).

[6] Arsenlis, A., Cai, W., Tang, M., Rhee, M., Oppelstrup, T., Hommes, G., Pierce, T. G., and Bulatov, V. V. *Modelling and Simulation in Materials Science and Engineering* **15**(6), 553–596 (2007).

[7] Bulatov, V. V., Cai, W., Fier, J., Hiratani, M., Hommes, G., Pierce, T. G., Tang, M., Rhee, M., Yates, K., and Arsenlis, T. In *Conference on High Performance Networking and Computing*, (2004).

[8] Lemaitre, J., Chaboche, J.-L., and Shrivastava, B. *Mechanics of Solid Materials*. Cambridge University Press, (1994).

[9] Crisfield, M. A. *Non-Linear Finite Element Analysis of Solids and Structures: Essentials*. Wiley, (1991).

[10] Hill, R. *The Mathematical Theory of Plasticity*. Oxford University Press, (1998).

[11] Dunne, F. and Petrinic, N. *Introduction to computational plasticity*. Oxford University Press, (2005).

[12] Hall, A. E. O. *Proceedings of the Physical Society. Section B* **9**, 747 (1951).

[13] Petch, N. J. *Journal of Iron Steel Institute* **174**(25-8) (1953).

[14] Fleck, N. A., Muller, G. M., Ashby, M. F., and Hutchinson, J. W. *Acta Metallurgica et Materialia* **42**(2), 475 (1994).

[15] Stölken, J. S. and Evans, A. G. *Acta Materialia* **46**(14), 5109–5115 (1998).

[16] McElhaney, K. W., Vlassak, J. J., and Nix, W. D. *Journal of Materials Research* **13**(5), 1300–1306 (1998).

[17] Lloyd, D. J. *International Materials Reviews* **39**(1), 1–23 (1994).

[18] Ashby, M. F. *Philosophical Magazine* **21**(170), 399 – 424 (1970).

[19] Aifantis, E. C. *International Journal of Plasticity* **3**(3), 211–247 (1987).

[20] Fleck, N. A. and Hutchinson, J. W. *Advances in Applied Mechanics* **33**, 295–361 (1997).

[21] Fleck, N. A. and Hutchinson, J. W. *Journal of the Mechanics and Physics of Solids* **49**(10), 2245–2271 (2001).

[22] Gurtin, M. E. *International Journal of Plasticity* **19**(1), 47–90 (2003).

[23] Gudmundson, P. *Journal of the Mechanics and Physics of Solids* **52**(6), 1379–1406 (2004).

[24] Dai, H. and Parks, D. M. In *Proceedings of Plasticity*. Neat Press, (1997).

[25] Busso, E. P., Meissonnier, F. T., and O'Dowd, N. P. *Journal of the Mechanics and Physics of Solids* **48**(11), 2333–2361 (2000).

[26] Bassani, J. L. *Journal of the Mechanics and Physics of Solids* **49**(9), 1983–1996 (2001).

[27] Arsenlis, A. and Parks, D. M. *Journal of the Mechanics and Physics of Solids* **50**(9), 1979–2009 (2002).

[28] Acharya, A. and Beaudoin, A. J. *Journal of the Mechanics and Physics of Solids* **48**(10), 2213–2230 (2000).

[29] Beaudoin, A. J., Acharya, A., Chen, S. R., Korzekwa, D. A., and Stout, M. G. *Acta Materialia* **48**(13), 3409–3423 (2000).

[30] Huang, Y., Qu, S., Hwang, K. C., Li, M., and Gao, H. *International Journal of Plasticity* **20**(4-5), 753–782 (2004).

[31] Cheong, K. S., Busso, E. P., and Arsenlis, A. *International Journal of Plasticity* **21**(9), 1797–1814 (2005).

[32] Meissonnier, F. T., Busso, E. P., and O'Dowd, N. P. *International Journal of Plasticity* **17**(4), 601–640 (2001).

[33] Hull, D. and Bacon, D. J. *Introduction to Dislocations*. Butterworth-Heinemann, Oxford, 4 edition, (2001).

[34] Warnes, W. H. *http://oregonstate.edu/instruct/engr322/Exams/Previous/S98 /ENGR322MT2.html* (1998).

[35] Monnet, G., Devincre, B., and Kubin, L. P. *Acta Materialia* **52**(14), 4317–4328 (2004).

[36] Olmsted, D. L., Hector Jr, L. G., Curtin, W. A., and Clifton, R. J. *Modelling and Simulation in Materials Science and Engineering* **13**, 371–388 (2005).

[37] Shenoy, V. B., Kukta, R. V., and Phillips, R. *Physical Review Letters* **84**(7), 1491 (2000).

[38] Rodney, D. and Phillips, R. *Physical Review Letters* **82**(8), 1704 (1999).

[39] Devincre, B., Kubin, L. P., Lemarchand, C., and Madec, R. *Materials Science and Engineering A* **309-310**, 211–219 (2001).

[40] Deshpande, V. S., Needleman, A., and Van der Giessen, E. *Journal of the Mechanics and Physics of Solids* **51**(11-12), 2057–2083 (2003).

[41] Benzerga, A. A., Bréchet, Y., Needleman, A., and Van der Giessen, E. *Modelling and Simulation in Materials Science and Engineering* **12**(1), 159–196 (2004).

[42] Bittencourt, E., Needleman, A., Gurtin, M. E., and Van der Giessen, E. *Journal of the Mechanics and Physics of Solids* **51**(2), 281–310 (2003).

[43] Gurtin, M. E. *Journal of the Mechanics and Physics of Solids* **50**(1), 5–32 (2002).

[44] Nicola, L., Van der Giessen, E., and Needleman, A. *Journal of Applied Physics* **93**(10), 5920–5928 (2003).

[45] Nicola, L., Xiang, Y., Vlassak, J. J., Van der Giessen, E., and Needleman, A. *Journal of the Mechanics and Physics of Solids* **54**(10), 2089–2110 (2006).

[46] Deshpande, V. S., Needleman, A., and Van der Giessen, E. *Materials Science and Engineering A* **400-401**, 154–157 (2005).

[47] Deshpande, V. S., Needleman, A., and Van der Giessen, E. *Journal of the Mechanics and Physics of Solids* **53**(12), 2661–2691 (2005).

[48] Balint, D. S., Deshpande, V. S., Needleman, A., and Van der Giessen, E. *Materials Science and Engineering A* **400-401**, 186–190 (2005).

[49] Balint, D. S., Deshpande, V. S., Needleman, A., and Van der Giessen, E. *Modelling and Simulation in Materials Science and Engineering* **14**(3), 409 – 422 (2006).

[50] Widjaja, A., Van der Giessen, E., and Needleman, A. *Materials Science and Engineering A* **400-401**, 456–459 (2005).

[51] Widjaja, A., Needleman, A., and Van der Giessen, E. *Modelling and Simulation in Materials Science and Engineering* **15**(1), 121–132 (2007).

[52] Widjaja, A., Van der Giessen, E., and Needleman, A. *Acta Materialia* **55**(19), 6408–6415 (2007).

[53] Balint, D. S., Deshpande, V. S., Needleman, A., and Van der Giessen, E. *Journal of the Mechanics and Physics of Solids* **54**(11), 2281–2303 (2006).

[54] Deshpande, V. S., Needleman, A., and Van der Giessen, E. *Acta Materialia* **51**(1), 1–15 (2003).

[55] Deshpande, V. S., Needleman, A., and Van der Giessen, E. *Acta Materialia* **51**(15), 4637–4651 (2003).

[56] Gaucherin, G., Hofmann, F., Belnoue, J. P., and Korsunsky, A. M. *Procedia Engineering* **1**(1), 241–244 (2009).

[57] Balint, D. S., Deshpande, V. S., Needleman, A., and Van der Giessen, E. *International Journal of Plasticity* **24**(12), 2149–2172 (2008).

[58] Kubin, L. P., Canova, G. R., Condat, M., Devincre, B., Pontikis, V., and Bréchet, Y. *Solid State Phenomena* **23**/**24**, 455–472 (1992).

[59] Devincre, B., Kirchner, H. O., Pontikis, V., and Kubin, L. P. *Mesoscale simulation of the dislocation dynamics*. Computer Simulation in Materials Science. Kluwer Academic Publishing, Dordrecht, (1996).

[60] Devincre, B., Hoc, T., and Kubin, L. P. *Materials Science and Engineering A* **400-401**, 182–185 (2005).

[61] Devincre, B., Kubin, L., and Hoc, T. *Scripta Materialia* **54**(5), 741–746 (2006).

[62] Devincre, B., Kubin, L., and Hoc, T. *Scripta Materialia* **57**(10), 905–908 (2007).

[63] Kubin, L. P., Devincre, B., and Hoc, T. *Philosophical Magazine* **86**(25-26), 4023–4036 (2006).

[64] Devincre, B., Hoc, T., and Kubin, L. *Science* **320**(5884), 1745–1748 (2008).

[65] Kubin, L., Devincre, B., and Hoc, T. *Materials Science and Engineering: A* **483-484**, 19–24 (2008).

[66] Madec, R. and Kubin, L. P. *Scripta Materialia* **58**(9), 767–770 (2008).

[67] Cai, W., Arsenlis, A., Weinberger, C. R., and Bulatov, V. V. *Journal of the Mechanics and Physics of Solids* **54**(3), 561–587 (2006).

[68] Greengard, L. and Rokhlin, V. *Acta Numerica* **6**, 229–270 (1997).

[69] Cai, W. and Bulatov, V. V. *Materials Science and Engineering A* **387-389**, 277–281 (2004).

[70] Marian, J., Cai, W., and Bulatov, V. V. *Nature Materials* **3**(3), 158–163 (2004).

[71] Deo, C. S., Srolovitz, D. J., Cai, W., and Bulatov, V. V. *Physical Review B* **71**(014106) (2005).

[72] Deo, C. S., Srolovitz, D. J., Cai, W., and Bulatov, V. V. *Journal of the Mechanics and Physics of Solids* **53**(6), 1223–1247 (2005).

[73] Schwarz, K. W. *Journal of Applied Physics* **85**(1), 108–119 (1999).

[74] Ghoniem, N. M., Tong, S. H., and Sun, L. Z. *Physical Review B* **61**(2), 913 (2000).

[75] Rhee, M., Zbib, H. M., Hirth, J. P., Huang, H., and Rubia, T. d. l. *Modelling and Simulation in Materials Science and Engineering* **6**, 467–492 (1998).

[76] Bulatov, V. V., Hsiung, L. L., Tang, M., Arsenlis, A., Bartelt, M. C., Cai, W., Florando, J. N., Hiratani, M., Rhee, M., and Hommes, G. *Nature* **440**(7088), 1174–1178 (2006).

[77] Friedrich, W., Knipping, P., and Laue, M. *Annalen der Physik* **346**(10), 971–988 (1913).

[78] Bragg, W. L. *Proceedings of the Cambridge Philosophical Society* **17**, 43–57 (1913).

[79] Ewald, P. *Acta Crystallographica Section A* **35**(1), 1–9 (1979).

[80] Hammond, C. *The Basics of Crystallography and Diffraction*. Oxford University Press, (2001).

[81] Warren, B. E. *X-ray Diffraction*. Courier Dover Publications, (1990).

[82] Authier, A. *Dynamical Theory of X-Ray Diffraction*. Oxford University Press, (2004).

[83] Debye, P. *Annalen der Physik* **351**(6), 809–823 (1914).

[84] Fewster, P. F. *Critical Reviews in Solid State and Materials Sciences* **22**(2), 69 – 110 (1997).

[85] Breuer, D., Klimanek, P., and Pantleon, W. *Journal of Applied Crystallography* **33**(5), 1284–1294 (2000).

[86] Mughrabi, H. *Acta Metallurgica* **31**(9), 1367–1379 (1983).

[87] Mughrabi, H. *Materials Science and Engineering* **85**, 15–31 (1987).

[88] Mughrabi, H. and Ungar, T. In *Dislocations in Solids,* Nabarro, F. R. N. and Duesbery, M., editors, volume 11, 343–411. Elsevier (2002).

[89] Pantleon, W., Poulsen, H. F., Almer, J., and Lienert, U. *Materials Science and Engineering A* **387-389**, 339–342 (2004).

[90] Lienert, U., Han, T. S., Almer, J., Dawson, P. R., Leffers, T., Margulies, L., Nielsen, S. F., Poulsen, H. F., and Schmidt, S. *Acta Materialia* **52**(15), 4461–4467 (2004).

[91] Jakobsen, B., Poulsen, H. F., Lienert, U., Almer, J., Shastri, S. D., Sorensen, H. O., Gundlach, C., and Pantleon, W. *Science* **312**(5775), 889–892 (2006).

[92] Jakobsen, B., Poulsen, H. F., Lienert, U., and Pantleon, W. *Acta Materialia* **55**(10), 3421–3430 (2007).

[93] Jakobsen, B., Lienert, U., Almer, J., Poulsen, H. F., and Pantleon, W. *Materials Science and Engineering: A* **483-484**, 641–643 (2008).

[94] Ribarik, G., Ungar, T., and Gubicza, J. *Journal of Applied Crystallography* **34**(5), 669–676 (2001).

[95] Jakobsen, B., Poulsen, H. F., Lienert, U., Huang, X., and Pantleon, W. *Scripta Materialia* **56**(9), 769–772 (2007).

[96] Jakobsen, B., Poulsen, H. F., Lienert, U., Bernier, J., Gundlach, C., and Pantleon, W. *physica status solidi (a)* **206**(1), 21–30 (2008).

[97] Chung, J.-S. and Ice, G. E. *Journal of Applied Physics* **86**(9), 5249–5255 (1999).

[98] Busing, W. R. and Levy, H. A. *Acta Crystallographica* **22**(4), 457–464 (1967).

[99] Tamura, N., Celestre, R. S., MacDowell, A. A., Padmore, H. A., Spolenak, R., Valek, B. C., Chang, N. M., Manceau, A., and Patel, J. R. In *Papers from the 12th National Synchrotron Radiation Instrumentation Conference*, volume 73, 1369–1372 (AIP, Madison, Wisconsin (USA), 2002).

[100] Ice, G. E., Chung, J.-S., Lowe, W., Williams, E., and Edelman, J. *Review of Scientific Instruments* **71**(5), 2001–2006 (2000).

[101] MacDowell, A. A., Celestre, R. S., Tamura, N., Spolenak, R., Valek, B., Brown, W. L., Bravman, J. C., Padmore, H. A., Batterman, B. W., and Patel, J. R. *Nuclear Instruments and Methods in Physics Research Section A: Accelerators, Spectrometers, Detectors and Associated Equipment* **467-468**(Part 2), 936–943 (2001).

[102] Ice, G. E. and Larson, B. C. *Advanced Engineering Materials* **2**(10), 643–646 (2000).

[103] Ice, G. E., Pang, J. W. L., Larson, B. C., Budai, J. D., Tischler, J. Z., Choi, J.-Y., Liu, W., Liu, C., Assoufid, L., Shu, D., and Khounsary, A. *Materials Science and Engineering: A* **524**(1-2), 3–9 (2009).

[104] Kirkpatrick, P. and Baez, A. V. *J. Opt. Soc. Am.* **38**(9), 766–773 (1948).

[105] Mimura, H., Handa, S., Kimura, T., Yumoto, H., Yamakawa, D., Yokoyama, H., Matsuyama, S., Inagaki, K., Yamamura, K., Sano, Y., Tamasaku, K., Nishino, Y., Yabashi, M., Ishikawa, T., and Yamauchi, K. *Nat Phys* **6**, 122–125 (2010).

[106] Tamura, N., MacDowell, A. A., Celestre, R. S., Padmore, H. A., Valek, B., Bravman, J. C., Spolenak, R., Brown, W. L., Marieb, T., Fujimoto, H., Batterman, B. W., and Patel, J. R. *Applied Physics Letters* **80**(20), 3724–3726 (2002).

[107] Tamura, N., MacDowell, A. A., Spolenak, R., Valek, B. C., Bravman, J. C., Brown, W. L., Celestre, R. S., Padmore, H. A., Batterman, B. W., and Patel, J. R. *Journal of Synchrotron Radiation* **10**(2), 137–143 (2003).

[108] Spolenak, R., Brown, W. L., Tamura, N., MacDowell, A. A., Celestre, R. S., Padmore, H. A., Valek, B., Bravman, J. C., Marieb, T., Fujimoto, H., Batterman, B. W., and Patel, J. R. *Physical Review Letters* **90**(9), 096102 (2003).

[109] Phillips, M. A., Spolenak, R., Tamura, N., Brown, W. L., MacDowell, A. A., Celestre, R. S., Padmore, H. A., Batterman, B. W., Arzt, E., and Patel, J. R. *Microelectronic Engineering* **75**(1), 117–126 (2004).

[110] Budai, J. D., Yang, W., Tamura, N., Chung, J.-S., Tischler, J. Z., Larson, B. C., Ice, G. E., Park, C., and Norton, D. P. *Nat Mater* **2**(7), 487–492 (2003).

[111] Barabash, R. I., Ice, G. E., Liu, W., Einfeldt, S., Roskowski, A. M., and Davis, R. F. *Journal of Applied Physics* **97**(1), 013504–5 (2005).

[112] Barabash, R. I., Roder, C., Ice, G. E., Einfeldt, S., Budai, J. D., Barabash, O. M., Figge, S., and Hommel, D. *Journal of Applied Physics* **100**(5), 053103–11 (2006).

[113] Choi, W. J., Lee, T. Y., Tu, K. N., Tamura, N., Celestre, R. S., MacDowell, A. A., Bong, Y. Y., Nguyen, L., and Sheng, G. T. T. In *Electronic Components and Technology Conference*, (2002).

[114] Choi, W. J., Lee, T. Y., Tu, K. N., Tamura, N., Celestre, R. S., MacDowell, A. A., Bong, Y. Y., and Nguyen, L. *Acta Materialia* **51**(20), 6253–6261 (2003).

[115] Suh, J. O., Tu, K. N., and Tamura, N. *Journal of Applied Physics* **102**(6), 063511 (2007).

[116] Barabash, R. I., Ice, G. E., Tamura, N., Valek, B. C., Bravman, J. C., Spolenak, R., and Patel, J. R. *Microelectronic Engineering* **75**(1), 24–30 (2004).

[117] Cargill, G. S., Moyer, L. E., Wang, G., Zhang, H., Hu, C. K., Yang, W., Larson, B. C., and Ice, G. E. *AIP Conference Proceedings* **817**(1), 303–309 (2006).

[118] Maaß, R., Van Petegem, S., Grolimund, D., Van Swygenhoven, H., and Uchic, M. D. *Applied Physics Letters* **91**(13), 131909–3 (2007).

[119] Maaß, R., Van Petegem, S., Van Swygenhoven, H., Derlet, P. M., Volkert, C. A., and Grolimund, D. *Physical Review Letters* **99**(14), 145505–4 (2007).

[120] Maaß, R., Van Petegem, S., Grolimund, D., Van Swygenhoven, H., Kiener, D., and Dehm, G. *Applied Physics Letters* **92**(7), 071905–3 (2008).

[121] Maaß, R., Van Petegem, S., Zimmermann, J., Borca, C. N., and Van Swygenhoven, H. *Scripta Materialia* **59**(4), 471–474 (2008).

[122] Gruber, P. A., Solenthaler, C., Arzt, E., and Spolenak, R. *Acta Materialia* **56**(8), 1876–1889 (2008).

[123] Barabash, R., Ice, G. E., Larson, B. C., Pharr, G. M., Chung, K. S., and Yang, W. *Applied Physics Letters* **79**(6), 749–751 (2001).

[124] Barabash, R. I., Ice, G. E., Larson, B. C., and Yang, W. In *Papers from the 12th National Synchrotron Radiation Instrumentation Conference*, volume 73, 1652–1654 (AIP, Madison, Wisconsin (USA), 2002).

[125] Barabash, R. I., Ice, G. E., and Walker, F. J. *Journal of Applied Physics* **93**(3), 1457–1464 (2003).

[126] Ice, G. E., Barabash, R. I., and Walker, F. J. *Composites Part B: Engineering* **36**(3), 271–277 (2005).

[127] Barabash, O. M., Horton, J. A., Babu, S. S., Vitek, J. M., David, S. A., Park, J. W., Ice, G. E., and Barabash, R. I. *Journal of Applied Physics* **96**(7), 3673–3679 (2004).

[128] Barabash, R. I., Ice, G. E., and Pang, J. W. L. *Materials Science and Engineering A* **400-401**, 125–131 (2005).

[129] Stock, S. R., Guvenilir, A., Piotrowski, D. P., and Rek, Z. U. In *Materials Research Society Symposium - Proceedings*, volume 375, 275–280, (1995).

[130] Larson, B. C., Tamura, N., Chung, J. S., Ice, G. E., Budai, J. D., Tischler, J. Z., Yang, W., Weiland, H., and Lowe, W. P. *Materials Research Society Symposium - Proceedings* **590**, 247–252 (2000).

[131] Larson, B. C., Yang, W., Tischler, J. Z., Ice, G. E., Budai, J. D., Liu, W., and Weiland, H. *International Journal of Plasticity* **20**(3), 543–560 (2004).

[132] Yang, W., Larson, B. C., Tischler, J. Z., Ice, G. E., Budai, J. D., and Liu, W. *Micron* **35**(6), 431–439 (2004).

[133] Larson, B. C., Yang, W., Ice, G. E., Budai, J. D., and Tischler, J. Z. *Nature* **415**(6874), 887–890 (2002).

[134] Yang, W., Larson, B. C., Ice, G. E., Tischler, J. Z., Budai, J. D., Chung, K. S., and Lowe, W. P. *Applied Physics Letters* **82**(22), 3856–3858 (2003).

[135] Liu, W., Ice, G. E., Larson, B. C., Yang, W., and Tischler, J. Z. *Ultramicroscopy* **103**(3), 199–204 (2005).

[136] Ohashi, T., Barabash, R. I., Pang, J. W. L., Ice, G. E., and Barabash, O. M. *International Journal of Plasticity* **25**(5), 920–941 (2009).

[137] Ice, G. E., Larson, B. C., Yang, W., Budai, J. D., Tischler, J. Z., Pang, J. W. L., Barabash, R. I., and Liu, W. *Journal of Synchrotron Radiation* **12**(2), 155–162 (2005).

[138] Ice, G. E., Larson, B. C., Tischler, J. Z., Liu, W., and Yang, W. *Materials Science and Engineering: A* **399**(1-2), 43–48 (2005).

[139] Barabash, R., Barabash, O. M., Ice, G. E., David, S. A., Feng, Z., and Horton Jr, J. A. *Reviews on Advanced Materials Science* **15**(1), 49–55 (2007).

[140] Barabash, R. I., Ice, G. E., Liu, W., and Barabash, O. M. *Micron* **40**(1), 28–36 (2009).

[141] Bei, H., Barabash, R. I., Ice, G. E., Liu, W., Tischler, J., and George, E. P. *Applied Physics Letters* **93**(7), 071904–3 (2008).

[142] Budai, J. D., Liu, W., Tischler, J. Z., Pan, Z. W., Norton, D. P., Larson, B. C., Yang, W., and Ice, G. E. *Thin Solid Films* **516**(22), 8013–8021 (2008).

[143] Poulsen, H. F., Nielsen, S. F., Lauridsen, E. M., Schmidt, S., Suter, R. M., Lienert, U., Margulies, L., Lorentzen, T., and Juul Jensen, D. *Journal of Applied Crystallography* **34**(6), 751–756 (2001).

[144] Nielsen, S. F., Lauridsen, E. M., Juul Jensen, D., and Poulsen, H. F. *Materials Science and Engineering A* **319-321**, 179–181 (2001).

[145] Fu, X., Poulsen, H. F., Schmidt, S., Nielsen, S. F., Lauridsen, E. M., and Juul Jensen, D. *Scripta Materialia* **49**(11), 1093–1096 (2003).

[146] Fu, X., Knudsen, E., Poulsen, H. F., Herman, G. T., Carvalho, B. M., and Liao, H. Y. *Optical Engineering* **45**(11), 116501–9 (2006).

[147] Poulsen, H. F., Andersen, N. H., Gottschalck Andersen, L., and Lienert, U. *Physica C: Superconductivity* **370**(3), 141–145 (2002).

[148] Schmidt, S., Olsen, U. L., Poulsen, H. F., Sørensen, H. O., Lauridsen, E. M., Margulies, L., Maurice, C., and Juul Jensen, D. *Scripta Materialia* **59**(5), 491–494 (2008).

[149] Offerman, S. E., van Dijk, N. H., Sietsma, J., Lauridsen, E. M., Margulies, L., Grigull, S., Poulsen, H. F., and van der Zwaag, S. *Nuclear Instruments and Methods in Physics Research Section B: Beam Interactions with Materials and Atoms* **238**(1-4), 107–110 (2005).

[150] Larsen, A. W., Poulsen, H. F., Margulies, L., Gundlach, C., Xing, Q., Huang, X., and Jensen, D. J. *Scripta Materialia* **53**(5), 553–557 (2005).

[151] Berveiller, S., Malard, B., and Patoor, E. In *European Symposium on Martensitic Transformations*, number 02003, 5, (2009).

[152] Hedstrøm, P., Lienert, U., Almer, J., and Odén, M. *Materials Letters* **62**(2), 338–340 (2008).

[153] Rodek, L., Poulsen, H. F., Knudsen, E., and Herman, G. T. *Journal of Applied Crystallography* **40**(2), 313–321 (2007).

[154] West, S. S., Schmidt, S., Sørensen, H. O., Winther, G., Poulsen, H. F., Margulies, L., Gundlach, C., and Juul Jensen, D. *Scripta Materialia* **61**(9), 875–878 (2009).

[155] Ludwig, W., Schmidt, S., Lauridsen, E. M., and Poulsen, H. F. *Journal of Applied Crystallography* **41**(2), 302–309 (2008).

[156] Johnson, G., King, A., Honnicke, M. G., Marrow, J., and Ludwig, W. *Journal of Applied Crystallography* **41**(2), 310–318 (2008).

[157] Ludwig, W., Reischig, P., King, A., Herbig, M., Lauridsen, E. M., Johnson, G., Marrow, T. J., and Buffière, J. Y. *Review of Scientific Instruments* **80**(3), 033905–9 (2009).

[158] Oddershede, J., Schmidt, S., Poulsen, H. F., Sorensen, H. O., Wright, J., and Reimers, W. *Journal of Applied Crystallography* **43**(3), 539–549 (2010).

[159] King, A., Johnson, G., Engelberg, D., Ludwig, W., and Marrow, J. *Science* **321**(5887), 382–385 (2008).

[160] King, A., Herbig, M., Ludwig, W., Reischig, P., Lauridsen, E. M., Marrow, T., and Buffière, J. Y. *Nuclear Instruments and Methods in Physics Research Section B: Beam Interactions with Materials and Atoms* **268**(3-4), 291–296 (2010).

[161] Hofmann, F., Song, X., Eve, S., Collins, S. P., and Korsunsky, A. M. *Materials Letters* **63**(12), 1077–1081 (2009).

[162] Abbey, B., Hofmann, F., Belnoue, J., Rack, A., Tucoulou, R., Hughes, G., Eve, S., and Korsunsky, A. M. *Scripta Materialia* **in press** (2011).

[163] Lang, A. *Acta Crystallographica* **12**(3), 249–250 (1959).

[164] Ramachandran, G. N. *Proceedings of the Indian Academy of Science* **19**(A), 280 (1944).

[165] Wooster, N. and Wooster, W. A. *Nature* **155**, 786–787 (1945).

[166] Tuomi, T., Naukkarinen, K., and Rabe, P. *physica status solidi (a)* **25**(1), 93–106 (1974).

[167] Polcarova, M. and Bradler, J. *Journal of Applied Crystallography* **20**(5), 374–378 (1987).

[168] Goto, K., Hondoh, T., and Higashi, A. *Japanese Journal of Applied Physics* **25**(Part 1, No. 3), 351–357 (1986).

[169] Shearwood, C. and Whitworth, R. W. *Journal of Glaciology* **35**(120), 281–283 (1989).

[170] Authier, A. and Lang, A. R. *Journal of Applied Physics* **35**(6), 1956–1959 (1964).

[171] Patel, J. R. and Authier, A. *Journal of Applied Physics* **46**(1), 118–125 (1975).

[172] Chikawa, J.-i., Fujimoto, I., and Abe, T. *Applied Physics Letters* **21**(6), 295–298 (1972).

[173] Hielscher, R. and Schaeben, H. *Journal of Applied Crystallography* **41**(6), 1024–1037 (2008).

[174] Déchamps, M., Baribier, F., and Marrouche, A. *Acta Metallurgica* **35**(1), 101–107 (1987).

[175] Winther, G. *Materials Science and Engineering: A* **483-484**, 40–46 (2008).

[176] Winther, G. *Acta Materialia* **51**(2), 417–429 (2003).

[177] Bay, B., Hansen, N., Hughes, D. A., and Kuhlmann-Wilsdorf, D. *Acta Metallurgica et Materialia* **40**(2), 205–219 (1992).

[178] Huang, X. *Scripta Materialia* **38**(11), 1697–1703 (1998).

[179] Nye, J. F. *Acta Metallurgica* **1**(2), 153–162 (1953).

[180] Norfleet, D. M., Dimiduk, D. M., Polasik, S. J., Uchic, M. D., and Mills, M. J. *Acta Materialia* **56**(13), 2988–3001 (2008).

[181] Korsunsky, A. M., Hofmann, F., Song, X., Eve, S., and Collins, S. P. *Journal of Nanoscience and Nanotechnology* **10**, 5935–5950 (2010).

[182] Robach, O., Micha, J.-S., Le Bourlot, C., Faurie, D., Chiron, R., and Castelnau, O. *Journal of Applied Crystallography* **under review** (2010).

[183] Korsunsky, A. M., Collins, S. P., Owen, R. A., Daymond, M. R., Achtioui, S., and James, K. E. *Journal of Synchrotron Radiation* **9**(2), 77–81 (2002).

[184] Zhang, S. Y. *High energy white beam x-ray diffraction studies of strains in engineering materials and components*. PhD thesis, University of Oxford, (2008).

[185] Korsunsky, A. M., Song, X., Hofmann, F., Abbey, B., Xie, M., Connolley, T., Reinhard, C., Atwood, R. C., Connor, L., and Drakopoulos, M. *Materials Letters* **64**(15), 1724–1727 (2010).

[186] Wortman, J. J. and Evans, R. A. *Journal of Applied Physics* **36**(1), 153–156 (1965).

[187] Muchmore, C. R. A. 22/10/2010 (2010).

[188] Agnew, S. R. and Weertman, J. R. *Materials Science and Engineering A* **242**(1-2), 174–180 (1998).

[189] Nye, J. F. *Physical Properties of Crystals*. Clarendon Press, Oxford, (1985).

[190] Kiener, D. *Size effects in single crystal plasticity of copper under uniaxial loading*. PhD thesis, Montanuniversität Leoben, (2007).

[191] Song, X., Hofmann, F., and Korsunsky, A. M. *Philosophical Magazine* **90**(30), 3999–4011 (2010).

[192] Bilby, B. A. and Eshelby, J. D. In *Microscopic and Macroscopic Fundamentals,* Liebowitz, H., editor, volume 1. Academic Press, New York and London (1968).

[193] Kreyszig, E. *Advanced Engineering Mathematics*. Wiley, 6 edition, (1988).

[194] Smithells, C. J. *Smithells Metals Reference Book*. Butterworths, London, (1983).

[195] Barnett, D. M. *Philosophical Magazine A* **51**(3), 383 – 387 (1985).

[196] Barnett, D. M. and Balluffi, R. W. *Philosophical Magazine Letters* **87**(12), 943 – 944 (2007).

[197] Hirth, J. P. and Lothe, J. *Theory of Dislocations*. Wiley, New York, 2 edition, (1982).

[198] Wanner, A. and Dunand, D. *Metallurgical and Materials Transactions A* **31**(11), 2949–2962 (2000).

[199] Cheng, S., Stoica, A. D., Wang, X. L., Ren, Y., Almer, J., Horton, J. A., Liu, C. T., Clausen, B., Brown, D. W., Liaw, P. K., and Zuo, L. *Physical Review Letters* **103**(3), 035502 (2009).

[200] Steuwer, A., Santisteban, J. R., Turski, M., Withers, P. J., and Buslaps, T. *Nuclear Instruments and Methods in Physics Research Section B: Beam Interactions with Materials and Atoms* **238**(1-4), 200–204 (2005).

[201] Mika, D. P. and Dawson, P. R. *Materials Science and Engineering: A* **257**(1), 62–76 (1998).

[202] Sun, S., Adams, B. L., and King, W. E. *Philosophical Magazine A* **80**(1), 9 – 25 (2000).

[203] Gupta, V. K. and Agnew, S. R. *Journal of Applied Crystallography* **42**(1), 116–124 (2009).

[204] DLS. *http://www.diamond.ac.uk/Home/Beamlines/I12.html* (2010).

[205] Thales. Technical report, (2010).

[206] Korsunsky, A. M., Baimpas, N., Song, X., Belnoue, J. P., Hofmann, F., Abbey, B., Xie, M., Andrieux, J., Buslaps, T., and Neo, T. K. *Acta Materialia* **in press** (2011).

[207] Ice, G. E. and Pang, J. W. L. *Materials Characterization* **60**(11), 1191–1201 (2009).

[208] Larson, B. C., El-Azab, A., Yang, W., Tischler, J. Z., Liu, W., and Ice, G. E. *Philosophical Magazine* **87**(8), 1327 – 1347 (2007).

[209] Hofmann, F., Song, X., Dolbnya, I., Abbey, B., and Korsunsky, A. M. *Procedia Engineering* **1**(1), 193–196 (2009).

[210] Hofmann, F., Abbey, B., Song, X., Dolbnya, I., and Korsunsky, A. M. *International Journal of Modern Physics B* **24**(1 and 2), 279–287 (2009).

[211] Hofmann, F., Korsunsky, A. M., Abbey, B., Dolbnya, I., Xie, M., and Song, X. *Diamond Light Source Proceedings* **1**(e112) (2010).

[212] Micha, J.-S. 13/02/2010 (Feb 2010).

[213] Hofmann, F., Song, X., Jun, T. S., Abbey, B., Peel, M., Daniels, J., Honkimäki, V., and Korsunsky, A. M. *Materials Letters* **64**(11), 1302–1305 (2010).

[214] Goodfellow. (2011).

[215] Mahajan, S., Pande, C. S., Imam, M. A., and Rath, B. B. *Acta Materialia* **45**(6), 2633–2638 (1997).

Appendix A

Methods

A.1 Ni foil samples

In this thesis a particular focus was placed on the study of the deformation behaviour of commercially pure (CP) nickel. It is an ideal prototype material for the development of crystal plasticity and dislocation dynamics simulations, due to its simple FCC crystal structure. The material be easily heat treated to produce large-grained samples with low initial defect density. This makes it very suitable for in situ studies of micro-deformation by micro-diffraction techniques.

A.1.1 Original state of the Ni foils

Two different thicknesses of commercially pure (99.9%) nickel foil supplied by Goodfellow [214] were considered: $15\mu\mathrm{m}$ and $300\mu\mathrm{m}$. The $300\mu\mathrm{m}$ thick foil was reduced to thickness by rolling and was supplied in as rolled state. The $15\mu\mathrm{m}$ thick foil was sputtered and supplied in as sputtered state.

A.1.2 Sample preparation and heat treatment

Samples were cut from the nickel foils by sandwiching them between the two halves of a sample-shaped former. Any excess material protruding from the former was removed using files ($300\mu\mathrm{m}$ thick foil) or a razor ($15\mu\mathrm{m}$ thick foil). The surface finish of the thin foils was sufficiently good not to require any further treatment or

polishing before heat treatment. The $300\mu\mathrm{m}$ thick foils were mechanically ground using SiC paper and lapping films down to $1\mu\mathrm{m}$ diamonds.

For the heat treatment samples were enclosed in evacuated quartz vials to prevent oxidation. Cleanliness of samples and vials was vital to minimise any contamination, which would reduce the quality of the heat treated sample surface. Heat treatment was carried out at 1200° C, followed by a furnace cool over 24 hours. For the $300\mu\mathrm{m}$ foils samples a heat treatment time of 4 hours was sufficient for complete recrystallisation. Longer treatment times resulted in some further grain growth. For all samples in this thesis, treatment times of 4 hours were used.

The $15\mu\mathrm{m}$ thick samples required a treatment time of 8 hours for complete recrystallisation. Longer treatment times only led to insignificant further grain growth.

A.1.3 Virgin material characterisation

The as heat treated material will be referred to in general as the virgin material. Figure A.1 shows a polarised light optical micrograph of a heat treated $300\mu\mathrm{m}$ thick nickel foil. Individual grains and twins can be clearly made out. Average grain size was of the order of $\sim 500\mu\mathrm{m}$ with maximum grain sizes in excess of $1\mathrm{mm}$ and minimum grain sizes of less than $100\mu\mathrm{m}$. Given the ration of grain diameter to sample thickness, most grains extended through the sample thickness.

In the $15\mu\mathrm{m}$ thick nickel foil, grains and twins were also readily identified in an optical polarised light micrograph (figure A.2). Grain size was of the order of $\sim 60\mu\mathrm{m}$, with some of the largest grains measuring in excess of $300\mu\mathrm{m}$ and a smallest grain size of $\sim 10\mu\mathrm{m}$. In most grains annealing twins are clearly visible. Whilst grain boundaries show a slight depression of the sample surface, this is not the case for twin boundaries.

To assess the orientation of grain boundaries and twin boundaries through the sample thickness, focused ion beam (FIB) sectioning was performed on the $15\mu\mathrm{m}$ thick foil. Such a FIB section is shown in figure A.3. Different lattice orientations are highlighted due to channeling contrast. Locations of twin boundaries are marked by yellow arrows. The grain boundary which was also sectioned is marked by red arrows. A number of sections were made on different samples. In general it was

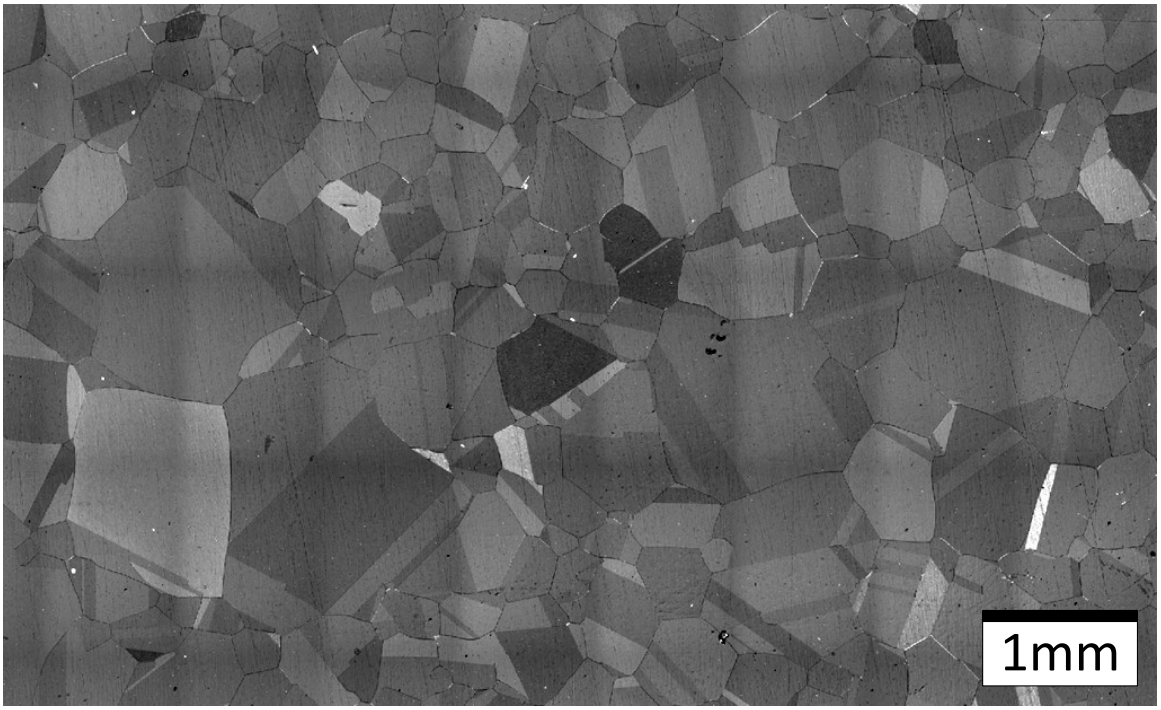

Figure A.1: Optical micrograph of a $300\mu\mathrm{m}$ thick nickel foil after heat treatment.

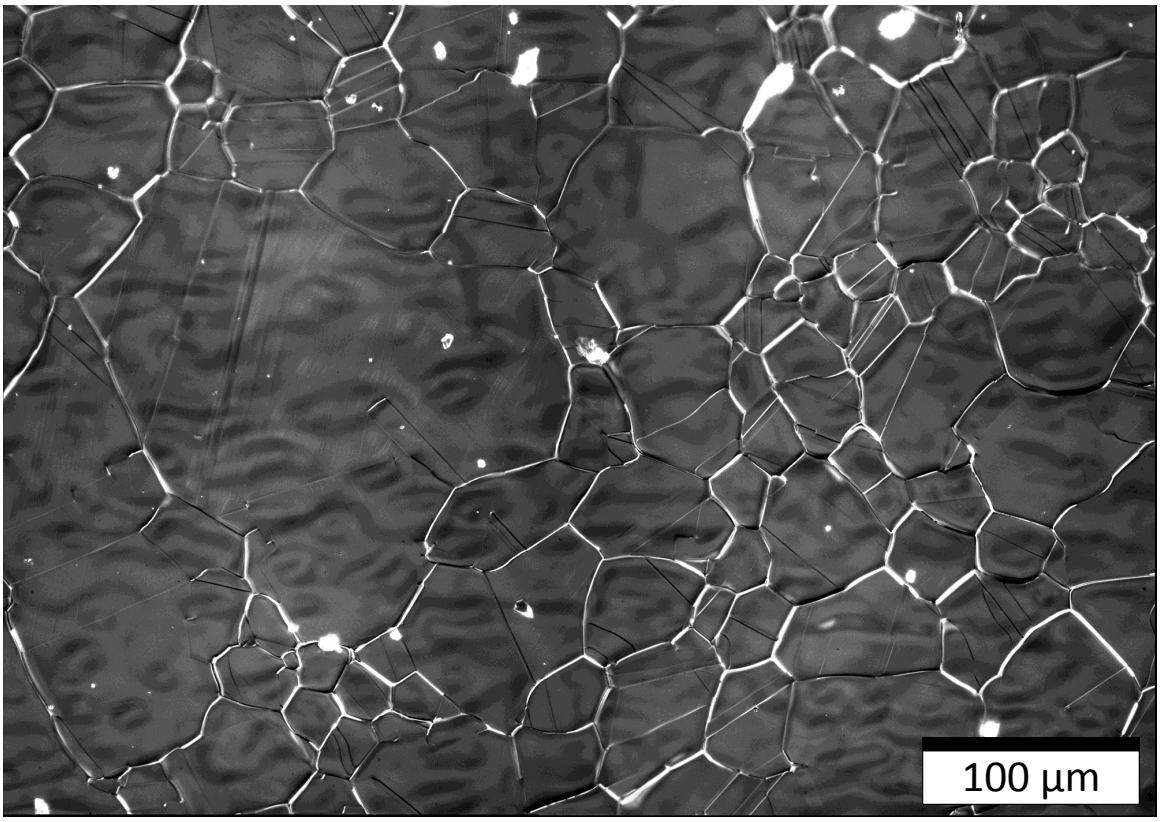

Figure A.2: Optical micrograph of a $15\mu\mathrm{m}$ thick nickel foil after heat treatment.

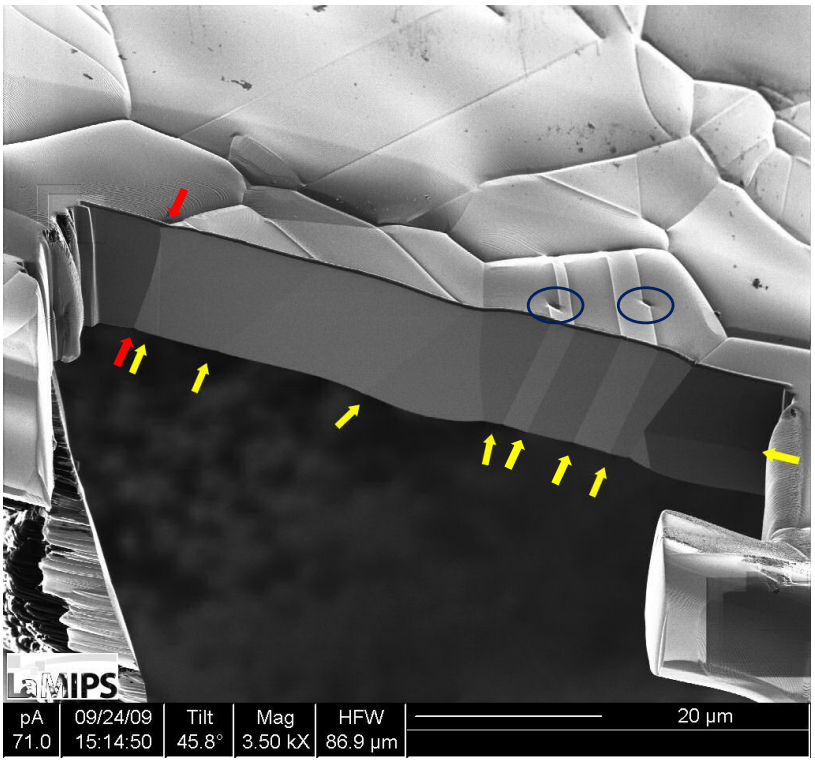

Figure A.3: FIB crossection of a $15\mu\mathrm{m}$ thick nickel foil after heat treatment, showing twin boundaries (yellow arrows), a grain boundary (red arrows) and stepped twin boundaries (blue circles).

found that grain boundaries were orientated approximately normal to the surface, whilst twin boundaries were often inclined and did not have a particular orientation relationship to the sample surface. In the optical and FIB micrographs stepped twin boundaries were frequently observed (figure A.3, blue circles), as mentioned elsewhere in the literature [215].

A.2 Image treatment

Before indexation it is essential that the background in Laue diffraction patterns due to diffuse scattering and fluorescence is subtracted. Only then can a correct search and indexation of the Laue peaks be performed. Here, as suggested elsewhere in the literature [203], a median filter was applied to the raw images $\mathbf{I}_{\mathrm{raw}}$ to compute the background $\mathbf{I}_{\mathrm{bkg}}$. A good compromise between reproducing the background and discriminating against reflections was found using an 80×80 pixel median

filter. The final image $\mathbf{I}_{\mathrm{f}}$ ready for indexation and analysis is given by:

$$\mathbf{I}_{\mathrm{f}} = \mathbf{I}_{\mathrm{raw}} - \mathbf{I}_{\mathrm{bkg}}. \tag{A.1}$$

For images recorded using optical taper coupled scintillator CCD cameras, a border of 50 pixels around the edge of the image was set to zero to remove any edge effects due to the optical taper and the distortion correction.

As an illustration a raw diffraction pattern collected from a nickel grain in transmission geometry on beamline ID15 (ESRF) was considered (§ 5.2). Figure A.4 a) shows the distortion corrected image, $\mathbf{I}_{\mathrm{raw}}$, displayed in a range from 900(white) to 1100(black) counts. The non-uniform background with superimposed diffraction peaks is clearly visible. For demonstration a square region of this image was selected. The 80×80 pixel median filtered background of this region is shown in figure A.4 b) with a display range from 900(white) to 1100(black) counts. This background is subtracted from the raw image to give $\mathbf{I}_{\mathrm{f}}$, shown in figure A.4 c) with a display range from 0(white) to 20(black) counts. Clearly the background subtraction is very effective. Diffraction peaks are now clearly visible against a near zero background. The maximum amplitude of any residual noise was ~ 5 counts.

A.3 Micro-beam Laue ray tracing framework

This section describes the forward ray tracing routine which was used to determine Laue diffraction spot positions on an area detector. For a given crystal with crystal axes $\mathbf{a}_1$, $\mathbf{a}_2$, $\mathbf{a}_3$ in the crystal reference frame, a set of reciprocal space vectors can be defined as:

$$\mathbf{b}_1 = \frac{\mathbf{a}_2 \times \mathbf{a}_3}{\mathbf{a}_1 \cdot \mathbf{a}_2 \times \mathbf{a}_3}, \tag{A.2}$$

$$\mathbf{b}_2 = \frac{\mathbf{a}_3 \times \mathbf{a}_1}{\mathbf{a}_1 \cdot \mathbf{a}_2 \times \mathbf{a}_3}, \tag{A.3}$$

$$\mathbf{b}_3 = \frac{\mathbf{a}_1 \times \mathbf{a}_2}{\mathbf{a}_1 \cdot \mathbf{a}_2 \times \mathbf{a}_3}. \tag{A.4}$$

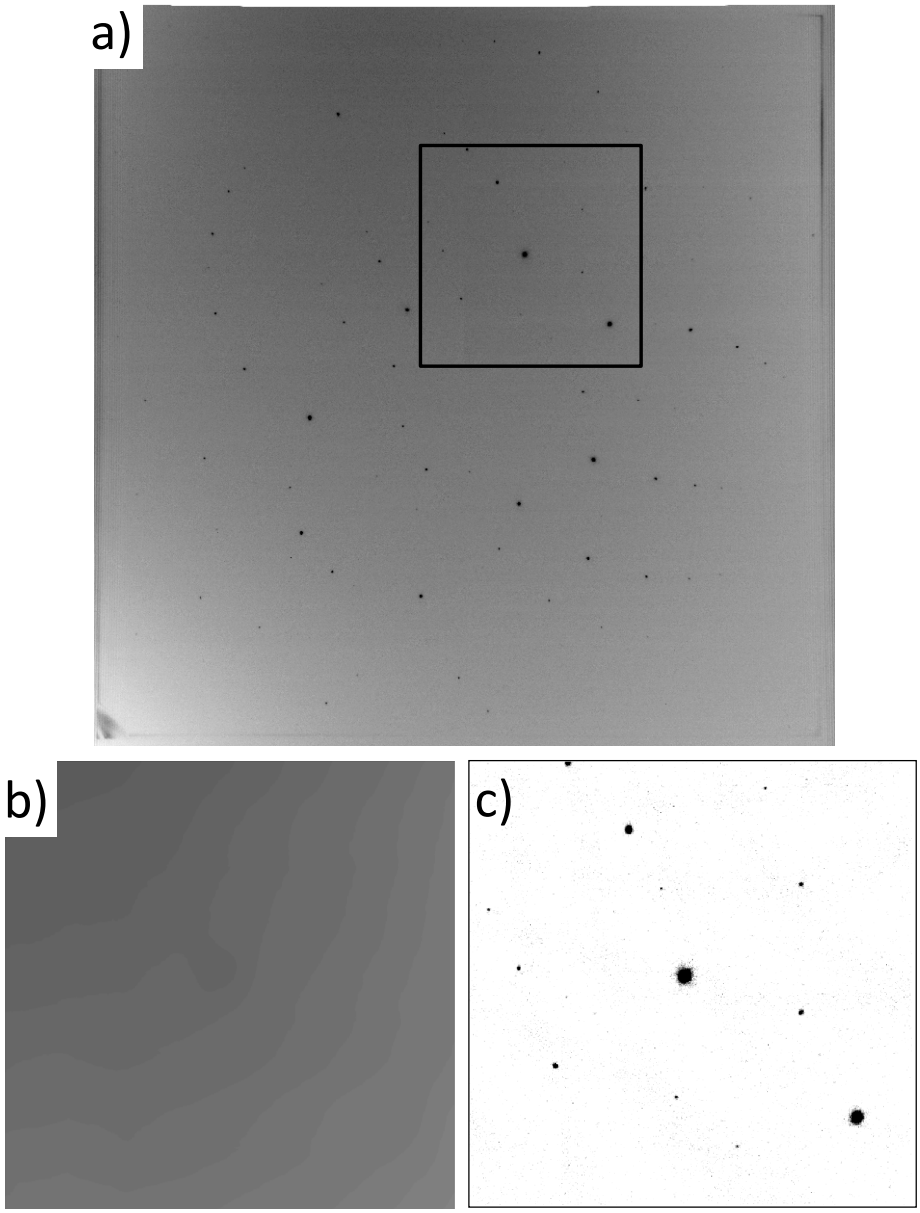

Figure A.4: Background subtraction from Laue diffraction images. a) Raw Laue diffraction image from an undeformed nickel grain recorded in transmission configuration at ID15 (ESRF) (§ 5.2). A small square region was selected for demonstration. b) Median filtered background for the region of interest. c) Region of interest in the background subtracted diffraction image.

For a scattering plane with Miller indices h,k, l a vector $\mathbf{H}_{hkl}$ can then be defined as:

$$\mathbf{H}_{hkl} = h\mathbf{b}_1 + k\mathbf{b}_2 + l\mathbf{b}_3. \tag{A.5}$$

The orientation relationship between the crystal and the lab reference frame can be captured by a rotation matrix $\mathbf{R}$ which maps any vector from the crystal reference frame into the lab reference frame. Hence in lab coordinates the normal to the scattering plane under consideration is:

$$\hat{\mathbf{n}} = \frac{\mathbf{R}\mathbf{H}_{hkl}}{|\mathbf{R}\mathbf{H}_{hkl}|}. \tag{A.6}$$

Figure A.5 shows the geometry of the setup. The incident beam direction $\hat{\mathbf{s}}_0$ is prescribed geometrically. Now, given that in the diffraction condition the plane normal $\hat{\mathbf{n}}$ bisects the angle between the incident beam direction $\hat{\mathbf{s}}_0$ and the scattered beam unit vector, $\hat{\mathbf{s}}$, the scattered beam unit vector $\hat{\mathbf{s}}$ can be computed as:

$$\hat{\mathbf{s}} = \hat{\mathbf{s}}_0 + 2(\hat{\mathbf{s}}_0 \cdot \hat{\mathbf{n}})\hat{\mathbf{n}}. \tag{A.7}$$

Based on the two perpendicular unit vectors $\hat{\mathbf{d}}_1$ and $\hat{\mathbf{d}}_2$ which define the primary and secondary detector axes in the detector plane, the normal to the detector plane, $\hat{\mathbf{d}}_s$, can be defined as:

$$\hat{\mathbf{d}}_s = \hat{\mathbf{d}}_1 \times \hat{\mathbf{d}}_2. \tag{A.8}$$

Vector $\mathbf{d}_c$, the shortest distance vector from the scattering centre to the detector surface is:

$$\mathbf{d}_c = (\mathbf{D} \cdot (-\hat{\mathbf{d}}_s))(-\hat{\mathbf{d}}_s). \tag{A.9}$$

where $\mathbf{D}$ is the vector from the scattering centre to the detector centre. Now the position vector $\mathbf{P}$ can be computed which captures the position of the reflection on the detector surface relative to the detector centre:

$$\mathbf{P} = \frac{|\mathbf{d}_c|}{\hat{\mathbf{s}} \cdot \hat{\mathbf{d}}_c}(\hat{\mathbf{s}} - \hat{\mathbf{d}}_c(\hat{\mathbf{s}} \cdot \hat{\mathbf{d}}_c)) - \mathbf{D} + \mathbf{d}_c. \tag{A.10}$$

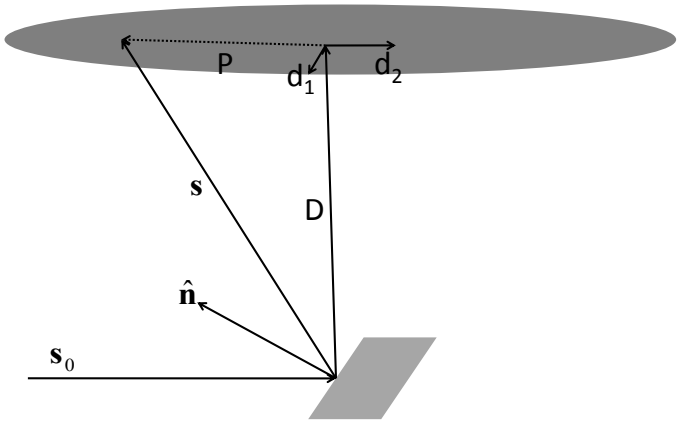

Figure A.5: General micro-beam Laue diffraction geometry

where $\hat{\mathbf{d}}_c$ is the unit vector in the direction of $\mathbf{d}_c$. Projection of vector $\mathbf{P}$ onto the detector axes $\hat{\mathbf{d}}_1$ and $\hat{\mathbf{d}}_2$ gives the position of the reflection on the detector in detector coordinates. To convert to pixel positions on the detector $\mathbf{P}_p$, $\mathbf{P}$ needs to be normalised by the Pixel size and the detector centre pixel positions, $xcent$ and $ycent$ added.

For a general crystal orientation defined by rotation matrix $\mathbf{R}$, it will not be known a priory which reflections will fall onto the detector. The simplest approach is to generate a list of all plane normals up to a given hkl order. For all of these plane normals ray tracing is carried out. For a reflection to actually occur, it needs to satisfy two conditions:

- It needs to lie within the angular range spanned by the detector. This can be checked by filtering the $\mathbf{P}_p$ positions and only allowing those that fall within the detector pixel matrix.

- The reflection needs to occur at an energy present within the incident beam photon energy spectrum. The energy E_{hkl} of a particular hkl reflection is given by $E_{hkl} = \frac{hc|\mathbf{H}_{hkl}|}{2\sin(\theta)}$, where $\theta = \frac{1}{2}\arccos(\hat{\mathbf{s}} \cdot \hat{\mathbf{s}}_0)$, h is Plank's constant and c the speed of light.

Further selection criteria can be included, for example to eliminate higher order reflections, etc. It should also be noted, that whilst in figure A.5 the reflection Laue geometry is shown, this ray tracing technique applies equally to the transmission Laue geometry.

A.4 Additive behaviour of Rodriguez vector for small rotations

A convenient representation of rotations is in terms of Rodriguez vector $\hat{\omega}$ and Rodriguez angle θ. It can be shown that for small rotations, Rodriguez vector contributions are additive.

A rotation matrix $\mathbf{R}_{\hat{\omega}}$ is defined in terms of unit Rodriguez vector $\hat{\omega} = (\omega_x, \omega_y, \omega_z)$ and Rodriguez angle θ as:

$$\mathbf{R}_{\hat{\omega}} = e^{\tilde{\omega}\theta} = \mathbf{I} + \tilde{\omega}\sin\theta + \tilde{\omega}^2(1 - \cos\theta), \tag{A.11}$$

where

$$\tilde{\omega} = \begin{bmatrix} 0 & -\omega_z & \omega_y \\ \omega_z & 0 & -\omega_x \\ -\omega_y & \omega_x & 0 \end{bmatrix}, \tag{A.12}$$

and $\mathbf{I}$ is the identity matrix and θ the angle of rotation around the axis of rotation given by unit vector $\hat{\omega}$. For small angles of θ, the following approximations can be made; $\sin\theta \approx \theta$ and $\cos\theta \approx 1$. Then the expression for Rodriguez vector simplifies to:

$$\mathbf{R}_{\hat{\omega}} = \mathbf{I} + \tilde{\omega}\theta. \tag{A.13}$$

Now consider a vector $\mathbf{r}$ which is rotated first about Rodriguez vector $\hat{\omega}_1$ by small angle θ_1 to give $\mathbf{r}_1$ and then about Rodriguez vector $\hat{\omega}_2$ by small angle θ_2 to give $\mathbf{r}_2$:

$$\mathbf{r}_1 = \mathbf{R}_1\mathbf{r} = (\mathbf{I} + \tilde{\omega}_1\theta_1)\mathbf{r} = \mathbf{r} + (\theta_1\hat{\omega}_1 \times \mathbf{r}), \tag{A.14}$$

$$\mathbf{r}_2 = \mathbf{R}_2\mathbf{r}_1 = (\mathbf{I} + \tilde{\omega}_2\theta_2)\mathbf{r}_1 = \mathbf{r}_1 + (\theta_2\hat{\omega}_2 \times \mathbf{r}_1) \tag{A.15}$$

$$= \mathbf{r} + \theta_1\hat{\omega}_1 \times \mathbf{r} + \theta_2\hat{\omega}_2 \times \mathbf{r} + \theta_2\hat{\omega}_2 \times (\theta_1\hat{\omega}_1 \times \mathbf{r}). \tag{A.16}$$

For small θ_1 and θ_2, the third term becomes small and $\mathbf{r}_2$ can be expressed as:

$$\mathbf{r}_2 = \mathbf{r} + (\theta_1\hat{\omega}_1 + \theta_2\hat{\omega}_2) \times \mathbf{r}. \tag{A.17}$$

This shows that for small rotations the individual Rodriguez vector contributions are additive.

Appendix B

Experimental visits

Data from a number of experimental visits is presented in this thesis:

May 08	I16 (DLS),	Al single grain reciprocal space mapping (§4.3).
July 08	I16 (DLS),	Al single grain reciprocal space mapping (§4.3).
Sept 08	B16 (DLS),	Micro-beam Laue, development of the experimental setup (§3.1.2).
Dec 08	B16 (DLS),	Micro-beam Laue, in situ deformation of Ni polycrystal (§3.1.2).
Mar 09	ID15A (ESRF),	High energy transmission Laue, in situ deformation of Ni polycrystal (§5.2).
May 09	B16 (DLS),	Reciprocal space mapping, energy scanning and micro-beam Laue diffraction (§3.1.3).
Sept 09	ID22 (ESRF),	Scanning white beam topography on deformed Ni polycrystal (§3.1.4).
Dec 09	B16 (DLS),	Combined micro-beam Laue and scanning white beam topography (§3.1.4).
Feb 10	BM32 (ESRF),	Four point bend silicon and copper bars (§3.2).
Feb 10	B16 (DLS),	Combined micro-beam Laue and scanning white beam topography (§3.1.4).
Sep 10	I12 (DLS),	Laue orientation tomography and high energy DAXM (§5.3 and §5.3.4).

Appendix C

Publications resulting from this thesis

Journal papers:

Analysis of the Internal Structure and Lattice (Mis)orientation in Individual Grains of Deformed Nickel Polycrystals by Synchrotron X-ray Micro-diffraction and Microscopy; AM Korsunsky, F Hofmann, B Abbey, X Song, J Belnoue, X Xu, C Mocuta, I Dolbnya, *Int. J. Fatigue*, accepted

Mapping the Dislocation Sub-structure of Deformed Polycrystalline Ni by Scanning Micro-beam Diffraction Topography; B Abbey, F Hofmann, J Belnoue, A Rack, R Tucoulou, G Hughes, S Eve, AM Korsunsky, *Scripta Materialia **64**, 9 (2011)*, pp. 884-887

Dislocation-based Plasticity Model and Micro-beam Laue Diffraction Analysis of Polycrystalline Ni Foil: A Forward Prediction; X Song, F Hofmann, AM Korsunsky, *Philosophical Magazine **90**, 29-30 (2010)*, pp. 3999-4011

High Energy Transmission Micro-beam Laue Synchrotron X-ray Diffraction; F Hofmann, X Song, TS Jun, B Abbey, M Peel, J Daniels, V Honkimäki, AM Korsunsky, *Materials Letters **64**, 11 (2010)*, pp. 1302-1305

On the Measurement and Interpretation of Residual Stress at the Micro-Scale; AM Korsunsky, E Bemporad; M Sebastiani, F Hofmann, S Dave; *International Journal of Modern Physics B **24**, 1-2 (2010)*, pp. 1-9

Intragranular Lattice Misorientation Mapping by Synchrotron X-ray Micro-Beams: Laue VS Energy-Resolved Laue VS Monochromatic Reciprocal Space Analysis; F Hofmann, B Abbey, X Song, I Dolbnya, AM Korsunsky; *International Journal of Modern Physics B **24**, 1-2 (2010)*, pp. 279-287

Probing Deformation Substructure by Synchrotron X-Ray Diffraction and Dislocation Dynamics Modelling; A M Korsunsky, F Hofmann, X Song, S Eve, S P Collins; *Journal of Nanoscience and Nanotechnology **10**, 9 (2010)*, pp. 5935-5950

Synchrotron X-ray Analysis of Microstructure and Micro-deformation in a Recast AA6063 Aluminium Alloy; AM Korsunsky, F Hofmann, B Abbey, G Gaucherin; *Journal of Strain Analysis **45**, 5 (2010)*, pp. 351-364

Synchrotron-based Reciprocal Space Mapping and Dislocation Substructure Analysis; F Hofmann, X Song, S Eve, S P Collins, A M Korsunsky; *Materials Letters **63**, 12 (2009)*, pp. 1077-1081

Conference papers:

Probing Mesoscopic Lattice Misorientation by Strain Gradient Crystal Plasticity Modelling and Micro-beam Laue Diffraction Experiments; X Song, F Hofmann, AM Korsunsky, *International Journal of Theoretical and Applied Multiscale Mechanics*, accepted

Combining Micro-beam Laue and White Beam Topography: Mapping Local Lattice Orientation and Misorientation; F Hofmann, AM Korsunsky, B Abbey, I Dolbnya, M Xie, X Song, Proceedings of SRMS-7 2010 Conference, *Diamond Light Source Proceedings **1**, e112 (2010)*, pp. 1-4

Micro-scale Characterisation of Deformation and Distortion in Ductile (Poly)Crystals by Synchrotron X-Ray Beams; AM Korsunsky, B Abbey, F Hofmann, I Dolbnya, SP Collins, M Xie, X Song, Proceedings of SRMS-7 2010 Conference, *Diamond Light Source Proceedings **1**, e101 (2010)*, pp. 1-5

Micro-beam Laue Diffraction: An Error Analysis; F Hofmann, AM Korsunsky, Proceedings of the Euromech 2010 Colloquium on metal fatigue, Ecole Polytechnique, Paris 2010

Probing Intragranular Deformation by Micro-Beam Laue Diffraction; F Hofmann, X Song, I Dolbnya, B Abbey, A M Korsunsky; Proceedings of Mesomechanics 2009 Conference; *Procedia Engineering **1**, 1 (2009)*, pp. 193-196

Other publications:

Studying Grain Level Deformation in Polycrystalline Engineering Materials - Micro-beam Laue and other Micro-diffraction Methods; F Hofmann, *Diamond Light Source Annual Report 2010*, pp. 31-34